KATHOLIEKE
UNIVERSITEIT
LEUVEN

Faculteit Wetenschappen
Departement Chemie
Moleculair Design en Synthese
Laboratorium voor Coördinatiechemie

Coordination of the uranyl ion in solution and ionic liquids

– A combined UV-Vis absorption and EXAFS study –

Proefschrift ingediend voor het behalen van de graad van

Doctor in de Wetenschappen

Kelly Servaes

Leuven, 5 juli 2007

Promotor: Prof. dr. C. Görller-Walrand

ISBN 978-90-8649-110-0

D/2007/10.705/32

EXAMINATION BOARD

Promotor:	Prof. dr. C. Görller-Walrand
Chairman:	Prof. dr. L. Vanquickenborne
Other members:	Prof. dr. K. Binnemans
	Prof. dr. K. Pierloot
	Prof. dr. M. Hendrickx
	Dr. M. Denecke (Forschungszentrum Karlsruhe, Institut für Nukleare Entsorgung)

EEN WOORDJE VAN DANK

Kijk dankbaar naar wat voorbij is!

Elk jaargetijde heeft zijn eigen pracht... Men mag van de herfst geen meiklokjes, en van de winter geen zomerzon verwachten.
Onvermijdelijk zijn samen met de lente ook de lentebloemen vergaan, en onherroepelijk nam de zomer de zomernachten mee. Ze zijn weg, maar hoe mooi waren zij! Hoe mooi waren de bloeiende kersenbomen in de boomgaarden, en de witte glanzende sleedoornhaag aan de wijngaardmuur, de dotterbloemen langs de beek en de madeliefjes in de zomerweide.
De herinnering is gebleven, en gebleven is daarmee ook een afstraling van het beleefde geluk.
Hoe belangrijk en bepalend het heden ook is, de rijkdom van een rijpe persoonlijkheid is dat men het verleden niet verliest, maar in de herinnering bewaart. Wie dankbaar het verleden gedenkt, kijkt vol hoop naar de toekomst.

Max Rössler

Na dit alleszeggende gedichtje zou ik het gewoon willen uitschreeuwen: “Bedankt allemaal!!!”. Toch zijn er een aantal mensen die ik eens extra in de bloemetjes wil zetten. Zonder hen zouden jullie immers dit boekje niet in jullie handen hebben.

Uiteraard gaat een (groot) woordje van dank uit naar mijn promotor, Prof. dr. C. Görller-Walrand. Ze heeft me de kans gegeven om me gedurende vijf jaar te verdiepen in de boeiende wereld van het uranylion en zijn verbindingen. Ze heeft me steeds met raad en daad bijgestaan. Menig uur hebben we dan ook samen gesleten in haar bureau, op zoek naar een mogelijke verklaring voor de vibrationele fijnstructuur in de spectra.

Verder moet ik Prof. dr. Koen Binnemans in de spotlight zetten. Bij hem kon ik steeds terecht met vragen over de praktische kant van mijn onderzoek. Met zijn uitgebreide kennis is hij me dikwijls ter hulp geschoten. Vooral tijdens het schrijven van mijn doctoraatsproefschrift stond hij steeds klaar met nuttige tips en voor het beantwoorden van mijn vragen.

The EXAFS part of this PhD thesis would not be so elaborate without dr. Christoph Hennig from the ROBL beamline at the ESRF. He was a great help in performing the sample preparation for EXAFS measurements in the correct way and in learning EXAFS data analysis. Thanks to Christoph I can now work with a soldering iron☺! He never hesitated to answer all my questions, and there were a lot during the past few months. Thank you, Christoph, for all your efforts and useful comments when correcting my PhD thesis! Also thanks to Andreas, André, Harald and Udo from the ROBL beamline for helping us during the EXAFS measurements. I have had a pleasant time at the ROBL beamline!

De kristalstructuurbepalingen en de NMR metingen zouden geen deel uitmaken van deze thesis zonder de hulp van Peter en Tanja. Verder wil ik Rik bedanken voor het afhandelen van de administratieve formaliteiten die steeds gepaard gingen met onze EXAFS metingen in Grenoble. Kris mag natuurlijk ook niet in het lijstje ontbreken. Bedankt voor de vele nuttige tips gedurende de afgelopen vijf jaar en het nalezen van mijn thesis!

Natuurlijk zijn er ook mijn thesisstudenten die elk hun steentje hebben bijgedragen aan dit eindresultaat: Ilse, Gitte en Juanjo. Ik vond het een waar genoegen om jullie te mogen begeleiden tijdens het afwerken van jullie licentiaatsthesis.☺

Tussen het harde werken door waren er gelukkig de labogenootjes die zorgden voor wat ontspanning en de vrolijke noot. Je kan je natuurlijk voorstellen dat het een komen en gaan geweest is van mensen op het labo COC. Toch wil ik proberen hier iedereen (oude en nieuwe garde) te vermelden: Els, Sandy, Katleen, Petra, Liesbet, Leen, Pascal, Philip, Antoine, Dries, Kristof, Jurgen, Steven, Rik, Linda, Thomas, Jan, Karel, Diederik, Ben, Dirk, Kyra, Andrei, Kris, Peter, Tanja, Ahmed, Karen, Nele en Gregory. Misschien een extra woordje van dank voor Sandy en Els! Sandy, ik weet dat het niet gemakkelijk moet geweest zijn om na 4 jaar je kennis over uranyl terug op te rakelen voor het corrigeren van deze thesis.☺ Ik kende mijn achternicht Els niet toen ik hier in Leuven aan mijn studies begon, maar ik denk dat ik nu mag zeggen dat ik de afgelopen jaren een hechte vriendschapsband heb opgebouwd. Bedankt, Els, voor het helpen met de NMR data en het verzorgen van de koerierdienst tussen Leuven en Hasselt!☺ Verder mag ik Rita niet vergeten te vermelden. Zij regelde steeds gedreven alle administratieve rompslomp en voor een gezellige babbel kon je steeds bij haar terecht.

Maar wat zou ik natuurlijk zijn zonder mijn familie? Ik wil mijn ouders bedanken voor de mogelijkheden die ze mij gegeven hebben. Vooral mijn mama mag een pluim op haar hoed steken. Ik weet dat je het niet gemakkelijk gehad hebt het laatste jaar. Toch ben je me altijd blijven steunen in alles wat ik deed en doe. En als ik het eventjes niet meer zag zitten, was je altijd daar met je oppeppende woorden! Natuurlijk mogen Katja en David en Veerle en Stijn hier ook niet ontbreken die op tijd en stond zorgden voor een vleugje humor.

Last but zeker niet least, wil ik Bart bedanken voor zijn medeleven, steun, zijn vertrouwen in mij en geruststellende woorden gedurende de afgelopen periode. Ik weet dat je veel geduld met mij hebt moeten hebben! Ik zie je graag!

Voilà, een hoofdstukje van mijn leven is op deze manier afgesloten. Op naar het volgende!

Kelly

ABSTRACT

The UV-Vis absorption spectrum of the uranyl ion is dominated by the vibration modes of the axial oxygen atoms. Among these, the symmetric stretching vibration ν_s (~ 750 cm^{-1}) is always superimposed on all electronic transitions as a progression, exhibiting anharmonicity. The other modes, i.e. the asymmetric stretching vibration ν_a (~ 830 cm^{-1}) and the bending vibration ν_b (~ 230 cm^{-1}) are sometimes coupled with one quantum. They appear as satellite peaks in various combinations with ν_s. The equatorial ligand vibrations are even less pronounced in the UV-Vis absorption spectra of uranyl compounds with the exception of one out-of-plane bending, i.e. ν_{10} (b_{1u} in D_{4h}), which is often mentioned in intensity mechanisms.

The positions and the intensities of the electronic transitions in the UV-Vis absorption and luminescence spectra of uranyl compounds are affected by the symmetry of the first coordination sphere. In addition, the frequency of the symmetric stretching vibration ν_s and the chemical nature of the ligands are related. The combination of both properties results in a characteristic vibrational fine structure in the spectra of uranyl complexes. These optical spectra can be used as fingerprints of a certain symmetry group. Therefore, optical spectroscopic techniques are of practical interest for studying the coordination environment of the uranyl ion in solution.

In this work, the spectroscopic data are complemented by uranium L_{III}-edge EXAFS spectroscopy. This modern experimental technique gives us the opportunity to obtain structural information like bond distances, on solution species. Moreover, the U-O_{eq} bond distances are related with the coordination number of the uranyl ion. It is obvious that the combination of UV-Vis absorption spectroscopy, luminescence spectroscopy and uranium L_{III}-edge EXAFS spectroscopy is a valuable tool for elucidating the structure of uranyl species in solution.

This unique combination of spectroscopic techniques has been applied to a number of uranyl systems in non-aqueous solvents. In this way, the formation of $[UO_2Cl_4]^{2-}$ (D_{4h}), $[UO_2(NO_3)_3]^-$ (D_{3h}), $[UO_2(CH_3COO)_3]^-$ (D_{3h}) and $UO_2(NO_3)_2(TBP)_2$ (D_{2h}) species as well as the presence of the inclusion complex $[UO_2(18\text{-crown-6})]^{2+}$ in non-aqueous solvents was demonstrated.

Ionic liquids are salts with a melting point below 100 °C and they are currently under investigation as potential alternatives to the classical organic solvents in different fields of chemistry. The fingerprint spectra obtained from non-aqueous solvents, were used to gain information on the first coordination sphere of the uranyl ion in ionic liquids. Therefore, the complex formation of the uranyl ion with chloride, nitrate and acetate ions as well as 18-crown-6 was studied in the ionic liquids $[C_4mim][Tf_2N]$ and [bmpyr][Tf_2N] by means of UV-Vis absorption spectroscopy. Uranium L_{III}-edge EXAFS spectroscopy has given evidence for the formation of a $[UO_2(NO_3)_3]^-$ species in the ionic liquid $[C_4mim][Tf_2N]$.

The photochemical behaviour of the uranyl ion is already known for centuries and has been extensively studied. Uranyl oxalate was the first actinometer ever used. We have gained new insight into the structure of uranyl oxalato complexes based on spectroscopic measurements in non-aqueous solvents.

ABSTRACT

Het UV-zichtbaar absorptiespectrum van het uranylion wordt gedomineerd door de vibraties van de axiale zuurstofatomen. De symmetrische rekvibratie ν_s (~ 750 cm^{-1}) is altijd op alle elektronische overgangen gesuperponeerd als een progressie, waarin de anharmoniciteit van het molecule tot uiting komt. De asymmetrische rekvibratie ν_a (~ 830 cm^{-1}) en de buigvibratie ν_b (~ 230 cm^{-1}) zijn soms gekoppeld met één kwantum. Ze worden waargenomen als satellietpieken in verschillende combinaties met ν_s. De equatoriale ligandvibraties zijn minder uitgesproken in de UV-zichtbaar absorptiespectra van uranylverbindingen met uitzondering van één buigvibratie uit het vlak, namelijk ν_{10} (b_{1u} in D_{4h}). Op deze equatoriale ligandvibratie wordt dikwijls beroep gedaan in intensiteitmechanismen.

De posities en de intensiteiten van de elektronische overgangen in de UV-zichtbaar absorptie- en luminescentiespectra van uranylverbindingen worden beïnvloed door de symmetrie van de eerste coördinatiesfeer. Bovendien bestaat er een verband tussen de frequentie van de symmetrische rekvibratie ν_s en de chemische aard van het ligand. De combinatie van de twee bovengenoemde eigenschappen leidt tot een karakteristieke vibratiefijnstructuur in de spectra van uranylcomplexen. Deze optische spectra zijn als het ware fingerprints voor een bepaalde coördinatiesymmetrie. Optische spectroscopische technieken zijn dan ook interessant voor het bestuderen van de coördinatieomgeving van het uranylion in oplossing.

In dit doctoraatsproefschrift worden de spectroscopische gegevens aangevuld met data verkregen uit uraan L_{III}-edge EXAFS spectroscopie. Deze moderne experimentele techniek laat toe om structurele parameters zoals bindingsafstanden te bepalen van deeltjes in oplossing. Bovendien bestaat er een verband tussen de U-O_{eq} bindingsafstanden en het coördinatiegetal van het uranylion. Het is duidelijk dat de combinatie

van UV-zichtbaar absorptiespectroscopie, luminescentiespectroscopie en uraan L_{III}-edge EXAFS spectroscopie waardevolle informatie biedt over de structuur van uranylcomplexen in oplossing.

Deze unieke combinatie van spectroscopische technieken werd toegepast op een aantal uranylsystemen in niet-waterige solventen. Op deze manier werd de vorming van $[UO_2Cl_4]^{2-}$ (D_{4h}), $[UO_2(NO_3)_3]^-$ (D_{3h}), $[UO_2(CH_3COO)_3]^-$ (D_{3h}) en $UO_2(NO_3)_2(TBP)_2$ (D_{2h}) complexen evenals de aanwezigheid van het insluitingcomplex $[UO_2(18\text{-crown-6})]^{2+}$ in niet-waterige oplossingen aangetoond.

Ionische vloeistoffen zijn zouten met een smeltpunt beneden 100 °C en deze worden momenteel onderzocht als mogelijke alternatieven voor de klassieke organische solventen in verschillende takken van de chemie. De fingerprint spectra verkregen in niet-waterige solventen, werden gebruikt om informatie in te winnen over de eerste coördinatiesfeer van het uranylion in ionische vloeistoffen. Daartoe werd de complexvorming van het uranylion met chloride-, nitraat- en acetaationen en de kroonether 18-kroon-6 in de ionische vloeistoffen $[C_4mim][Tf_2N]$ en $[bmpyr][Tf_2N]$ bestudeerd door middel van UV-zichtbaar absorptiespectroscopie. Uraan L_{III}-edge EXAFS spectroscopie leverde een bijkomende aanwijzing voor de vorming van $[UO_2(NO_3)_3]^-$ in de ionische vloeistof $[C_4mim][Tf_2N]$.

Het fotochemische gedrag van het uranylion is al eeuwen gekend. Uranyloxalaat was de eerste actinometer ooit gebruikt. Spectroscopische metingen in aceton leidden tot een nieuwe kijk op de structuur van oxalato-uranylcomplexen.

LIST OF SYMBOLS AND ABBREVIATIONS*

A	Absorbance
A (±)	Positive/negative A-term in MCD
B (±)	Positive/negative B-term in MCD
B_q^k	Crystal-field parameter (k = rank, q = component)
bet	Betaine, $(CH_3)_3N^+CH_2COO^-$
BF_4^-	Tetrafluoroborate
bmpyr	1-butyl-1-methylpyrrolidinium
C_q^k	Tensor operator (k = rank, q = component)
$C_n$mim	1-alkyl-3-methylimidazolium (n = number of carbon atoms in the alkyl chain)
CMPO	Octyl(phenyl)-*N,N*-diisobutylcarbamoylmethyl-phosphine oxide
ε, ε_r, ε_l	Molar absorptivity, molar absorptivity of right and left circularly polarized light
EXAFS	Extended X-ray Absorption Fine Structure
Γ_i	Irreducible representation
H_z, H_x, H_y	Magnetic field along z-, x- and y- direction
$\mathcal{H}$	Total Hamiltonian
$\mathcal{H}_{ax}$	Axial ligand field due to the two oxygen atoms of uranyl
$\mathcal{H}_{eq}$	Ligand field Hamiltonian from equatorially coordinated ligands
$\mathcal{H}_{ER}$	Electron repulsion Hamiltonian
$\mathcal{H}_{s.o.c}$	Spin-orbit coupling Hamiltonian
ħ	h/2π (h is Planck's constant)

* In alphabetical order

l	Left circularly polarized light
Λ	Total orbital angular momentum
λ_{ex}, λ_{em}	Excitation and emission wavelength
$m_{\pm1}$	z-component of the angular momentum of right (+1) and left (-1) circularly polarized light
(M)CD	(Magnetic) circular dichroism
M_Ω	z-component of the total angular momentum quantum number
MS	Multiple scattering path
N	Coordination number
NMR	Nuclear Magnetic Resonance
ν	Vibration mode
ν_a	Asymmetric stretching vibration of uranyl
ν_b	Bending vibration of uranyl
ν_s	Symmetric stretching vibration of uranyl
Ω	Total angular momentum quantum number
OTf^-	Trifluoromethanesulfonate or triflate, $CF_3SO_3^-$
ψ, Ψ	Wavefunction
PF_6^-	Hexafluorophosphate
PMMA	Polymethylmethacrylate
r	Right circularly polarized light
R	Bond distance
ρ	Polarization number
($\mathcal{R}_x$, $\mathcal{R}_y$, $\mathcal{R}_z$)	Basis functions transforming as the magnetic dipole operator
σ^2	Debye-Waller factor
Σ	Total spin angular momentum
solv.	Solvent molecules
Θ	Ellipticity $\left(\Delta\varepsilon = \Theta/_{33Cd}\right)$
TBP	Tri-*n*-butylphosphate
TiBP	Tri-*iso*-butylphosphate

TMP	Trimethylphosphate
TPhP	Triphenylphosphate
Tf_2N^-	Bis(trifluoromethylsulfonyl)imide anion, $[(CF_3SO_2)_2N]^-$
V_{eq}	Crystal-field potential of equatorially coordinated ligands
U_q^k	Unit tensor (k = rank, q = component)
UV-Vis	UV-Visible absorption spectroscopy
XANES	X-ray Absorption Near Edge Structure
(x, y, z)	Basis functions transforming as the electric dipole operator
Y_q^k	Spherical harmonic (k = rank, q = component)
$\begin{pmatrix} \Omega & \lambda & \Omega' \\ -M_\Omega & \rho+q & M'_\Omega \end{pmatrix}$	3j-symbol
18-crown-6	1, 4, 7, 10, 13, 16-hexacyclooctadecane, $C_{12}H_{24}O_6$

TABLE OF CONTENTS

APPENDIX 3:

APPENDIX 4:

INTRODUCTION

1 Aim of this study

Despite its applications as a colouring agent for glass and ceramics as well as in early photography, the crucial importance of uranium became clear after the discovery of nuclear fission by Otto Hahn, Fritz Strassmann and Lise Meitner in 1938 [1]. Naturally occurring uranium-235, fertile uranium-238 or the artificial fissionable uranium-233 can all be used to release nuclear energy. Although nuclear energy has been promoted for a long time as a cheap and clean alternative to fossil fuels, the public opinion has now turned against the production of nuclear energy. Hot discussions are ongoing about the possible shutting-down of the nuclear reactors. However, there are no alternatives to nuclear energy available at the moment. In addition, nuclear energy contributes 40% to our production of electricity [2]. The cease of the production of nuclear energy is only conceivable in the long term [3]. Furthermore, the uranium rods 'used up' in nuclear reactors create dangerous radioactive wastes that must be disposed of. Therefore, a suitable nuclear waste treatment and management is required. But, a system of safe long-term waste disposal is not yet available [4].

Besides these problems of nuclear waste treatment, uranium is also a hot topic in health care. A lot of attention is paid to the development of *sequestering agents*, which are able to selectively bind to uranium and remove it from the human body [5]. This issue has been brought into prominence since it appears that soldiers who served in Bosnia and in

Kosovo experienced negative consequences as a result of the use of uranium-containing alloys in ammunition to improve its armour penetrating capacity. The variety of medical symptoms experienced, are grouped under the name '*Balkan syndrome*'. However, investigations by the Medical Service of the Belgian Army indicated no relation between the Balkan syndrome and the use of depleted uranium. No depleted uranium contamination was diagnosed among the soldiers. All test results on urine- and blood samples, performed by SCK-CEN (Mol) were negative, as written in the letter shown below [6,7].

BELGISCHE STRIJDKRACHTEN

Datum :08 Jan 02
Nr : 000100

ACOS WB E&B
Kwartier Koningin Astrid
Bruynstraat 1
1120 Brussel

Juffrouw Servaes Kelly
Ringlaan 1
3530 Houthalen

ONDERWERP : Uranylcomplexen, balkansyndroom
Ref : Uw brief van 4 Jan 2002

Geachte Jufrouw Servaes,

Wij zouden u graag verder helpen. Eerst kan u informatie en referenties vinden op onze Website (http://www.smd.be/msw/ned/infores/uranium.htm) .
Volgens onze metingen waren de Belgische soldaten in ex-Yougoslavië niet blootgesteld aan radioactiviteit boven de natuurlijke achtergrondradioactiviteit. Verarmd uranium heeft dus zeker niets te maken met een eventueel "Balkansyndroom".
Verarmd uranium is een zwaar metaal en heeft dus andere effecten, maar ook op dit vlak is er geen bewijs vanbesmetting. Al de proeven (urine- en bloedtesten) zijn tot nu toe negatief .

Wij hebben en aantal wetenschapelijke artikels over de verschillende aspecten van dit probleem ter uwe beschikking (de referenties van de website kunnen ook geraadpleegd worden).

De meeste artikels zijn in het Engels of in het Frans.

Indien U het wenst kan u ons steeds een bezoek brengen.

Hoogachtend ,

Voor alle contacten:

Med Capt DUGAUQUIER C.
Acos WB E&B
Kwartier Koningin Astrid
Bruynstraat 1
1120 Brussel

Letter received from the Medical Service of the Belgian Army in January 2002.

In solvent extraction processes for nuclear waste treatment and in the research on intravenously incorporated medicines for safe removal of uranium from the human body, knowledge of the solution chemistry of uranium plays an important role. The most stable oxidation state of uranium in solution is uranium(VI), present in the form of the uranyl ion (UO_2^{2+}). Therefore, we investigated the coordination properties of several uranyl complexes with both inorganic (Cl^-, NO_3^-, CO_3^{2-}) and organic (CH_3COO^-, 18-crown-6) ligands in aqueous solution and non-aqueous solvents (acetonitrile, acetone) at room temperature, important for the problems at hand. Especially, a understanding of the geometry of the $UO_2(NO_3)_2(TBP)_2$ species, where TBP (tri-*n*-butylphosphate) is a commonly used neutral extracting agent in liquid-liquid extraction procedures, can reveal a correlation with the extracting ability of the agent. Thereby, this study can contribute to the development of new, more selective extracting agents.

Ionic liquids are salts composed of an organic cation and an organic/inorganic anion with a melting point below 100 °C. Several types of ionic liquids are even liquid at room temperature. These ionic liquids are currently under investigation as potential "green" alternatives to conventional solvents like in solvent extraction processes. However, the potential application of ionic liquids in extraction processes demands an insight in the behaviour of metal ions in this kind of solvents. Therefore, we have studied the uranyl ion itself and its coordination behaviour with several ligands (Cl^-, NO_3^-, CH_3COO^- and 18-crown-6) in imidazolium-based and pyrrolidinium-based ionic liquids.

Due to its characteristic spectral properties, optical spectroscopic techniques like UV-Vis absorption spectroscopy, luminescence and excitation spectroscopy as well as magnetic circular dichroism (MCD) spectroscopy, are very appropriate for studying the coordination sphere of the uranyl ion. Thereby, we will mainly focus on some typical features in the spectra regarding intensity enhancement and sharpness of transitions. These spectroscopic data combined with ligand field theory are the ideal

tools to study the electronic structure of the uranyl ion and the observed electronic transitions in the spectra. We have to remark that the spectra in solution exhibit different phenomenological features with respect to the spectra of single crystals of uranyl compounds, studied in detail by Denning [8]. There are two reasons for these differences:

- The absorption bands are much broader for solution species. Consequently, overlap between the different transitions is inevitable and this makes the spectrum in solution even more complex to analyze.
- The molecules are randomly oriented in solution, so any orientation can be observed. This means that statistically one third of the molecules are oriented in the x-direction, one third in the y-direction and one third in the z-direction. The spectra are thus a superposition of x-, y- and z-polarization.

Nowadays, a modern experimental technique is available to obtain structural information, e.g. bond distances, on solution species: *Extended X-ray Absorption Fine Structure* (*EXAFS*). We have complemented the optical spectroscopic data of several uranyl complexes with uranium L_{III}-edge EXAFS spectroscopy. These EXAFS measurements confirm the coordination environment of the uranyl ion proposed by the classical spectroscopic techniques.

At the end, understanding of the coordination behaviour of the uranyl ion as well as insight in the geometry of uranyl complexes can provide useful information to contribute to the research on the problems mentioned above.

2 Outline

The first part of this thesis will focus on the theoretical aspects of the uranyl ion and *Extended X-ray Absorption Fine Structure* (EXAFS) spectroscopy. In *Chapter 1*, a short overview of the scientific history and the occurrence of uranium will be given. Since many people make up their mind too fast about the risks of working with uranyl compounds, the radiation hazards are discussed. Furthermore, we will describe the remarkable properties of the uranyl ion, with emphasis on its typical spectroscopic features. In *Chapter 2*, the formation of the molecular orbitals of UO_2^{2+}, stemming from the valence orbitals of uranium and the two oxygen atoms, will be disclosed. We will elaborate on the perturbations affecting the electronic states of the uranyl ion. The axial ligand field, the electron repulsion, the spin-orbit coupling, the equatorial ligand field and the Zeeman perturbation will be discussed in this order, corresponding with the magnitude of the perturbation. The Zeeman perturbation is explained in terms of the magnetic circular dichroism technique. All electronic transitions in the uranyl ion ($D_{\infty h}$) are parity forbidden by the Laporte selection rule. Therefore, intensity has to be induced either by the static or the dynamic ligand field. Both intensity mechanisms together with the magnetic dipole transitions will be considered by means of some striking examples.

Chapter 3 deals with the basics of EXAFS spectroscopy. This description is intended as a general overview of the theory and the data analysis. The sample preparation, the experimental setup and the data analysis of the uranium L_{III}-edge EXAFS measurements performed will be discussed

The experimental section will start with an overview of the experimental procedures used (*Chapter 4*). The geometry of the first coordination sphere of the uranyl ion affects the vibrational fine structure in the spectra. In *Chapter 5*, the coordination effects on the spectra of the uranyl ion will be discussed. The typical UV-Vis absorption, luminescence and where necessary MCD spectra of a complex with D_{5h}

symmetry ($[UO_2(H_2O)_5]^{2+}$), a complex with D_{4h} symmetry ($[UO_2Cl_4]^{2-}$), complexes with D_{3h} symmetry ($[UO_2(NO_3)_3]^-$, $[UO_2(CH_3COO)_3]^-$, $[UO_2(CO_3)_3]^{4-}$) and a complex with D_3 symmetry ($[UO_2(18\text{-crown-6})]^{2+}$) are revealed. These optical spectra can be used as fingerprints of a certain symmetry group. The assignments of the electronic transitions in the spectra of these solution species are compared with the data of the corresponding single crystals. Structural information like bond distances, on these solution species is determined by means of uranium L_{III}-edge EXAFS spectroscopy. In this way, the combination of UV-Vis absorption spectroscopy and uranium L_{III}-edge EXAFS spectroscopy provides us with a valuable tool for solving the coordination environment in unknown uranyl complexes.

The fingerprint spectra obtained from non-aqueous solvents are applied to elucidate the coordination behaviour of the uranyl ion with Tf_2N^-, Cl^-, NO_3^-, Br^-, CH_3COO^- and 18-crown-6 in ionic liquids in *Chapter 6*. *Chapter 7* deals with the spectroscopic properties of the $UO_2(NO_3)_2(TBP)_2$ complex, encountered in solvent extraction processes. Complex formation constants and thermodynamic data are determined by means of ^{31}P NMR spectroscopy.

Finally, in *Chapter 8*, a new insight in the structure of uranyl oxalato complexes is brought forward based on spectroscopic measurements in acetone.

The *appendices* treat some safety issues on handling uranyl samples (*Appendix 1*). *Appendix 2* contains the group orbitals of the axial oxygen atoms of the uranyl ion and the final molecular orbitals of UO_2^{2+}. The important UV-Vis, luminescence and where possible MCD data as well as an assignment of each peak in the spectra of the uranyl complexes discussed throughout this work, are listed in *Appendix 3*. Crystal structure data are given in *Appendix 4*.

References

[1] *Uranium's scientific history Part 2*: http://socrates.berkeley.~rochlin/ushista.html.

[2] Vlaamse Milieumaatschappij, *Milieurapport Vlaanderen: Focusrapport, MIRA-T-2006*, **2006**, Lannoo Campus, Leuven.

[3] *"Gedachtewisseling over de prioriteiten van het Duitse EU-voorzitterschap met de Heer Christoph Jessen, ambassadeur van de Bondsrepubliek Duitsland: verslag" Vlaams Parlement, 12 februari 2007,* http://jsp.vlaamsparlement.be/docs/stukken/2006-2007/g1100-1.pdf.

[4] *"Een langetermijnoplossing voor het Belgisch laag- en middelradioactief kortlevend afval – samen maken we het mogelijk"*, brochure NIRAS, **2006**.

[5] (a) Durbin, P.W.; Kullgren, B.; Xu, J.; Raymond, K.N. *Int. Radiat. Biol.* **2000**, *76*, 199-214. (b) Durbin, P.W.; Kullgren, B.; Xu, J.; Raymond, K.N. *Health Phys.* **1997**, *72*, 865-879. (c) Xu, J.; Raymond, K.N. *Inorg. Chem.* **1999**, *38*, 308-315. (d) Walton, P.H.; Raymond, K.N. *Inorg. Chim. Acta* **1995**, *240*, 593-601. (e) Franczyk, T.S.; Czerwinski, K.R.; Raymond, K.N. *J. Am. Chem. Soc.* **1992**, *114*, 8138-8146.

[6] Uyttenhove, J.; Lemmens, M.; Zizi, M. *Health Phys.* **2002**, *83*, 543-548.

[7] EU depleted uranium final report "*Opinion of the group of experts established according to article 31 of the Euratom Treaty: Depleted Uranium"*, **2001**.

[8] (a) Denning, R.G. *J. Phys. Chem. A* (Feature Article) **2007**, *111*, 4125-4143. (b) Denning, R.G.; Dallera, C.; Tagliaferri, A.; Giarda, K.; Brookes, N.B.; Braicovich, L. *J. Chem. Phys.* **2002**, *117*, 8008-8020. (c) Barker, T.J.; Denning, R.G.; Thorne, R.G. *Inorg. Chem.* **1992**, *31*, 1344-1353. (d) Denning, R.G. *Struct. Bond.* **1992**, *79*, 215-276. (e) Denning, R.G.; Morrison, I.D. *Chem. Phys. Lett.* **1991**, *180*, 101-104. (f) Watkin, D.J.;

Denning, R.G.; Prout, K. *Acta Cryst.* **1991**, *C47*, 2517-2519. (g) Barker, T.J.; Denning, R.G.; Thorne, R.G. *Inorg. Chem.* **1987**, *26*, 1721-1732. (h) Barker, T.J.; Denning, R.G.; Thorne, J.R.G. *J. Lumin.* **1987**, *38*, 144-146. (i) Thorne, J.R.G.; Denning, R.G.; Barker, T.J.; Grimley, D.I. *J. Lumin.* **1985**, *34*, 147-165. (j) Thorne, J.R.G.; Denning, R.G. *Mol. Phys.* **1985**, *54*, 701-711. (k) Denning, R.G.; Ironside, C.N.; Thorne, J.R.G.; Woodwark, D.R. *Mol. Phys.* **1981**, *44*, 209-224. (l) Denning, R.G.; Short, L.G.; Woodwark, D.R. *Mol. Phys.* **1980**, *39*, 1281-1285. (m) Denning, R.G.; Foster, D.N.P.; Snellgrove, T.R.; Woodwark, D.R. *Mol. Phys*. **1979**, *37*, 1089-1107. (n) Denning, R.G.; Foster, D.N.P.; Snellgrove, T.R.; Woodwark, D.R. *Mol. Phys.* **1979**, *37*, 1109-1143. (o) Denning, R.G.; Snellgrove, T.R.; Woodwark, D.R. *Mol. Phys.* **1976**, *32*, 419-442. (p) Denning, R.G.; Snellgrove, T.R.; Woodwark, D.R. *Mol. Phys.* **1975**, *30*, 1819-1828.

1 THE URANYL ION UO_2^{2+}: A UNIQUE CHEMICAL SPECIES

1 Scientific history of uranium and discovery of radioactivity

The element uranium was discovered by Martin Heinrich Klaproth, a German chemist, in the mineral pitchblende (uraninite) in 1789. He managed to precipitate a yellow compound by dissolving pitchblende in nitric acid and neutralizing the solution with sodium hydroxide. He attempted to isolate the metal by heating the yellow substance with charcoal. A black powder was obtained, which he assumed was the metal itself. He named the new element after the planet Uranus, which had just been discovered. Fifty years later, however, the French chemist Eugène Péligot showed that Klaproth's 'metallic' substance was in reality the oxide UO_2. Péligot himself isolated the first sample of uranium metal by reducing uranium tetrachloride with potassium [1,2].

Later, in 1870, an important fact was established: uranium was the heaviest and the last element present on earth, known at that time. This was demonstrated by Mendeljev in his periodic table of elements by assigning an atomic weight of 240 to uranium. It was not until 1882 that Zimmerman confirmed the atomic weight to be correct [2-4].

Uranium was not seen as particularly dangerous during the 19th century, leading to the development of various applications of the element. The main application was derived from the vivid colours of uranium oxides and its salts. These were used to produce yellow glass with a green fluorescence (Figure 1.1) as well as ceramics and porcelain in orange, yellow, red, green and black shades. Later, uranyl nitrate was used in early photography to give a sepia tint to prints and films and to reinforce negative plates.

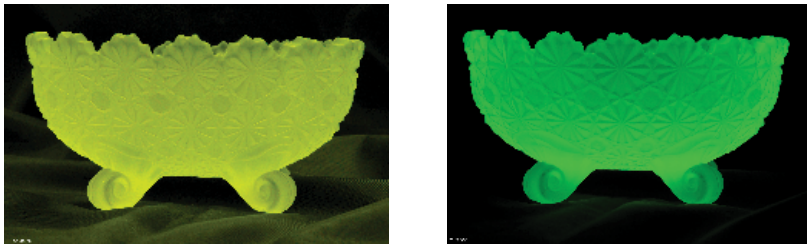

Figure 1.1. A yellow coloured uranyl glass, exhibiting green fluorescence.

It was the intense study of the fluorescence properties (then referred to as phosphorescence) of uranium salts, which led to the discovery of radioactivity by Henri Becquerel in 1896. He was the third generation of his family, interested in the behaviour and the properties of phosphorescent and fluorescent substances, including uranium salts. He reported the pronounced phosphorescence of uranyl sulphate, $K_2UO_2(SO_4)_2 \cdot 2H_2O$, after exposure to the sun. The crystals emitted a radiation that blackened a photographic plate covered in black paper. Further investigation revealed that all uranium compounds, minerals, solutions and the metal itself behaved in the same way, in each case with an intensity proportional to the uranium content. Furthermore, he found that the effect was independent of the exposure to the sun (weak or bright sunlight). Therefore, he linked the emission of the radiation to the presence of uranium. Exactly four months after the X-rays, a second revolutionary discovery of the so-called Becquerel or uranium rays had

taken place. Still, in 1898, it was Marie Curie who concluded that the uranium rays were an atomic phenomenon, characteristic to the element and not related to its chemical and physical state. She introduced the name 'radioactivity' [1-4].

2 Occurrence of uranium and radiation hazards*

Uranium is the highest-numbered naturally occurring element that can be found in low levels within rocks, soil and water. Indeed, uranium is not as rare as it was once thought. It is now considered to be more plentiful than antimony, tin, cadmium, mercury or silver and it is as abundant as arsenic or molybdenum. It is found in numerous minerals, including uraninite (UO_2, the most common uranium ore), autunite ($Ca(UO_2)_2(PO_4)_2 \cdot 10H_2O$), carnotite ($K_2(UO_2)_2(VO_4)_2 \cdot 3H_2O$), uranophane ($Ca(UO_2)_2(SiO_3OH)_2 \cdot 5H_2O$), torbernite ($Cu(UO_2)_2(PO_4)_2 \cdot 8\text{-}12H_2O$) and coffinite ($U(SiO_4)_{1-x}(OH)_{4x}$). Phosphate rock deposits as well as minerals like lignite (brown coal) and monazite ((Ce, La, Pr, Nd, Th, Y)PO_4) also contain significant amounts of uranium. The average concentration of uranium in seawater is 3.3×10^{-3} mg per litre and in surface waters 0.01×10^{-3} mg per litre to 5×10^{-3} mg per litre.

Uranium can be commercially recovered from the several uranium ores. A uranium ore typically contains 0.1% to 0.25% of actual uranium oxides. Therefore, extensive measures have to be employed to extract the metal from its ores. In 2005, seventeen countries produced concentrated uranium oxides, with Canada (27.9% of world production) and Australia (22.8%) being the largest producers (Figure 1.2) [1].

* See Appendix 1: Safety issues on handling uranyl samples

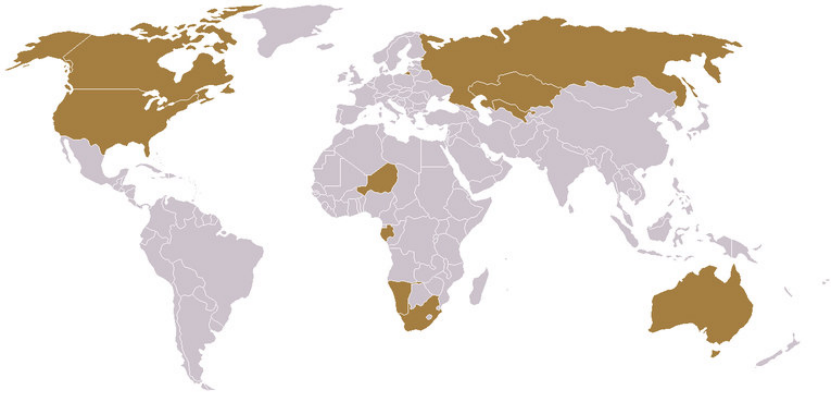

Figure 1.2. World production of concentrated uranium oxides.

Naturally occurring uranium is composed of three isotopes. Uranium-238 and uranium-235 are the parent isotopes of two separate radioactive decay series, while uranium-234 is formed by decay in the ^{238}U series. Uranium-238 has the highest abundance (99.27%), compared with only 0.72% of uranium-235 and 0.0054% of uranium-234. All three isotopes are radioactive, with a half-life of 4.468×10^9 years for ^{238}U, 7.03×10^8 years for ^{235}U and 2.48×10^5 years for ^{234}U. Only uranium-235 is fissile and can be used for the production of nuclear power. Although it does not occur naturally, uranium-233 is also a fissionable material that can be used as a fuel in nuclear reactors. To produce uranium-233, atoms of thorium-232 are exposed to neutrons, thereby forming thorium-233. Thorium-233 decays into protactinium-233 through β-decay, which in turn decays into uranium-233, also through β-decay. Uranium-238 is a pure α-emitter. Alpha-rays have a penetration ability of 2.8 cm to 8.6 cm in air and 0.0025 cm to 0.0089 cm in water. α-Radiation is already stopped by a sheet of paper!

However, most of the radioactivity in uranium ores is not due to uranium itself. Isotopes of protactinium, polonium, radium and radon, which are formed during the decay of uranium-238 and uranium-235, are much more active than uranium. During the extraction and the refining

process of uranium ores, uranium is separated from these decay products. Furthermore, a separation occurs between uranium-238 and uranium-235, because only the latter is used in nuclear core splitting.

One has to warn people not to jump to conclusions about the risks of doing research on uranium compounds. The commercially available uranyl salts are rich in uranium-238, depleted in uranium-235 and with a low content of high-radioactive decay products. With a half-life resembling the lifetime of the earth, one can imagine that it takes several years before significant amounts of uranium-238 decay products are formed. The very large half-life of uranium-238 is also the reason for its low radioactivity with respect to artificial radioisotopes used for scientific and medical applications. This is easy to understand when one compares the radionuclide masses needed to create a radioactive source with an activity of one Curie* (Table 1.1).

Table 1.1. Radionuclide masses (in g) corresponding to an activity of 1 Curie.

Radionuclide	Mass (g) for 1 Curie
iodine-131	8×10^{-6}
strontium-90	0.0071
cesium-137	0.012
radium-236	1.009
plutonium-239	16.287
uranium-238	3.09×10^{6} (more than 3 tons!)

* The Curie is a unit of radioactivity, defined as 1 Ci = 3.7×10^{10} decays per second. This is the activity of one gram of the radium isotope ^{226}Ra, assuming its half-life to be 1580 years. One Curie equals 3.7×10^{10} Bq.

3 The uranyl ion UO_2^{2+}

Uranium has an atomic number of 92. This implies that the electronic configuration of uranium is given by [Rn] $5f^3 6d^1 7s^2$. The main oxidation states of uranium in nature are uranium(IV) and uranium(VI). Uranium(III) and uranium(V) occur only rarely. In solution, uranium(VI), in the form of the uranyl ion (UO_2^{2+}), is the most stable oxidation state. Free U^{6+} ions are not found in solution. The U(VI) state (UO_2^{2+}) is highly soluble in solution, unlike U(IV) [2,5].

Actinyl ions AnO_2^{n+} are commonly observed in actinide chemistry. *An* represents the actinide elements uranium, neptunium, plutonium and americium. Their most stable oxidation states under non-extreme chemical conditions are uranium(VI), neptunium(V), plutonium(IV) and americium(III). In the strictest sense, the actinides have in the AnO_2^{n+} moiety oxidation state +VI, but the name is often extended to the AnO_2^{+} and AnO_2^{3+} ions as well, designating them as actinyl(V) and actinyl(VII) ions, respectively. Examples are UO_2^{+}, NpO_2^{+}, NpO_2^{3+} [2,6]. The chemical properties of the actinyl ions are most clearly displayed in the chemistry of uranium. For uranium(VI), there are only a few compounds which do not contain the UO_2^{2+} unit [7].

The uranyl ion exhibits remarkable properties, thereby reflecting its extraordinary stability. In a solution with a pH value $\geq$ 2.5, hydrolysis products of the uranyl ion, with the general formula $[(UO_2)_m(OH)_n]^{2m-n}$, are formed. First dimers and then trimers are formed, with bridging hydroxide groups. But, Raman spectroscopy indicates that there is little change in the structure of the dioxo group upon oligomerization. Even in alkaline solution, this group remains intact. Thermodynamic data also point to the strength of the uranium-oxygen bond. The mean U-O bond dissociation enthalpy is 701 kJ mol^{-1} for $UO_2^{2+}{}_{(g)}$ and 710 kJ mol^{-1} for $UO_{2(g)}$, which resembles data on gaseous transition metal dioxides and even approaches the strength of the carbon dioxide bond. The uranyl ion is also kinetically inert. The half-life for ^{18}O exchange between UO_2^{2+} and water is longer than 4.5 years at room temperature, compared with

less than 5 seconds for VO^{2+} [7,8]. This remarkable strength of the uranium-oxygen bond can be attributed, according to Denning, to the presence of both *f* and *d* metal orbitals in the valence shell, giving each actinide-oxygen bond a formal bond order of three [7].

Actinyl ions are also unusual in the sense that the dioxo metal(VI) unit is close to linear ($D_{\infty h}$ symmetry) in all actinyl ions. This contrasts to *d*-block transition metal dioxo cations such as MoO_2^{2+} and other actinides such as ThO_2, where *d* orbitals play a dominant role in the bonding, stabilizing a bent geometry. In case of ThO_2, the molecule has a bent geometry with an equilibrium bond angle of 118° [7].

4 Spectral properties of the uranyl ion UO_2^{2+}

Concerning its shape, the UV-Vis absorption spectrum of the uranyl ion can be placed between the sharp line transitions of the trivalent lanthanide ions and the very broad absorption bands of organic molecules. The characteristic UV-Vis absorption spectrum of the uranyl ion is found between 18000 cm^{-1} and 30000 cm^{-1} (Figure 1.3). The formation of different complexes in solution is observed in the spectroscopic changes, because all uranyl complexes exhibit typical structured absorption spectra in this spectral region. Hence, uranyl compounds are yellow.

The assignment of the absorption peaks in the beginning of the spectrum is more or less clear (Figure 1.3). According to Denning et al., the low energy part of the spectrum contains the transitions between the totally symmetric ground state Σ_g^+ and the Π_g, Δ_g and Φ_g states with $^3\Delta_g$ character. The middle part and the end of the spectrum originate from overlap of transitions to the $^1\Delta_g$ and $^3\Phi_g$ states [7-9]. However, recent theoretical calculations revealed that the UV-Vis absorption spectrum of the hydrated uranyl ion is almost completely built up of transitions to the triplet states $^3\Delta_g$ and $^3\Phi_g$. Indeed, $^3\Phi_g$ lies lower in energy than $^1\Delta_g$. The

singlet states $^1\Delta_g$ and $^1\Phi_g$ only play a dominant role at higher energies (30000 cm^{-1} - 31000 cm^{-1}). The relative ordering of the electronic states, without the inclusion of spin-orbit interaction, was found to be $^3\Delta_g < {}^3\Phi_g < {}^1\Delta_g < {}^1\Phi_g$ [10]. The electronic configurations controlling the spectrum of the uranyl ion as well as the electronic states arising from these configurations will be discussed in more detail in Chapter 2. Electronic transitions in the spectra of uranyl complexes are characterized by molar absorptivities of approximately 10 - 100 L mol^{-1} cm^{-1}.

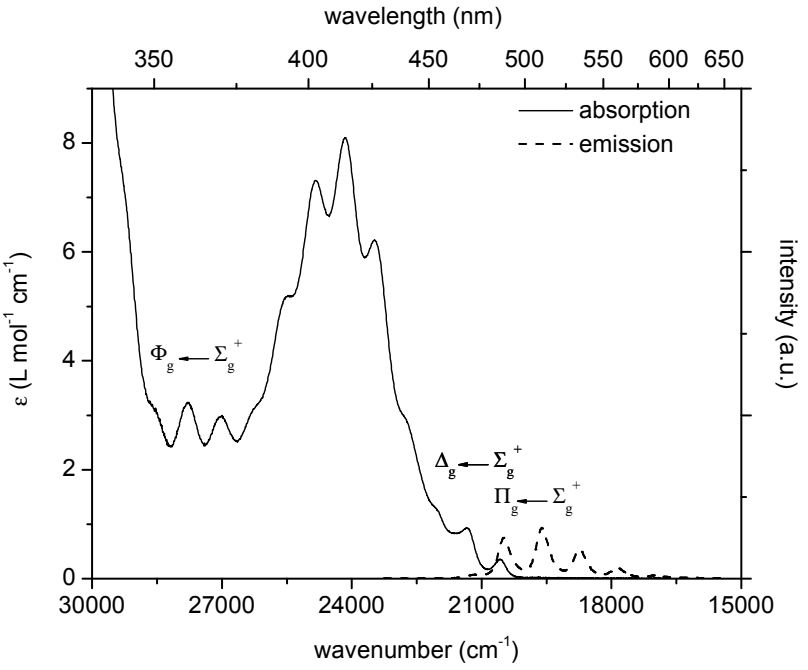

Figure 1.3. UV-Vis absorption and emission spectra of the uranyl ion in water at room temperature.

The green luminescence of the uranyl ion can be detected between 15000 cm^{-1} and 22000 cm^{-1}. Complex formation enhances uranyl luminescence with respect to its luminescence in a non-complexing medium, like the (hydrated) "free" uranyl ion [11]. The coordinated

ligands inhibit quenching by the vibrational modes of the water molecules [12]. Therefore, the spectral intensities can be influenced by the choice of the ligand and/or the solvent.

The uranyl ion has three fundamental vibration modes: the symmetric stretching vibration (ν_s), the asymmetric stretching vibration (ν_a) and the bending vibration (ν_b) (Figure 1.4) [2,7,13,14]. The corresponding spherical harmonics for the different vibrational modes in Figure 1.4 will be used in the expressions of the matrix elements determining the coupling of vibrations to the electronic transitions (see Chapter 2). The symmetric stretching vibration corresponds to the totally symmetric representation σ_g^+ ($D_{\infty h}$). The asymmetric stretching and the bending modes transform like the p_z orbital (σ_u^+) and the (p_x, p_y) orbitals (π_u), respectively. Indeed, the bending vibration is degenerate. The ground state vibrational frequencies of uranyl in an equatorial ligand field are around 830 cm^{-1} for the symmetric stretching vibration, 915 cm^{-1} for the asymmetric stretching and 250 cm^{-1} for the bending vibration. Excited state values are: 750 cm^{-1} (ν_s), 830 cm^{-1} (ν_a) and 230 cm^{-1} (ν_b), also in the presence of equatorial ligands. The frequencies mentioned above are an average value. Indeed, large variations in ν_s and ν_a can be produced by complex formation of the uranyl ion in the equatorial plane [13].

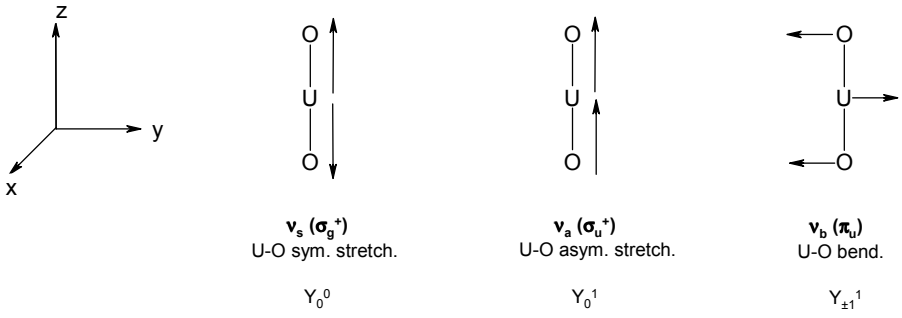

Figure 1.4. Vibrational modes of the uranyl ion with the corresponding spherical harmonics. The representations between parentheses are given for a $D_{\infty h}$ coordination symmetry.

The symmetric stretching mode ν_s is always superimposed as a progression on all electronic transitions. When the complexes are centrosymmetric, the odd parity vibrations like ν_a, ν_b or equatorial vibrations, induce vibronic transitions [7,9,14-17]. This gives a series of homologous lines, which is called a *vibrational progression*. The wavenumber interval between peaks belonging to the same progression decreases regularly because of the anharmonicity of the uranyl ion ($\omega_e\chi_e \propto 15$ cm^{-1}). One progression seldom shows more than three bands due to the considerable overlap of electronic transitions in the spectrum of the uranyl ion [16,17].

Because of the vibrational fine structure in the UV-Vis absorption spectrum, the maxima in the spectrum of the uranyl ion can be described by the following equation [14,16,17]:

$$\nu_{abs} = \nu_E + n_s\nu_s + n_a\nu_a + n_b\nu_b + \sum_i n_i\nu_i \qquad (1.1)$$

ν_E refers to the wavenumber of the pure electronic transition, ν_s to the symmetric stretching vibration, ν_a to the asymmetric one and ν_b to the bending mode. ν_i concerns all ligand or crystal lattice vibrations coupled to the electronic transition. The numbers n_s, n_a, n_b and n_i give the number of quanta of the vibrations involved. Still, to analyse the spectrum, a simplification can be made. Only ν_s is predominantly coupled to all electronic transitions. The other vibration modes appear in various combinations with ν_s as (weak) satellite peaks. Therefore, the spectrum is mainly described by:

$$\nu_{abs} = \nu_E + n_s\nu_s \qquad (1.2)$$

A similar equation can be written to explain the maxima in the emission spectrum of the uranyl ion:

$$\nu_{em} = \nu_E - n_s\nu_s - n_a\nu_a - n_b\nu_b - \sum_i n_i\nu_i \qquad (1.3)$$

with a simplification to:

$$\nu_{em} = \nu_E - n_s\nu_s \qquad (1.4)$$

By looking at these equations, describing the maxima in absorption and emission spectra of uranyl compounds, it is obvious that there exists a mirror-relationship between the fluorescence spectrum and the first electronic transition in absorption.

References

[1] *Wikipedia*: http://en.wikipedia.org/wiki/Uranium.

[2] Katz, J.J.; Seaborg, G.T.; Morss, L.R. *The Chemistry of the Actinide Elements*, **1986**, Chapman and Hall, New York.

[3] De Houwer, S. *Intensities of vibronic transitions in uranyl spectra: application to uranyl complexes in non-aqueous solvents*, **2003**, PhD thesis, Katholieke Universiteit Leuven and references therein.

[4] *Uranium's scientific history 1789-1939*: http://socrates.berkeley.edu./~rochlin/ushist.html.

[5] Rabinowitch, E.; Belford, R.L. *Spectroscopy and Photochemistry of Uranyl Compounds*, **1964**, Pergamon, Oxford.

[6] Matsika, S.; Zhang, Z.; Brozell, S.R.; Blaudeau, J.-P.; Wang, Q.; Pitzer, R.M. *J. Phys. Chem. A* **2001**, *105*, 3825-3828.

[7] Denning, R.G. *Struct. Bond.* **1992**, *79*, 215-276.

[8] Denning, R.G.; Snellgrove, T.R.; Woodwark, D.R. *Mol. Phys.* **1976**, *32*, 419-442.

[9] Denning, R.G.; Snellgrove, T.R.; Woodwark, D.R. *Mol. Phys.* **1979**, *37*, 1109-1143.

[10] van Besien, E. *De invloed van complexvorming op het elektronische spectrum van uranyl: een computationele studie*, **2006**, PhD thesis, Katholieke Universiteit Leuven and references therein.

[11] Baird, C.P.; Kemp, T.J. *Prog. React. Kinet.* **1997**, *22*, 87-139 and references therein.

[12] Billard, I.; Rustenholtz, A.; Sémon, L.; Lützenkirchen, K. *Chem. Phys.* **2001**, *270*, 345-354.

[13] McGlynn, S.P.; Smith, J.K.; Neely, W.C. *J. Chem. Phys.* **1961**, *35*, 105-116.

[14] Dieke, D.H.; Duncan, A.B.F. *Spectroscopic Properties of Uranium Compounds*, **1965**, McGraw-Hill, New York.

[15] McGlynn, S.P.; Smith, J.K. *J. Mol. Spectrosc.* **1961**, *6*, 164-187.

[16] De Jaegere, S.; Görller-Walrand, C. *Spectrochim. Acta* **1969**, *25A*, 559-568.

[17] Görller-Walrand, C.; De Jaegere, S. *Spectrochim. Acta* **1972**, *28A*, 257-268.

2 THEORY

1 Molecular orbitals*

Uranium occurs in its most stable oxidation state, +VI, in the uranyl ion. Hence, the uranyl ion is formally a f^0 system. The uranyl ion consists of a uranium atom covalently bound to two oxygen atoms. Thus, UO_2^{2+} is a molecular unit, which implies the formation of molecular orbitals, stemming from the valence orbitals of uranium and the two oxygen atoms. However, working out the electronic structure of the uranyl ion has been a long and slow process. The electronic structure of the uranyl ion is described by the relative energies of the 5*f* and 6*d* valence orbitals of uranium and the 2*s* and 2*p* orbitals of the oxygen atoms [1-5]. The resulting molecular orbitals of the uranyl ion are

* Supporting material (see Appendix 2): Altmann-Herzig definition, oxygen group orbitals and molecular orbitals of the uranyl ion.

summarized in Table 2.1. The p_σ orbitals of the oxygen atoms may be considered as *sp* hybrids of *s* and p_z.

Table 2.1. Symmetry adapted wavefunctions for the uranyl ion UO_2^{2+} [2].

Uranium A.O.	Oxygen group orbitals	Molecular orbitals
d_{z^2}	$(2)^{-1/2}\,(p_{\sigma 1} + p_{\sigma 2})$	σ_g^{+}
f_{z^3}	$(2)^{-1/2}\,(p_{\sigma 1} - p_{\sigma 2})$	σ_u^{+}
f_{xz^2}	$(2)^{-1/2}\,(p_{x1} + p_{x2})$	π_u
f_{yz^2}	$(2)^{-1/2}\,(p_{y1} + p_{y2})$	
d_{xz}	$(2)^{-1/2}\,(p_{x1} - p_{x2})$	π_g
d_{yz}	$(2)^{-1/2}\,(p_{y1} - p_{y2})$	
$f_{z(x^2-y^2)}$		δ_u
f_{xyz}		
$f_{x(x^2-3y^2)}$		ϕ_u
$f_{y(3x^2-y^2)}$		
$d_{x^2-y^2}$		δ_g
d_{xy}		

The oxygen group orbitals are readily formed by simple addition and substraction, followed by multiplication by an appropriate normalizing factor. The combination of two p_σ orbitals results in a σ molecular orbital, because their interaction occurs along the axis connecting the two nuclei. On the contrary, two p_x or two p_y orbitals interact above and below the bonding axis, thereby forming a π molecular orbital. Notice that the plus combination of two p_x or two p_y orbitals has *ungerade* parity, whereas the minus combination is *gerade*. These oxygen group orbitals mix then with uranium orbitals of the appropriate symmetry. The U d_{z^2} orbital (σ_g^{+} symmetry) and the U $5f_{z^3}$ orbital (σ_u^{+} symmetry) can mix with the σ_g^{+} and the σ_u^{+} oxygen group orbitals, respectively. The U 5*f* orbitals transforming as π_u (f_{xz^2} and f_{yz^2}), interact with the π_u O 2*p* orbitals. The π_g U 6*d* orbitals, i.e. d_{xz} and d_{yz}, can mix with the oxygen group orbitals of

the same symmetry. For the U 5*f* orbitals transforming as δ_u ($f_{z(x^2-y^2)}$ and f_{xyz}) and ϕ_u ($f_{x(x^2-3y^2)}$ and $f_{y(3x^2-y^2)}$) as well as for the U 6*d* orbitals with δ_g symmetry ($d_{x^2-y^2}$ and d_{xy}), however, there are no corresponding orbitals on the oxygen atoms.

A qualitative energy level scheme of the valence molecular orbitals of the uranyl ion is depicted in Figure 2.1. For an atom as heavy as uranium, theoretical calculations of the molecular electronic structure are strongly dependent on approximations. One has to rely on a semi-empirical approach as a basis for detailed discussion. Eventually, comparisons of theoretical and experimental data gave rise to this scheme [2-16].

The bonding orbitals of interest are σ_g^+, σ_u^+, π_u and π_g. They accommodate the twelve valence electrons of uranium and the two oxygen atoms. The σ orbitals accommodate two electrons and the π orbitals four. In this way, a closed shell is generated, thereby giving a ground state with Σ_g^+ ($D_{\infty h}$) symmetry, $D_{\infty h}$ being an axial symmetry. Numerous theoretical attempts have been made to arrive at the ordering of the bonding molecular orbitals within the uranyl unit. In 1957, Jørgensen stated that the highest filled orbital would be the weakly bonding π_u [15]. In 1961, a new hypothesis, now known to be incorrect, was introduced by McGlynn and Smith, based on the results of their overlap calculations [2,4]. The criteria of maximum overlap gave the ordering of the occupied valence orbitals as $\sigma_u^+ < \sigma_g^+ < \pi_u < \pi_g$. More sophisticated overlap calculations using SCF wavefunctions give results that are rather dependent on the details of the wavefunction and on the interatomic distances. For example, Belford and Belford [14] and Newman [17] favoured $\pi_g < \sigma_g^+ < \pi_u < \sigma_u^+$. An example of a comprehensive calculation is a recent SW-Xα treatment, giving a set of filled orbitals in the order $\sigma_g^+ < \pi_u < \sigma_u^+ < \pi_g$ [5].

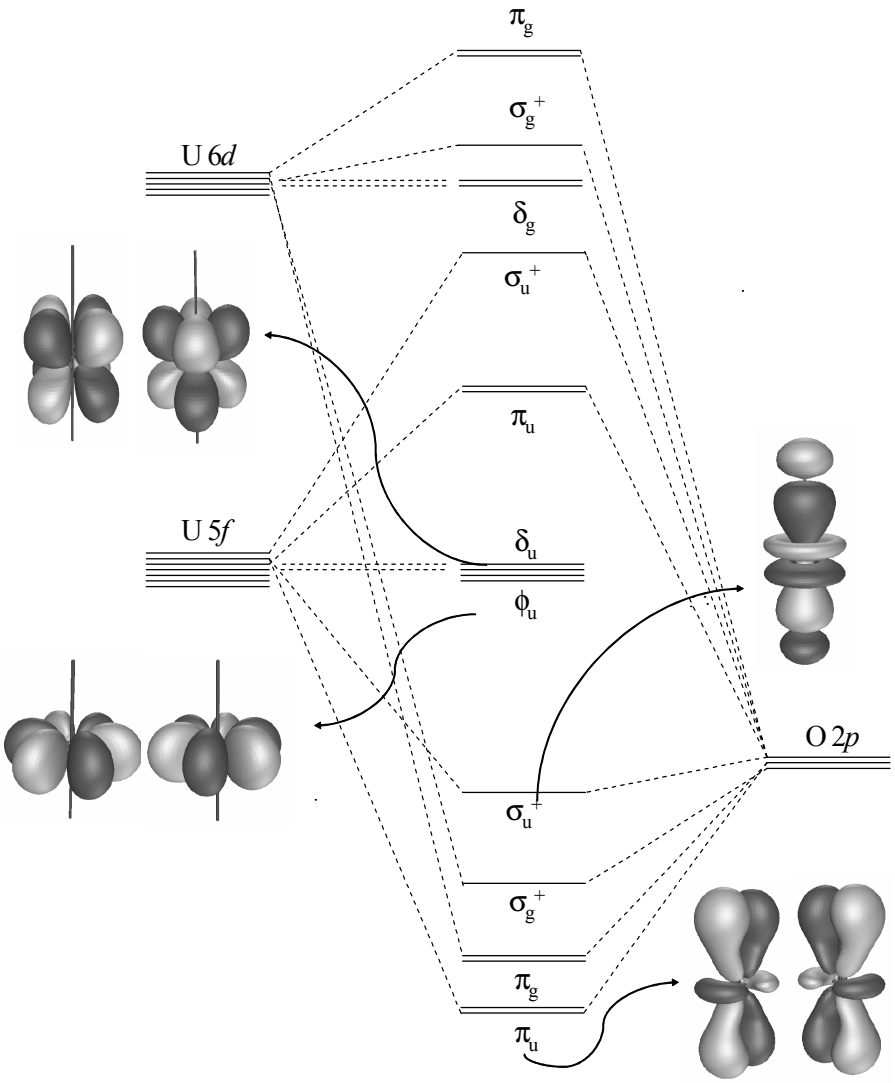

Figure 2.1. Qualitative energy level scheme of the valence molecular orbitals of the uranyl ion UO_2^{2+} in $D_{\infty h}$ symmetry [3,4,6a]. A picture of the molecular orbitals, not shown in this figure, is included in Appendix 2.

Nowadays, it is generally accepted that the highest filled valence orbital has σ_u^+ symmetry [3-5,6a,7,8a,11]. The relative energy of the bonding valence orbitals of UO_2^{2+} is according to Denning et al. $\sigma_u^+ > \sigma_g^+$

> π_g, π_u. Excited state absorption experiments place the σ_u^+ molecular orbital approximately 17700 cm^{-1} above the σ_g^+ orbital. The π orbitals are positioned well below the σ_g^+ orbital, although it is not possible to define the relative positions of π_g and π_u [3,4,6a]. In a recent CASSCF/CASPT2 study on the spectrum of UO_2^{2+} by Pierloot et al., the ordering of the bonding valence orbitals was found to be $\pi_g < \sigma_g^+ \approx \pi_u << \sigma_u^+$, giving a more precise determination of the relative energies of the π_g and π_u orbitals [7].

The highest relative energy of the σ_u^+ orbital can be explained by a "pushing from below" mechanism, as reported in the literature [6a,7,18]. The valence orbitals σ_u^+, σ_g^+, π_g and π_u are built from a bonding interaction between O 2*p* and U 5*f* (σ_u^+, π_u) or U 6*d* (σ_g^+, π_g) orbitals. However, the pseudocore U 6*p* orbitals contribute significantly to the σ_u^+ orbital. This contribution of U 6*p* orbitals is much smaller or even absent in the other bonding valence orbitals. The interaction between the U 6*p* orbitals and the U 5*f*/O 2*p* combination is anti-bonding, which results in a destabilization, and thus in the higher energy of the σ_u^+ orbital.

The molecular orbitals δ_u and ϕ_u only originate from the 5*f* orbitals of uranium. Consequently, they are non-bonding and empty. The ϕ_u orbital lies only slightly above the δ_u orbital (~ 2000 cm^{-1}) in the presence of an equatorial ligand field. This energy difference between the δ_u and ϕ_u orbitals has been determined by optical measurements on uranyl and neptunyl single crystals [4]. Nevertheless, a slight distinction has to be made when taking into account recent theoretical calculations. It has been found that the relative position of the δ_u and ϕ_u orbitals can change. In UO_2^{2+}, i.e. the uranyl ion without any ligands or solvent molecules in its equatorial plane, the non-bonding orbitals have approximately the same energy, $E(\delta_u) \cong E(\phi_u)$. However, when ligands are surrounding the uranyl ion in the equatorial plane, the energy of the ϕ_u orbital is raised due to ionic interactions with the equatorial field [7,19]. The anti-bonding $5f_\pi$ orbital is placed about 14000 cm^{-1} above ϕ_u. The same

overall ordering $5f_\delta < 5f_\phi < 5f_\pi < 5f_\sigma$ was recently found as a result for the lowest lying virtual orbitals by Hay et al. by performing DFT calculations on aquo complexes of AnO_2^{2+} and AnO_2^{+} ions (An = U, Pu, Np) [4,16].

Concerning the relative energies of the anti-bonding molecular orbitals with primarily uranium 5*f* and 6*d* character, Denning et al. established their order to be $5f_\pi < 5f_\sigma \sim 6d_\delta \sim 6d_\sigma < 6d_\pi$ using polarized oxygen Kα X-ray absorption and emission spectroscopy on a $Cs_2UO_2Cl_4$ single crystal. The $5f_\sigma$ orbital is situated approximately 21500 cm^{-1} above $5f_\pi$ and the more anti-bonding $6d_\pi$ orbital lies approximately 16100 cm^{-1} higher in energy than $6d_\sigma$, which is nearly degenerate with $6d_\delta$ [6a].

Rather than the ordering of the molecular orbitals, a more fundamental question is from which molecular orbital occur the excitations in the UV-Vis absorption spectrum. Jørgensen argued that the low intensities in the absorption spectra of uranyl compounds (ε = 10 - 100 L mol^{-1} cm^{-1}) are due to a parity selection rule, which was confirmed by Görller-Walrand and Vanquickenborne. The orbitals to which the electron is excited, are either δ_u or ϕ_u. This means that in accordance to the parity selection rule the excitation must come from an ungerade orbital, thereby leaving only the σ_u^+ and π_u orbitals as being eligible. Consequently, the excited states are formed from an electron configuration of the type $\gamma_u\delta_u$ or $\gamma_u\phi_u$, where $\gamma_u = \sigma_u^+$ or π_u^3 [3-5,8,11,15]. But the optical spectra are completely explicable in terms of excitations from a σ_u^+ orbital to the δ_u and ϕ_u orbitals.

Comparison of the UV-Vis absorption spectra of several uranyl compounds with a wide range of ligands reveals that all spectra exhibit a relatively weak absorption with characteristic progressions in the same spectral region, i.e. between 20000 cm^{-1} and 30000 cm^{-1} [5,11]. This implies that the spectrum is primarily controlled by the axial field of the oxygen atoms, while the perturbation induced by the equatorial ligands is small in comparison. The perturbations on the energy levels can be classified in the following order of magnitude:

$$V_{ax} >> V_{ER} \approx V_{s.o.c.} > V_{eq} >> V_{Zeeman} \quad (2.1)$$

where V_{ax} and V_{eq} are the ligand field by the axial oxygen atoms (ax) and the equatorial coordinated ligands (eq), respectively. V_{ER} and $V_{s.o.c}$ refer to electron repulsion and spin-orbit coupling. For MCD measurements, we consider the induced Zeeman perturbation (V_{Zeeman}). In the following sections, these perturbations on the energy levels of the uranyl ion will be introduced and briefly discussed.

2 Λ-Σ or ω-ω coupling scheme in the uranyl ion?

Taking into account the perturbations caused by the strong axial field of the oxygen atoms as well as by electron repulsion and spin-orbit interaction, the Hamiltonian for the valence electrons can be written as:

$$\mathcal{H} = \mathcal{H}_{ax} + \mathcal{H}_{ER} + \mathcal{H}_{s.o.c.} \quad (2.2)$$

with $V_{ax} >> V_{ER} \approx V_{s.o.c.}$.

While it is known that the axial field (V_{ax}) induces an extremely strong perturbation, it is hard to determine whether the electron repulsion or the spin-orbit interaction has the largest contribution to the perturbations on the energy levels. The spin-orbit interaction is clearly large in a uranium-centred orbital, whilst small in an oxygen-centred orbital. It is therefore not clear whether a Λ-Σ or a ω-ω coupling scheme is the most appropriate starting point. Nowadays, most authors agree that an intermediate coupling scheme provides an adequate description of the energy levels, although it is closer to the Λ-Σ limit than to the ω-ω limit [4,8,11a].

By applying the Λ-Σ Russell-Saunders coupling scheme, the assumption is made that the electron repulsion exceeds the spin-orbit interaction. At first, the electron repulsion is introduced, thereby generating eigenfunctions of $\hat{S}^2$, $\hat{S}_z$ (Σ) and $\hat{L}_z$ (Λ). When spin-orbit interaction is included, the final states are characterized by $\hat{J}_z$ (Ω). On the other hand, one considers the spin-orbit interaction to be larger than the electron repulsion in the ω-ω coupling scheme. The individual wavefunctions are eigenfunctions of j_z (ω). Taking into account the electron repulsion, the final states are constructed, again characterized by Ω. The comparison between the resulting electronic states in the Λ-Σ and ω-ω coupling schemes is listed in Table 2.2 [11a].

Since an intermediate coupling scheme is the most appropriate way to describe the electronic excited states of the uranyl ion, Denning et al. have constructed correlation diagrams relating the Λ-Σ and the ω-ω limits for the $\sigma_u^+\delta_u$, $\sigma_u^+\phi_u$, $\pi_u^3\delta_u$ and $\pi_u^3\phi_u$ configurations [4,5]. In this way, the correlation diagram of the $\sigma_u^+\delta_u$ configuration reveals that the lowest lying excited states in an intermediate coupling scheme are $\Pi_g < \Delta_g < \Phi_g < \Delta_g$, when an equatorial ligand field is applied. These states correspond to $^3\Delta_g$ (Π_g, Δ_g, Φ_g) and $^1\Delta_g$ (Δ_g) in the Λ-Σ Russell-Saunders coupling scheme and to Π_g, Δ_g and Φ_g, Δ_g in the ω-ω coupling scheme, respectively [4,5]. Conversely, recent theoretical calculations revealed that the luminescent state in UO_2^{2+}, i.e. in the absence of ligands or solvent molecules in the equatorial plane, is Δ_g, arising from the $\sigma_u^+\phi_u$ configuration. Thus, the lowest lying excited state of the uranyl ion is affected by the presence of an equatorial ligand field [7,19,20].

Table 2.2. Comparison of the Λ-Σ and ω-ω coupling schemes [11a].

Λ-Σ coupling			ω-ω coupling		
V_{ax}	V_{ER}	$V_{s.o.c.}$	V_{ER}	$V_{s.o.c.}$	V_{ax}
$\pi_u^3\phi_u$	$^1\Delta_g$	Δ_g	Γ_g Φ_g	$(1/2)(3/2)^2(7/2)$	$\pi_u^3\phi_u$
	$^1\Gamma_g$	Γ_g			
	$^3\Delta_g$	Φ_g Δ_g Π_g	Δ_g H_g	$(1/2)^2(3/2)(7/2)$	
			Δ_g Φ_g	$(1/2)(3/2)^2(5/2)$	
	$^3\Gamma_g$	H_g Γ_g Φ_g	Γ_g Π_g	$(1/2)^2(3/2)(5/2)$	
$\pi_u^3\delta_u$	$^1\Pi_g$	Π_g	Φ_g Δ_g	$(1/2)(3/2)^2(5/2)$	$\pi_u^3\delta_u$
	$^1\Phi_g$	Φ_g			
	$^3\Pi_g$	Δ_g Π_g Σ_g	Γ_g Π_g	$(1/2)^2(3/2)(5/2)$	
			Δ_g Π_g	$(1/2)(3/2)^2(3/2)$	
	$^3\Phi_g$	Γ_g Φ_g Δ_g	Φ_g Σ_g	$(1/2)^2(3/2)(3/2)$	
$\sigma_u^+\phi_u$	$^1\Phi_g$	Φ_g	Φ_g Γ_g	$(1/2)(7/2)$	$\sigma_u^+\phi_u$
	$^3\Phi_g$	Γ_g Φ_g Δ_g	Φ_g Δ_g	$(1/2)(5/2)$	
$\sigma_u^+\delta_u$	$^1\Delta_g$	Δ_g	Δ_g Φ_g	$(1/2)(5/2)$	$\sigma_u^+\delta_u$
	$^3\Delta_g$	Φ_g Δ_g Π_g	Δ_g Π_g	$(1/2)(3/2)$	
V_{ax}	V_{ER}	$V_{s.o.c.}$	V_{ER}	$V_{s.o.c.}$	V_{ax}

The final electronic states in Table 2.2 are all doubly degenerate. Due to the axial field, the angular momentum is constrained to be directed along the internuclear axis, i.e. the O-U-O axis. Consequently, there are only two components of Ω, i.e. $M_\Omega = \pm \Omega$. No orbital angular momentum perpendicular to the O-U-O axis is observed [5]. Furthermore, mixing occurs between states of the same Ω value [5,8]. This implies, for example, Ω-Ω mixing between the two Δ_g states ($^3\Delta_g$ and $^1\Delta_g$) of the $\sigma_u^+\delta_u$ configuration. Notice that a Π_g electronic state at lower energy can only originate from the $\sigma_u^+\delta_u$ configuration, that the detection of a Γ_g state is only possible at energies at least high enough for the $\sigma_u^+\phi_u$ region and that a H_g state always points to a $\pi_u^3\phi_u$ configuration.

Whereas the beginning of the UV-Vis absorption spectrum is controlled by the $\sigma_u^+\delta_u$ configuration, additional states from the $\sigma_u^+\phi_u$, $\pi_u^3\delta_u$ and $\pi_u^3\phi_u$ configurations have to be considered at higher energies. Fortunately, there is sufficient theoretical and experimental evidence to exclude the presence of states derived from excitations to the anti-bonding $5f\sigma_u^+$ and $5f\pi_u$ orbitals as well as of states originated from 'double' configurations like δ_u^2 or ϕ_u^2 [21].

3 Equatorial ligand field perturbation

By surrounding the uranyl ion with ligands in the first coordination sphere, an additional perturbation, caused by the equatorial ligand field, is generated on the electronic states of the uranyl ion. In the presence of ligands in the equatorial plane, the Hamiltonian can be rewritten as follows:

$$\mathcal{H} = \mathcal{H}_{ax} + \mathcal{H}_{ER} + \mathcal{H}_{s.o.c.} + \mathcal{H}_{eq} \qquad (2.3)$$

with $V_{ax} >> V_{ER} \approx V_{s.o.c.} > V_{eq}$.

The effect of the equatorial ligand field on the axial field eigenstates has been extensively studied by Görller-Walrand and Vanquickenborne in uranyl complexes with small inorganic ligands [11a,22]. These experimental results have been confirmed by recent theoretical calculations on this type of compounds [8b,23].

By applying V_{eq}, the double degeneracy of the cylindrical field states is lifted in certain point groups. Table 2.3 shows what happens to a $D_{\infty h}$ state when it is subjected to an equatorial ligation with the appropriate symmetry properties [11b].

The double degeneracy of the $D_{\infty h}$ states can be described by two complex wavefunctions $\Psi(\Omega)$ and $\Psi(-\Omega) = \Psi^*(\Omega)$, which are eigenfunctions of $\hat{J}_z$ [11a]:

$$\hat{J}_z \Psi(\Omega) = \Omega \hbar \Psi(\Omega) \tag{2.4}$$

$$\hat{J}_z \Psi(-\Omega) = -\Omega \hbar \Psi(-\Omega) \tag{2.5}$$

The equatorial ligand field V_{eq} will remove the degeneracy in some point groups. If so, the two non-degenerate, real wavefunctions, describing the two resulting states, will be given by:

$$\Psi^+ = {}^{1}\!/_{\sqrt{2}} \left[\Psi(\Omega) + \Psi(-\Omega)\right] \tag{2.6}$$

$$\Psi^- = {}^{1}\!/_{\sqrt{2}} \left[\Psi(\Omega) - \Psi(-\Omega)\right] \tag{2.7}$$

Thus, the energy splitting can be expressed as:

$$\Delta E = 2\langle \Psi(\Omega) | V_{eq} | \Psi(-\Omega) \rangle \tag{2.8}$$

Since V_{eq} can be approximated as a sum of one-electron spin-independent operators, this energy splitting will be zero whenever $\Psi(\Omega)$ and $\Psi(-\Omega)$ differ by more than one spin orbital [5,11a].

Table 2.3. Correlation of the irreducible representations in the different D_{nh} point groups. If the transition between the totally symmetric ground state (Σ_g^+) and the excited state under consideration is electronically allowed, its polarization is given in parentheses. In all cases, the z-axis corresponds to the O-U-O axis [11b].

$D_{\infty h}$	D_{2h}	D_{2d}	D_2	D_{3h}	D_{3d}	D_3	D_{4h}	D_{5h}	D_{6h}	C_{6v}
Σ_g^+	A_g	A_1	A	A'_1	A_{1g}	A_1	A_{1g}	A'_1	A_{1g}	A_1 (z)
Σ_g^-	B_{1g}	A_2	B_1 (z)	A'_2	A_{2g}	A_2 (z)	A_{2g}	A'_2	A_{2g}	A_2
Π_g	B_{2g} B_{3g}	E (x,y)	B_2 (y) B_3 (x)	E"	E_g	E (x,y)	E_g	E''_1	E_{1g}	E_1 (x,y)
Δ_g	A_g B_{1g}	B_1 B_2 (z)	A B_1 (z)	E' (x,y)	E_g	E (x,y)	B_{1g} B_{2g}	E'_2	E_{2g}	E_2
Φ_g	B_{2g} B_{3g}	E (x,y)	B_2 (y) B_3 (x)	A''_1 A''_2 (z)	A_{1g} A_{2g}	A_1 A_2 (z)	E_g	E''_2	B_{1g} B_{2g}	B_2 B_1

(Table 2.3 continued)

Γ_g	A_g B_{1g}	A_1 A_2	A B_1 (z)	E' (x,y)	E_g	E (x,y)	A_{1g} A_{2g}	E'_1 (x,y)	E_{2g}	E_2
H_g	B_{2g} B_{3g}	E (x,y)	B_2 (y) B_3 (x)	E''	E_g	E (x,y)	E_g	A''_1 A''_2 (z)	E_{1g}	E_1 (x,y)
I_g	A_g B_{1g}	B_1 B_2 (z)	A B_1 (z)	A'_1 A'_2	A_{1g} A_{2g}	A_1 A_2 (z)	B_{1g} B_{2g}	E'_1 (x,y)	A_{1g} A_{2g}	A_1 (z) A_2
$D_{\infty h}$	D_{2h}	D_{2d}	D_2	D_{3h}	D_{3d}	D_3	D_{4h}	D_{5h}	D_{6h}	C_{6v}

The equatorial ligand field potential V_{eq} can be expressed in a spherical harmonic expansion by terms of the type Y_q^k. In this way, V_{eq} can be written as [21,24,25]:

$$V_{eq} = \sum_{k,q} B_q^k C_q^k \tag{2.9}$$

with V_{even} if $k = 2, 4, 6$ and V_{odd} if $k = 3, 5, 7$ with $q = \pm k$. C_q^k is a tensor operator related to the spherical harmonics – that represent the angular position of the electron – in the following manner:

$$C_q^k = \sqrt{\frac{4\pi}{2k+1}} Y_q^k \tag{2.10}$$

B_q^k is a parameter containing the spherical harmonics that represent the angular position of the ligands.

It is more convenient to work with tesseral harmonics, which are real unlike the spherical ones. This can be compared with using p_x, p_y and p_z instead of p_{+1}, p_{-1} and p_0. The potential can be described as:

$$V_{eq} = \sum_k \left[B_0^k C_0^k + \sum_{q=1}^{k} \left(B_q^k \left(C_{-q}^k + (-1)^q C_q^k \right) + B'^k_q \, i \left(C_{-q}^k - (-1)^q C_q^k \right) \right) \right] \tag{2.11}$$

For a complete definition and more detailed information, we refer to Görller-Walrand and Binnemans [24,25].

We will now consider the equatorial ligand field potential and the corresponding ligand field splittings in two point groups of interest, i.e. D_{4h} (e.g. $[UO_2Cl_4]^{2-}$) and D_{3h} (e.g. $[UO_2(NO_3)_3]^-$). The ligand field potential for a D_{4h} coordination symmetry can be written as:

$$V_{even}(D_{4h}) = B_0^2 C_0^2 + B_0^4 C_0^4 + B_4^4 \left(C_{-4}^4 + C_4^4\right) + B_0^6 C_0^6 + B_4^6 \left(C_{-4}^6 + C_4^6\right)$$
$$V_{odd}(D_{4h}) = 0 \tag{2.12}$$

The even part of the ligand field potential is responsible for the splitting of the Δ_g states in B_{1g} and B_{2g} in D_{4h} symmetry [5]. The corresponding perturbation matrix can be written as:

$$\left\langle \Delta_{g\pm 2} \left| C_{\pm 4}^{6,4} \right| \Delta_{g\mp 2} \right\rangle \tag{2.13}$$

The non-degenerate states B_{1g} and B_{2g}, originating from Δ_g, transform as $d_{x^2-y^2}$ and d_{xy}, respectively.
Under influence of the even terms of the ligand field potential, a second-order interaction between the Π_g and Φ_g states is induced [5]. Indeed, these states both transform as E_g in D_{4h}. Therefore, they mix with another under influence of the equatorial ligand field matrix element:

$$\left\langle \Pi_{g\pm 1} \left| C_{\pm 4}^{6,4} \right| \Phi_{g\mp 3} \right\rangle \tag{2.14}$$

The equatorial ligand field potential for a D_{3h} coordination symmetry is given in Equation 2.15. Unlike the potential for a D_{4h} symmetry, the odd part is non-zero. However, only the even terms are responsible for the ligand field splitting. Possible induced electric dipole transitions can be evaluated using the odd part (see 5.2 (Chapter 2)) [24,25].

$$V_{even}(D_{3h}) = B_0^2 C_0^2 + B_0^4 C_0^4 + B_0^6 C_0^6 + B_6^6 \left(C_{-6}^6 + C_6^6\right)$$
$$V_{odd}(D_{3h}) = B'^3_3\, i\left(C_{-3}^3 + C_3^3\right) + B'^5_3\, i\left(C_{-3}^5 + C_3^5\right) + B'^7_3\, i\left(C_{-3}^7 + C_3^7\right) \tag{2.15}$$

The Φ_g states in $D_{\infty h}$ split under influence of the D_{3h} ligand field into the components A''_1 and A''_2, according to the perturbation matrix element:

$$\left\langle \Phi_{g\pm 3} \left| C^6_{\pm 6} \right| \Phi_{g\mp 3} \right\rangle \tag{2.16}$$

Mixing occurs between the Δ_g and Γ_g electronic states, both transforming as E' in D_{3h}, under influence of the trigonal ligand field [5]. This second-order effect can be expressed by the matrix element:

$$\left\langle \Delta_{g\pm 2} \left| C^6_{\pm 6} \right| \Gamma_{g\mp 4} \right\rangle \tag{2.17}$$

The relative energy of the non-degenerate states, denoted as Γ_i and Γ_j, after the equatorial ligand field perturbation is determined – to a good approximation – by the orbital parts of the wavefunctions alone. Therefore, if Γ_i is the higher in energy for the singlet state, it will be lower in energy for the triplet state. In other words, the splitting of the triplet state will be equal but opposite in sign to that of the singlet state [5,11a]. A good example to illustrate this is the ligand field splitting of the second and the fourth excited states, i.e. Δ_g, into B_{1g} and B_{2g} in a D_{4h} coordination symmetry, e.g. $Cs_2UO_2Cl_4$. The first Δ_g state contains more triplet character, compared with the larger singlet character of the latter. For Δ_g ($^3\Delta_g$), the B_{2g} component has the lowest energy, whilst B_{1g} is at lower energy for Δ_g ($^1\Delta_g$). Theoretically, the energy splitting should be the same for both Δ_g states ($^3\Delta_g$ and $^1\Delta_g$). However, a reduction of the ligand field splitting is observed in an intermediate coupling scheme. The tetragonal field splitting is 903.5 cm^{-1} for B_{1g}-B_{2g} ($^3\Delta_g$) and -340 cm^{-1} for B_{1g}-B_{2g} ($^1\Delta_g$). The smaller value for the Δ_g state, arising from $^1\Delta_g$ ($\sigma_u^+\delta_u$), can be explained by configuration interaction with Δ_g ($\sigma_u^+\phi_u$), which is not observed for Δ_g ($^3\Delta_g$, $\sigma_u^+\delta_u$) [5,7,19]. Furthermore, the intensity of a transition arising from $^1\Delta_g$ is about five times higher than from the $^3\Delta_g$ state [4,5,11a].

The energy splitting patterns for a D_{4h} and D_{3h} coordination symmetry are depicted in Figure 2.2 between the two extreme coupling schemes: ω-ω coupling on one side and Λ-Σ coupling on the other [21]. We have to remark that this scheme of the equatorial ligand field splitting in a D_{4h} and D_{3h} coordination symmetry has been simplified and is more or less out of date. Nowadays, much more excited states as well as the extensive mixing of different electronic states have to be taken into account, based on the results of theoretical calculations on various uranyl complexes.

4 Zeeman perturbation and magnetic circular dichroism (MCD)

When a magnetic field is applied, the Zeeman perturbation is induced and Equation 2.3 becomes:

$$\mathcal{H} = \mathcal{H}_{ax} + \mathcal{H}_{ER} + \mathcal{H}_{s.o.c.} + \mathcal{H}_{eq} + \mathcal{H}_{Zeeman} \qquad (2.18)$$

with $V_{ax} >> V_{ER} \approx V_{s.o.c.} > V_{eq} >> V_{Zeeman}$ and where $\mathcal{H}_{Zeeman} = -\mu_z H_Z$ with $-\mu_z$ the magnetic dipole associated with the angular momentum defined by Ω and H_z the magnetic field along the z-direction. Thereby, the z-axis corresponds to the O-U-O axis. The Zeeman perturbation lifts the degeneracy in doubly degenerate states and induces mixing of states with the same Ω value [21].

Magnetic circular dichroism (MCD) spectroscopy is based on the Zeeman effect, thereby measuring the differential absorption of left and right circularly polarized light of a sample in a longitudinal magnetic field. In a longitudinal magnetic field, the magnetic field lines are parallel to the light beam. MCD spectroscopy has the advantage over regular Zeeman spectroscopy that MCD spectra can be recorded also in cases where the band width is larger than the Zeeman splitting [26].

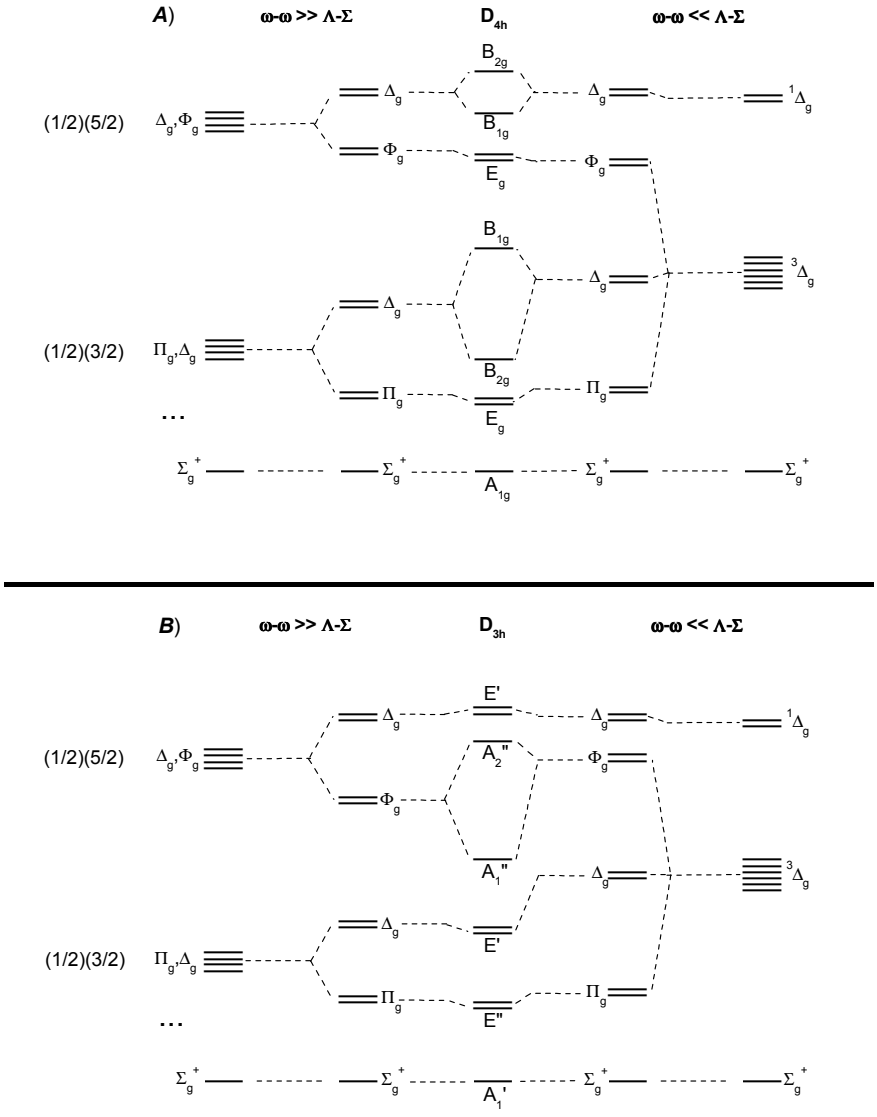

Figure 2.2. Energy splitting scheme of the $\sigma_u^{+}\delta_u$ configuration for UO_2^{2+} in a D_{4h} (**A**) and D_{3h} (**B**) equatorial coordination symmetry [21].

Light absorbing, chiral complexes have different absorption coefficients for left and right circularly polarized light. The amplitudes of both components are changed. This is called *circular dichroism*:

$$\Delta\varepsilon = \varepsilon_l - \varepsilon_r \tag{2.19}$$

In a magnetic field, this property is induced on every complex, independent of its chirality [21,27].

While an absorption spectrum measures the molar absorptivity ε (L mol^{-1} cm^{-1}) as a function of the wavenumber, an MCD spectrum expresses Δε/H (L mol^{-1} cm^{-1} T^{-1}) in function of the wavenumber, leading to A-, B- (or C-) terms in the MCD formalism. An A-term has the shape of the first derivative of an absorption curve and is observed when the excited state is degenerate. Both B- and C-terms resemble an absorption peak. A B-term originates from a degenerate excited state, which is already split under influence of the equatorial ligand field, thus before applying the magnetic field. A- and B-terms are temperature independent, whereas a C-term is temperature dependent. Since Δε is a difference of two quantities, an MCD signal can have either a positive or a negative sign [26]. To illustrate the definition of A- and B-terms, we have used a hypothetical simple example, e.g. the transition $^1\Pi_u \leftarrow {}^1\Sigma_g^+$ in D_{4h} and D_{2h} coordination symmetry. A $^1\Pi_u$ state splits into +1 βH_z and -1 βH_z (corresponding to + Ω βH_z and – Ω βH_z) by applying a magnetic field in D_{4h} symmetry. Consequently, this transition gives rise to a positive A-term (Figure 2.3). In D_{2h}, on the other hand, $^1\Pi_u$ is already split into $^1B_{2u}$ and $^1B_{3u}$ under influence of the equatorial ligand field, resulting in $\left(1/\sqrt{2}\left(|-1\rangle - |+1\rangle\right)\right)$ and $\left(1/\sqrt{2}\left(|-1\rangle + |+1\rangle\right)\right)$, respectively. Therefore, B-terms (positive and negative) are observed in D_{2h} (Figure 2.4) [21,28]. The magnetic field mixes the B_{2u} and B_{3u} states in second order, introducing some $|+1\rangle$ character at higher energy and $|-1\rangle$ at lower energy.

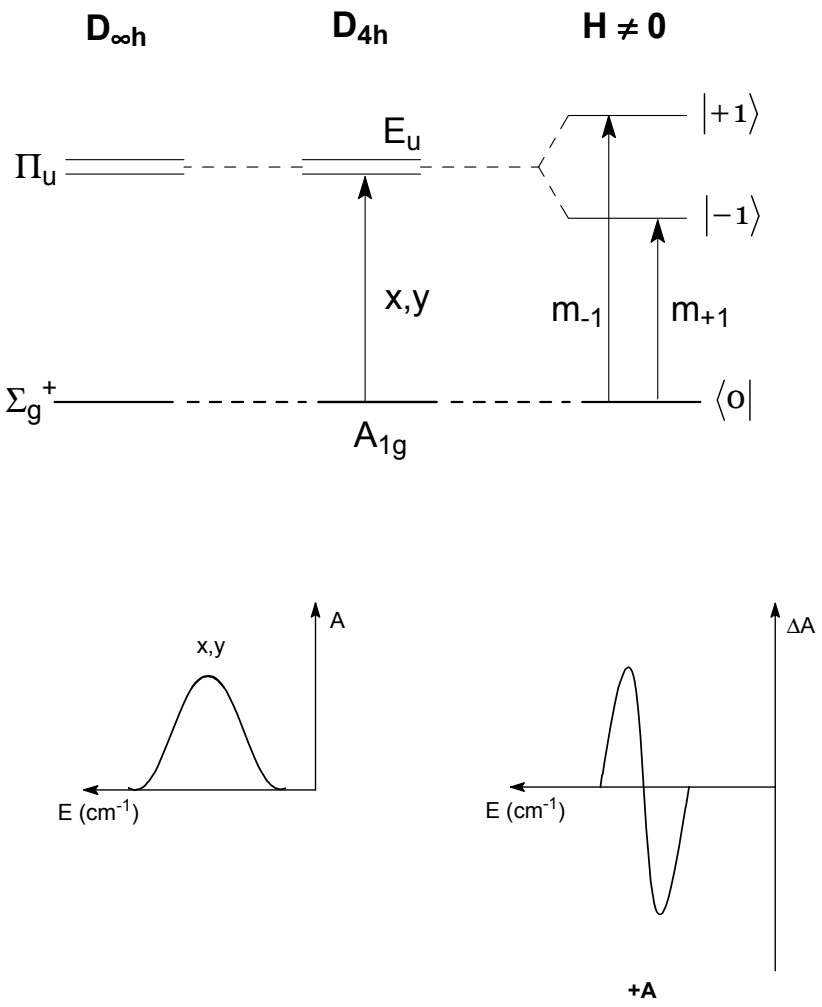

Figure 2.3. Shape and sign of the MCD terms (positive A-term) for the hypothetical $^1\Pi_u \leftarrow {}^1\Sigma_g^+$ transition in a *D4h* symmetry (m_{-1}, l = left circularly polarized light; m_{+1}, r = right circularly polarized light). The corresponding peak in the UV-Vis absorption spectrum is also shown [21,28].

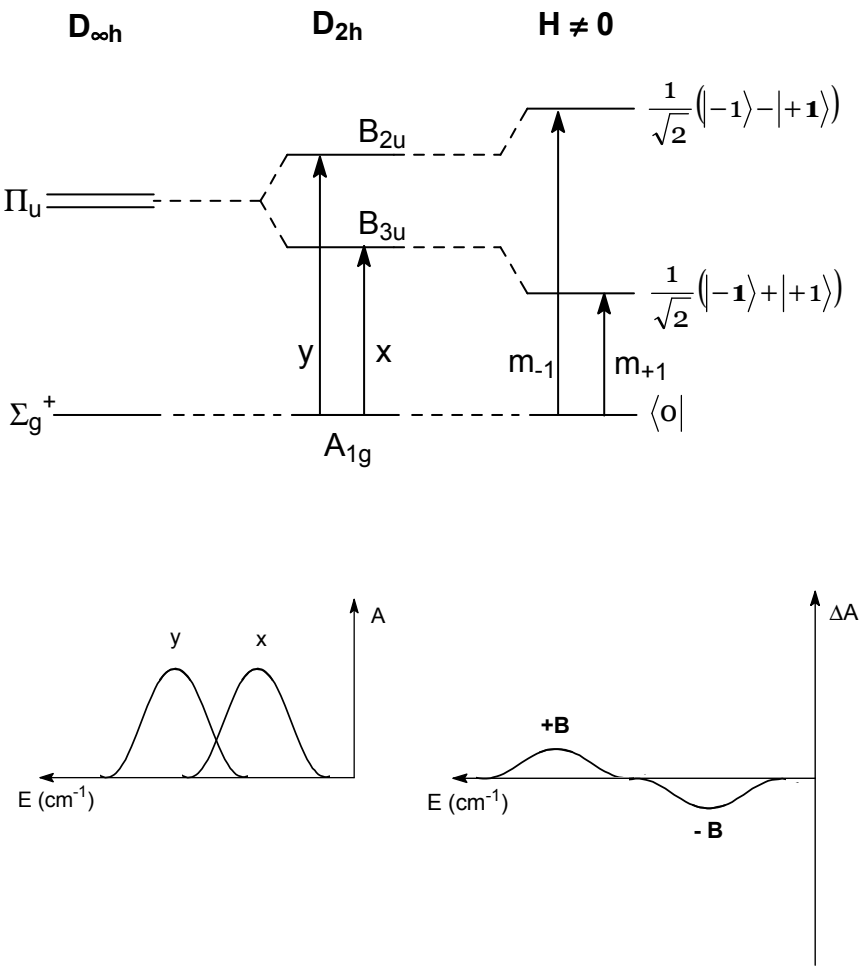

Figure 2.4. Shape and sign of the MCD terms (positive and negative B-terms or 'pseudo' positive A-term) for the hypothetical $^1\Pi_u \leftarrow {}^1\Sigma_g{}^+$ transition in a D_{2h} symmetry (m_{-1}, l = left circularly polarized light; m_{+1}, r = right circularly polarized light; either $|+1\rangle$ or $|-1\rangle$ (bold) predominate in the diagonalized functions). Two distinct absorption peaks are observed in the corresponding UV-Vis absorption spectrum [21,28].

To develop selection rules for absorption and the sign of the MCD terms, we use the properties of circularly polarized light. Left and right circularly polarized light have a well-defined z-component of the angular momentum, m_J = -1 and m_J = +1, respectively. If the orbital angular momentum is considered as the only contribution to the Zeeman interaction, the *sign convention* is as follows: left circularly polarized light, indicated by m_{-1} or simply l, allows transitions towards the positive Zeeman component, whereas right circularly polarized light (m_{+1} or r) gives transitions towards the negative Zeeman component, resulting in a positive A-term. However, it is very important to include the spin contribution to the magnetic moment as well. Indeed, the spin contribution can oppose and even exceed the orbital contribution, thereby inverting the sign of the MCD term, derived only from the orbital contribution [6d,21].

Taking into account the properties of circularly polarized light as well as the ligand field perturbation, the intensity matrix element, which can be used to determine the sign of the MCD signal, is proportional to a 3*j*-symbol including the symmetry dependent component *q* [21,26,29,30]:

$$\left\langle \Psi(\Omega M_\Omega) \middle| U^{\lambda}_{\rho+q} \middle| \Psi(\Omega' M'_\Omega) \right\rangle \propto (-1)^{\Omega - M_\Omega} \times \begin{pmatrix} \Omega & \lambda & \Omega' \\ -M_\Omega & \rho+q & M'_\Omega \end{pmatrix} \left\langle \Psi(\Omega) \middle\| U^{\lambda} \middle\| \Psi(\Omega') \right\rangle \tag{2.20}$$

where $\Omega = \Lambda+\Sigma$ is the total angular momentum quantum number and M_Ω its components along the z axial field; λ is the orbital angular momentum quantum number; ρ gives the polarization number (ρ = -1, +1 for left and right circularly polarized light, respectively); *k* and *q* are rank and component of the odd terms in the expansion of the equatorial ligand field potential (see Equation 2.9) with λ = 2 for *k* = 1, 3; λ = 4 for *k* = 3,

5; $\lambda = 6$ for $k = 5, 7$. This 3*j*-symbol $\begin{pmatrix} \Omega & \lambda & \Omega' \\ -M_\Omega & \rho+q & M'_\Omega \end{pmatrix}$ is zero unless $-M_\Omega + \rho + q + M'_\Omega = 0$.

Using Equation 2.20, one can find, for example, that in a D_3 coordination symmetry, the transition $\Delta_g \leftarrow \Sigma_g^+$ ($E \leftarrow A_1$) is characterized by a negative A-term, because the transition between $M_\Omega = 0$ and $M_\Omega = +2$ occurs for right circularly polarized light. On the other hand, for $\Gamma_g \leftarrow \Sigma_g^+$ ($E \leftarrow A_1$) absorption occurs between $M_\Omega = 0$ and $M_\Omega = +4$ for left circularly polarized light, leading to a positive A-term. These observations are related to the following 3*j*-symbols [31]:

$$\Delta_g \leftarrow \Sigma_g^+ \qquad \begin{pmatrix} 0 & 2 \textit{ or } 4 & 2 \\ 0 & \mp 1 \pm 3 & \mp 2 \end{pmatrix} \qquad A(-) \qquad (2.21)$$

$$\Gamma_g \leftarrow \Sigma_g^+ \qquad \begin{pmatrix} 0 & 4 \textit{ or } 6 & 4 \\ 0 & \pm 1 \pm 3 & \mp 4 \end{pmatrix} \qquad A(+) \qquad (2.22)$$

NOTE: In the chapters describing the experimental results and in Appendix 3, the MCD spectra of different uranyl complexes are displayed together with the variation of the dynode voltage as a function of the wavenumber. The dynode voltage variation has the shape of the UV-Vis absorption spectrum. However, this spectrum can not be compared with the UV-Vis absorption spectrum concerning the intensities of the electronic and the vibronic transitions.

5 Selection rules and intensity mechanisms

The spin selection rule ($\Delta\Sigma = 0$) allowing singlet-singlet transitions is the most important selection mechanism. This selection rule, however, is relaxed by spin-orbit coupling in an intermediate coupling scheme. For example, the transition $\Delta_g(^3\Delta_g) \leftarrow {}^1\Sigma_g^+$ is partly allowed due to the

admixture of $\Delta_g(^1\Delta_g)$ into $\Delta_g(^3\Delta_g)$, giving the latter some singlet character. Nevertheless, the transitions in the beginning of the spectrum, originating from the totally symmetric ground state $^1\Sigma_g^+$ to states with (mostly) triplet character ($^3\Delta_g$), exhibit lower intensities – approximately one tenth – with respect to the middle part of the spectrum.

More important is the fact that all electronic transitions between the totally symmetric ground state Σ_g^+ and the excited states in the uranyl ion ($D_{\infty h}$ symmetry) are parity forbidden by the Laporte selection rule (g↔g, u↔u) [4,5,8,11,15]. Consequently, the Laporte selection rule must be lifted to some extent by an intensity mechanism, giving rise to electronic transitions with ε-values of 10 - 100 L mol^{-1} cm^{-1}. Currently, three intensity mechanisms are invoked to interpret the observed transitions in the UV-Vis absorption spectra of uranyl complexes: the *magnetic dipole transitions*, the *static ligand field* (able to destroy the inversion centre) and the *dynamic ligand field* or *vibronic coupling*. In the following, each of these mechanisms will be briefly discussed by means of a few key examples. For a more complete description of the different intensity mechanisms, we refer to Judd and Ofelt [32,33], Görller-Walrand and Binnemans [24,25] and Denning et al. [4,5].

5.1 Magnetic dipole transitions

Magnetic dipole transitions occur in both centrosymmetric and non-centrosymmetric point groups. Transitions are allowed by the magnetic dipole mechanism if the matrix element $\langle \Psi_i | O_{MD} | \Psi_f \rangle$ is non-zero, where Ψ_i and Ψ_f represent the initial and the final states, respectively. The magnetic dipole operator (O_{MD}) transforms as the rotation operators $\mathcal{R}_x$, $\mathcal{R}_y$ and $\mathcal{R}_z$, because a magnetic dipole transition can be interpreted as a rotational displacement of electric charge. The magnetic dipole operators are described by $|10\rangle$ ($\mathcal{R}_z$), $|11\rangle_-$ ($\mathcal{R}_x$) or $|11\rangle_+$ ($\mathcal{R}_y$). In addition, this

magnetic dipole operator has gerade parity. In general, magnetic dipole transitions are characterized by a lower intensity with respect to the electric dipole transitions [21,24-26].

When an equatorial ligand field is present, the lowest lying transition $\Pi_g \leftarrow \Sigma_g^+$, arising from the $\sigma_u^+ \delta_u$ configuration, is basically magnetic dipole allowed in $\mathcal{R}_x$ and $\mathcal{R}_y$ in $D_{\infty h}$. The magnetic dipole intensity of this first electronic transition is confirmed in D_{3h} and D_{4h} coordination symmetry, where the transitions E" $\leftarrow$ A'$_1$ and $E_g \leftarrow A_{1g}$, respectively, are both allowed in $\mathcal{R}_x$ and $\mathcal{R}_y$ [4,5,6e-f]. A magnetic dipole transition allowed in $\mathcal{R}_z$, $\Sigma_g^- \leftarrow \Sigma_g^+$ in $D_{\infty h}$, would be observed at much higher energies, because this transition can only originate from the $\pi_u^3 \delta_u$ configuration [5].

5.2 Static ligand field – induced electric dipole transitions

Induced electric dipole transitions are the most common intensity mechanism in *f-f* and *d-d* transitions. The static ligand field, in our case the equatorial field, can induce electric dipole transitions. These induced electric dipole transitions occur under the odd terms of the equatorial ligand field potential, expanded in spherical harmonics (Y_q^k with k odd) (Equation 2.9). According to the Judd-Ofelt theory, induced electric dipole transitions can only be observed if the point group contains no centre of symmetry. Indeed, only for non-centrosymmetric point groups, the odd part of the ligand field potential is non-zero (Equation 2.12 vs. Equation 2.15) [21,24-26,32,33].

The electric dipole operator transforms as x, y and z, because an electric dipole operator induces a linear displacement of electric charge in the ion. These operators can be described by the corresponding *p* orbital:

$|10\rangle_+$ (z), $|11\rangle_-$ (x) and $|11\rangle_+$ (y). Consequently, the electric dipole operator is ungerade [21,26].

The most striking example of an electric dipole transition generated by the static ligand field, is encountered in the uranyl trinitrato complex $[UO_2(NO_3)_3]^-$ (D_{3h} symmetry) [5,6,12,22a,29,34,35]. In D_{3h}, the transition $\Delta_g \leftarrow \Sigma_g^+$ ($E' \leftarrow A'_1$) is electric dipole allowed perpendicular to the O-U-O axis. This means that the static electric dipole intensity in $\Delta_{g\pm2}$ is induced by the odd crystal field term, $C_{\pm3}^{3,5}$, along the x- and y-axis ($\Pi_{u\pm1}$) according to the matrix element:

$$\left\langle \Delta_{g\pm2} \left| C_{\pm3}^{3,5} \right| \Pi_{u\mp1} \right\rangle \tag{2.23}$$

Visually, one can imagine this as the mixing of a $d_{x^2-y^2}$ orbital with a p_y orbital under a tesseral harmonic of the type $f_{y(3x^2-y^2)}$ [5,6e,21].

Besides the strong absorption intensity due to the admixture between $\Delta_{g\pm2}$ and $\Pi_{u\mp1}$, another interesting feature of the transition $\Delta_g \leftarrow \Sigma_g^+$ is found in the MCD spectrum (see Chapter 5, Figure 5.20). Indeed, this transition is characterized by very intense negative A-terms, since the absorption of right circularly polarized light occurs to the energetically highest Zeeman component. This can be explained by the $|-1\rangle$ character of $\Pi_{u\mp1}$ in $|+2\rangle$ of the $\Delta_{g\pm2}$ state and the fact that the transition to the $|-1\rangle$ component of $\Pi_{u\mp1}$ is allowed by right circularly polarized light. This is illustrated in Figure 2.5 [5,21].

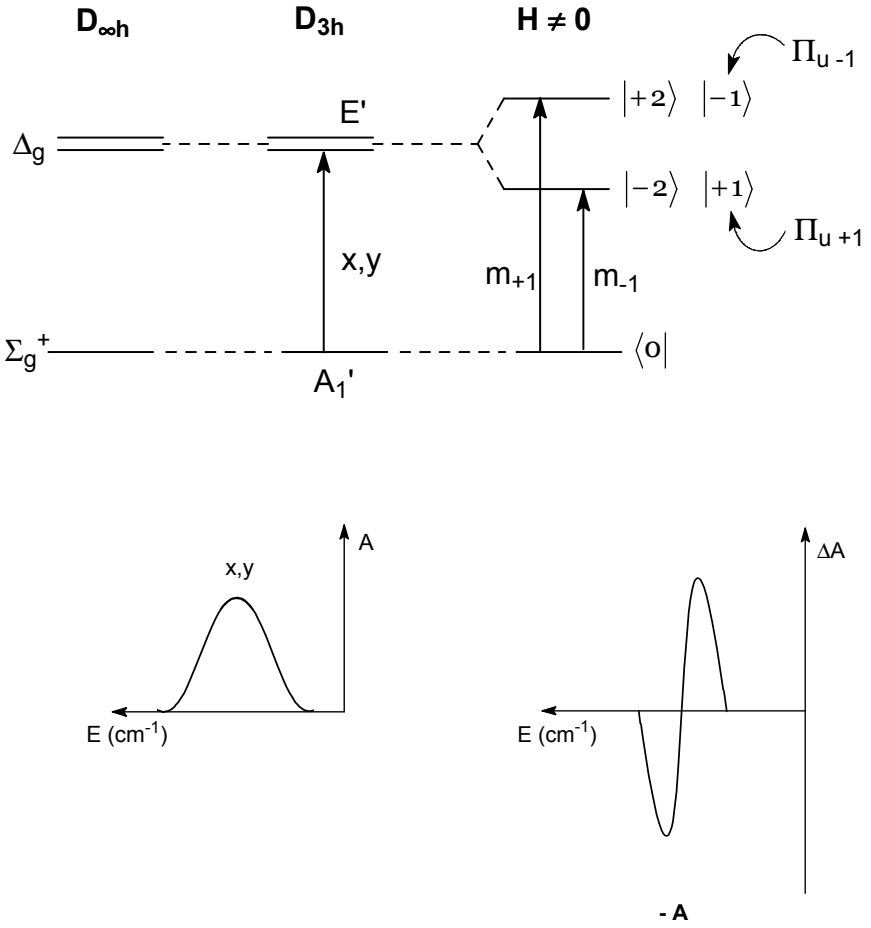

Figure 2.5. Energy diagram and corresponding MCD term (negative A) for a $\Delta_g \leftarrow \Sigma_g^+$ transition in D_{3h} symmetry [21].

5.3 Dynamic ligand field or vibronic coupling

In centrosymmetric point groups, where the inversion centre is still present, electric dipole transitions can only be induced by the dynamic ligand field. This implies the coupling of ungerade vibrational modes to the gerade electronic states, thereby allowing certain components of the

electric dipole transition moment. For example, the transition moment along m_z can indicate a vibration that is coupled to an electronic transition and in this way intensity is induced in the z-polarization [5,21,24,25].

The vibrations of ungerade parity include the vibrations of the uranyl unit itself as well as equatorial ligand vibrations. As mentioned before, the uranyl ion has three fundamental vibration modes: the symmetric stretching vibration (ν_s), the asymmetric stretching vibration (ν_a) and the bending vibration (ν_b). The symmetric stretching vibration has gerade parity (σ_g^+) and is superimposed on all electronic transitions (magnetic dipole and electric dipole) as a progression. On the other hand, the asymmetric stretching vibration (σ_u^+) and the bending mode (π_u), which are both ungerade, are able to generate intensity in centrosymmetric systems. In practice, the asymmetric stretching and bending vibrations are generally only coupled with one quantum, simplifying the spectra.

The electric dipole intensity, which is purely vibronic in nature, in the UV-Vis absorption spectrum of the uranyl tetrachloro complex $[UO_2Cl_4]^{2-}$ (D_{4h} symmetry) is a well-known example (see Chapter 5, Figure 5.12). The selection rules for vibronic coupling in a D_{4h} coordination symmetry are summarized in Table 2.4 [5,6f-g,36,37].

From this table, it is obvious that the $\Pi_g \leftarrow \Sigma_g^+$ transition is vibronically allowed along m_x and m_y by the ungerade vibrations ν_a (a_{2u}) and ν_{10} (b_{1u}). The a_{2u} vibration, which is related to Y_0^1 (p_z), induces intensity in Π_g (E_g) through the matrix element:

$$\left\langle \Pi_{g\pm1} \left| Y_0^1 \right| \Pi_{u\pm1} \right\rangle \tag{2.24}$$

Table 2.4. Selection rules for vibronic coupling in a D_{4h} coordination symmetry [6f].

Symmetry		Vibrations allowing components of the electric dipole transition moment		
$D_{\infty h}$	D_{4h}	$\mathbf{m_x}$	$\mathbf{m_y}$	$\mathbf{m_z}$
Σ_g^+	A_{1g}	e_u	e_u	a_{2u}
Π_g	E_g	b_{1u}	a_{2u}	e_u
		a_{2u}	b_{1u}	e_u
Δ_g	B_{1g}	e_u	e_u	--
	B_{2g}	e_u	e_u	b_{1u}

On the other hand, the ligand vibration b_{1u} transforms as the f_{xyz} orbital ($Y_{\pm 2}^3$). The intensity inducing effect of this vibration, thereby allowing the m_x and m_y components of the electric dipole transition moment, can be described by the matrix element:

$$\left\langle \Pi_{g\pm 1} \left| Y_{\pm 2}^3 \right| \Pi_{u\mp 1} \right\rangle \tag{2.25}$$

The vibration b_{1u} is also coupled to the B_{2g} (Δ_g) states. Intensity is induced by mixing this state with an excited state of Σ_u^+ symmetry, which is allowed by the z-component of the dipole operator, according to the matrix element:

$$\left\langle \Delta_{g\pm 2} \left| Y_{\pm 2}^3 \right| \Sigma_u^+ \right\rangle \tag{2.26}$$

Besides the asymmetric stretching vibration a_{2u} and the equatorial ligand vibration b_{1u}, the bending vibration e_u is coupled to the lowest lying excited states as well. The e_u vibration allows the $\Pi_g \leftarrow \Sigma_g^+$

transition along m_z, whereas this vibration induces intensity in one component of the $\Delta_g \leftarrow \Sigma_g^+$ transition along m_x and m_y.

Also for the uranyl trinitrato complex, vibronic coupling is observed. Indeed, the bending vibration ν_b (e' in D_{3h}) couples to the $\Delta_g \leftarrow \Sigma_g^+$ transition (E' $\leftarrow$ A'$_1$ in D_{3h}), which appears as small satellite peaks of the pure induced electric dipole transition at higher energies. The bending vibration transforms as $Y_{\pm 1}^1$, leading to the admixture of $|+1\rangle$ character in the $|+2\rangle$ Zeeman component of $\Delta_{g\pm 2}$ following:

$$\left\langle \Delta_{g\pm 2} \left| Y_{\pm 1}^1 \right| \Pi_{u\pm 1} \right\rangle \tag{2.27}$$

Whereas the corresponding MCD terms for the pure induced electric dipole transition $\Delta_g \leftarrow \Sigma_g^+$ are negative A-terms, the coupling of the bending vibration to this transition should result in positive A-terms [5,6e,21].

6 Summary

At the end of this chapter we will give an overview of the most important conclusions concerning the electronic structure of the uranyl ion and the observed electronic transitions in uranyl spectra:

1 The valence electronic structure of the uranyl ion can be explained by the overlap of the 5*f* and 6*d* orbitals of uranium and the 2*s* and 2*p* orbitals of the two oxygen atoms.
2 There are four bonding orbitals: σ_g^+, σ_u^+, π_g and π_u. These orbitals accommodate the twelve valence electrons of UO_2^{2+}, which results in a totally symmetric ground state: $^1\Sigma_g^+$ in $D_{\infty h}$.
3 It is generally accepted that the highest occupied molecular orbital (HOMO) is σ_u^+.

4 The lowest unoccupied molecular orbitals (LUMO) are the non-bonding δ_u (f_{xyz}, $f_{z(x^2-y^2)}$) and ϕ_u ($f_{y(3x^2-y^2)}$, $f_{x(x^2-3y^2)}$), originating from the 5*f* orbitals of uranium.

5 δ_u lies approximately 2000 cm^{-1} lower in energy than ϕ_u, when an equatorial ligand field is applied.

6 The excited states arise from configurations of the type $\gamma_u\delta_u$ or $\gamma_u\phi_u$ with $\gamma_u = \sigma_u^+$ or π_u^3.

7 The predominant field is the $D_{\infty h}$ axial field of the oxygen atoms.

8 The most appropriate way to describe the excited states of the uranyl ion is the use of an intermediate coupling scheme, but it is closer to the Λ-Σ limit than to the ω-ω limit.

9 In an intermediate coupling scheme the lowest lying excited states, in the presence of an equatorial ligand field, are Π_g, Δ_g, Φ_g and Δ_g, resulting from the $\sigma_u^+\delta_u$ configuration. These states correspond to $^3\Delta_g$ (Π_g, Δ_g, Φ_g) and $^1\Delta_g$ (Δ_g) in the Λ-Σ Russell-Saunders coupling scheme and to Π_g, Δ_g and Φ_g, Δ_g in the ω-ω coupling scheme, respectively [4,5].

10 The lowest lying state is always Π_g, originating from the $\sigma_u^+\delta_u$ configuration, while the highest observable state is H_g, resulting from the $\pi_u^3\phi_u$ configuration. Thereby, the assumption is made that ligands are surrounding the uranyl ion in the equatorial plane.

11 All excited states are doubly degenerate, with $M_\Omega = \pm\,\Omega$. Between states with the same Ω value mixing occurs.

12 The $\sigma_u^+\delta_u$ configuration dominates the beginning of the spectrum. At higher energies, the excited states of the $\sigma_u^+\phi_u$, $\pi_u^3\delta_u$ and $\pi_u^3\phi_u$ configurations interplay. However, the spectra of uranyl compounds can be completely explained in terms of the $\sigma_u^+\delta_u$ and $\sigma_u^+\phi_u$ configurations.

13 The perturbation of the equatorial ligand field is small compared to the strong field of the axial oxygen atoms. In certain point groups

the degeneracy of the cylindrical field excited states is lifted under influence of the equatorial ligand field.

14 The ligand field splitting occurs under the even terms of the equatorial ligand field potential, expressed in spherical harmonics.

15 The Zeeman perturbation lifts the degeneracy in doubly degenerate states and induces mixing of states with the same Ω value.

16 Magnetic circular dichroism spectroscopy is a valuable tool for the identification of electronic transitions and therefore for the determination of the equatorial coordination symmetry of the uranyl ion. In the MCD formalism, we speak about A- and B-terms, which can have either a positive or a negative sign.

17 Singlet-singlet transitions, like $^1\Delta_g \leftarrow {}^1\Sigma_g^+$, are characterized by higher intensities with respect to singlet-triplet transitions according to the spin selection rule ($\Delta\Sigma = 0$). However, this selection rule is relaxed by spin-orbit coupling in an intermediate coupling scheme.

18 All electronic transitions in uranyl spectra are parity forbidden by the Laporte selection rule. Therefore, intensity must be induced either by the static ligand field (e.g. $[UO_2(NO_3)_3]^-$ D_{3h}) or by the dynamic ligand field, also referred to as vibronic coupling (e.g. $[UO_2Cl_4]^{2-}$ D_{4h}). Magnetic dipole transitions have to be considered for the interpretation of the observed transitions as well.

19 Electric dipole transitions induced by the static ligand field can only be observed in non-centrosymmetric point groups, whereas vibronic coupling can occur in both centrosymmetric and non-centrosymmetric point groups.

20 Induced electric dipole transitions under influence of the static ligand field can be retrieved using the odd terms of the equatorial ligand field potential.

21 The symmetric stretching vibration ν_s is always superimposed on all electronic transitions as a progression.

22 Ungerade vibrational modes, i.e. the asymmetric stretching vibration ν_a and the bending mode ν_b of the uranyl ion itself and ungerade equatorial ligand vibrations, are coupled to the gerade electronic states in the vibronic coupling intensity mechanism.

23 The electronic transition $\Pi_g \leftarrow \Sigma_g^+$ ($\sigma_u^+ \delta_u$) is basically magnetic dipole allowed in $D_{\infty h}$ symmetry. Although, in several symmetries electric dipole character can be induced by vibronic coupling (e.g. D_{4h}).

References

[1] Katz, J.J.; Seaborg, G.T.; Morss, L.R. *The Chemistry of the Actinide Elements*, **1986**, Chapman and Hall, New York.

[2] McGlynn, S.P.; Smith, J.K. *J. Mol. Spectrosc* . **1961**, *6*, 164-187.

[3] Denning, R.G. *J. Phys. Chem. A* (Feature Article) **2007**, *111*, 4125-4143.

[4] Denning, R.G. *Struct. Bond.* **1992**, *79*, 215-276.

[5] Denning, R.G.; Snellgrove, T.R.; Woodwark, D.R. *Mol. Phys.* **1979**, *37*, 1109-1143.

[6] (a) Denning, R.G.; Dallera, C.; Tagliaferri, A.; Giarda, K.; Brookes, N.B.; Braicovich, L. *J. Chem. Phys.* **2002**, *117*, 8008-8020. (b) Barker, T.J.; Denning, R.G.; Thorne, R.G. *Inorg. Chem.* **1992**, *31*, 1344-1353. (c) Denning, R.G.; Morrison, I.D. *Chem. Phys. Lett.* **1991**, *180*, 101-104. (d) Barker, T.J.; Denning, R.G.; Thorne, R.G. *Inorg. Chem.* **1987**, *26*, 1721-1732. (e) Denning, R.G.; Foster, D.N.P.; Snellgrove, T.R.; Woodwark, D.R. *Mol. Phys.* **1979**, *37*, 1089-1107. (f) Denning, R.G.; Snellgrove, T.R.; Woodwark, D.R. *Mol. Phys.* **1976**, *32*, 419-442. (g) Denning, R.G.; Snellgrove, T.R.; Woodwark, D.R. *Mol. Phys.* **1975**, *30*, 1819-1828.

[7] Pierloot, K.; van Besien, E. *J. Chem. Phys.* **2005**, *123*, 204309.

[8] (a) Matsika, S.; Zhang, Z.; Brozell, S.R.; Blaudeau, J.-P.; Wang, Q.; Pitzer, R.M. *J. Phys. Chem. A* **2001**, *105*, 3825-3828. (b) Matsika, S.; Pitzer, R.M. *J. Phys. Chem. A* **2001**, *105*, 637-645. (c) Zhang, Z.; Pitzer, R.M. *J. Phys. Chem. A* **1999**, *103*, 6880-6886.

[9] Ismail, N.; Heully, J.-L.; Saue, T; Daudey, J.-P.; Marsden, C.J. *Chem. Phys. Lett.* **1999**, *300*, 296-302.

[10] Wahlgren, U.; Schimmelpfennig, B.; Jusuf, S.; Stromnes, H.; Gropen, O.; Maron, L. *Chem. Phys. Lett.* **1998**, *287*, 525-530.

[11] (a) Görller-Walrand, C.; Vanquickenborne, L.G. *J. Chem. Phys.* **1972**, *57*, 1436-1440. (b) Görller-Walrand, C.; Vanquickenborne, L.G. *J. Chem. Phys.* **1971**, *54*, 4178-4186.

[12] Dieke, G.H.; Duncan, A.B.F. *Spectroscopic Properties of Uranium Compounds*, **1965**, McGraw Hill, New York.

[13] Rabinowitch, E.; Belford, R.L. *Spectroscopy and Photochemistry of Uranyl Compounds*, **1964**, Pergamon, Oxford.

[14] Belford, R.L.; Belford, G. *J. Chem. Phys.* **1961**, *34*, 1330-1332.

[15] Jørgensen, C.K. *Acta Chem. Scand.* **1957**, *11*, 166-178.

[16] Hay, P.J.; Martin, R.L.; Schreckenbach, G. *J. Phys. Chem. A* **2000**, *104*, 6259-6270.

[17] Newman, J.B. *J. Chem. Phys.* **1965**, *43*, 1691-1694.

[18] Kaltsoyannis, N. *Chem. Soc. Rev.* **2003**, *32*, 9-16.

[19] van Besien, E. *De invloed van complexvorming op het elektronische spectrum van uranyl: een computationele studie*, **2006**, PhD thesis, Katholieke Universiteit Leuven and references therein.

[20] Pierloot, K.; van Besien, E.; van Lenthe, E.; Baerends, E.J. *J. Chem. Phys.* **2007**, *126*, 194311.

[21] De Houwer, S. *Intensities of vibronic transitions in uranyl spectra: application to uranyl complexes in non-aqueous solvents*, **2003**, PhD thesis, Katholieke Universiteit Leuven and references therein.

[22] (a) Görller-Walrand, C.; De Jaegere, S. *J. Chim. Phys.* **1972**, *4*, 726-736. (b) Görller-Walrand, C.; De Jaegere, S. *J. Chim. Phys.* **1973**, *2*, 360-366. (c) Görller-Walrand, C.; De Jaegere, S. *Spectrochim. Acta* **1972**, *28A*, 257-268.

[23] Oda, Y.; Funasaka, H.; Nakamura, Y.; Adachi, H. *J. Alloys Compd.* **1997**, *255*, 24-30.

[24] Görller-Walrand, C.; Binnemans, K. in *Handbook on the Physics and Chemistry of Rare Earths*, *Vol. 25*, *Chapter 167*; Eds. Gschneidner, K. jr.; Eyring, L., **1998**, Elsevier, Amsterdam.

[25] Görller-Walrand, C.; Binnemans, K. in *Handbook on the Physics and Chemistry of Rare Earths*, *Vol. 23*, *Chapter 155*; Eds. Gschneidner, K. jr.; Eyring, L., **1996**, Elsevier, Amsterdam.

[26] Binnemans, K.; Görller-Walrand, C. *J. Rare Earths* **1998**, *16*, 204-210.

[27] Shriver, D.F.; Atkins, P.W. *Inorganic Chemistry, Third Edition*, **1999**, Oxford University Press, Oxford.

[28] Colen, W. *Bijdrage tot de kennis van de electronenstructuur van uranylkompleksen*, **1980**, PhD thesis, Katholieke Universiteit Leuven.

[29] Görller-Walrand, C.; Colen, W. *Inorg. Chim. Acta* **1984**, *84*, 183-188.

[30] Görller-Walrand, C.; Colen, W.; Dao, N.Q. *J. Chem. Phys.* **1982**, *76*, 13-19.

[31] De Houwer, S.; Servaes, K.; Görller-Walrand, C. *Phys. Chem. Chem. Phys.* **2003**, *5*, 1164-1168.

[32] Judd, B.R. *Phys. Rev.* **1962**, *127*, 750-761.

[33] Ofelt, G.S. *J. Chem. Phys.* **1962**, *37*, 511-520.

[34] (a) Servaes, K.; Hennig, C.; Billard, I.; Gaillard, C.; Binnemans, K.; Van Deun, R.; Görller-Walrand, C. *Eur. J. Inorg. Chem.,* accepted. (b) De Houwer, S.; Görller-Walrand, C. *J. Alloys Compd.* **2001**, *323-324*, 683-687.

[35] Brint, P.; McCaffery, A.J. *Mol. Phys.* **1973**, *25*, 311-322.

[36] (a) Servaes, K.; Hennig, C.; Van Deun, R.; Görller-Walrand, C. *Inorg. Chem.* **2005**, *44*, 7705-7707. (b) Görller-Walrand, C.; De Houwer, S.; Fluyt, L.; Binnemans, K. *Phys. Chem. Chem. Phys.* **2004**, *6*, 3292-3298. (c) Görller-Walrand, C.; De Jaegere, S. *J. Chim. Phys.* **1973**, *2*, 360-366.

[37] (a) Barker, T.J.; Denning, R.G.; Thorne, J.R.G. *J. Lumin.* **1987**, *38*, 144-146.

3 EXTENDED X-RAY ABSORPTION FINE STRUCTURE (EXAFS) SPECTROSCOPY

X-ray scattering and spectroscopic techniques are very helpful methods for speciation and structure analysis. The application of synchrotron radiation based techniques in actinide science experiences a growing interest. Here, the basics of *Extended X-ray Absorption Fine Structure* (EXAFS) will be described. This description is intended as a general overview of the theory and the data analysis. For more detailed information, we refer to the books of Teo [1] and Koningsberger [2] and recent reviews on EXAFS spectroscopy [3-6].

1 X-rays and synchrotron radiation

X-rays are electromagnetic rays with wavelengths between ultraviolet light and gamma rays in the electromagnetic spectrum. X-rays are characterized by the relative short wavelengths of 0.01 Å to 100 Å, with

hard X-rays on one end and soft X-rays on the other. Conventionally, they are produced in two ways: either the conversion of the kinetic energy of charged particles into radiation (continuous spectrum of X-rays) or the excitation of atoms in a target upon which fast moving electrons impinge (characteristic lines of nearly monochromatic X-rays).

A particular way of generating X-rays is the use of a synchrotron. A synchrotron is a type of a cyclic particle accelerator in which the magnetic field (to turn the particles so they circulate) and the electric field (to accelerate the particles) are carefully synchronized with the travelling particle beam. Synchrotron radiation is then emitted when charged particles (electrons or positrons) travel with a speed approaching that of light in curved paths (storage ring) in a magnetic field. Synchrotron radiation is characterized by (a) high intensity and high brightness, (b) high brilliance, (c) high collimation, (d) tunability over a wide energy range with a continuous spectrum, (e) pulsed light emission.

X-ray energies are sufficiently high to eject, via the photoelectric effect, a core electron from an atom. Each core-electron has a well-defined binding energy. When the energy of the incident X-ray reaches this energy, the core-electron is excited from a core state to the continuum. In the X-ray absorption spectrum, an abrupt increase in the absorption coefficient μ is observed, the so-called *absorption edge* of the element (Figure 3.1).

Absorption edges are denominated according to the electron that is excited. In the Sommerfeld notation, we speak, in order of increasing energy, of K, L_I, L_{II}, L_{III}, etc. edges corresponding to the excitation of an electron from the $1s_{1/2}$, $2s_{1/2}$, $2p_{1/2}$, $2p_{3/2}$, etc. orbitals (states), respectively. There are two L absorption edges (L_{II} and L_{III}) for the $2p$ initial state due to spin-orbit coupling ($2p_{1/2}$ and $2p_{3/2}$) and one (L_I) related with the $2s_{1/2}$ state. The energies of the K- to N-edges for uranium are tabulated in Table 3.1. The term $\Delta\mu x$, i.e. the difference between the absorption coefficient below and above the absorption edge $\Delta\mu$, multiplied by the optical path length x is called the *edge jump* (Figure 3.1). Further

increase of the X-ray energy causes a decrease in the absorption coefficient μ.

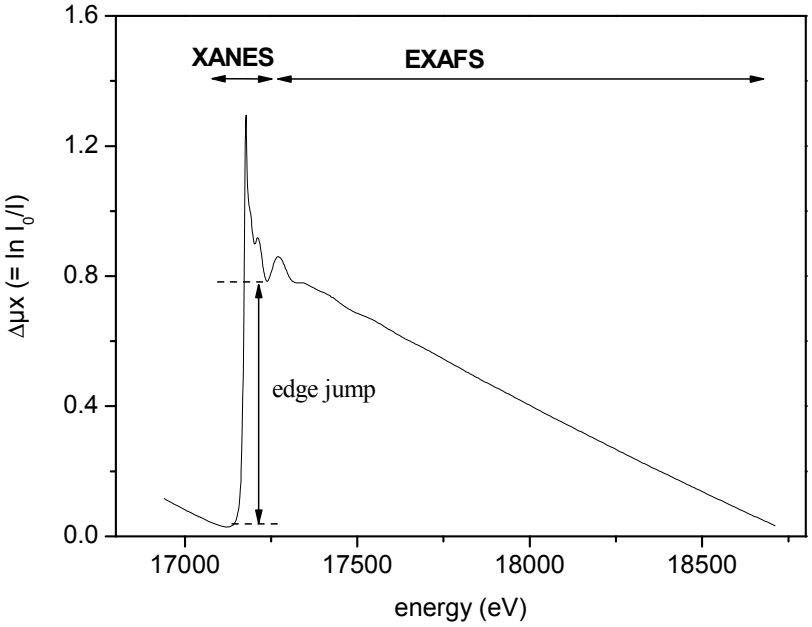

Figure 3.1. Uranium L_{III} absorption edge.

EXAFS measurements at the uranium K-edge would need either a high uranium concentration or a long scattering path length. In the energy range of the uranium M-edges the absorption by air and confinement material is not negligible. The uranium L-edges are a good compromise between necessary uranium concentration and intensity loss from confinement material. Among the L-series, the L_{III}-edge has the highest electron occupation and therefore the highest signal strength.

Table 3.1. Energies of the absorption edges of uranium.

Edge		Energy (keV)
K-series	K	115.606
L-series	L_I	21.757
	L_{II}	20.948
	L_{III}	17.166
M-series	M_I	5.548
	M_{II}	5.182
	M_{III}	4.303
	M_{IV}	3.728
	M_V	3.551
N-series	N_I	1.441
	N_{II}	1.273
	N_{III}	1.045

2 Physical principles of EXAFS and EXAFS equation

The physical basis of XAS spectroscopy lies in the oscillatory fine structure superimposed on the absorption edge. This fine structure is divided into *X-ray Absorption Near Edge Structure* (XANES) and *Extended X-ray Absorption Fine Structure* (EXAFS). For an isolated atom, the absorption coefficient μ decreases readily after the absorption edge in function of the photon energy. Isolated atoms as present in noble gases show no EXAFS signal [7]. However, when the atom is part of a molecule or embedded in a condensed phase, the variation of the absorption coefficient displays an oscillatory structure at energies above the absorption edge.

The XANES region is the part of the oscillatory structure in the vicinity of the edge and refers to the excitation of the core electron to

unoccupied valence states (Figure 3.2). At the uranium L_{III}-edge, $2p_{3/2} \rightarrow 7s$, $6d$ transitions occur. The natural line width Γ_i of electronic transitions at the uranium L_{III}-edge are 7.4 eV, which makes the analysis of this transitions difficult [8]. The XANES region also comprises multiple scattering effects. This part of the spectrum gives information on the oxidation state of the absorbing atom, the site symmetry and the valence orbitals. On the other hand, the EXAFS region ranges 40-1000 eV above the absorption edge (Figure 3.1) and refers to the excitation of a core electron into the continuum. One can obtain information on the number of neighbouring atoms of the absorbing atom and the bond distances between the absorbing atom and its neighbours by applying EXAFS spectroscopy on a molecule. EXAFS and XANES spectra can be recorded in both transmittance and fluorescence mode. In the following, we will describe the theory of EXAFS spectroscopy in more detail. Analysis of XANES spectra was not a topic of this study.

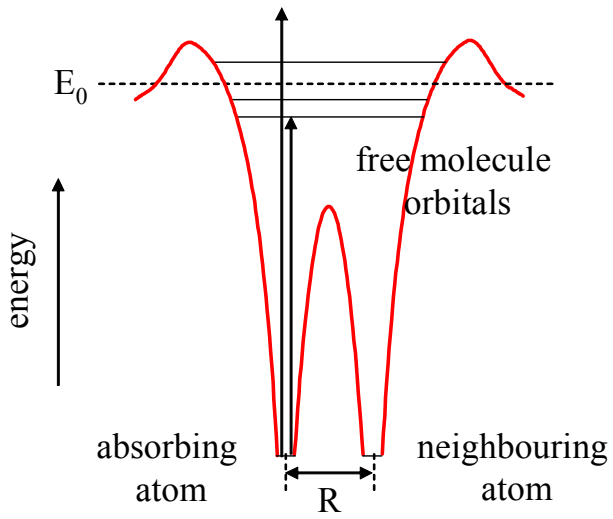

Figure 3.2. X-ray Absorption Near Edge Structure (XANES).

EXAFS is a final state interference effect involving scattering of the outgoing photoelectron from neighbouring atoms. The ejected photoelectron can be regarded as an outgoing spherical wave originating from the excited atom, characterized by the wavelength $\lambda = 2\pi/k$, where k is given by

$$k = \sqrt{\frac{2m}{\hbar^2}(E - E_0)} \tag{3.1}$$

E is the incident photon energy and E_0 is the threshold energy of the absorption edge. If the absorbing atom has neighbouring atoms, the outgoing photoelectron wave can be backscattered from the neighbouring atoms. Thereby, an incoming photoelectron wave is produced (Figure 3.3).

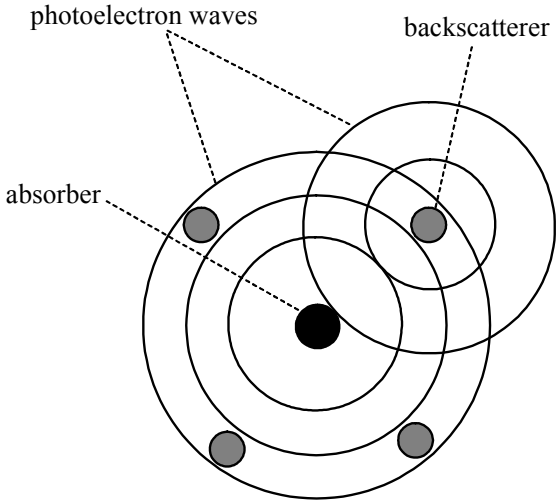

Figure 3.3. Outgoing and incoming photoelectron waves at the X-ray absorbing atom.

The outgoing and incoming photoelectron waves can interfere either constructively or destructively. Constructive interference leads to

maxima, whereas destructive interference results in minima of the absorption (Figure 3.4). This interference of the outgoing and all the incoming waves gives rise to the sinusoidal variation of the absorption coefficient μ as a function of the excitation energy. Indeed, one can regard the EXAFS spectrum as an interferrogram of the atomic arrangement around the absorbing atom. The amplitude and frequency of this sinusoidal fine structure depend on the type of the neighbouring atoms and the bond distances to the absorber, respectively.

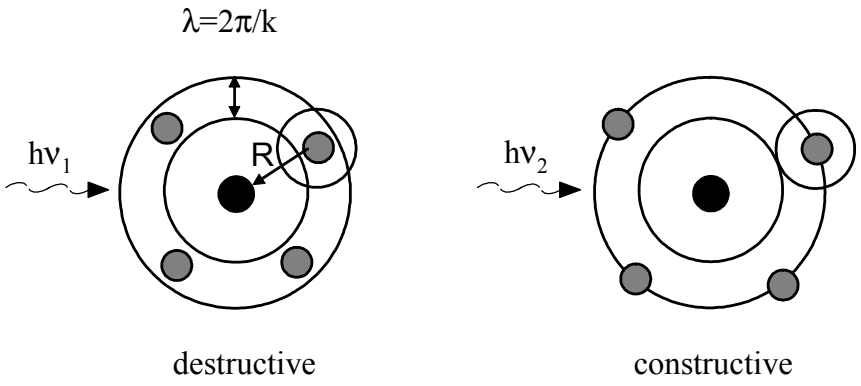

Figure 3.4. Destructive and constructive interference of outgoing photoelectron waves and backscattered waves.

The modulation of the absorption coefficient μ by scattering on the surrounding atoms, normalized to the absorption coefficient of an isolated atom of the absorbing atom type (μ_0), is called the EXAFS function $\chi(E)$ and given by Equation 3.2. μ_0 is generally not known.

$$\chi(E) = \frac{\mu(E) - \mu_0(E)}{\mu_0(E)} \tag{3.2}$$

In order to obtain structural parameters from EXAFS measurements, it is necessary to convert the energy E into the photoelectron wavevector k via Equation 3.1, resulting in χ(k) in k-space:

$$\chi(k) = \sum_j N_j S_i(k) F_j(k) e^{-2\sigma_j^2 k^2} e^{-2r_j/\lambda_j(k)} \frac{\sin\left(2kr_j + \phi_{ij}(k)\right)}{kr_j^2} \qquad (3.3)$$

The subscripts *i* and *j* represent the central absorbing atom and a neighbouring atom, respectively. The summation over *j* reflects that all neighbouring atoms contribute to the observed EXAFS oscillation and all these absorber-scatterer pathways have to be taken into account. However, in practice, even a relatively simple molecule may have ten to hundreds of relevant pathways. To simplify the analysis, these are typically divided into *'shells'*. A *shell* represents the scattering from several chemically similar atoms, all at approximately the same distance from the absorber. In the following paragraphs, a short explanation of each term in the EXAFS equation (Equation 3.3) will be given.

The photoelectron wave undergoes different modifications during scattering in the potentials of the absorbing and backscattering atoms. This phenomenon is expressed by the terms $\phi_{ij}(k)$, $F_j(k)$, $S_i(k)$ and $e^{-2r_j/\lambda_j(k)}$ in the EXAFS equation (Equation 3.3). $\phi_{ij}(k)$ is the total phase shift experienced by the photoelectron wave during the scattering in the surrounding atomic potentials. The phase function includes contributions of the absorber as well as of the backscatterer:

$$\phi_{ij}^l(k) = \phi_i^l(k) + \phi_j(k) - l\pi \qquad (3.4)$$

where l = 1 for K and L_I edges and l = 2 or 0 for $L_{II, III}$. The photoelectron wave experiences the phase shift of the absorbing atom twice (i.e. once going out and backscattering) and a phase shift of the neighbouring atom once. Therefore, the function $\phi(k)$ is dependent on the type of

neighbouring atom. However, since the phase shift is a function of k, it also alters the frequency of the oscillation. $F_j(k)$ represents the amplitude function and depends only on the type of the backscatterer. The backscattering amplitude $F_j(k)$ increases with the number of neighbours N_j as well as with their atomic number Z. For an element with low atomic number Z, the amplitude maximum is situated at low k-values and shifts to higher k-values with increasing Z. Since both $\phi(k)$ and $F(k)$ depend on the type of backscattering atom, identification of elements in the environment of the absorber is with some limitations possible, providing the types of atoms differ sufficiently in atomic number, in the order of $Z \pm 5$.

Two categories of inelastic scattering processes cause a reduction of the EXAFS amplitude: multiple excitation at the central atom and excitation of the neighbouring environment. The former is expressed by the term $S_i(k)$ in Equation 3.3, where $S_i(k) \leq 1$. Multiple excitation at the central atom includes shake-up and shake-off processes. When a photoelectron is produced, other "passive" electrons can be excited along with the photoelectron, either to one of the bound states (shake-up) or into the continuum (shake-off). The physical origin of this loss mechanism is that the excess energy ($E-E_0$) of the photoelectron can excite other electrons, mainly valence electrons, resulting in an energy loss of the photoelectron. These shake-up/off processes are only important when the excess energy ($E-E_0$) reaches a value that is several times the binding energy of the valence electrons. Assuming the binding energy of the valence electrons is approximately 60 eV, the energy ($E-E_0$) has to be higher than 200 eV. $S_i(k)$ considers the loss of the primary photoelectrons in the scattering channel. Shake-up processes can occur in the EXAFS region as discrete resonances. One shake-up process is observed in the uranium L_{III}-edge spectra of some uranyl compounds as a small and sharp feature at $k = 10.5$ Å^{-1}. This feature can be attributed to the excitation of a core $2p_{3/2}$ electron accompanied by the autoionization of a $4f$ electron. This phenomenon is denoted as a $[2p_{3/2}4f_{5/2}/4f_{7/2}]$ double

electron excitation [9]. The excitation of the environment is represented by $e^{-2r_j/\lambda_j(k)}$ (Equation 3.3), where λ is the electron inelastic mean free path. The amplitude reduction by the factor $e^{-2r_j/\lambda_j(k)}$ is more pronounced at low k-range and high distances r.

The Debye-Waller factor σ contains structural and chemical information. In general, the Debye-Waller factor σ exists of two components σ_{vib} and σ_{stat} due to thermal vibrations and static disorder. The component σ_{vib} is higher at high temperature and for weak bonds, whereas the component σ_{stat} represents the order/disorder in the structure. Large differences in the bond distances of one shell result in a high Debye-Waller factor (see Chapter 5). A reduction of the EXAFS amplitude originating from a large disorder, may lower the apparent coordination number and sometimes may cause a contraction of the bond distances. The Debye-Waller factor is introduced into the EXAFS equation (Equation 3.3) by the exponent $e^{-2\sigma_j^2 k^2}$, which reduces the amplitude in the high k-region, more than at low k- values.

The amplitude reduction factors diminish the EXAFS amplitude with $1/r^2$. This means that the larger the distance r, the weaker will be the EXAFS signal.

The EXAFS oscillation has a frequency of 2r in k-space. The frequency depends on the distance between the absorber and the backscattering atom. The larger the distance r, the higher will be the frequency of the oscillation. A change in the distance r affects mainly the high k-region since the movement of the waves is linearly proportional to k. The frequency is not only influenced by the distance r. Changing the threshold energy E_0 results in an increase or decrease of the frequency. The effect of increasing (decreasing) ΔE_0 is to increase (decrease) the slope of the function 2kr, thereby resulting in a higher (lower) frequency for the sine wave sin(2kr). Since $k^2 \sim \Delta E$, changing ΔE_0 is mostly felt at low k-values.

In conclusion, it is clear that each EXAFS wave is determined on one hand by the backscattering amplitude ($N_jF_j(k)$), modified by the reduction factors $S_i(k)$, $e^{-2\sigma_j^2k^2}$, $e^{-2r_j/\lambda_j(k)}$ and the $1/kr_j^2$ distance dependence, and on the other hand by the sinusoidal oscillation which is a function of interatomic distances ($2kr_j$) and the phase shift ($\phi_{ij}(k)$).

3 Data analysis

3.1 Data reduction

Once the necessary data have been recorded, different steps of data reduction have to be carried out to obtain the EXAFS spectrum and the corresponding Fourier transform. The data reduction can be summarized as the conversion of the experimentally measured total absorption data $\mu(E)$ in energy space to the interference function $\chi(k)$ in k-space. This procedure involves background removal, conversion of E to k, normalization, μ_0 correction, weighting scheme and Fourier transform. In the following, these different steps will be briefly discussed and are shown in Figure 3.5.

In a first step, a pre-edge substraction is performed. The pre-edge absorption curve can be fitted with a polynomial function. The pre-edge fit is extrapolated beyond the absorption edge and substracted from the entire data set (Figure 3.5 A). For the uranium L_{III}-edge EXAFS data analysis described in the following chapters, a polynomial with order -1 is used. Given that the EXAFS function $\chi(E)$ above the absorption edge is defined as Equation 3.2, the next step involves the substraction of the absorption coefficient of an isolated atom $\mu_0(E)$. However, $\mu_0(E)$ is generally not known. The atomic background above the absorption edge, $\mu_0(E)$, is approximated by a spline function (Figure 3.5 B). A spline function is a function defined over a series of intervals with each interval containing a polynomial of some order. This spline function goes

through the center of all oscillations, in order to obtain a regular sine wave around the spline function. Attention has to be paid that too low orders or not enough sections of the spline function will result in a low distance peak (at around 1 Å) in the Fourier transform, which may distort the real peaks.

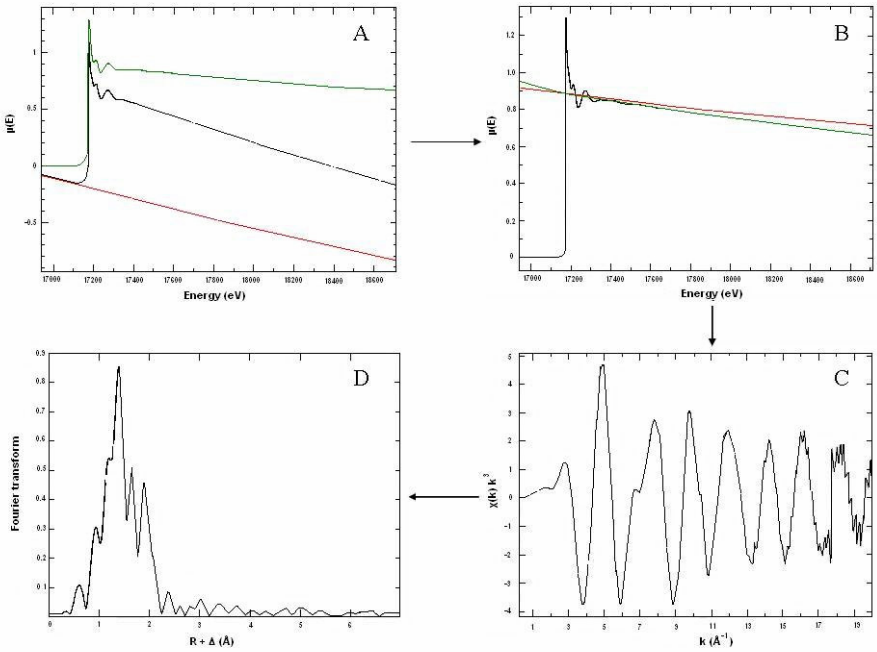

Figure 3.5. Data reduction in EXAFS analysis. A) Pre-edge substraction (red: polynomial, green: resulting spectrum after pre-edge substraction). B) Normalization using a spline function (green) and Victoreen function (red). C) k^3-weighted EXAFS spectrum. D) Corresponding Fourier transform.

Furthermore, the background-removed $\Delta\mu(E)$ has to be normalized with respect to $\mu_0(E)$, according to Equation 3.2. One commonly used method for normalization of the data is the use of the Victoreen polynomial (Figure 3.5 B). The Victoreen polynomial is an expression

for the absorption cross-section above a particular edge and the absorption coefficient μ_{vic} is given by:

$$\begin{aligned} \mu_{vic} &= C_{vic}\lambda^3 + D_{vic}\lambda^4 \\ &= C_{vic}\left(\frac{hc}{E}\right)^3 + D_{vic}\left(\frac{hc}{E}\right)^4 \end{aligned} \tag{3.5}$$

where λ is the X-ray wavelength in Å. C_{vic} and D_{vic} are tabulated Victoreen coefficients for a particular edge and element. So, when the spline and Victoreen functions are used, the EXAFS $\chi(E)$ is calculated as

$$\chi(E) = \frac{\mu_{\exp} - \mu_{spline}}{\mu_{vic}} \tag{3.6}$$

Now, the fine structure $\chi(E)$ can be converted to $\chi(k)$ according to Equation 3.1. The value of E_0 is not exactly known. Therefore, it is assumed that E_0 is in the vicinity of the absorption edge, ca. 20 eV. For uranium, the value of E_0 is arbitrarily defined at 17185 eV, i.e. the uranium L_{III} absorption edge energy (17166 eV) + 20 eV. However, the exact choice of E_0 is not important here because in the curve fitting procedure E_0 is allowed to vary. The final step is applying the weighting factor to compensate for the attenuation of the EXAFS signal at high k-values. Therefore, $\chi(k)$ is multiplied by a power of k to give $k^n\chi(k)$ (Figure 3.5 C). This procedure is important to prevent the larger amplitude oscillations from dominating the smaller ones in the determination of bond distances. The k^3-weighting scheme is applied in the majority of EXAFS analysis and has the effect of weighting the EXAFS oscillations more uniformly over the data range k = 3 – 16 $Å^{-1}$. We note that the weighting factor can have a significant effect on the peak heights and peak positions in the Fourier transforms as well as on

the fitting parameters in the curve fitting. Therefore, it is important to use the same weighting scheme for all data reductions, if possible.

Although the EXAFS equation $\chi(k)$ and the corresponding EXAFS spectrum (Figure 3.5 C) contain all structural information, it is not a convenient way of visualizing this information. Therefore, Fourier transforms can be used to transfer an oscillatory signal and its different constituent frequencies from k-space (in $Å^{-1}$) to peaks in r-space (in Å). As a consequence of the phase shift $\phi(k)$, the apparent distances in the Fourier transform are shifted by a factor Δ of approximately -0.2 Å to -0.5 Å. Some problems are encountered using Fourier transforms, including background peaks at distances $\leq$ 1 Å and side lobes due to the limited k-range. The position, the magnitude and the shape of peaks can be affected to some extent by E_0, the weighting scheme and the k-range.

As a final remark of the data reduction, we note that all discontinuities like glitches and spikes in the data have to be removed before or after the background removal. Otherwise, they will adversely affect the background removal and hence the accuracy of the EXAFS analysis.

3.2 Curve fitting

In order to obtain reliable structural parameters, it is necessary to use curve fitting to model the data. In practice, quantitative analysis of EXAFS data involves fitting the experimental data to the EXAFS equation (Equation 3.3), using amplitude and phase functions. Indeed, to determine N and σ, the amplitude function $F(k)$ must be known, whereas the determination of r requires an accurate knowledge of the phase function $\phi(k)$. These amplitude and phase functions as well as the electron mean free path λ can be derived either from model compounds or theoretical ab initio calculations. In our study of the uranyl coordination in solution, we used the FEFF 8.2. code for calculating

theoretical phase and amplitude functions [10]. Scattering amplitudes and phases are calculated using a hypothetical cluster based on a crystal structure, resembling the compound studied. The outcome is a set of feff000N.dat files that are incorporated in the curve fit. Once the parameters $F(k)$, $\phi(k)$, λ and S_0^2 are specified, the structurally related parameters N, σ and r are refined, usually via a non-linear least-squares fitting procedure. A schematic overview of the quantitative EXAFS data treatment is given in Scheme 3.1.

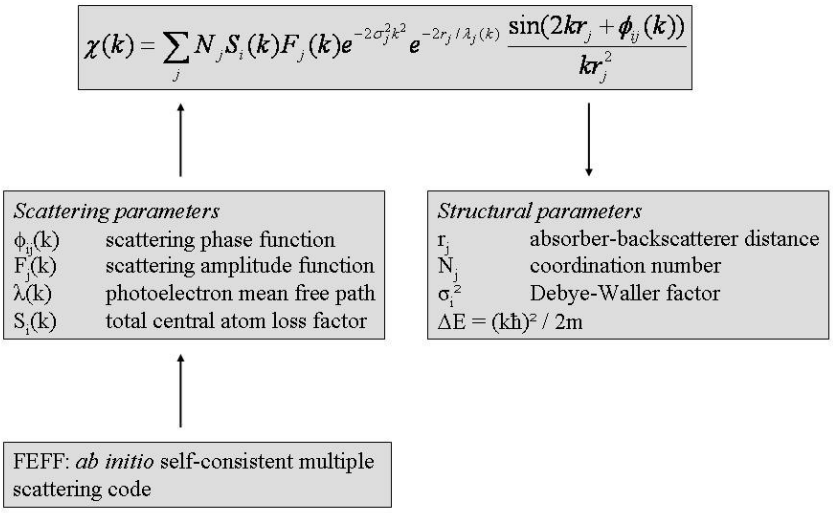

Scheme 3.1. Quantitative EXAFS data treatment.

Although curve fitting provides accurate results, curve fitting deals with correlation problems. Indeed, each EXAFS wave contains two sets of highly correlated parameters: {$F(k)$, σ^2, λ, N} and {$\phi(k)$, E_0, r}. Significant correlations can occur both within and between these two sets of variables as well as between different scattering terms. There exists a high correlation between the coordination number N and the Debye-

Waller factor σ^2. Furthermore, increasing E_0 by approximately 3 eV causes an increase in r by ca. 0.01 Å.

EXAFS analysis can determine bond distances r with an error of 0.01-0.02 Å. The error in the determination of the coordination number N is 10-25%. The coordination number is highly correlated with other parameters contributing to the overall EXAFS amplitude in the EXAFS equation, which is the source of the relatively large error in its determination. These include the Debye-Waller factor σ^2, the electron inelastic mean free path λ, the backscattering amplitude $F_j(k)$ and multiple electron excitations at the central atom, expressed by $S_i(k)$. Part of this error lies in the question of transferability of λ and $F_j(k)$, which have either been extracted from reference compounds or calculated theoretically. Note that care must be taken to avoid experimental artefacts, as these can lead to erroneous EXAFS amplitudes and, thus, to errors in coordination number determinations.

3.3 Scattering paths

In addition to relevant single scattering paths of the photoelectron from the absorber to the neighbouring atoms and back, multiple scattering pathways with one or two intervening atoms can also play an important role in EXAFS data analysis. Note that the effective path length (r_{eff}) of a multiple scattering path is equal to one-half of the sum of the path distances involved. The scattering intensity, and thus the significance, of multiple scattering paths is strongly dependent on the bond angle between the considered atoms.

The importance of multiple scattering paths in EXAFS data treatment is especially true for systems with a collinear arrangement of the atoms, with bond angles of approximately 180°. In such cases, the outgoing photoelectron is strongly forward-scattered by the intervening atom(s), resulting in a significant amplitude enhancement. In fact, both the

amplitude and the phase of the more distant neighbour are significantly affected by the intervening atom(s). This phenomenon is referred to as the *'lensing'* or *'focusing'* effect. This focusing effect makes the determination of atoms at large distances (R > 4 Å) possible (see Chapter 5 for the EXAFS data analysis of $[UO_2(NO_3)_3]^-$, $[UO_2(CO_3)_3]^{4-}$, $[UO_2(CH_3COO)_3]^-$). However, this effect falls off very rapidly for bond angles ≤ 150°.

A special case of multiple scattering paths, including the focusing effect, is observed in uranium L_{III}-edge EXAFS spectra. The trans-oxo uranyl ion is a linear entity, resulting in significant multiple scattering paths that can not be ignored in EXAFS data analysis (Figure 3.6). These multiple scattering paths are visible in the Fourier transform as a small peak at R + Δ ≅ 3 Å. However, Hudson and coworkers indicated that the scattering contributions from the multiple scattering paths U-O_{ax1}-O_{ax2} and U-O_{ax1}-U-O_{ax1} tend to cancel each other out [11]. Therefore, only the twofold degenerated four-legged multiple scattering path U-O_{ax1}-U-O_{ax2} (abbreviated as MS U-O_{ax}) was included in all curve fit procedures by constraining its Debye-Waller factor σ^2 and its effective path length R to twice the values of the corresponding freely fitted U-O_{ax} single scattering path.

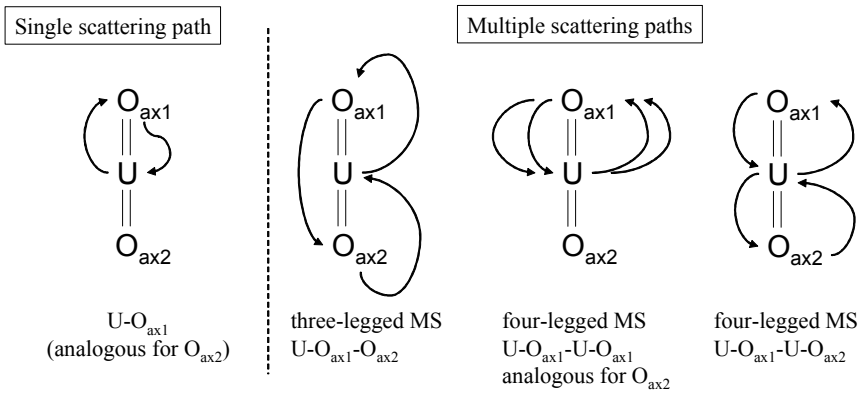

Figure 3.6. Single and multiple scattering paths of the linear uranyl entity.

4 Advantages and limitations of EXAFS spectroscopy

EXAFS spectroscopy is a technique that probes the local environment of an atom: bond distances up to 6 Å can be determined, corresponding with 1-3 coordination shells, depending on the system studied. This means that no long-range order is required to apply EXAFS spectroscopy. Solids, liquids and non-crystalline samples can be measured. It is even possible to compare the structure in solid state with the structure in solution. Furthermore, EXAFS spectroscopy is highly element specific. Structural information on each type of atom in a molecule can be obtained by tuning the energy to coincide with the absorption edge of each type of atom. The influence of impurities which do not contain the absorbing atom or are not bound to the absorber, can be neglected.

Like every available technique, EXAFS spectroscopy has also limitations. The most obvious limitation of EXAFS spectroscopy is that only the average structure can be determined. If the element of interest occurs in multiple environments, only the average structure is determined. EXAFS spectra are measured over a limited k-range, resulting in a limited resolution of the bond length. Two scattering shells can be resolved in the Fourier transform if they differ sufficiently in frequency to cause a detectable change in the EXAFS amplitude. Two distances should become resolvable when the difference in their distances, δR, is large enough to cause a 'beat node' in the scattering amplitude. This occurs at $\delta R \geq \pi/2k_{max}$, where k_{max} is the maximum value of k for which a signal can be measured. In typical EXAFS measurements the k_{max} value ranges from 14 $Å^{-1}$ to 20 $Å^{-1}$, giving δR = 0.08 - 0.13 Å. A third limitation is the restricted number of fit parameters given by the degrees of freedom. The number of degrees of freedom is calculated as:

$$N_{idp} = \frac{2\Delta k \Delta R}{\pi} \tag{3.7}$$

For ΔR = 2 Å (useful information between 1 - 3 Å) and Δk = 12 $Å^{-1}$, this gives approximately sixteen degrees of freedom. For EXAFS data analysis, the limited number of degrees of freedom implies that it is pointless for trying to fit data with model compounds containing more parameters than N_{idp}. The limitations caused by N_{idp} are a general property of EXAFS and are not caused by the type of data analysis used.

5 Sample preparation, experimental setup and data analysis used

For all EXAFS measurements performed to study the coordination environment of the uranyl ion in solution and discussed in the following chapters, the same sample preparation, experimental setup and data analysis have been used. Both sample preparation, experimental setup and data analysis are described in the following paragraphs.

The solutions prepared in volumetric flasks, were transferred into the back of a polyethylene pipette for the uranium L_{III}-edge EXAFS measurements. These polyethylene pipettes have an optical path length of 13 mm. After filling, the pipette was hot-sealed with a soldering iron. Finally, the pipette was encapsulated in a hot-sealed polyethylene bag, which serves as the second confinement (Figure 3.7).

Figure 3.7. Sample holder for the EXAFS measurements.

Optimal experimental conditions are obtained when a jump across the absorption edge of unity is observed in the spectrum of μ(E) in function of energy (eV). For an edge jump of one, the ideal actinide concentration [An] is given by

$$[An] = \frac{1}{d \cdot \Delta\mu \cdot M} \tag{3.8}$$

where d and M are the path length and the actinide atomic weight, respectively. $\Delta\mu$ is the change in total cross-section across the edge and has a value around 65-50 cm²/g for the L_{III}-edges of thorium to curium. For uranium, $\Delta\mu$ is equal to 64.4 cm²/g. Using Equation 3.8, the optimal uranyl concentration for EXAFS measurements across the L_{III}-edge giving an edge jump of ~1.0, is calculated as 5×10^{-2} mol L^{-1}. This uranyl concentration was used in all sample preparations.

Uranium L_{III}-edge EXAFS measurements were collected at the Rossendorf Beamline (ROBL, BM20) at the European Synchrotron Radiation Facility (ESRF, Grenoble, France) [12]. The measurements were carried out in transmittance mode at ambient temperature and pressure. The experimental setup of an EXAFS measurement in transmittance mode is shown in Figure 3.8. The measurements were performed using a double crystal Si(111) monochromator in equidistant k-steps of 0.05 $Å^{-1}$ across the EXAFS region. Higher harmonics were rejected by two platinum-coated mirrors. The signals were registered with three argon-filled ionization chambers. The sample is placed between the first and the second ionization chamber, whereas the sample for energy reference is situated between the second and the third ionization chamber. An yttrium metal foil (first inflection point at 17038 eV) was used for the energy calibration. Several scans were recorded for each sample and then averaged. In all data analyses, EXAFS data were extracted from the raw absorption spectra by standard methods including a spline approximation for the atomic background using the program

EXAFSPAK [13]. The uranium L_{III}-edge threshold energy, $E_{k=0}$, was defined at 17185 eV. Theoretical phase and amplitude functions were calculated with FEFF 8.2., using model compounds [10]. The amplitude reduction factor, S_0^2, was defined at 0.9 in all FEFF calculations and fixed to that value in all data fits. In all uranium L_{III}-edge k^3-weighted EXAFS data and corresponding Fourier transforms depicted in this work, the peaks in the Fourier transform are not corrected for the phase shift.

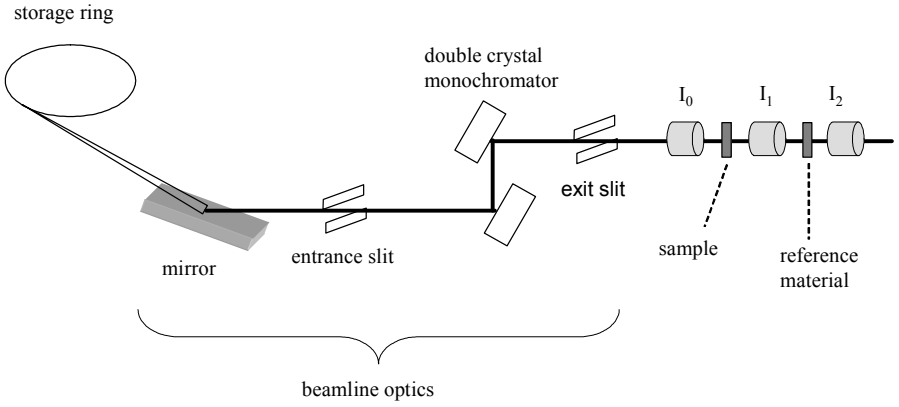

Figure 3.8. Experimental setup of an EXAFS experiment in transmittance mode using synchrotron radiation.

References

[1] Teo, B.K. *EXAFS: Basic Principles and Data Analysis*, **1986**, Springer, Berlin, Heidelberg, New York.

[2] Koningsberger, D.C.; Prins, R. *X-ray Absorption: Principles, Applications, Techniques of EXAFS, SEXAFS and XANES*, **1988**, John Wiley & Sons, New York.

[3] Denecke, M.A. *Coord. Chem. Rev.* **2006**, *250*, 730-754.

[4] Antonio, M.R.; Soderholm, L. "X-ray Absorption Spectroscopy of the Actinides" in *The Chemistry of the Actinide and Transactinide Elements* (3rd edition); Eds. Morss, L.R.; Edelstein, N.M.; Fuger, J., **2006**, Springer, Dordrecht, The Netherlands, p. 3086-3189.

[5] Penner-Hahn, J.E. *Coord. Chem. Rev.* **2005**, *249*, 161-177.

[6] Penner-Hahn, J.E. *Coord. Chem. Rev.* **1999**, *190-192*, 1101-1123.

[7] Deutsch, M.; Kitzler, P. *Phys. Rev. A* **1992**, *45*, 2112-2115.

[8] Krause, M.O.; Oliver, J.H. *J. Phys. Chem. Ref. Data* **1972**, *8*, 329-338.

[9] Hennig, C. *Phys. Rev. B* **2007**, *75*, 035120.

[10] Ankudinov, A.L.; Ravel, B.; Rehr, J.J.; Conradson, S.D. *Phys. Rev. B* **1998**, *58*, 7565-7576.

[11] Hudson, E.A.; Allen, P.G.; Terminello, L.J.; Denecke, M.A.; Reich, T. *Phys. Rev. B* **1996**, *54*, 156-165.

[12] Matz, W.; Schell, N.; Bernhard, G.; Prokert, F.; Reich, T.; Claussner, J.; Oehme, W.; Schlenk, R.; Dienel, S.; Funke, H.; Eichhorn, F.; Betzl, M.; Pröhl, D.; Strauch, U.; Hüttig, G.; Krug, H.; Neumann, W.; Brendler, V.; Reichel, P.; Denecke, M.A.; Nitsche, H. *J. Synchrotron Rad.* **1999**, *6*, 1076-1085.

[13] George, G.N.; Pickering, I.J. *EXAFSPAK, a suite of computer programs for analysis of X-ray absorption spectra*, **2000**, Stanford Synchrotron Radiation Laboratory, Stanford.

4 EXPERIMENTAL PROCEDURES

1 Reagents

The uranyl salts $UO_2(NO_3)_2 \cdot 6H_2O$, UO_2Cl_2 and $UO_2(CH_3COO)_2 \cdot 2H_2O$ were purchased from Merck, whereas uranium(VI) oxide UO_3 was obtained from Ventron Alpha Products. Tetrabutylammonium chloride and tetrabutylammonium nitrate were purchased from Fluka, tetrabutylammonium acetate from Aldrich, the crown ether 18-crown-6 from Acros and oxalic acid from Merck. Lithium bis(trifluoromethylsulfonyl)imide Li(Tf_2N) was supplied from Io-Li-Tec.

For the measurements in non-aqueous solution, acetonitrile was used instead of acetone due to its higher stability. Extra dry acetonitrile with less than 50 ppm water, dried on molecular sieves, was purchased from Acros.

2 Synthesis of uranyl salts

***$UO_2(ClO_4)_2 \cdot xH_2O$*:** UO_3 was dissolved in perchloric acid (2 mol L^{-1}). The solution was boiled to expel free chlorine gas. After dilution with water, the solution was subsequently evaporated close to dryness. This

procedure was repeated until white fumes were no longer formed. Finally, a yellow powder was obtained [1,2]. Various hydrates of uranyl perchlorate $UO_2(ClO_4)_2 \cdot xH_2O$ (x = 0, 1, 2, 3, 5, 6, 7) have been reported in the literature [3]. The treatment of the initial solid probably governs the degree of hydration. However, it is difficult to determine the exact number of water molecules in the uranyl perchlorate salt due to its hygroscopic behaviour. Even if we could determine the exact number of water molecules in the initial batch, this number can change during the course of the experiment. Therefore, to have more or less an idea about the uranyl concentration in our samples, we use the molecular weight of the hexahydrate for calculating concentrations (MW = 577.02 g mol^{-1}). Comparison of the ε-values of an aqueous solution of the uranyl ion with 5, 6 or 7 water molecules in the initial perchlorate salt yields an error of about 3%.

CAUTION: Perchloric acid is extremely hazardous. It is very corrosive to skin and eyes and should be handled with the utmost care. It can also ignite or explode when it comes in contact with common organic material such as cloth or wood. Perchlorate salts are shock-sensitive. Scraping of a spatula on the side of the container and/or crushing perchlorate salt crystals with a metal pestil can initiate an explosion.

***UO_2Br_2*:** Hydrogen bromide (1.25 mL of an aqueous solution of HBr (47%), which corresponds to 0.01 mol HBr) was added to a suspension of UO_3 (4 g; 0.014 mol) in water whilst stirring and heating the solution. The excess of UO_3 was filtered off and the filtrate was evaporated in a beaker. The remaining amount of water was expelled under reduced pressure. UO_2Br_2 is a yellow powder. Due to its hygroscopic character, UO_2Br_2 was kept in a dessicator.

***$UO_2(Tf_2N)_2$*:** In a first step, lithium bis(trifluoromethylsulfonyl)imide was converted into the corresponding acid. Therefore, 30 mL of an aqueous solution of $Li(Tf_2N)$ (2 mol L^{-1}) was mixed with an excess of a 20%

aqueous H_2SO_4 solution, resulting in $H(Tf_2N)$ and $LiSO_4$. The colourless aqueous phase was extracted with diethyl ether. The organic phase and the aqueous phase contained the desired acid and $LiSO_4$, respectively. The aqueous phase was washed several times with diethyl ether to remove possible traces of $H(Tf_2N)$. Evaporating diethyl ether under reduced pressure gave hydrogen bis(trifluoromethylsulfonyl)imide $H(Tf_2N)$.

Into a round-bottom flask, equipped with a magnetic stirrer and a cooler, a small excess of $H(Tf_2N)$ (9 g; 0.033 mol) was added to a suspension of UO_3 (0.023 mol) in water. This reaction mixture was refluxed at 50 °C for three days. Then the temperature was raised to 80 °C, thereby refluxing the mixture for another 24 hours. Water was evaporated under reduced pressure until a yellow oil-like substance was obtained. This substance was washed with dichloromethane to remove the remaining traces of the acid $H(Tf_2N)$. Under stirring and slightly heating for an hour, methanol was added to dissolve the obtained product. The non-reacted UO_3 was filtered off, resulting in a bright yellow solution. Finally, methanol was expelled on a rotary evaporator under reduced pressure, leaving the viscous, dark yellowish $UO_2(Tf_2N)_2$ in the flask.

3 Spectrophotometric measurements

UV-Vis absorption spectra were measured at room temperature as well as at low temperatures, ranging from 273 K to 213 K, on a Varian Cary 5000 spectrophotometer between 600 nm and 300 nm. For the low temperature measurements, a cryostat of Oxford Instruments, cooled with liquid nitrogen, was used.

Luminescence measurements have been carried out at room temperature on an Edinburgh Instruments FS-900 spectrofluorimeter. The light source used was a 450 W xenon arc lamp. Emission spectra were recorded between 430 nm and 650 nm, whereas excitation spectra

were measured between 300 nm and 530 nm. The excitation and emission wavelengths depend on the uranyl complex present in the solution. Table 4.1 gives an overview of the excitation and emission wavelengths used for the different ligands in aqueous and non-aqueous solution as well as in the ionic liquids.

Table 4.1. Overview of the excitation and emission wavelengths (nm) for the different ligands in aqueous and non-aqueous solution and the ionic liquid [bmpyr][Tf_2N].

Ligand	Aqueous solution		Non-aqueous solution		[bmpyr][Tf_2N] (ionic liquid)	
	λ_{ex}	λ_{em}	λ_{ex}	λ_{em}	λ_{ex}	λ_{em}
Cl^-	414.0	510.2	415.0	540.0	418.5	540.0
NO_3^-	414.3	510.0	420.0	509.6	438.2	509.6
CH_3COO^-	414.0	518.6	420.0	514.4	420.0	509.6
18C6	--	--	420.0	540.0	429.0	540.0
TBP	--	--	425.6	509.0	--	--
$C_2O_4^{2-}$	--	--	420.0	513.8	--	--

18C6 = 18-crown-6, TBP = tri-*n*-butylphosphate.

Magnetic circular dichroism (MCD) spectra were recorded at room temperature on an AVIV 62 DS circular dichroism spectrometer (extended with an electromagnet to create a magnetic field of 1 T) over the wavelength interval 570 nm - 300 nm.

All solutions were freshly prepared before each measurement.

4 ^{31}P NMR spectroscopy

Proton decoupling ^{31}P NMR spectra were recorded at 161.98 MHz using a Bruker AMX-400 spectrometer, with H_3PO_4 as external reference. In variable temperature experiments ranging from 298 K to 213 K, the temperature error within was 0.1 K.

References

[1] De Houwer, S.; Görller-Walrand, C. *J. Alloys Compd.* **2001**, *323-324*, 683-687.

[2] Silverman, L.; Moudy, L. *Anal. Chem.* **1956**, *28*, 45-47.

[3] Gmelin Handbook, U, Uranium Suppl. C9, *Compounds with chlorine, bromine, iodine*, System Number 55, **1979**, Springer, Berlin.

5 COORDINATION EFFECTS ON THE SPECTRA OF THE URANYL ION UO_2^{2+}

1 Introduction

The uranyl ion has the tendency to form complexes with a variety of ligands: small inorganic ligands (e.g. Cl^-, NO_3^-, SO_4^{2-}), small organic ligands (e.g. CH_3COO^-, $C_2O_4^{2-}$) and macrocyclic ligands (e.g. Schiff's bases, crown ethers). The complex formation of the uranyl ion with this variety of ligands results in UV-Vis absorption spectra with a typical vibrational fine structure, depending on the symmetry group of the complex formed [1]. The main features of these spectra, such as positions and intensities of electronic transitions, are primarily determined by the geometry of the first coordination sphere of the uranium atom. In this chapter, we will discuss the typical UV-Vis absorption spectra of a complex of D_{5h} symmetry ($[UO_2(H_2O)_5]^{2+}$), a complex of D_{4h} symmetry ($[UO_2Cl_4]^{2-}$), complexes of D_{3h} symmetry ($[UO_2(NO_3)_3]^-$, $[UO_2(CH_3COO)_3]^-$ and $[UO_2(CO_3)_3]^{4-}$) and a complex with D_3 symmetry ($[UO_2(18\text{-crown-6})]^{2+}$). These UV-Vis absorption spectra can be used as fingerprints of a certain symmetry group.

In aqueous solution, the affinity of the uranyl ion UO_2^{2+} to coordinate to small ligands decreases as following [2,3]:

$$F^- \approx C_2O_4^{2-} > CO_3^{2-} > CH_3COO^- > SO_4^{2-} > SCN^- \text{(thio)} >> Cl^- \geq Br^- \approx NO_3^-$$

In organic solvents, this ligand affinity series towards uranyl changes. For example, the complex formation with nitrate ions is often strongly favoured in such environments, although nitrate ions form very weak complexes with uranyl in water. With respect to the stability of the trinitrato complex $[UO_2(NO_3)_3]^-$, the solvent order is: ketones > ethers > alcohols > water. A comparison between the coordination of the uranyl ion with chloride, nitrate and acetate ions in aqueous solution and organic solvents will be discussed here.

The speciation and structure analysis of uranyl complexes in solution has some limitations. Unlike the solid state structure, which can be determined by X-ray diffraction on single crystals, the structure of solution species could only be investigated in the past via symmetry

effects, e.g. by UV-Vis absorption, luminescence and MCD spectroscopy. Because of the characteristic optical properties of the uranyl ion, spectroscopic methods combined with ligand field theory are a powerful tool for the identification of the complex structure in solution.

Nowadays, a modern experimental technique is available to determine some limited structural parameters like bond distances, of solution species: *Extended X-Ray Absorption Fine Structure* (EXAFS). In this chapter, the UV-Vis data and the known crystal structures of $[UO_2Cl_4]^{2-}$, $[UO_2(NO_3)_3]^-$, $[UO_2(CH_3COO)_3]^-$ and of the inclusion complex $[UO_2(18\text{-crown-}6)]^{2+}$ will be combined with uranium L_{III}-edge EXAFS spectroscopy. In this way, the structure of the complexes can be unambiguously determined. This combination of UV-Vis absorption spectroscopy, available fingerprint spectra and uranium L_{III}-edge EXAFS spectroscopy is a helpful tool for solving the structure of complexes formed in other uranyl-ligand systems. Furthermore, the weak complex forming behaviour of nitrate and chloride ions with the uranyl ion in aqueous solution will be demonstrated by means of uranium L_{III}-edge EXAFS measurements.

NMR spectroscopy can be applied to investigate the coordination behaviour of the uranyl ion. Indeed, a determination of the coordination number is possible with NMR spectroscopy by integrating the area of the NMR signals of free and coordinated ligands. From this stoichiometric information, one can deduce the equilibrium constants for complex formation reactions. Different NMR studies on uranyl complexes with various ligands have been reported in the literature [4-9]. The possibility of identifying various complexes or isomers in rapid equilibrium with another depends on the rates of inter- and intramolecular exchange reactions. Therefore, especially ligand dynamics in uranyl complexes are studied by NMR techniques, thereby determining the rate constants for these ligand exchange reactions [10-13].

The uranyl ion is active in vibrational spectroscopy, principally through its symmetric (ν_s) and asymmetric (ν_a) stretching vibrations in

Raman scattering and infrared spectroscopy, respectively. Raman spectroscopy is mainly used to study the complex formation of the uranyl ion with inorganic or organic ligands in aqueous solution [14-20]. Upon coordination, shifts in the values of these active vibrations of the uranyl ion are observed. Nguyen-Trung et al. have found a linear correlation between the value of the symmetric stretching vibration and the average number of equatorially coordinated ligands [15]. Furthermore, it is possible to distinguish between a monodentate and a bidentate coordination mode of the ligands, based on their characteristic vibrational frequencies. However, equatorial ligand vibrations of uranyl complexes like the U-Cl out-of-plane bending in $[UO_2Cl_4]^{2-}$, have a vibrational frequency between 100 cm^{-1} and 300 cm^{-1}. Consequently, these vibrational modes which are Raman or IR active, can only be studied by Raman and IR spectroscopy if the available apparatus has the proper measuring range.

In conclusion, NMR, Raman and IR spectroscopy give information on the kind of ligands coordinated to the uranyl ion and the coordination mode of the ligands. In some cases, it is possible to determine the coordination number. But, no information on the symmetry of the first coordination sphere is obtained using the former spectroscopic techniques.

2 Experimental details

- *Solutions of chloro complexes*

$UO_2(ClO_4)_2{\cdot}xH_2O$ was mixed with tetrabutylammonium chloride in acetonitrile in uranyl-to-chloride ratios ranging from 1:0 to 1:6. The uranyl concentration was approximately 5×10^{-2} mol L^{-1}. The tetrabutylammonium chloride concentration was varied from 5×10^{-2} mol L^{-1} to 3×10^{-1} mol L^{-1}. In aqueous solution (1 mol L^{-1} $HClO_4$), NaCl was added to a solution of $UO_2(ClO_4)_2{\cdot}xH_2O$ in metal-to-ligand ratios of 1:0

to 1:8. For chloride concentrations up to 0.2 mol L^{-1}, a hydrochloric acid solution of 1 mol L^{-1} was used instead of NaCl, thereby keeping the ionic strength constant at μ = 1 mol L^{-1}. For chloride concentrations above 0.2 mol L^{-1}, concentrated hydrochloric acid (12 mol L^{-1}) was used. The uranyl concentration in aqueous solution was approximately 5×10^{-3} mol L^{-1}. Furthermore, an aqueous solution was prepared by dissolving the UO_2Cl_2 salt (5×10^{-2} mol L^{-1}) in distilled water.

- *Solutions of nitrato complexes*

Tetrabutylammonium nitrate was added to a solution of $UO_2(NO_3)_2 \cdot 6H_2O$ in acetonitrile with varying total metal-to-ligand ratios ranging from 1:2 to 1:4. The uranyl concentration was approximately 5×10^{-2} mol L^{-1}. An aqueous solution (5×10^{-2} mol L^{-1}) was prepared by dissolving $UO_2(NO_3)_2 \cdot 6H_2O$ in distilled water. The pH of this solution was 2.4. For the subsequent coordination with nitrate ions in aqueous solution (1 mol L^{-1} $HClO_4$), $NaNO_3$ was mixed with $UO_2(ClO_4)_2 \cdot xH_2O$ in metal-to-ligand ratios of 1:0 to 1:4. For nitrate concentrations up to 0.2 mol L^{-1}, a nitric acid solution (1 mol L^{-1}) was added instead of $NaNO_3$. The ionic strength was held constant at μ = 1 mol L^{-1}. For higher nitrate concentrations (> 0.2 mol L^{-1}), concentrated nitric acid (16 mol L^{-1}) was used. The uranyl concentration in aqueous solution was approximately 5×10^{-3} mol L^{-1}.

- *Solutions of acetato complexes*

$UO_2(ClO_4)_2 \cdot xH_2O$ was mixed with tetrabutylammonium acetate in acetone in metal-to-ligand ratios ranging from 1:0 to 1:5. The uranyl concentration was approximately 5×10^{-2} mol L^{-1}, whereas the tetrabutylammonium acetate concentration was varied between 5×10^{-2} mol L^{-1} and 2.5×10^{-1} mol L^{-1}. Sodium acetate was added to an aqueous solution of $UO_2(ClO_4)_2 \cdot xH_2O$ in uranyl-to-acetate ratios of 1:0 to 1:4. The uranyl concentration was approximately 5×10^{-3} mol L^{-1}.

- *Solutions of 18-crown-6 complexes*

$UO_2(ClO_4)_2{\cdot}xH_2O$ was mixed with the crown ether 18-crown-6 (Figure 5.1) in acetonitrile in the metal-to-ligand ratio of 1:2. An excess of ligand was added to guarantee the maximum coordination, because an EXAFS study showed that a partial de-insertion of the uranyl ion occurs in acetonitrile [21,22].

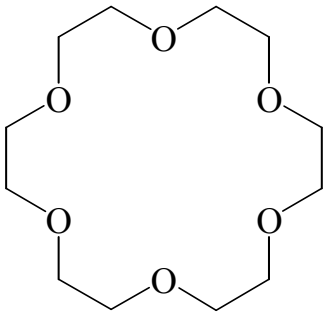

Figure 5.1. The crown ether 18-crown-6.

3 Data analysis of uranium L_{III}-edge EXAFS spectra

The EXAFS measurements were performed using the experimental setup, the sample preparation and the data analysis, as described in Chapter 3. Theoretical phase and amplitude functions were calculated using a hypothetical cluster based on the structures of $UO_2(ClO_4)_2{\cdot}5H_2O$ [23], $Cs_2UO_2Cl_4$ [24], $(UO_2(NO_3)_2(H_2O)_2){\cdot}H_2O$ [25], $RbUO_2(NO_3)_3$ [26], $NaUO_2(CH_3COO)_3$ [27] and $[UO_2(18\text{-crown-6})](CF_3SO_3)_2$ [28]. In all curve fit procedures the coordination number of the uranyl axial oxygen atoms (O_{ax}) was held constant at two, except for the hydrated uranyl ion and $[UO_2Cl_4]^{2-}$, in order to reduce the number of degrees of freedom. Furthermore, scattering contributions of less than 5% were not considered.

3.1 $[UO_2(H_2O)_5]^{2+}$ and $[UO_2Cl_4]^{2-}$

The curve fit procedure of the EXAFS data of $[UO_2(H_2O)_5]^{2+}$ and $[UO_2Cl_4]^{2-}$ is rather straightforward. Besides the single and multiple scattering paths of the axial oxygen atoms, the single scattering paths U-O_{eq} and U-Cl were included for $[UO_2(H_2O)_5]^{2+}$ and $[UO_2Cl_4]^{2-}$, respectively. In case of $[UO_2Cl_4]^{2-}$, an additional three-legged multiple scattering path, i.e. MS U-Cl-O_{ax}, was taken into account by constraining its degeneracy to 16 and its effective path length R to 3.82 Å.

3.2 $[UO_2(NO_3)_3]^-$

The main (multiple) scattering paths, with their relative importance, of the uranyl trinitrato unit $[UO_2(NO_3)_3]^-$ are defined according to the notation in Figure 5.2 and shown in Table 5.1.

The degeneracy of the multiple scattering paths was included in the coordination numbers N. So, the degeneracy of the dominating multiple scattering paths including the distal oxygen atom O_{dist}, namely U-N-O_{dist}-N (four-legged scattering path) and U-O_{dist}-N (three-legged scattering path, abbreviated as MS O_{dist}) was held constant at the number of distal oxygen atoms present and to twice its value, respectively. Furthermore, the distances R and Debye-Waller factors σ^2 of these multiple scattering paths were linked to R and σ^2 of the single scattering path U-O_{dist}. The number of scattering paths of the three-legged multiple scattering path U-N-O_{eq} was constrained to twice the coordination number of the equatorial oxygen atoms O_{eq}, whereas R and σ^2 were kept free in the fit.

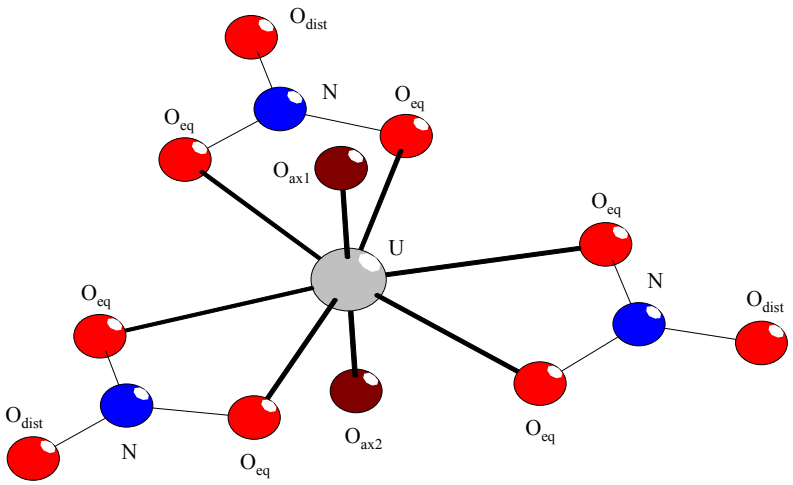

Figure 5.2. First coordination sphere of $[UO_2(NO_3)_3]^-$ [26].

Table 5.1. Principal scattering pathways[a], taken from $RbUO_2(NO_3)_3$ [26].

Pathway	Scattering length (Å)	Intensity (normalized)
$U\text{-}O_{ax}$	1.746	100
$U\text{-}O_{ax1}\text{-}O_{ax2}$	3.492	22.8
$U\text{-}O_{ax1}\text{-}U\text{-}O_{ax2}$	3.492	44.9
$U\text{-}O_{ax1}\text{-}U\text{-}O_{ax1}$	3.492	13.9
$U\text{-}O_{eq}$	2.473	43.1
U-N	2.911	25.1
$U\text{-}N\text{-}O_{eq}$	3.327	7.1
$U\text{-}O_{dist}$	4.118	8.9
$U\text{-}O_{dist}\text{-}N$	4.118	24.6
$U\text{-}N\text{-}O_{dist}\text{-}N$	4.118	16.7
$U\text{-}O_{dist}\text{-}O_{eq}$	4.381	3.3
$U\text{-}N\text{-}O_{dist}\text{-}O_{eq}$	4.381	4.9

[a] Scattering pathways only multiplied by a symmetry degeneration or with a scattering amplitude of less than 3% were not considered in the table.

3.3 $[UO_2(CH_3COO)_3]^-$

For the curve fit of the EXAFS spectrum and the corresponding Fourier transform of the uranyl triacetato complex $[UO_2(CH_3COO)_3]^-$, we used the same procedure as for $[UO_2(NO_3)_3]^-$. The principal scattering pathways, with their amplitude, are defined according to the notation in Figure 5.3 and listed in Table 5.2. The degeneracy of the multiple scattering paths of the distal carbon atom C_{dist}, namely U-C-C_{dist}-C (four-legged scattering path) and U-C_{dist}-C (three-legged scattering path, abbreviated as MS C_{dist}) was held constant at the number of distal carbon atoms present and to twice its value, respectively. On the other hand, the path lengths R and the Debye-Waller factors σ^2 of these multiple scattering paths were linked to R and σ^2 of the single scattering path U-C_{dist}. The number of scattering paths of the three-legged multiple scattering path U-C-O_{eq} was constrained to twice the coordination number of the equatorial oxygen atoms O_{eq}. The distance R and Debye-Waller factor σ^2 of the former scattering path were linked to R and σ^2 of the single scattering path U-C.

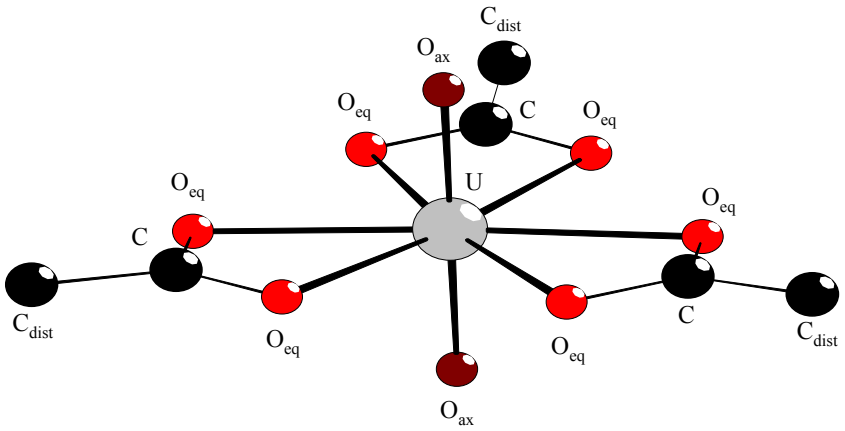

Figure 5.3. Structure of the $[UO_2(CH_3COO)_3]^-$ polyhedron [27].

Table 5.2. Dominating scattering pathways[a], calculated for solid $NaUO_2(CH_3COO)_3$ [27].

Pathway	Scattering length (Å)	Intensity (normalized)
U-O_{ax}	1.756	100
U-O_{ax1}-O_{ax2}	3.516	22.9
U-O_{ax1}-U-O_{ax2}	3.516	50.5
U-O_{ax1}-U-O_{ax1}	3.512	14.7
U-O_{eq}	2.462	127
U-C	2.852	72.3
U-C-O_{eq}	3.285	24.6
U-C_{dist}	4.349	18.7
U-C_{dist}-C	4.349	46.0
U-C-C_{dist}-C	4.350	28.3
U-C_{dist}-O_{eq}	4.604	8.3
U-C-C_{dist}-O_{eq}	4.604	10.9

[a] Scattering pathways only multiplied by a symmetry degeneration or with a scattering amplitude of less than 3% were not considered in the table.

3.4 $[UO_2(18\text{-crown-6})]^{2+}$

For calculating the theoretical phase and amplitude functions of the $[UO_2(18\text{-crown-6})]^{2+}$ complex, we used the crystal structure of $[UO_2(18\text{-crown-6})](CF_3SO_3)_2$ [28]. The main multiple scattering paths, with their relative importance, are defined according to the notation in Figure 5.4 and shown in Table 5.3.

To take into account the degeneracy of the dominating multiple scattering paths, the number of possible scattering pathways of the three-legged multiple scattering path U-C_{eq}-O_{eq} was determined by identifying the coordination number N as four times the value of the coordination number of O_{eq}. Furthermore, the number of equatorial carbon atoms C_{eq} and the degeneracy of the multiple scattering path U-C_{eq}-O_{eq} were linked to the number of equatorial oxygen atoms O_{eq} present. In contrast, the

effective path lengths R and the Debye-Waller factors σ^2 of the scattering paths U-C_{eq} and U-C_{eq}-O_{eq} were kept free in the fit.

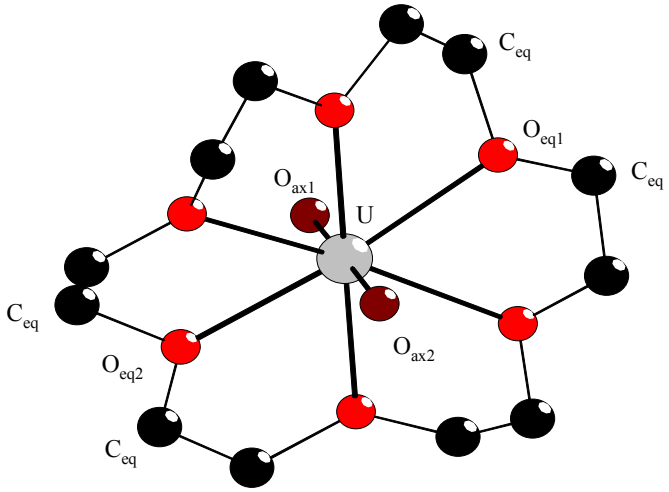

Figure 5.4. $[UO_2(18\text{-crown-}6)]^{2+}$ cation [28].

Table 5.3. Principal scattering pathways[a], estimated for solid $[UO_2(18\text{-crown-}6)](CF_3SO_3)_2$ [28].

Pathway	Scattering length (Å)	Intensity (normalized)
U-O_{ax}	1.628	100
U-O_{ax1}-O_{ax2}	3.270	25.3
U-O_{ax1}-U-O_{ax2}	3.270	47.3
U-O_{ax1}-U-O_{ax1}	3.255	16.6
U-O_{eq}	2.440	38.0
U-C_{eq}	3.349	12.4
U-C_{eq}-O_{eq}	3.782	7.4
U-O_{eq1}-O_{eq2}	4.942	3.8
U-O_{eq1}-U-O_{eq2}	4.955	5.3

[a] Scattering pathways only multiplied by a symmetry degeneration or with a scattering amplitude of less than 3% were not considered in the table.

4 Results and discussion

4.1 "Free" uranyl ion (hydrated uranyl ion)

Per definition, the "free" uranyl ion is observed in a solution of a strongly dissociated salt like uranyl perchlorate $UO_2(ClO_4)_2 \cdot xH_2O$. By dissolving $UO_2(ClO_4)_2 \cdot xH_2O$ in aqueous solution, the perchlorate ions are removed from the first coordination sphere. Indeed, perchlorate ions are known for their weak-coordinating properties. In reality, the "free" uranyl ion is a hydrated ion [23,29,30]. The hydrated uranyl ion, present in the solid perchlorate pentahydrate, is $[UO_2(H_2O)_5]^{2+}$ [3,23]. With the term "free" uranyl ion, we mean the uranyl ion interacting with only solvent molecules and not with coordinating ligands.

4.1.1 Aqueous solution

The UV-Vis absorption and emission spectra of the "free" uranyl ion in aqueous solution are well-known [31]. The uranyl ion exhibits an absorption spectrum with a typical vibrational fine structure between 18000 cm^{-1} and 30000 cm^{-1} (Figure 5.5). The absorption maximum is situated at approximately 24140 cm^{-1} (~ 414 nm).

The typical green luminescence of the uranyl ion is observed in the wavenumber range 15000 cm^{-1} - 22000 cm^{-1} (Figure 5.5). The maximum in luminescence intensity is determined at approximately 19600 cm^{-1} (~ 510 nm). A vibronic spacing of approximately 876 cm^{-1} can be attributed to the frequency of the symmetric stretching vibration (ν_s) of the uranyl ion in the ground state. The vibrational progression in ν_s in the emission spectrum clearly demonstrates the anharmonicity of the uranyl ion: 876 cm^{-1}, 874 cm^{-1}, 870 cm^{-1}, 863 cm^{-1}. The small peak in the beginning of the emission spectrum can be assigned as a hot band. This peak disappears at low temperature, as indicated by measuring the emission of the uranyl ion in a glycerol-water glass at 80 K [30].

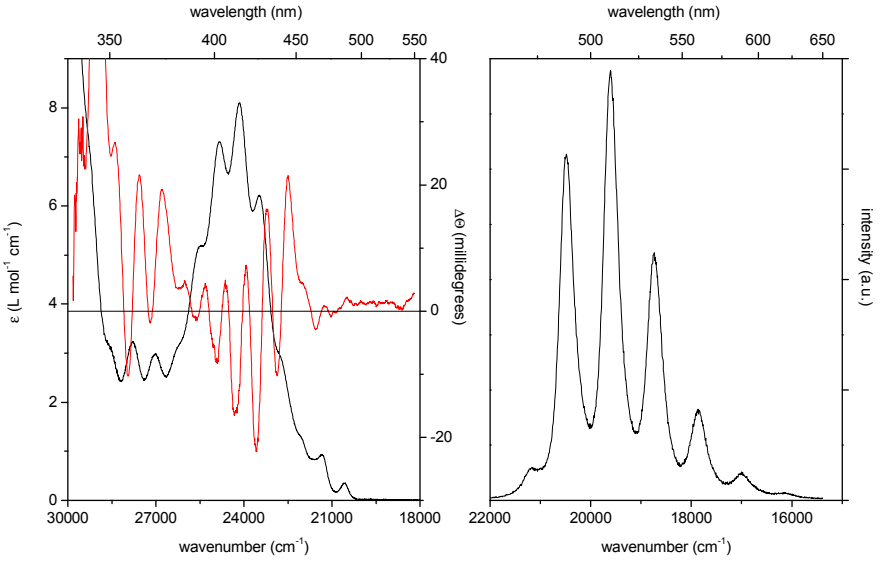

Figure 5.5. UV-Vis absorption spectrum (black curve) and MCD spectrum (red curve) (left) and emission spectrum (right) of the "free" uranyl ion UO_2^{2+} in aqueous solution at room temperature. The uranyl concentration is 5×10^{-2} mol L^{-1}. The excitation wavelength was set at 414 nm (24154 cm^{-1}).

The coordination sphere of the hydrated "free" uranyl ion has always been a point of discussion. Models with four to six water molecules in the equatorial plane have been proposed [32,33]. Presently, it is generally accepted that the uranyl ion is coordinated with five water molecules in the equatorial plane [30,34-40]. Consequently, the UV-Vis absorption spectrum corresponds to a D_{5h} coordination symmetry [40]. In this symmetry group, no intense absorption bands or distinct MCD signals are observed in the spectrum (Figure 5.5). Only the transition $\Gamma_g \leftarrow \Sigma_g^+$ ($E'_1 \leftarrow A'_1$ in D_{5h}) is electronically allowed along the x- and y-axis. However, the energy of this transition is according to theoretical calculations too high to be observed experimentally [41]. The first absorption peak (20576 cm^{-1}) arises from the first electronic transition $\Pi_g \leftarrow \Sigma_g^+$ in $D_{\infty h}$ or $E''_1 \leftarrow A'_1$ in D_{5h} symmetry. This transition is magnetic

dipole allowed in $\mathcal{R}_x$ and $\mathcal{R}_y$ and has low intensity. The electronic state Π_g has almost completely $^3\Delta_g$ character. The electronic origin of the second transition $\Delta_g \leftarrow \Sigma_g^+$ ($D_{\infty h}$) or $E'_2 \leftarrow A'_1$ (D_{5h}) is positioned at 21349 cm^{-1}. This transition is electric dipole forbidden in D_{5h}. Here, it is obvious that Δ_g (E'_2) is situated only slightly above Π_g (E''_1). The transitions to the Π_g (E''_1) and Δ_g (E'_2) excited states are well distinguishable in the spectrum. The other peaks in the UV-Vis absorption spectrum are according to Denning et al. the result of transitions between the totally symmetric ground state Σ_g^+ (A'_1) and the $^3\Delta_g$, $^1\Delta_g$ and $^3\Phi_g$ states [42-44]. The band origins of these electronic transitions are not exactly identified. However, recent theoretical calculations revealed that the UV-Vis absorption spectrum of the hydrated uranyl ion is almost completely built up of transitions to the triplet states $^3\Delta_g$ and $^3\Phi_g$. Indeed, $^3\Phi_g$ lies lower in energy than $^1\Delta_g$. The singlet states $^1\Delta_g$ and $^1\Phi_g$ only play a dominant role at higher energies (30000 cm^{-1} - 31000 cm^{-1}). Furthermore, a strong mixing of the $^3\Delta_g$ and $^3\Phi_g$ states is observed [41]. A comparison between the experimental and calculated excitation energies of $[UO_2(H_2O)_5]^{2+}$ is given in Table 5.4 [41].

Table 5.4. Comparison between the experimental and calculated excitation energies (cm^{-1}) of $[UO_2(H_2O)_5]^{2+}$.

Symmetry		$UO_2(ClO_4)_2 \cdot xH_2O$	$[UO_2(H_2O)_5]^{2+}$
$D_{\infty h}$	D_{5h}	aqueous solution	CASPT2 [41]
$\Pi_g \leftarrow \Sigma_g^+$	$E''_1 \leftarrow A'_1$	20576	20705
$\Delta_g \leftarrow \Sigma_g^+$	$E'_2 \leftarrow A'_1$	21349	21354

Dynamic processes, however, exist between the coordinated water molecules and the solvent water molecules, as studied by NMR spectroscopy [10-13]. The interaction between the uranyl ion and the water molecules is not strong, resulting in a slight distortion of the ideal D_{5h} coordination symmetry. Therefore, the typical vibrational fine

structure of a D_{5h} symmetry is less pronounced compared with the spectrum of the $[UO_2F_5]^{3-}$ complex, which exhibits a real D_{5h} symmetry [45]. Indeed, fluoride ligands are according to the ligand affinity series strongly bound to the uranyl ion [3].

Uranium L_{III}-edge EXAFS measurements on $UO_2(ClO_4)_2 \cdot xH_2O$ in aqueous solution confirm the presence of the hydrated uranyl ion $[UO_2(H_2O)_5]^{2+}$. There is no evidence that perchlorate ions coordinate to the uranyl ion in aqueous solution. Indeed, Sémon et al. demonstrated that no perchlorate coordination to the uranyl ion is observed in aqueous solution below 10 mol L^{-1} ClO_4^- [39]. The raw uranium L_{III}-edge k^3-weighted EXAFS data and the corresponding Fourier transform are given in Figure 5.6.

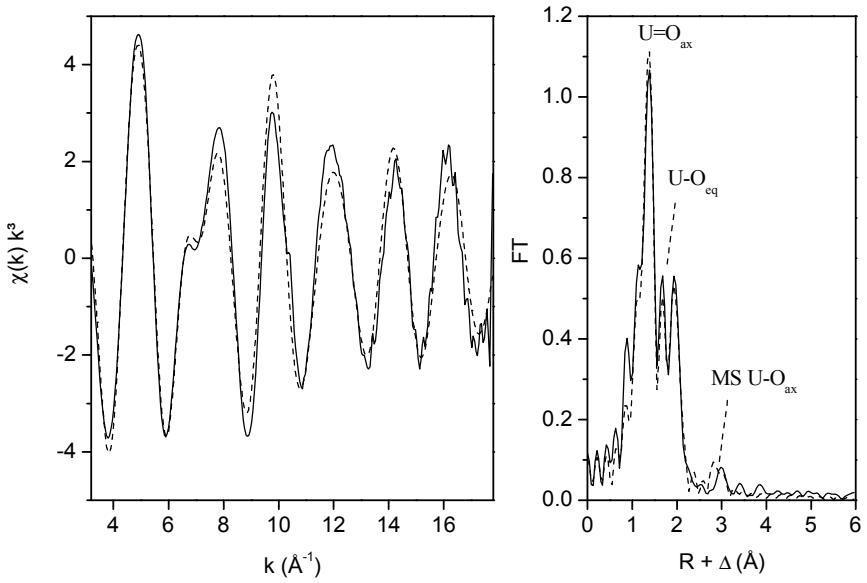

Figure 5.6. Uranium L_{III}-edge k^3-weighted EXAFS data (left) and corresponding Fourier transform (right), taken over k = 3.2 - 17.8 $Å^{-1}$, of the hydrated uranyl ion $[UO_2(H_2O)_5]^{2+}$ in aqueous solution. Experimental data are presented as a continuous line with the theoretical curve presented as a dashed line.

The large peak at R + Δ = 1.4 Å represents the scattering contribution of the two uranyl axial oxygen atoms O_{ax}. The double peak at R + Δ ≅ 2 Å arises from one single shell of equatorial oxygen atoms O_{eq}. Indeed, this peak can be completely covered by including one single shell of equatorial oxygen atoms at 2.42 Å in the fitting procedure. The splitting of the O_{eq} shell arises from a superposition of the O_{ax} peak with a side lobe of the O_{eq} peak. Side lobes occur in the Fourier transform due to the limited k-range. The rather large side lobe at high R-values of the O_{ax} peak coincides with the O_{eq} peak, giving rise to the splitting of this peak (Figure 5.7).

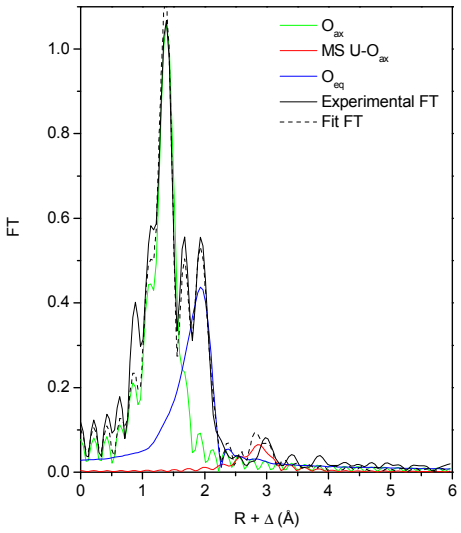

Figure 5.7. Fourier transform and its components of the hydrated uranyl ion in aqueous solution. The total Fourier transform is presented as a black curve.

Table 5.5 summarizes the EXAFS structural parameters of the $[UO_2(H_2O)_5]^{2+}$ polyhedron. There are two axial oxygen atoms at 1.77 ± 0.01 Å and five equatorial oxygen atoms at 2.41 ± 0.01 Å. Indeed, an average U-O_{eq} distance between 2.34 Å and 2.42 Å is characteristic for a

fivefold coordination of the uranyl unit [46]. These values are in good agreement with the crystal structure data of $UO_2(ClO_4)_2 \cdot 5H_2O$ [23], structural parameters previously obtained for the uranyl aquo ion in perchloric acid solution [34,35,39] and theoretical calculations [38].

Table 5.5. EXAFS structural parameters of the $[UO_2(H_2O)_5]^{2+}$ polyhedron.

	R (Å)	N	σ^2 (Å^2)
U-O_{ax}	1.77	2.2	0.0014
MS U-O_{ax}	3.53	2.2	0.0028
U-O_{eq}	2.41	5.2	0.0071

Error in distances R is ± 0.01 Å, error in coordination numbers N is ± 10%, ΔE = 1.6 eV.

4.1.2 Non-aqueous solvents

The UV-Vis absorption and emission spectra of the uranyl ion in acetonitrile are given in Figure 5.8. Both spectra exhibit the same spectral features as the spectra of the uranyl ion in aqueous solution. The frequency of the symmetric stretching vibration (ν_s) of the uranyl ion in the ground state in acetonitrile is approximately 885 cm^{-1}, exhibiting anharmonicity: 885 cm^{-1}, 876 cm^{-1}, 873 cm^{-1}.

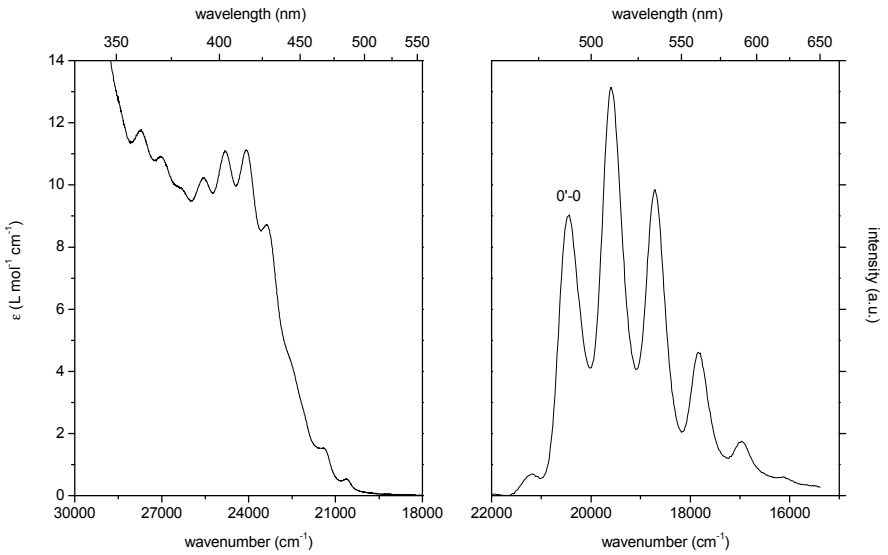

Figure 5.8. UV-Vis absorption spectrum (left) and emission spectrum (right) of the uranyl ion in acetonitrile at room temperature. The uranyl concentration is 5×10^{-2} mol L^{-1}. The excitation wavelength is 420 nm (23809 cm^{-1}).

Whereas the uranyl ion in aqueous solution is surrounded by five water molecules in the equatorial plane ($[UO_2(H_2O)_5]^{2+}$), the environment of the uranyl ion in acetonitrile solution is rather complicated. In anhydrous acetonitrile, there is a competition between the perchlorate ions and the solvent molecules for coordination with UO_2^{2+} [32]. An average coordination number of 4.4 is proposed, acetonitrile contributing 2.6 and perchlorate 1.8. However, if there is still a certain amount of water present in acetonitrile, water molecules will form the coordination environment of the uranyl ion. This is clearly indicated by uranium L_{III}-edge EXAFS spectroscopy (Figure 5.9). The EXAFS spectrum and the corresponding Fourier transform of the uranyl ion in acetonitrile exhibit the same structural features as the EXAFS measurements on UO_2^{2+} in aqueous solution. Moreover, the curve fit procedure also indicates the

formation of a pentahydrate, $[UO_2(H_2O)_5]^{2+}$. The structural parameters are given in Table 5.6.

The coordination of perchlorate ions would be demonstrated by a weak peak indicating a U-Cl distance at ~ 3.8 Å [39]. Interaction of acetonitrile would be revealed from a multiple scattering peak of the $N{\equiv}C\text{-}CH_3$ chain. The absence of these features points to the coordination of water molecules.

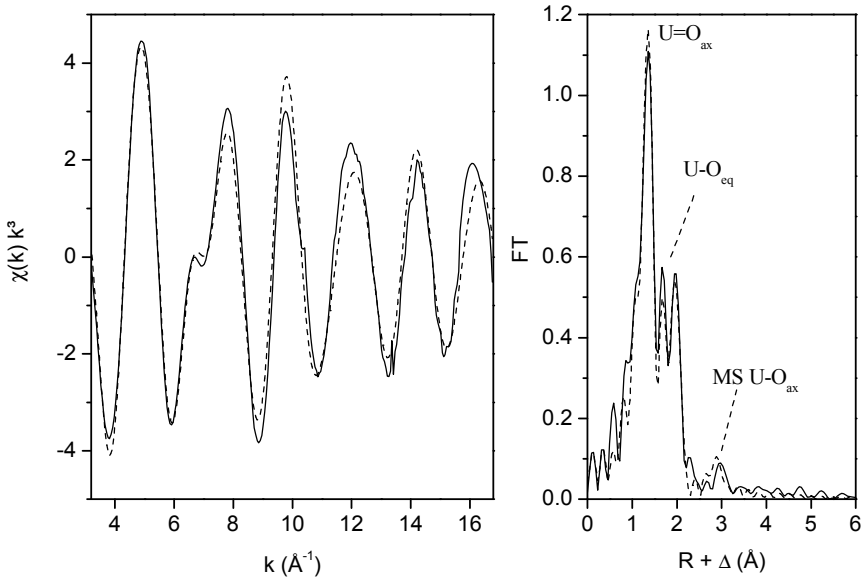

Figure 5.9. Uranium L_{III}-edge k^3-weighted EXAFS data (left) and corresponding Fourier transform (right), taken over k = 3.2 - 16.8 $Å^{-1}$, of the uranyl ion $(UO_2(ClO_4)_2{\cdot}xH_2O)$ in acetonitrile. Experimental data are presented as a continuous line with the theoretical curve presented as a dashed line.

We were not able to collect the EXAFS data of $UO_2(ClO_4)_2{\cdot}xH_2O$ in anhydrous acetonitrile in order to detect coordination of perchlorate ions instead of solvent molecules. It would be very useful to know the

limiting species* of UO_2^{2+} in anhydrous acetonitrile. Knowing the limiting species will help solving the coordination of the uranyl ion with other ligands in acetonitrile, like the intermediate chloro and nitrato complexes.

Table 5.6. EXAFS structural parameters of the uranyl ion UO_2^{2+} in acetonitrile.

	R (Å)	N	σ^2 (Å^2)
U-O_{ax}	1.76	2.3	0.0017
MS U-O_{ax}	3.53	2.3	0.0034
U-O_{eq}	2.42	5.1	0.0071

Error in distances R is ± 0.01 Å, error in coordination numbers N is ± 10%, ΔE = 1.4 eV.

4.2 Coordination with chloride ions

In the past, optical properties of uranyl chloro complexes in the solid state have been extensively studied. Crystals of the type $M_2UO_2Cl_4$ with M = Cs^+, K^+, Rb^+, NH_4^+, etc. have been thoroughly investigated by the groups of Denning, Tanner, Flint and Görller-Walrand [2b,44,47-49]. Thermodynamic data of U(VI) aquo chloro complexes have been reported in comprehensive reviews by Grenthe et al. [50] and their complex structures in aqueous solution by Allen et al. [51] and Hennig et al. [35]. In contrast, little is known on the coordination of the uranyl ion with chloride ions in non-aqueous solution. Görller-Walrand and coworkers have investigated the complex formation with chloride ions in acetone by UV-Vis absorption, luminescence and MCD spectroscopy [52]. The limiting species in acetone is $[UO_2Cl_4]^{2-}$ with D_{4h} coordination

* With "limiting species", we mean on one hand the solvated uranyl ion, i.e. the starting point, and on the other hand the finally formed complex, i.e. when the uranyl ion has reached its maximum coordination in the equatorial plane.

symmetry. Therefore, the spectrum is purely vibronic in nature, which implies that intensity of electronic transitions is only induced through coupling of vibrations with ungerade symmetry [44a,52].

4.2.1 Aqueous solution

The UV-Vis absorption spectra of the uranyl ion in aqueous solution in the presence of different concentrations of chloride ions are given in Figure 5.10.

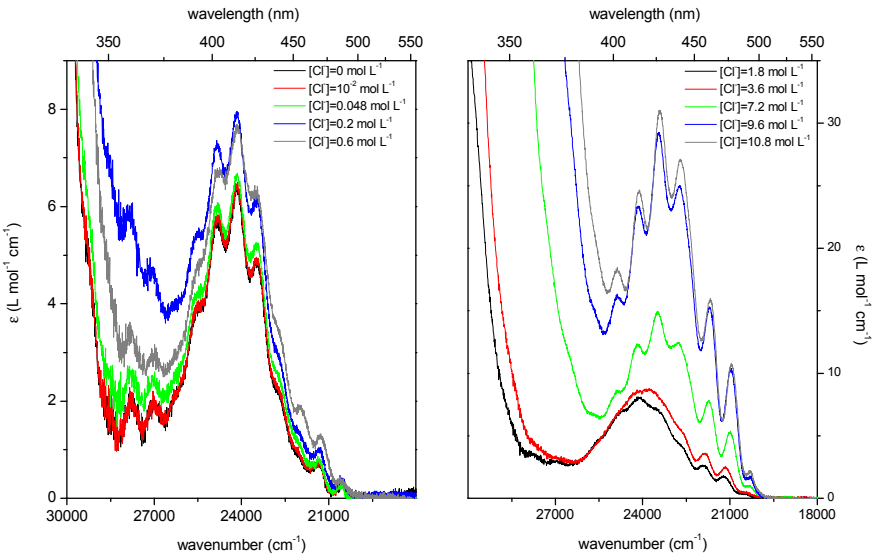

Figure 5.10. UV-Vis absorption spectra of the uranyl ion in the presence of different concentrations of chloride ions in aqueous solution at room temperature. The $[UO_2^{2+}]$ concentration is 5×10^{-3} mol L^{-1}.

At low chloride concentrations, no changes in vibrational fine structure or shift of the absorption peaks are observed in the spectra. However, a broad band with less fine structure appears with a chloride concentration of 1.8 mol L^{-1}. By further raising the chloride

concentration, the UV-Vis absorption spectra exhibit spectral features differing from the spectrum of the "free" uranyl ion in aqueous solution. Intense peaks, observed as shoulders in the spectrum of hydrated UO_2^{2+}, are detected at the low energy end of the spectrum. Moreover, the absorption peaks exhibit a shift to lower energies with respect to the spectrum of the "free" uranyl ion (λ_{max} = 427 nm). These spectral changes can be attributed to the existence of uranyl chloro complexes in aqueous solution. High chloride concentrations are necessary to remove water molecules from the first coordination sphere of the uranyl ion.

In contrast, no emission is observed after the addition of chloride ions in aqueous solution, which contrasts to the detection of luminescence of uranyl chloro complexes in acetonitrile or acetone (see 4.2.2). The fluorescence of the uranyl ion is inhibited by the chloride ions in aqueous solution. The quenching of the uranyl luminescence by chloride ions has already been reported in the literature [29,53]. Meinrath and coworkers stated that chloride ions are able to either abstract the excited electron from the uranyl entity or transfer an electron to electronically excited (U(VI))* and thus reducing the emission yield from the excited uranyl species [29].

It is known that the complex formation with chloride ions in aqueous solution is very weak [3,31]. Typical stability constants for the reaction $UO_2^{2+} + nCl^- \rightleftharpoons UO_2Cl_n^{2-n}$ have been reported in the literature: K_1 = 0.79 L mol^{-1}, K_2 = 0.15 L mol^{-1} and K_3 = 0.02 L mol^{-1} [54]. Large difficulties are encountered in determining these stability constants due to the weak complex formation in aqueous solution. Using the former stability constants for an aqueous solution of the UO_2Cl_2 salt (5×10^{-2} mol L^{-1}, metal-to-ligand ratio = 1:2), the species distribution is dominated by the hydrated uranyl ion, whereas the concentration of uranyl chloro complexes is low (92.7% UO_2^{2+}, 7.2% $[UO_2Cl]^+$ and 0.1% UO_2Cl_2). The species $[UO_2Cl_3]^-$ can be neglected from the thermodynamic data. UV-Vis absorption spectroscopy is not sensitive for these low concentrated chloro species. Therefore, no spectral changes appear for the low

chloride concentrations. Hence, the UV-Vis absorption spectra are dominated by the vibrational fine structure of the hydrated uranyl ion.

The weak complex formation of the uranyl ion with chloride ions in aqueous solution is confirmed by uranium L_{III}-edge EXAFS spectroscopy. The raw k^3-weighted EXAFS data of an aqueous solution of the UO_2Cl_2 salt (5×10^{-2} mol L^{-1}) and the corresponding Fourier transform are shown in Figure 5.11. The structural parameters are summarized in Table 5.7.

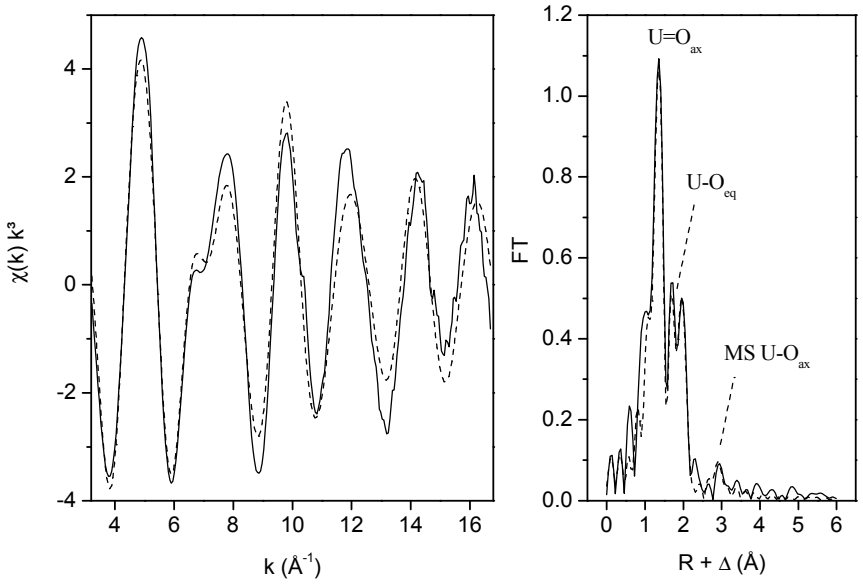

Figure 5.11. Uranium L_{III}-edge k^3-weighted EXAFS data (left) and corresponding Fourier transform (right), taken over k = 3.2 - 16.7 $Å^{-1}$, of the UO_2Cl_2 salt in aqueous solution. Experimental data are presented as a continuous line with the theoretical curve presented as a dashed line.

The EXAFS spectrum and the corresponding Fourier transform exhibit the same features as the EXAFS data of the "free" hydrated uranyl ion (Figure 5.6). Especially the shoulder of the oscillation at k = 7 $Å^{-1}$ is characteristic for the hydrated uranyl ion $[UO_2(H_2O)_5]^{2+}$ [34,35,39].

The fit results indicate the presence of five equatorial oxygen atoms in the equatorial plane, which is confirmed by the U-O_{eq} bond distance [46]. EXAFS is not sensitive to species at low concentrations. Therefore the spectrum shows no significant sign of chloride coordination.

Table 5.7. EXAFS structural parameters of the UO_2Cl_2 salt in aqueous solution.

	R (Å)	N	σ^2 (Å^2)
U-O_{ax}	1.77	2*	0.0015
MS U-O_{ax}	3.54	2*	0.0030
U-O_{eq}	2.40	5.4	0.0081

* value fixed during the fit procedure, error in distances R is ± 0.01 Å, error in coordination numbers N is ± 10%, ΔE = 0.9 eV.

It can be concluded that in a sample containing 5×10^{-2} mol L^{-1} UO_2Cl_2 ($[UO_2^{2+}]/[Cl^-]$ = 1:2) no significant chloride coordination is observed. This agrees well with the observation that a $[UO_2^{2+}]/[Cl^-]$ ratio of approximately 1:60 is required to detect the formation of a $[UO_2Cl]^+$ complex in the EXAFS spectrum [35].

The spectral changes in the UV-Vis absorption spectra at chloride concentrations higher than 1.8 mol L^{-1} in aqueous solution have been attributed to the presence of a mixture of UO_2^{2+}, $[UO_2Cl]^+$ and UO_2Cl_2 [55]. The existence of the species $[UO_2(H_2O)_4Cl]^+$ and $[UO_2(H_2O)_3Cl_2]$ in aqueous solution was proven by uranium L_{III}-edge EXAFS spectroscopy. The U-Cl distance varies from 2.71 Å to 2.73 Å. A $[UO_2(H_2O)_2Cl_3]^-$ species in aqueous solution has also been reported in the literature [35,51].

4.2.2 *Non-aqueous solvents*[*]

Whereas a complete removal of water molecules from the first coordination sphere of the uranyl ion is not observed in aqueous solution, organic solvents like acetone and acetonitrile, promote the coordination of the uranyl ion with chloride ions. Figure 5.12 shows the UV-Vis absorption spectrum of the uranyl ion with chloride ions in a metal-to-ligand ratio of 1:5 in acetonitrile. For comparison, the spectrum of the "free" uranyl ion in acetonitrile is also included.

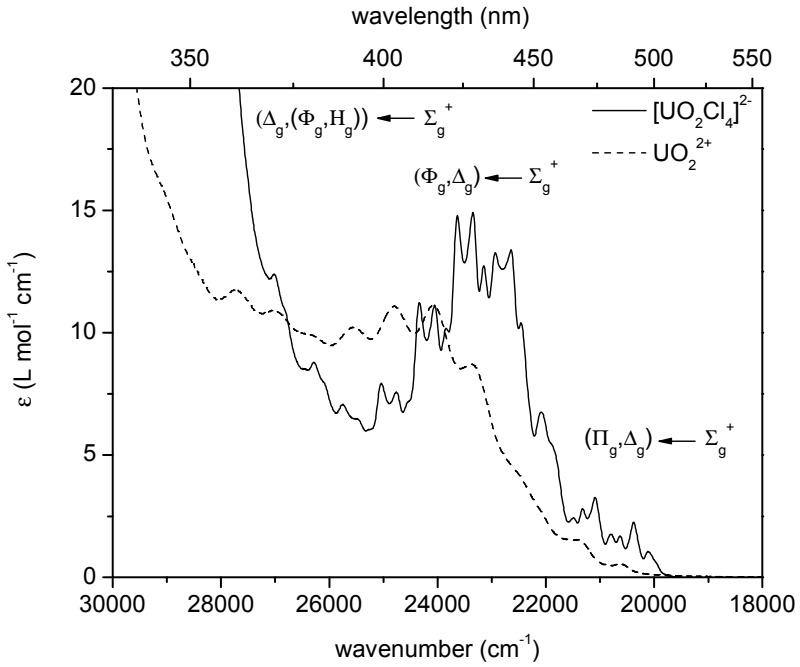

Figure 5.12. UV-Vis absorption spectra of the "free" uranyl ion (dashed line) and $[UO_2Cl_4]^{2-}$ (solid line) in acetonitrile at room temperature. The uranyl concentration is 5×10^{-2} mol L^{-1}. The metal-to-ligand ratio is 1:5.

[*] Supporting material (see Appendix 3): absorption, luminescence and MCD spectra and numerical data on $[UO_2Cl_4]^{2-}$ in acetonitrile.

Upon coordination with chloride ions, the spectrum exhibits a shift to lower energies with respect to the spectrum of the "free" uranyl ion. When a metal-to-ligand ratio of 1:5 is reached, no further changes appear in the spectrum upon the addition of extra chloride ions. The finally formed complex is identified as the $[UO_2Cl_4]^{2-}$ species as we will discuss in the next section [44b].

In the emission spectrum, we also observe remarkable changes upon the coordination of uranyl with chloride ions (Figure 5.13). The peaks are shifted towards lower energies (λ_{max} = 523 nm). In addition, the splitting of the peaks, as detected in the absorption spectrum, appears in the emission spectrum as well. The ground state value of ν_s is approximately 834 cm^{-1}.

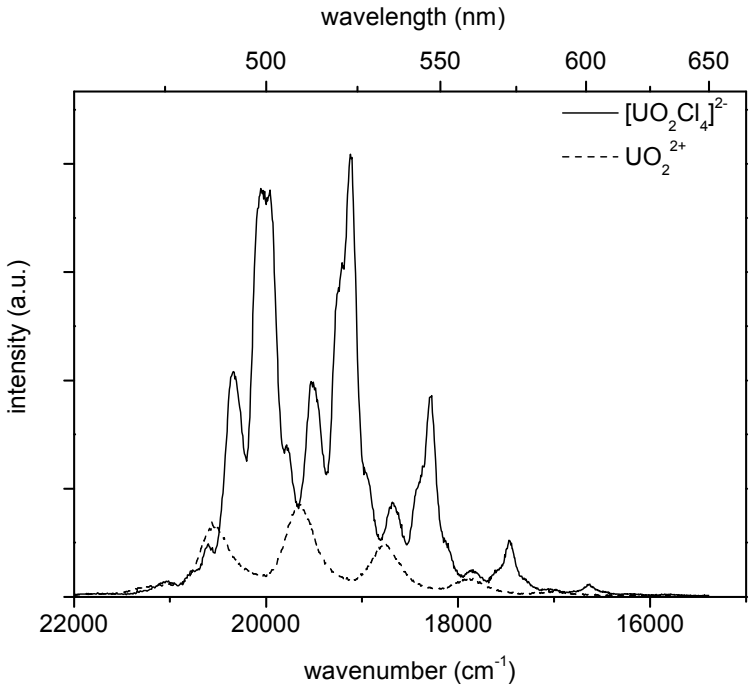

Figure 5.13. Emission spectra of the "free" uranyl ion (dashed line) and $[UO_2Cl_4]^{2-}$ (solid line) in acetonitrile at room temperature. The uranyl concentration is 5×10^{-2} mol L^{-1} and the metal-to-ligand ratio is 1:5. The excitation wavelength is 415 nm (24096 cm^{-1}).

By investigating the complex formation behaviour of the uranyl ion with chloride ions in acetone by means of optical spectroscopic techniques, Görller-Walrand and coworkers noticed that the main features in the spectrum remain constant when a metal-to-ligand ratio of 1:5 is reached [52]. Hence, the uranyl ion has reached its maximum coordination of chloride ions in the equatorial plane. Based on the similarity between the spectra of single crystals of the type $M_2UO_2Cl_4$ and the solution species, they concluded that a $[UO_2Cl_4]^{2-}$ complex with D_{4h} coordination symmetry is present in acetone solution [52]. The UV-Vis absorption spectrum in acetonitrile exhibits the same vibrational fine structure as that in acetone. Consequently, a complex with four equatorial chloride ligands (D_{4h}) is also formed in acetonitrile. Indeed, the maximum coordination of uranyl with chloride ions in organic solvents is four. An equatorial coordination of UO_2^{2+} with five chloride ions has never been observed in crystal structures.

The UV-Vis absorption and luminescence spectra of $[UO_2Cl_4]^{2-}$ have been studied in great detail [2b,42,44b,48,52,56-59]. Presently, the derived energy levels of UO_2^{2+} in $[UO_2Cl_4]^{2-}$ and their positions are generally accepted. The transitions in the spectrum mainly originate from the electronic configurations $(\sigma_u^{+})^2 \rightarrow \sigma_u^{+}\delta_u$ and $(\sigma_u^{+})^2 \rightarrow \sigma_u^{+}\phi_u$. In an intermediate coupling scheme, this corresponds to $\Sigma_g^{+} \rightarrow \Pi_g$, $\Sigma_g^{+} \rightarrow \Delta_g$, $\Sigma_g^{+} \rightarrow \Phi_g$ and $\Sigma_g^{+} \rightarrow \Delta_g$ for $(\sigma_u^{+})^2 \rightarrow \sigma_u^{+}\delta_u$ [44b,49]. Table 5.8 lists the transitions we assign for $[UO_2Cl_4]^{2-}$ in acetonitrile as well as an overview of the energy values of $Cs_2UO_2Cl_4$ single crystals, studied in detail by Denning et al. [44b], and of $[UO_2Cl_4]^{2-}$ in acetone [52] in D_{4h} symmetry. For comparison, the energy values calculated with *ab initio* methods are also included [41,58]. All calculated values correspond to their respective experimental values of $Cs_2UO_2Cl_4$ single crystals [44b] and $[UO_2Cl_4]^{2-}$ in non-aqueous solution [52].

Table 5.8. Observed electronic transitions of $[UO_2Cl_4]^{2-}$ in acetonitrile at room temperature, assigned in $D_{\infty h}$ and D_{4h} symmetry. For an assignment of each peak in the spectrum, we refer to previous work [44b,52] and Appendix 3. Energies are given in wavenumber units (cm^{-1}). The frequency in the ground state of the U-Cl out-of-plane bending ν_{10} is approximately 100 cm^{-1}.

Symmetry		$Cs_2UO_2Cl_4$ [44b]		$[UO_2Cl_4]^{2-}$ acetone [52]	$[UO_2Cl_4]^{2-}$ acetonitrile	$[UO_2Cl_4]^{2-}$
$D_{\infty h}$	D_{4h}	Band origin	+ ν_{10}	Origin + ν_{10}	Origin + ν_{10}	CASPT2 [58]
$\Pi_g \leftarrow \Sigma_g^+$	$E_g \leftarrow A_{1g}$	20095	20200	20195	20208	20028
		20097				
$\Delta_g \leftarrow \Sigma_g^+$	$B_{2g} \leftarrow A_{1g}$	20406	20512	20575	20635	20330
$\Phi_g \leftarrow \Sigma_g^+$	$E_g \leftarrow A_{1g}$	22026	22135			21809
		22076				
$\Delta_g \leftarrow \Sigma_g^+$	$B_{2g} \leftarrow A_{1g}$	22750	(22850)	22840	22935	23228
$(\Phi_g, H_g) \leftarrow \Sigma_g^+$	$E_g \leftarrow A_{1g}$	26197	26365	26290	26388	26534
		26248				

The centrosymmetric D_{4h} coordination symmetry implies that the spectrum is purely vibronic in nature, which means that intensity can only be induced by coupling of vibrations with ungerade symmetry [44a]. The symmetric stretching vibration ν_s (a_{1g} in D_{4h}) of the uranyl ion itself is always superimposed on each vibronic transition. Besides this vibration with gerade symmetry, three ungerade, intensity inducing vibrations are coupled to the electronic transitions, namely the asymmetric stretching vibration ν_a (a_{2u}) and the degenerate bending vibration ν_b (e_u) of the axial oxygen atoms of the uranyl ion itself and mainly one vibration of the equatorial ligands, ν_{10}. The U-Cl out-of-plane bending ν_{10}, which has a b_{1u} symmetry in D_{4h}, transforms in the same way as the f_{xyz} orbital does (Figure 5.14). This U-Cl out-of-plane bending is coupled to the first electronic transition $\Pi_g \leftarrow \Sigma_g^+$ ($E_g \leftarrow A_{1g}$ in D_{4h}) and to one component of the transition $\Delta_g \leftarrow \Sigma_g^+$ ($B_{2g} \leftarrow A_{1g}$ in D_{4h}) [44b,52]. The spectrum of the uranyl tetrachloro complex $[UO_2Cl_4]^{2-}$ is dominated by electronic transitions arising from the $\sigma_u^+ \delta_u$ configuration.

The presence of a $[UO_2Cl_4]^{2-}$ species in acetonitrile, as determined by UV-Vis absorption and luminescence spectroscopy, is confirmed by uranium L_{III}-edge EXAFS spectroscopy. The uranium L_{III}-edge k^3-weighted EXAFS spectrum and the corresponding Fourier transform are shown in Figure 5.15 and the structural parameters of the standard EXAFS shell fitting including phase correction are summarized in Table 5.9.

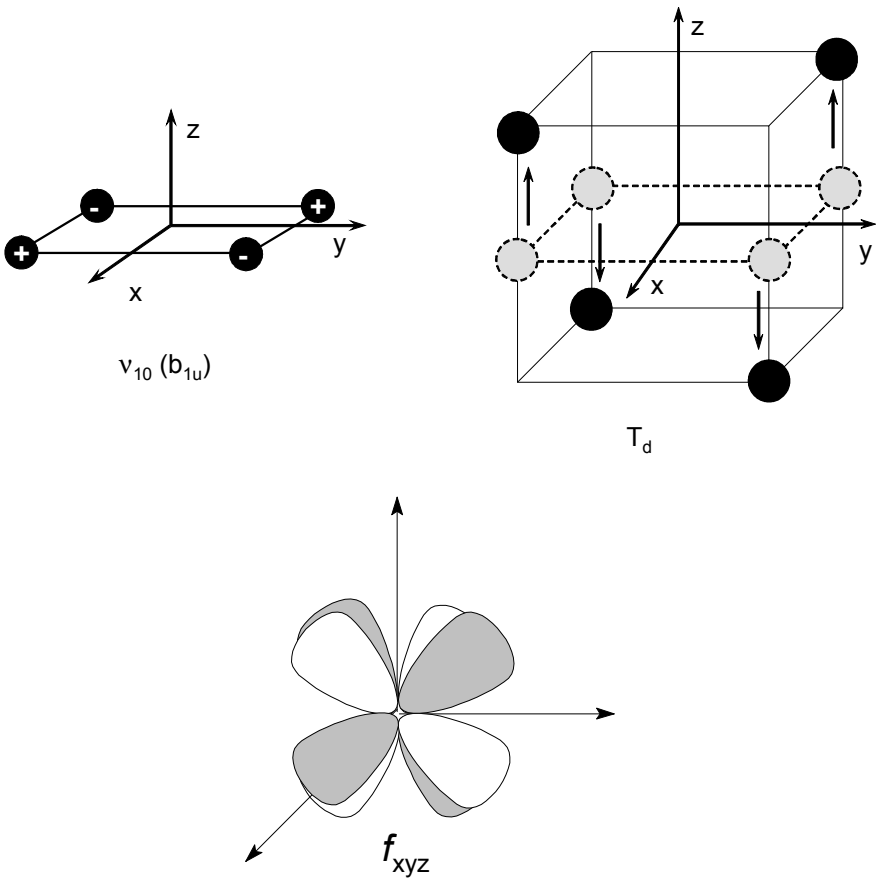

Figure 5.14. Symmetry of the vibration ν_{10} (U-Cl out-of-plane bending) and comparison with f_{xyz} [60].

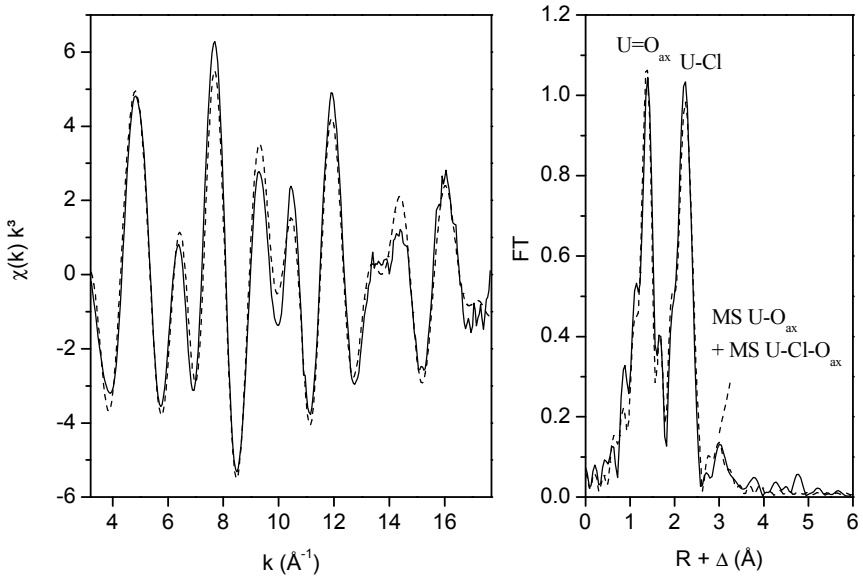

Figure 5.15. Uranium L_{III}-edge k^3-weighted EXAFS data (left) and corresponding Fourier transform (right), taken over k = 3.2 - 17.7 $Å^{-1}$, of $[UO_2Cl_4]^{2-}$ in acetonitrile. Experimental data are presented as a continuous line with the theoretical curve presented as a dashed line.

Table 4.9. EXAFS structural parameters of the $[UO_2Cl_4]^{2-}$ coordination polyhedron in acetonitrile.

	R (Å)	N	σ^2 (Å²)
U-O_{ax}	1.77	2.1	0.0014
MS U-O_{ax}	3.55	2.1	0.0029
U-Cl	2.68	4.0	0.0040
MS U-Cl-O_{ax}	3.82*	16*	0.0056

* value fixed during the fit procedure, error in distances R is ± 0.01 Å, error in coordination numbers N is ± 10%, ΔE = 0.8 eV.

The Fourier transform exhibits two significant peaks which arise from two axial oxygen atoms (O_{ax}) at 1.77 ± 0.01 Å and four equatorial

chloride atoms at 2.68 ± 0.01 Å. The determination of the coordination number by EXAFS spectroscopy may have a high error (10% of the value) due to its strong correlation with the Debye-Waller factor σ^2. However, the estimated coordination number of the chloride ligands is in good agreement with the UV-Vis results. It can be concluded that the uranyl ion is surrounded by four chloride ions in the equatorial plane in acetonitrile, as shown in Figure 5.16, when a metal-to-ligand ratio of 1:5 is reached.

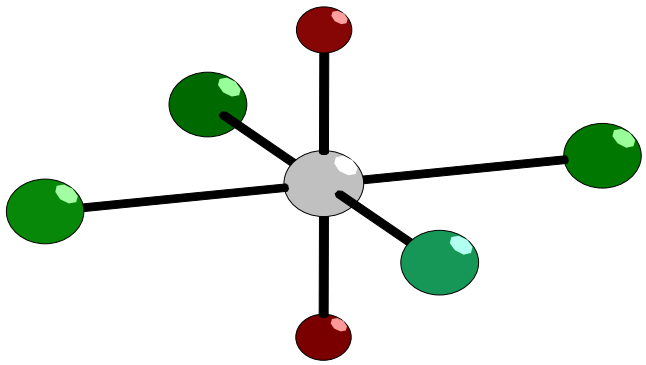

Figure 5.16. Structure of the $[UO_2Cl_4]^{2-}$ unit [24].

The bond lengths of $[UO_2Cl_4]^{2-}$ in non-aqueous solution correspond to the structural parameters previously obtained for the solid compound $Cs_2UO_2Cl_4$ [24]. Yet, the use of crystalline reference compounds is not always useful because distances can be influenced by interactions with the next neighbours, especially when the environment in a crystal is different from the environment in solution [61]. In this case, however, the $[UO_2Cl_4]^{2-}$ units are isolated in the crystal structure, resulting in comparable U-Cl bond lengths in the solid state and in solution.

The Fourier transform shows a weak peak between the main O_{ax} and Cl peaks and an asymmetry of the Cl shell. These features are completely described by only using a two-shell fit. These features can be

indicated as peak overlap effects with the side lobes of the main peaks, in a similar way as discussed for the $[UO_2(H_2O)_5]^{2+}$ hydrated ion (Figure 5.7). The peak overlap is here less intense because the U-Cl distance in $[UO_2Cl_4]^{2-}$ is larger than the U-O_{eq} distance in $[UO_2(H_2O)_5]^{2+}$.

In conclusion, UV-Vis absorption and luminescence spectroscopy as well as uranium L_{III}-edge EXAFS spectroscopy have given evidence for the complete replacement of solvent molecules by chloride ions in the first coordination sphere of the uranyl ion in acetonitrile, resulting in the limiting species $[UO_2Cl_4]^{2-}$.

4.3 Coordination with nitrate ions

The crystal structure of the uranyl trinitrato complex $[UO_2(NO_3)_3]^-$ is well-known [26,62,63]. The characteristic UV-Vis absorption spectrum of this uranyl complex was first presented over 50 years ago. In 1949, Dieke and Duncan were the first to record the absorption spectrum of a $CsUO_2(NO_3)_3$ crystal with a spectrograph [31,64]. They identified a *"fluorescent series"* and a *"magnetic series"* in the spectrum. The MCD spectrum of $[UO_2(NO_3)_3]^-$ at 4 K has been described by Brint and McCaffery [65,66]. The electronic transitions and vibrational progressions have been identified by Denning and coworkers by measuring σ- and π-spectra of $CsUO_2(NO_3)_3$ single crystals [67]. In 1950, Kaplan and coworkers observed the typical UV-Vis absorption spectrum of $[UO_2(NO_3)_3]^-$ in ketonic solvents like acetone, by adding tetrabutylammonium nitrate to a solution containing 2×10^{-2} mol L^{-1} of $UO_2(NO_3)_2$ [31]. They noticed a close agreement between the spectra in solution and those of $CsUO_2(NO_3)_3$ single crystals. In contrast, they did not find proof for nitrate coordination in aqueous solution [31].

EXAFS spectra of uranyl nitrato compounds are rather scarce. Thompson and coworkers investigated the uranyl trinitrato unit in $UO_2(NO_3)_2 \cdot 6H_2O$ in the solid state [68]. The uranyl nitrate dimer in solid

$Him_2[\{UO_2(\mu\text{-}OH)(NO_3)_2\}_2]$ (Him = imidazolium) was characterized by Barnes et al. [69]. Solvent extraction processes of uranyl nitrate solutions have been extensively studied, because of its significance for nuclear waste treatment [3,70-75]. These research activities included EXAFS measurements on uranyl nitrate in different tri-L-phosphate solvents (with L = butyl, methyl, phenyl, *iso*-butyl) indicating a coordination of two bidentate nitrate groups and two monodentate organophosphate ligands [75]. All these experimental data obtained to date now suffer from competing scattering contributions from uranium that cover the important multiple scattering features within the nitrate group. Pure uranyl nitrato species in aqueous or non-aqueous solutions have not been studied in depth by EXAFS spectroscopy yet.

4.3.1 Aqueous solution

The UV-Vis absorption and emission spectra of the uranyl ion in the presence of different concentrations of nitrate ions in aqueous solution are given in Figure 5.17 and Figure 5.18.

No significant complex formation of the uranyl ion with nitrate ions occurs in aqueous solution at low nitrate concentrations. The absorption spectra exhibit the same vibrational fine structure as the spectrum of the "free" uranyl ion. Moreover, no red or blue shift of the absorption peaks is observed. On the basis of this similarity between both spectra, one can state that the hydrated "free" uranyl ion is the dominant species in aqueous solution at low nitrate concentrations. The same conclusions can be drawn based on the emission spectra (Figure 5.18). The typical spectral features of the emission spectrum of the hydrated uranyl ion $[UO_2(H_2O)_5]^{2+}$ are detected at nitrate concentrations below 2.1 mol L^{-1}.

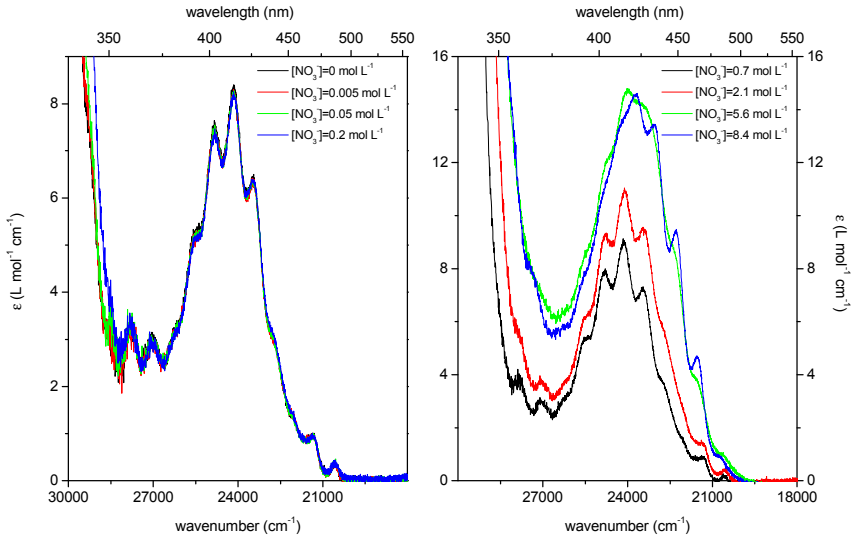

Figure 5.17. UV-Vis absorption spectra of the uranyl ion in the presence of different concentrations of nitrate ions in aqueous solution at room temperature. The uranyl concentration is 5×10^{-3} mol L^{-1}.

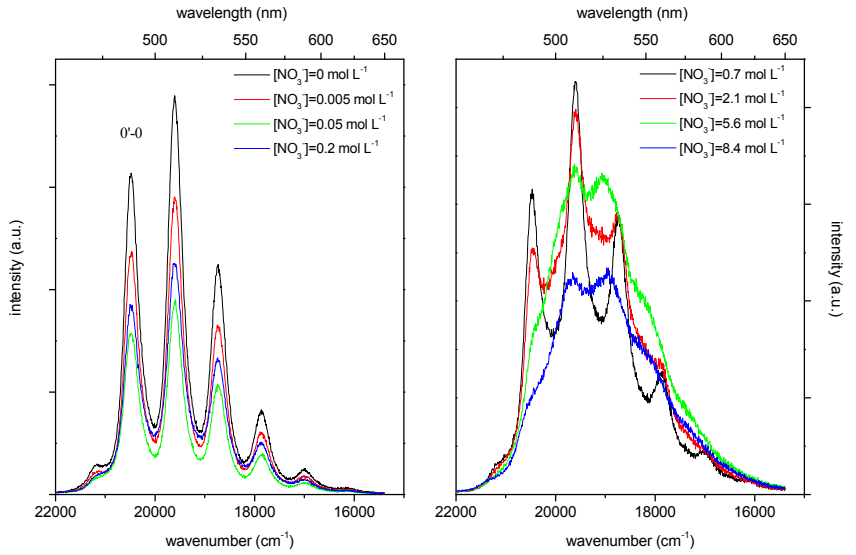

Figure 5.18. Emission spectra of the uranyl ion in the presence of different concentrations of nitrate ions in aqueous solution at room temperature. The uranyl concentration is 5×10^{-3} mol L^{-1}. The excitation wavelength is 414.3 nm (24137 cm^{-1}).

However, spectral changes are observed at higher nitrate concentrations, above 5.6 mol L^{-1} (Figure 5.17). At first, the UV-Vis absorption spectrum becomes a broad structureless band. By further raising the nitrate concentration, a vibrational fine structure appears which differs from the fine structure in the spectrum of the "free" uranyl ion, especially at the low energy side. The corresponding emission spectra reveal the same spectroscopic properties (Figure 5.18). The emission spectrum of the hydrated uranyl ion changes to a broad band with little vibrational fine structure. These changes in the UV-Vis absorption and emission spectra can be attributed to the formation of uranyl nitrato species in aqueous solution. However, high nitrate concentrations are required to remove the water molecules from the first coordination sphere of the uranyl ion, thereby replacing them by nitrate ions.

In comparison with the complex formation behaviour of UO_2^{2+} with chloride ions in aqueous solution, the coordination with nitrate ions is even weaker, as already indicated by the ligand affinity series [3]. Therefore, typical intense absorption maxima of uranyl nitrato complexes are absent. The uranyl-nitrate system in aqueous solution can be characterized by three formation constants: K_1 = 0.5 L mol^{-1}, K_2 = 1.0 L mol^{-1} and K_3 = 0.9 L mol^{-1} [3,54]. K_1 and K_2 were determined in a $NaClO_4$ medium at an ionic strength of μ = 1.0 mol L^{-1}, K_3 in media of varying HNO_3 concentrations. The weak complex formation in aqueous solution is demonstrated by calculating the species distribution using these formation constants. In an aqueous solution of the $UO_2(NO_3)_2 \cdot 6H_2O$ salt (5×10^{-2} mol L^{-1}, pH 2.4, metal-to-ligand ratio = 1:2), the species distribution is dominated by the hydrated uranyl ion $[UO_2(H_2O)_5]^{2+}$ (94.9%), whereas the distribution coefficients of the nitrato species are low (4.6% $[UO_2NO_3]^+$, 0.45% $UO_2(NO_3)_2$ and 0.04% $[UO_2(NO_3)_3]^-$). The low concentrated nitrato complexes can not be distinguished by UV-Vis absorption spectroscopy, giving no changes in vibrational fine structure. In a recent paper, Ruas and coworkers clearly

state that the equilibrium constants of the 1:1 and 1:2 nitrato complexes are so low, that the trinitrato complex can be neglected in a solution of $UO_2(NO_3)_2 \cdot 6H_2O$ in water [76]. For a nitrate concentration of 8.4 mol L^{-1} the spectroscopic changes are more pronounced, indicating a higher concentration of nitrato complexes formed.

Uranium L_{III}-edge EXAFS measurements were performed to provide further information on the coordination environment of the uranyl ion in the presence of nitrate ions in aqueous solution. The raw k^3-weighted EXAFS data of the uranyl ion with different concentrations of nitrate ions (0.1 mol L^{-1}, 0.2 mol L^{-1} and 2 mol L^{-1}) in aqueous solution are shown in Figure 5.19.

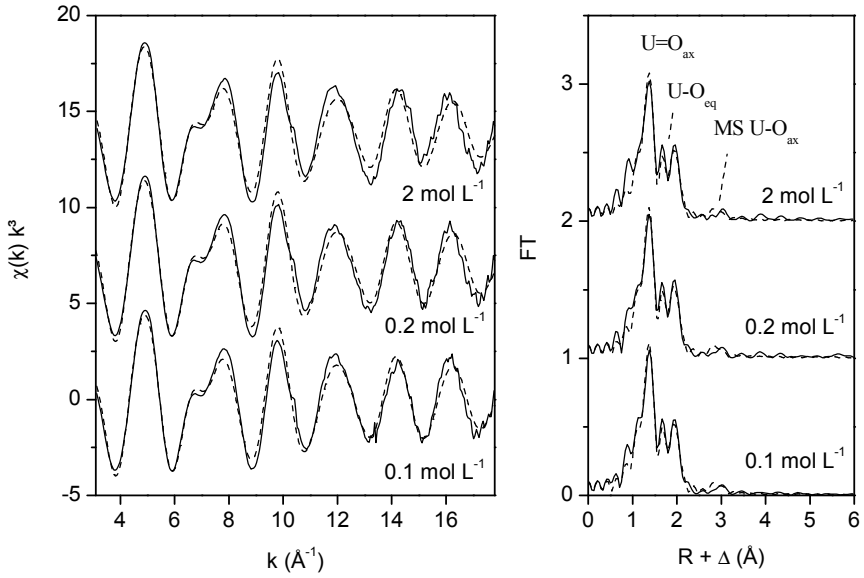

Figure 5.19. Uranium L_{III}-edge k^3-weighted EXAFS data (left) and the corresponding Fourier transforms (right), taken over k = 3.1 - 17.8 $Å^{-1}$, of the uranyl ion in the presence of different concentrations of nitrate ions in aqueous solution. Experimental data are presented as a continuous line with the theoretical curve presented as a dashed line.

Like the UV-Vis absorption spectra, we only notice the typical scattering features of the dominating hydrated uranyl ion in the EXAFS spectra. Especially the shoulder at k = 7 $Å^{-1}$ is characteristic for the aquo ion [34,35,39]. As already mentioned in the previous sections, the splitting of the O_{eq} shell can be explained by a superposition of the O_{ax} peak and the O_{eq} peak (Figure 5.7). The structural parameters of the EXAFS shell fitting including phase correction are listed in Table 5.10.

Table 5.10. EXAFS structural parameters of the uranyl ion in the presence of different concentrations of nitrate ions in aqueous solution.

0.1 mol L^{-1} NO_3^- in aqueous solution			
	R (Å)	N	σ^2 ($Å^2$)
U-O_{ax}	1.77	2.2	0.0015
MS U-O_{ax}	3.54	2.2	0.0030
U-O_{eq}	2.41	5.1	0.0071
0.2 mol L^{-1} NO_3^- in aqueous solution			
	R (Å)	N	σ^2 ($Å^2$)
U-O_{ax}	1.77	2.2	0.0015
MS U-O_{ax}	3.53	2.2	0.0031
U-O_{eq}	2.41	5.1	0.0069
2 mol L^{-1} NO_3^- in aqueous solution			
	R (Å)	N	σ^2 ($Å^2$)
U-O_{ax}	1.77	2.2	0.0017
MS U-O_{ax}	3.54	2.2	0.0034
U-O_{eq}	2.41	5.0	0.0068

Error in distances R is ± 0.01 Å, error in coordination numbers N is ± 10%, ΔE = 1.5 eV, 0.96 eV and 1.3 eV, respectively.

The same conclusions can be drawn for the three nitrate concentrations used. There are two axial oxygen atoms at 1.77 ± 0.01 Å and five equatorial oxygen atoms at 2.41 ± 0.01 Å. Indeed, a fivefold

coordination of the uranyl ion is characterized by a variation of the U-O_{eq} distance between 2.34 Å and 2.42 Å [46]. These values agree well with structural parameters previously obtained for the uranyl aquo ion in perchloric acid solution [34,35,39] and uranyl nitrate in aqueous solution [68]. No significant sign of nitrate coordination is detected because of the lack of sensitivity of EXAFS spectroscopy to low concentrated species.

4.3.2 Non-aqueous solvents[*]

In contrast to an aqueous solution, an organic solvent like acetonitrile supports the coordination of nitrate ions to the uranyl ion without competition of water molecules. Figure 5.20 contains the UV-Vis absorption and MCD spectra of uranyl nitrate $UO_2(NO_3)_2 \cdot 6H_2O$ with tetrabutylammonium nitrate in acetonitrile.

No further changes are observed by raising the nitrate concentration above a metal-to-ligand ratio of 1:4, which points to a maximum coordination of UO_2^{2+} with nitrate ions in the equatorial plane. The most striking feature in the UV-Vis absorption spectrum is the increase in intensity of four bands in the long-wavelength part (21000 cm^{-1} - 24000 cm^{-1}) with respect to the spectrum of the "free" uranyl ion in acetonitrile (Figure 5.8).

[*] Supporting material (see Appendix 3): absorption and MCD spectra and numerical data on $[UO_2(NO_3)_3]^-$ in acetonitrile.

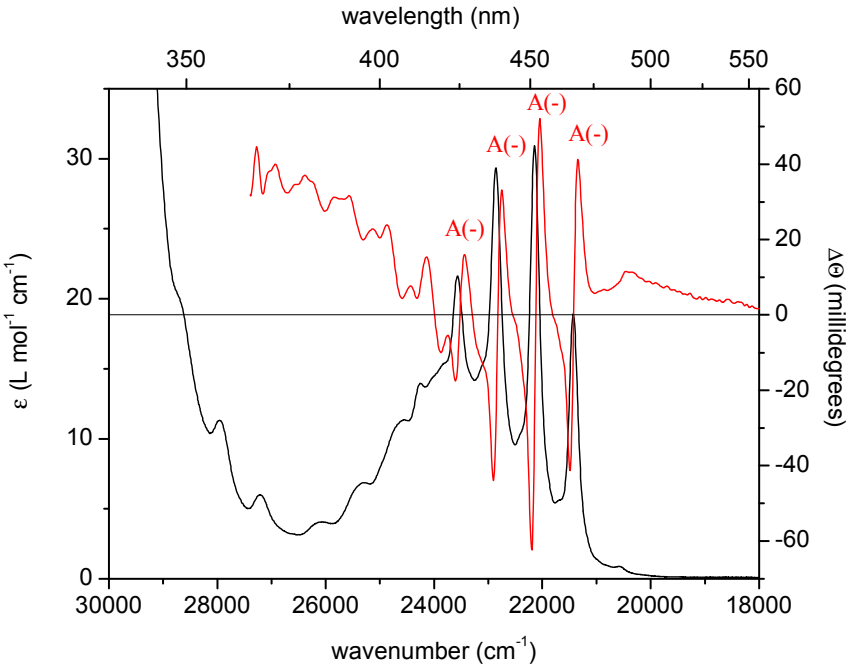

Figure 5.20. UV-Vis absorption (black line) and MCD spectra (red line) of $[UO_2(NO_3)_3]^-$ in acetonitrile at room temperature. The concentrations are $[UO_2^{2+}] = 5 \times 10^{-2}$ mol L^{-1} ($UO_2(NO_3)_2 \cdot 6H_2O$) and $[NO_3^-]_{tot} = 0.2$ mol L^{-1} (metal-to-ligand ratio = 1:4).

Dieke and Duncan were the first to discover these sharp peaks in the spectrum of $CsUO_2(NO_3)_3$ [64]. In earlier papers, these peaks at the low energy end of the spectrum were called the *"magnetic series"* [31]. In addition, the presence of this *"magnetic series"* in the spectrum of $[UO_2(NO_3)_3]^-$ has been confirmed by means of MCD measurements, performed by Brint and McCaffery [65]. These peaks give rise to very intense, negative A-terms in the MCD spectrum (Figure 5.20). Each negative A-term is accompanied by a positive A-term, which is reduced to only a shoulder in the spectrum in acetonitrile. These positive A-terms are much more pronounced in the MCD spectrum of $NBu_4UO_2(NO_3)_3$ in a PMMA matrix at 4 K [66]. Furthermore, the absorption peaks are

shifted by approximately 500 cm^{-1} to higher energies, which is typical for the coordination by nitrate ions [67a].

The emission spectrum of the uranyl trinitrato complex $[UO_2(NO_3)_3]^-$ is depicted in Figure 5.21. The ground state value of ν_s is approximately 872 cm^{-1}.

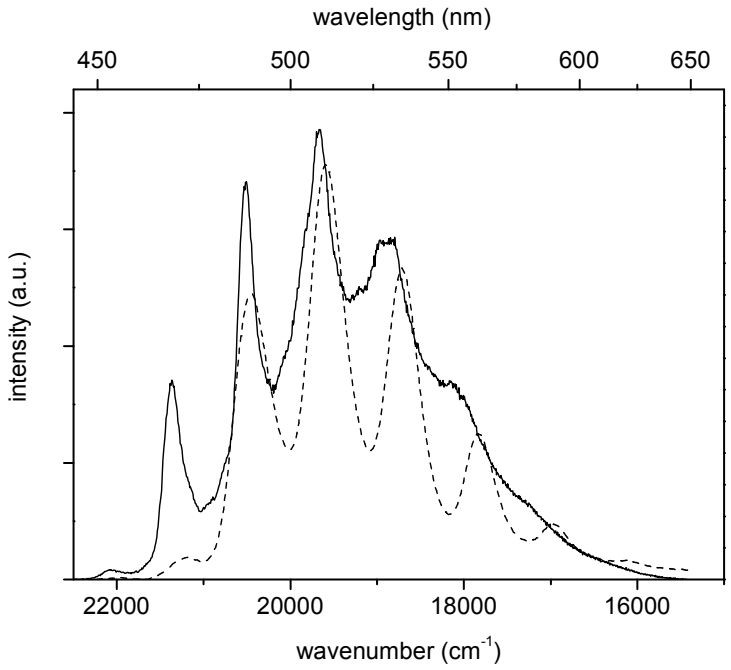

Figure 5.21. Emission spectrum of $[UO_2(NO_3)_3]^-$ in acetonitrile at room temperature. The concentrations are $[UO_2^{2+}] = 5 \times 10^{-3}$ mol L^{-1} and $[NO_3^-] = 2 \times 10^{-2}$ mol L^{-1} (metal-to-ligand ratio = 1:4). The excitation wavelength is 420 nm (23809 cm^{-1}).

The coordination symmetry as well as the electronic transitions in the UV-Vis absorption, MCD and luminescence spectra of $[UO_2(NO_3)_3]^-$ have been studied in detail by the groups of McCaffery [65], Denning [67] and Görller-Walrand [1,2a,66]. The transitions between the totally symmetric ground state Σ_g^+ and the excited states in the uranyl ion ($D_{\infty h}$)

are parity forbidden by the Laporte selection rule. However, the intensity is induced by the static ligand field in case of the trinitrato complex $[UO_2(NO_3)_3]^-$ (D_{3h}).

As demonstrated by the mirror-relationship between the first electronic transition in absorption (excitation) and the emission spectrum, only the first peak (20627 cm^{-1}) in the UV-Vis absorption spectrum originates from the first electronic transition E" ← A'$_1$ ($\Pi_g \leftarrow \Sigma_g^+$ in $D_{\infty h}$) (Figure 5.22). This electronic transition is magnetic dipole allowed in $\mathcal{R}_x$ and $\mathcal{R}_y$ in D_{3h} and has low intensity. Furthermore, no distinct MCD signal is observed for this transition (Figure 5.20).

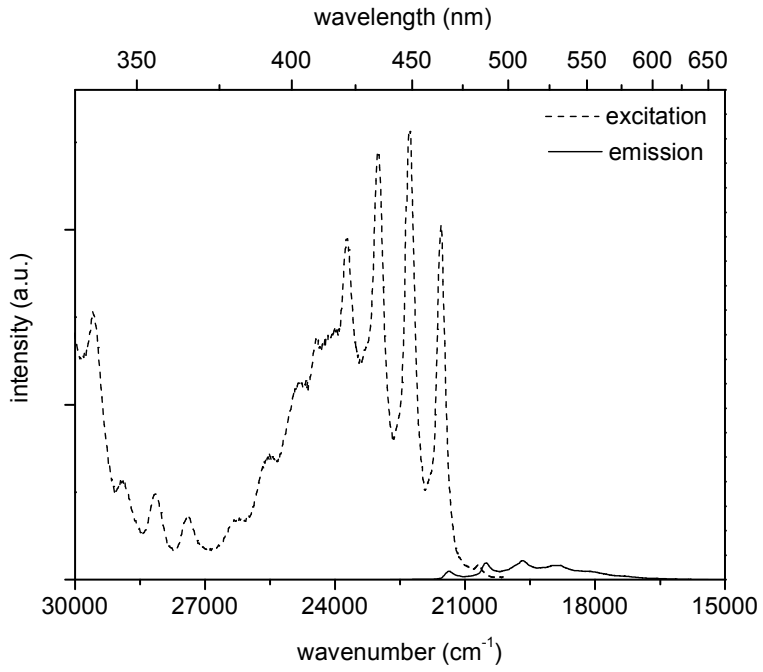

Figure 5.22. Excitation and emission spectra of $[UO_2(NO_3)_3]^-$ in acetonitrile at room temperature (metal-to-ligand ratio = 1:4). The excitation and emission wavelengths are 420 nm (23809 cm^{-1}) and 508.6 nm (19662 cm^{-1}), respectively.

On the other hand, the very sharp, intense peaks represent the electronic transition between the totally symmetric ground state A'_1 (Σ_g^+ in $D_{\infty h}$) and the excited state E' (Δ_g in $D_{\infty h}$). This transition is electronically allowed along the x- and y-axis, which induces intensity. In the MCD spectrum, this transition generates very intense, negative A-terms (Figure 5.20) [65,66]. A vibrational progression in the symmetric stretching vibration ν_s (σ_g^+) is observed in the UV-Vis absorption spectrum. Besides ν_s (σ_g^+), the bending vibration ν_b (π_u) is also superimposed on the transition E' ← A'_1. This coupling of the bending vibration ν_b to E' (Δ_g) results in positive A-terms in the MCD spectrum (Figure 5.20) [65,66]. The electronic states Δ_g and Γ_g ($D_{\infty h}$) transform in the same way in D_{3h} symmetry, namely as E' (x,y). Consequently, mixing occurs between these electronic states under influence of the equatorial ligand field. Table 5.11 summarizes the electronic transitions in the UV-Vis absorption spectrum of $[UO_2(NO_3)_3]^-$ in acetonitrile. For comparison, the energy values of $CsUO_2(NO_3)_3$ single crystals [67] and of $NBu_4UO_2(NO_3)_3$ in a PMMA matrix [66] as well as the calculated excitation energies of $[UO_2(NO_3)_3]^-$ [41] are also included. The calculated value of the oscillator strength for the transition $\Delta_g \leftarrow \Sigma_g^+$ (E' ← A'_1) is 10^{-8}, which exceeds the values found for the lower lying transition ($\Pi_g \leftarrow \Sigma_g^+$) and the transition observed at higher excitation energies ($\Phi_g \leftarrow \Sigma_g^+$). Nevertheless, this value (10^{-8}) of the oscillator strength is much lower than expected based on the experimentally observed intensities of the $\Delta_g \leftarrow \Sigma_g^+$ transition [41].

Table 5.11. Observed electronic transitions of $[UO_2(NO_3)_3]^-$ in acetonitrile at room temperature, assigned in $D_{\infty h}$ and D_{3h} symmetry. Energy values are compared with those of $CsUO_2(NO_3)_3$ single crystals [67], $NBu_4UO_2(NO_3)_3$ in a PMMA matrix [66] and with the calculated excitation energies (CASPT2) of $[UO_2(NO_3)_3]^-$ [41]. Energies are given in wavenumber units (cm^{-1}).

Symmetry		$[UO_2(NO_3)_3]^-$ acetonitrile	$CsUO_2(NO_3)_3$ single crystal [67]	$[UO_2(NO_3)_3]^-$ PMMA matrix [66]	$[UO_2(NO_3)_3]^-$ CASPT2 [41]
$D_{\infty h}$	D_{3h}				
$\Pi_g \leftarrow \Sigma_g^+$	$E'' \leftarrow A'_1$	20585	21090	20830	21335
$\Delta_g \leftarrow \Sigma_g^+$	$E' (x,y) \leftarrow A'_1$	21432	21694	21475	21808
$\Phi_g \leftarrow \Sigma_g^+$	$A''_1 \leftarrow A'_1$	--	22300	--	22383
$(\Delta_g, \Gamma_g) \leftarrow \Sigma_g^+$	$E' (x,y) \leftarrow A'_1$	--	23475	23337	24023
$\Phi_g \leftarrow \Sigma_g^+$	$A''_1 \leftarrow A'_1$	--	26640	--	26943
$\Phi_g \leftarrow \Sigma_g^+$	$A''_2 \leftarrow A'_1$	27218	27480	27210	28095

EXAFS measurements on a solution containing the uranyl dinitrate salt, $UO_2(NO_3)_2 \cdot 6H_2O$, with tetrabutylammonium nitrate added in acetonitrile were performed to confirm the formation of a $[UO_2(NO_3)_3]^-$ species, as indicated by UV-Vis absorption and MCD spectroscopy. The uranium L_{III}-edge EXAFS spectrum and the corresponding Fourier transform are given in Figure 5.23.

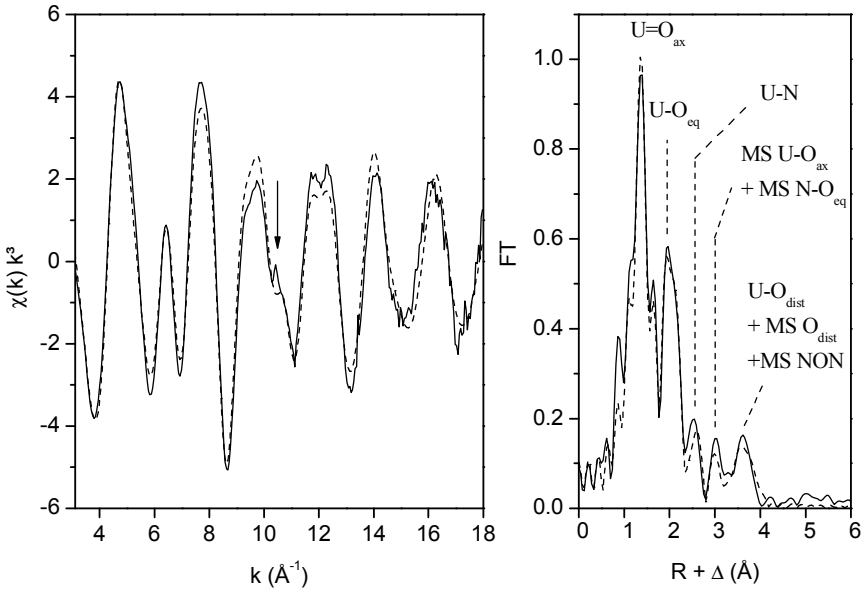

Figure 5.23. Uranium L_{III}-edge k^3-weighted EXAFS data (left) and corresponding Fourier transform, taken over k = 3.1 - 18 $Å^{-1}$, of $[UO_2(NO_3)_3]^-$ in acetonitrile. Experimental data are presented as a continuous line with the theoretical curve presented as a dashed line. The multiple scattering path N-O_{dist}-N is abbreviated as MS NON. The arrow indicates the [2p4f] double electron excitation [77].

The results of the shell fitting procedure including phase correction are listed in Table 5.12. The coordination numbers of the equatorial oxygen (O_{eq}) and nitrogen atoms were determined in an iterative manner, by a free fit. Subsequently, these coordination numbers were fixed during the shell fit procedure in order to avoid correlation problems

between N and σ^2. The coordination number of the distal oxygen atoms (O_{dist}) was set equal to the number of nitrogen atoms present.

Table 5.12. EXAFS structural parameters of $[UO_2(NO_3)_3]^-$ in acetonitrile.

	R (Å)	N	σ^2 (Å^2)
U-O_{ax}	1.77	2*	0.0012
MS U-O_{ax}	3.54	2*	0.0024
U-O_{eq}	2.48	6.4	0.0069
U-N	2.92	3.1	0.0032
MS N-O_{eq}	3.29	12.7	0.0031
U-O_{dist}	4.16	3.1	0.0061
MS O_{dist}	4.16	6.2	0.0061
MS N-O_{dist}-N	4.16	3.1	0.0061

* value fixed during the shell fit procedure, error in distances R is ± 0.01 Å, error in coordination numbers N is ± 10%, ΔE = 3.85 eV.

Like UV-Vis absorption spectroscopy, the fit results of the EXAFS data also reveal that three nitrate groups coordinate to the uranyl ion in a bidentate mode, as shown in Figure 5.2. The increase in the coordination number from N_{Oeq} = 5 in the hydrated uranyl ion formed in aqueous solution at low nitrate concentrations, to N_{Oeq} = 6 in the uranyl trinitrato complex is related with an increase of the U-O_{eq} bond length from 2.41 Å to 2.48 Å. The U-O_{eq} distance of 2.48 Å confirms the sixfold coordination of the uranyl ion. Indeed, a U-O_{eq} distance between 2.44 Å and 2.54 Å corresponds to a coordination number of six [46]. Furthermore, there is a weak peak from nitrogen backscattering at R + Δ = 2.55 Å in the Fourier transform indicating a U-N distance of 2.94 Å in the phase corrected fit procedure (Figure 5.23). This U-N distance points to a bidentate coordination of the nitrate groups and is in good agreement with the U-N distance in solid $RbUO_2(NO_3)_3$ (2.88 Å) [26].

The three coordinated nitrate ligands result in complex backscattering features, mainly originating from the linear arrangement of the nitrogen

and the distal oxygen atoms (O_{dist}) with respect to uranium. Indeed, the angle between U, N and O_{dist} in the crystal structure of $RbUO_2(NO_3)_3$ is 180° [26]. As mentioned in Chapter 3, the scattering amplitude is greatly enhanced in the forward scattering direction in case of a linear arrangement due to focusing of the electron wave to the next neighbour (focusing effect) [78]. This focusing effect makes the distal oxygen atoms O_{dist} at a large distance of 4.16 Å visible. This U-O_{dist} bond length corresponds well to the U-O_{dist} distance (4.09 Å) in solid $RbUO_2(NO_3)_3$ [26]. The amplitudes of the multiple scattering paths MS O_{dist} (U-N-O_{dist}) and MS U-N-O_{dist}-N are much more pronounced than that of the single scattering path U-O_{dist} due to this focusing effect. Indeed, the corresponding peak in the Fourier transform is only completely fitted by including both multiple scattering paths. The single scattering path alone has no significant contribution to the fit. A similar strong multiple scattering effect was observed for the tricarbonato species $Ca_2UO_2(CO_3)_3$ in aqueous solution, resulting in a U-O_{dist} distance of 4.22 Å [79].

4.3.3 Other complexes with D_{3h} symmetry

The presence of very sharp, intense peaks at the low energy side of the UV-Vis absorption spectrum is characteristic for complexes exhibiting a D_{3h} trigonal symmetry like $[UO_2(CO_3)_3]^{4-}$, $[UO_2(CH_3COO)_3]^-$ and complexes with carboxylic acids of the type $C_nH_{2n+1}COO^-$ [2,3,49,66,67]. Indeed, the UV-Vis absorption spectra of $[UO_2(CH_3COO)_3]^-$ and $[UO_2(CO_3)_3]^{4-}$ show the typical features of a D_{3h} coordination symmetry in the beginning of their spectrum between 21000 cm^{-1} and 24000 cm^{-1} (Figure 5.24). The uranyl triacetato complex is observed in acetone when a metal-to-ligand ratio of 1:4 is reached. In contrast to the very weak complex formation of the uranyl ion with nitrate ions in aqueous solution, the tricarbonato complex $[UO_2(CO_3)_3]^{4-}$ is already formed in a metal-to-ligand ratio of 1:4.

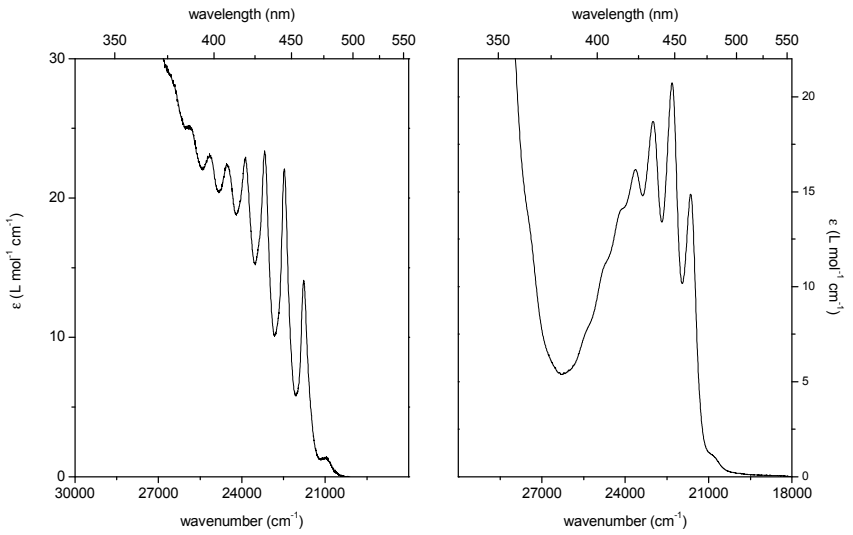

Figure 5.24. UV-Vis absorption spectra of $[UO_2(CH_3COO)_3]^-$ in acetone (left) and $[UO_2(CO_3)_3]^{4-}$ in aqueous solution (right). Metal-to-ligand ratio is 1:4 in both cases.

Also acetate ions can more easily form complexes with UO_2^{2+} in aqueous solution compared with chloride and nitrate ions. The UV-Vis absorption spectra for a metal-to-ligand ratio ranging from 1:0 to 1:4 are depicted in Figure 5.25. The UV-Vis absorption spectrum of the "free" uranyl ion changes into a structureless, intense band already at low acetate concentrations, whereas no spectral changes were observed in the presence of low concentrations of nitrate or chloride ions (Figures 5.10 and 5.17). At higher acetate concentrations, a further increase of the molar absorptivity is detected.

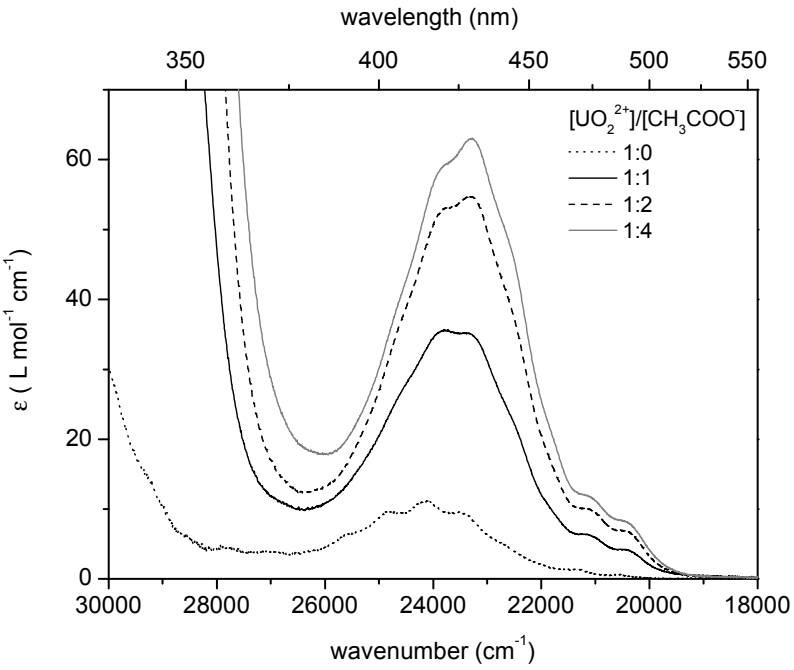

Figure 5.25. UV-Vis absorption spectra of uranyl complexes with acetate ions in aqueous solution. The uranyl concentration is 5×10^{-3} mol L^{-1}.

Typical stability constants for the complex formation with acetate ions in aqueous solution are $K_1 = 240$ L mol^{-1}, $K_2 = 95.5$ L mol^{-1} and $K_3 = 95.4$ L mol^{-1} [54]. Calculating the species distribution for an aqueous solution containing $UO_2(ClO_4)_2 \cdot xH_2O$ (5×10^{-3} mol L^{-1}) with sodium acetate added (2×10^{-2} mol L^{-1}) reveals that the uranyl acetato complexes are already the dominant species present (30.8% $[UO_2CH_3COO]^+$, 32% $UO_2(CH_3COO)_2$ and 34% $[UO_2(CH_3COO)_3]^-$), which explains the spectral changes in the UV-Vis absorption spectrum already at low acetate concentrations.

The uranium L_{III}-edge EXAFS spectrum and the corresponding Fourier transform of $[UO_2(CH_3COO)_3]^-$ in acetonitrile display the same structural features as the corresponding spectra of $[UO_2(NO_3)_3]^-$ in

acetonitrile (Figure 5.26). The structural parameters of the standard EXAFS shell fitting including phase correction are listed in Table 5.13.

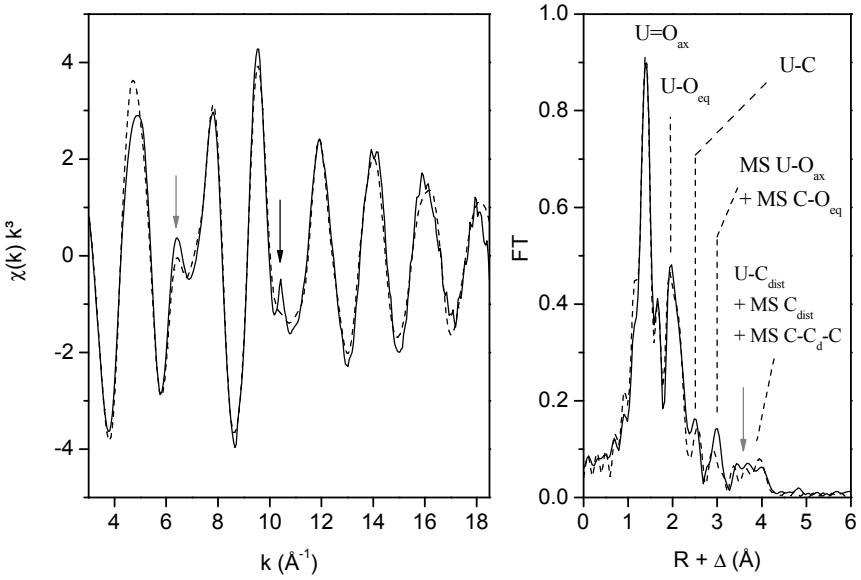

Figure 5.26. Uranium L_{III}-edge k^3-weighted EXAFS data (left) and corresponding Fourier transform (right), taken over k = 3 - 18.5 Å^{-1}, of $[UO_2(CH_3COO)_3]^-$ in acetonitrile. Experimental data are presented as a continuous line with the theoretical curve presented as a dashed line. The multiple scattering path C-C_{dist}-C is abbreviated as MS C-C_d-C. The black arrow indicates the [2p4f] double electron excitation [77]. The gray arrows indicate the characteristic features for bidentate coordinated carboxylate groups.

Three bidentate acetate ligands are coordinated to the uranyl ion in the equatorial plane according to the fit results. This is consistent with the trigonal D_{3h} symmetry, indicated by the typical spectroscopic features in the UV-Vis absorption spectrum (Figure 5.24). Moreover, the sixfold coordination of the uranyl ion is confirmed by the U-O_{eq} distance of 2.48 Å [46]. This U-O_{eq} distance reveals also a bidentate coordination of the acetate groups. Uranyl complexes with bidentate coordinated carboxylate

groups can be distinguished from their monodentate coordinated counterparts by their relatively long bond distances between uranium and the equatorial oxygen atoms [80]. The $U\text{-}O_{eq}$ bond length in $NaUO_2(CH_3COO)_3$ is 2.48 Å, whereas $UO_2[C_6H_5(COO)]_2$ with monodentate carboxylate groups is characterized by a $U\text{-}O_{eq}$ distance of 2.29 Å [81].

Table 5.13. EXAFS structural parameters of the $[UO_2(CH_3COO)_3]^-$ coordination polyhedron in acetonitrile.

	R (Å)	N	σ^2 (Å²)
$U\text{-}O_{ax}$	1.79	2*	0.0014
MS $U\text{-}O_{ax}$	3.58	2*	0.0029
$U\text{-}O_{eq}$	2.48	6	0.0072
U-C	2.88	3	0.0035
MS $C\text{-}O_{eq}$	3.31	11.9	0.0042
$U\text{-}C_{dist}$	4.37	3	0.0061
MS C_{dist}	4.37	6	0.0061
MS $C\text{-}C_{dist}\text{-}C$	4.37	6	0.0061

* value fixed during the shell fit procedure, error in distances R is ± 0.01 Å, error in coordination numbers N is ± 10%, ΔE = 4.1 eV.

In addition, the EXAFS spectrum and the Fourier transform exhibit a characteristic feature for bidentate carboxylate ions, indicated by the gray arrows in Figure 5.26 [81]. This peak in the Fourier transform represents the single and the multiple scattering paths of the distal carbon atoms C_{dist}. The linear arrangement in a bidentate coordinated acetate group makes the determination of the $U\text{-}C_{dist}$ distance of 4.37 Å possible (focusing effect). Indeed, the angle between U, C and C_{dist} in the crystal structure of $NaUO_2(CH_3COO)_3$ is close to linear (177°) [27]. In contrast, for monodentate coordinated carboxylate groups it is often impossible to detect even the presence of carbonyl carbon atoms. As mentioned for $[UO_2(NO_3)_3]^-$, the amplitudes of the multiple scattering paths MS C_{dist} and

MS C-C_{dist}-C are much more pronounced than of the corresponding single scattering path U-C_{dist}.

The structural parameters of $[UO_2(CH_3COO)_3]^-$ in acetonitrile, obtained by EXAFS spectroscopy, are in good agreement with crystal structure data of $NaUO_2(CH_3COO)_3$ [27] and previously determined EXAFS parameters for $NaUO_2(CH_3COO)_3$ [81] as well as for aqueous solutions of acetate species at different temperatures [82].

4.3.4 *Comparison of the bond distances in relation with the effective ligand charge and the value of ν_s*

The influence of the effective ligand charge on the bond lengths can be revealed by comparing the uranyl ion coordinated with nitrate, carbonate and acetate ions. The uranyl tricarbonato complex $[UO_2(CO_3)_3]^{4-}$ and the uranyl triacetato complex $[UO_2(CH_3COO)_3]^-$ are isostructural with the trinitrato complex $[UO_2(NO_3)_3]^-$. However, the U-O_{eq} distance of 2.44 Å in the uranyl tricarbonato complex [79] is shorter than the corresponding distance in the uranyl trinitrato and triacetato complexes (2.48 Å). Obviously, there is an influence of the U-O_{eq} electron density on the U-O_{ax} bond length resulting in a longer U-O_{ax} distance (1.81 Å) for the tricarbonato complex compared with a shorter one (1.77 Å) for the trinitrato complex. The correlation between the formal charge of the equatorial ligand atoms and the U-O_{ax} bond distance has already been studied by Denning [43]. If we assume that the nitrate ion is a covalent unit with a charge of -1/3 on each oxygen, the uranyl ion is exposed to an equatorial charge of -2 in $[UO_2(NO_3)_3]^-$. In the same way, one can calculate that the equatorial charges in $[UO_2(CH_3COO)_3]^-$ and $[UO_2(CO_3)_3]^{4-}$ are -3 and -4, respectively. The higher the equatorial charge, the longer the U-O_{ax} distance, which is in good agreement with

experimental data. Indeed, the longest U-O_{ax} distance is found for $[UO_2(CO_3)_3]^{4-}$ (1.81 Å) [79].

The lengthening of the U-O_{ax} bond distance with increasing effective ligand charge can be reconciled with the bonding scheme of the uranyl ion (Chapter 2, Figure 2.1). Increasing the charge in the equatorial field, with the U-O bond length frozen, raises the energy of the metal orbitals in relation to those on the oxygen atoms. In this way, the 5*f*-2*p* bonding interaction decreases, while the 6*p*-2*p* anti-bonding interaction increases. The U-O_{ax} bond will lengthen, as implied by the vibrational frequencies [43]. On the other hand, in a theoretical study on complexes of the type $[UO_2(H_2O)_m(OH)_n]^{2-n}$ (n + m = 5), the weakening of the U-O_{ax} bond distance is explained by a reduction of the ionic character, due to the decrease of the partial positive charge on uranium [83]. The higher effective ligand charge in the tricarbonato complex also induces a decrease of the partial positive charge on uranium, resulting in a larger U-O_{ax} distance.

The symmetric stretching vibration ν_s (σ_g^+) is always superimposed on the electronic transitions and has in the excited state a frequency of about 750 cm^{-1}. Small differences in its value are observed, depending on the chemical nature of the ligands. The frequencies of the symmetric and the asymmetric stretching vibrations of the uranyl ion in $[UO_2(NO_3)_3]^-$ are 884 cm^{-1} and 956 cm^{-1}, respectively [84,85]. For the uranyl tricarbonato complex $[UO_2(CO_3)_3]^{4-}$, the corresponding frequencies are 808 cm^{-1} and 856 cm^{-1} [84,85]. These values of both $[UO_2(NO_3)_3]^-$ and $[UO_2(CO_3)_3]^{4-}$ are in good agreement with the frequencies obtained by UV-Vis absorption and Raman spectroscopy as well as by theoretical calculations [2a,86]. In addition, the shorter U-O_{ax} distance for the uranyl trinitrato complex can be deduced from the ground state vibrational frequencies of the uranyl vibrations. Indeed, the U-O_{ax} bond distance can be related to the vibrational data through a version of Badger's rule [43,84]. A survey of 27 uranyl compounds on bond length correlations with either force constants or with symmetric or asymmetric stretching frequencies, gives

an overall relation between the symmetric stretching frequency and the bond lengths [43,85]:

$$R_{U-O} = \left(10650 \cdot \nu^{-2/3}\right) + 57.5 \qquad (4.1)$$

$R_{U\text{-}O}$ is given in pm and the frequency is expressed in cm^{-1}. Using this relation, we can calculate the U-O_{ax} bond distance in $[UO_2(NO_3)_3]^-$ (1.73 Å) to be smaller than in the uranyl tricarbonato complex $[UO_2(CO_3)_3]^{4-}$ (1.80 Å). The U-O_{ax} bond distance in the triacetato complex $[UO_2(CH_3COO)_3]^-$, obtained by uranium L_{III}-edge EXAFS spectroscopy, is 1.79 Å, situated between the U-O_{ax} bond length in $[UO_2(NO_3)_3]^-$ and $[UO_2(CO_3)_3]^{4-}$. This implies according to Badger's rule that the ground state frequency of the symmetric stretching vibration for $[UO_2(CH_3COO)_3]^-$ is smaller than for $[UO_2(CO_3)_3]^-$, but larger than for $[UO_2(NO_3)_3]^-$. Actually, the frequencies of the symmetric and asymmetric stretching vibrations for $[UO_2(CH_3COO)_3]^-$ are 842.2 cm^{-1} and 920 cm^{-1}, respectively [84].

4.4 Coordination with the crown ether 18-crown-6

The study of crown ether complexes has always been an important research topic since Pederson was the first to synthesize these multidentate ligands in 1967 [87]. In the beginning, one was only interested in alkali, alkaline earth and transition metal complexes. Using UV-Vis absorption spectroscopy, NMR spectroscopy and conductometry, insight was gained in the thermodynamic and the kinetic properties of these complexes. A decade later, research on lanthanide and actinide complexes started. Different types of crown ethers with or without side groups (dibenzo-18-crown-6, dibenzo-24-crown-8, dicyclohexano-18-crown-6, etc.) are used in solvent extraction processes to separate

mixtures of actinides and rare earths [70]. Polymeric sorbents containing crown ethers in their chains have been used to extract metals from natural waters and uranium from seawater [70]. Nowadays, studies are performed in an attempt to modify the classical solvent extraction procedures for metal ions by using room temperature ionic liquids with crown ethers as extracting agents [88-90].

Study of the complex formation of the uranyl ion with crown ethers mainly occurred in the solid state. The crystal structure of several crown ether complexes has been determined by X-ray diffraction. Outer-sphere as well as inner-sphere complexes have been described in the literature [28,91-97]. Conversely, studies in solution are scarce. A lot of research on uranyl crown ether complexes in solution was for a long time limited to empirical data on the extraction of the uranyl ion from aqueous solution by crown ethers, dissolved in organic solvents [98,99]. Thereby, only the metal-to-crown ether ratio seemed relevant to predict the structure of the formed complexes. The possibility to include the uranyl ion in the cavity of a crown ether of appropriate size has been found in the solid state [28,95b,97]. In contrast, the inclusion of the uranyl ion in solution is in competition with the solvation of the ligand cavity and the solvation of UO_2^{2+} itself. Moreover, the inclusion of a metal ion into the ring strongly depends on the solvent used. In the 1980's, Lagrange and coworkers pioneered the study of the complex formation of uranyl with oxacrown ethers and azacrown ethers in water, acetonitrile and propylene carbonate [100]. Inclusion complexes of the uranyl ion with the crown ethers of appropriate size (18-crown-6, dicyclohexano-18-crown-6, dibenzo-18-crown-6) are reported in acetonitrile and propylene carbonate, whereas water suppresses the formation of inclusion complexes. Outer-sphere complexes of the uranyl ion with a variety of crown ethers are formed in aqueous solution. The uranyl ion is surrounded by water molecules, with the crown ethers in the second coordination sphere. The crown ethers are coordinated with UO_2^{2+} through hydrogen bonds [100].

De Houwer et al. have studied the complex formation of the uranyl ion with different types of crown ethers in acetonitrile and propylene carbonate by UV-Vis absorption, luminescence and where possible MCD spectroscopy [101]. In this section, the spectroscopic properties of the $[UO_2(18\text{-crown-}6)]^{2+}$ complex are complemented by structural data obtained by uranium L_{III}-edge EXAFS spectroscopy.

A limited number of EXAFS measurements on uranyl crown ether complexes can be found in the literature. An EXAFS study on the complex $[UO_2(18\text{-crown-}6)](ClO_4)_2$ has given evidence for the inclusion of the uranyl ion in the crown ether cavity in the solid state [22]. Furthermore, a partial de-insertion of uranyl in acetonitrile has been demonstrated [22]. A comparative study of uranyl-triflate-crown systems carried out in aqueous solution and acetonitrile by uranium L_{III}-edge EXAFS spectroscopy, revealed that an inclusion complex $[UO_2(18\text{-crown-}6)]^{2+}$ is formed in acetonitrile. Nevertheless, in aqueous solution the uranyl ion is surrounded by five water molecules and does not coordinate to 18-crown-6 in the first coordination sphere (outer-sphere complex) [28].

*4.4.1 Non-aqueous solvents**

The formation of inclusion complexes with macrocyclic ligands depends on the solvating power of the solvent used as well as on the compatibility of the crown ether cavity with the size of the ion [87]. The solvating power of acetonitrile is low. In addition, acetonitrile promotes the inclusion of the uranyl ion in the crown ether ring due to its high dielectric constant ($\varepsilon_R = 36$) [101b]. If the ring cavity is well adjusted to

* Supporting material (see Appendix 3): absorption, MCD and luminescence spectra and numerical data on $[UO_2(18\text{-crown-}6)]^{2+}$ in acetonitrile.

the diameter of the metal ion and competitive reactions are of minor importance, the cation may be inserted into the ring.

The UV-Vis absorption spectrum of the uranyl ion in the presence of the crown ether 18-crown-6 in acetonitrile exhibits a remarkable vibrational fine structure (Figure 5.27).

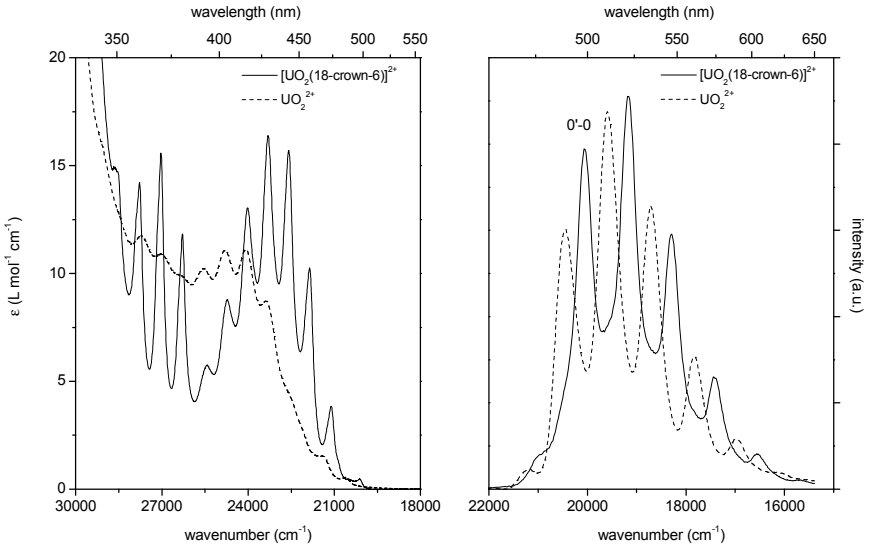

Figure 5.27. UV-Vis absorption (left) and emission (right) spectra of UO_2^{2+} (dashed line) and $[UO_2(18\text{-crown-6})]^{2+}$ (solid line) in acetonitrile at room temperature. The uranyl concentration is 5×10^{-2} mol L^{-1}. The metal-to-ligand ratio is 1:2. The excitation wavelength is 420 nm (23809 cm^{-1}).

The intense absorption peaks are shifted to lower energies by approximately 1500 cm^{-1} with respect to those of the "free" uranyl ion in acetonitrile. A change in the peak maxima is also observed in the emission spectrum (~ 410 cm^{-1}) (Figure 5.27). All these spectroscopic features including the remarkable vibrational fine structure point to a high coordination symmetry of the uranyl ion. Consequently, the inclusion complex $[UO_2(18\text{-crown-6})]^{2+}$ is formed in acetonitrile. Indeed, the

cavity of the considered crown ether (2.6 - 3.2 Å) matches perfectly with the ionic diameter of uranium(VI), 2.8 Å [100a].

The symmetric stretching vibration ν_s has a value of approximately 756 cm^{-1} in the excited state. This value is derived from the region 21500 cm^{-1} - 25000 cm^{-1}, where the anharmonicity of the uranyl ion is clearly demonstrated. A vibrational progression in ν_s also appears in the emission spectrum. The frequency of the symmetrical stretching vibration ν_s in the ground state is approximately 889 cm^{-1}. The interval between the peaks belonging to the first electronic transition in the emission spectrum decreases due to the anharmonicity of the uranyl ion: 889 cm^{-1}, 884 cm^{-1}, 854 cm^{-1}. These values are higher than for one of the excited states, due to the longer bond length in the excited states [43]. The small peak in the beginning of the emission spectrum can be assigned as a hot band.

Studies on the electronic transitions of $[UO_2(18\text{-crown-}6)]^{2+}$ in acetonitrile and propylene carbonate have been performed by means of UV-Vis absorption, luminescence and MCD spectroscopy by De Houwer et al. [101a]. The uranyl ion in the inclusion complex $[UO_2(18\text{-crown-}6)]^{2+}$ is surrounded by six oxygen atoms in the equatorial plane. Therefore, one would suggest a D_{6h} coordination symmetry. All electronic transitions are parity forbidden by the Laporte selection rule in the centrosymmetric D_{6h} symmetry group, which does not coincide with the intense absorption peaks in the spectrum. Yet, the crown ether 18-crown-6 is not a planar molecule. The structure of the ligand is defined by the torsion angles (O-C-C-O) of +60° and -60° [70,95-97]. These torsion angles are denominated as gauche$^+$ (g^+) and gauche$^-$ (g^-), respectively (Figure 5.28). The most commonly observed conformation of metal 18-crown-6 complexes is $g^+g^-g^+g^-g^+g^-$ (Figure 5.28). This implies a reduction of the symmetry around the uranyl ion from D_{6h} to D_{3d}. However, no electronic transitions are allowed in D_{3d} symmetry either: they are all parity forbidden. A distortion of the ideal D_{3d} symmetry, twisting the upper plane of the coordinating oxygen atoms

with respect to the lower plane of oxygen atoms, lifts the inversion centre and reduces the coordination symmetry to D_3 [101a].

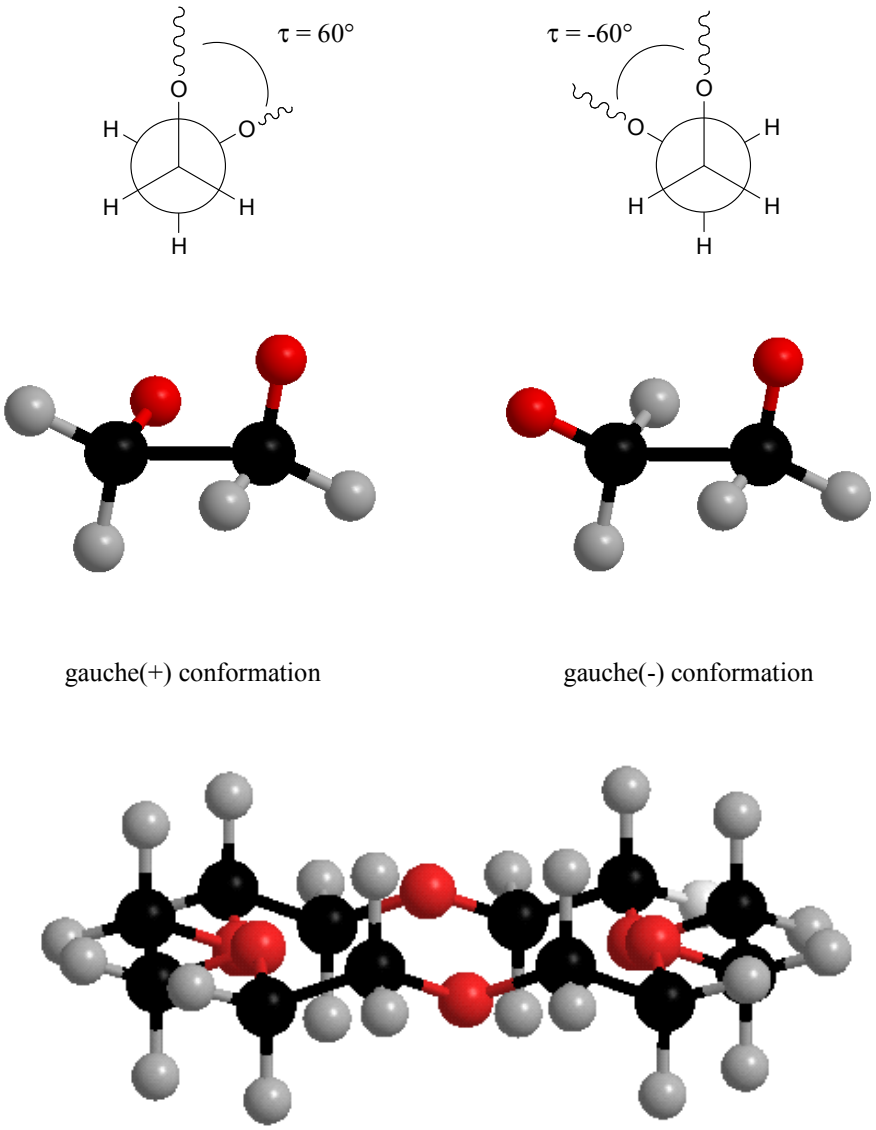

Figure 5.28. Difference between a gauche(+) and a gauche(-) conformation (upper part) and the crown ether 18-crown-6 exhibiting a $g^+g^-g^+g^-g^+g^-$ conformation (lower part).

Only the first peak in the UV-Vis absorption spectrum originates from the first electronic transition $\Pi_g \leftarrow \Sigma_g^+$, as demonstrated by the mirror-relationship between the first electronic transition in absorption and the emission spectrum (Figure 5.29). This $\Pi_g \leftarrow \Sigma_g^+$ transition is not allowed in D_{3d}, resulting in the low molar absorptivity of this peak in the spectrum.

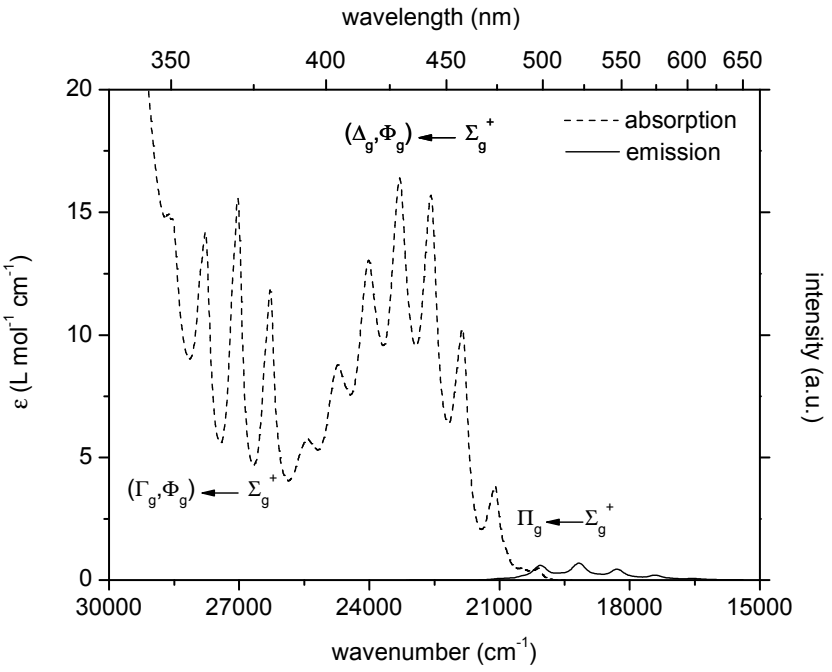

Figure 5.29. UV-Vis absorption and emission spectra of $[UO_2(18\text{-crown-6})]^{2+}$ in acetonitrile at room temperature. The uranyl concentration is 5×10^{-2} mol L^{-1}. The excitation wavelength is 420 nm (23809 cm^{-1}).

The special features at the high energy end of the spectrum can only be attributed to the transition $\Gamma_g \leftarrow \Sigma_g^+$. In the corresponding part of the MCD spectrum, positive A-terms are observed. This transition to the Γ_g ($^3\Phi_g$) electronic excited state is very characteristic for a D_3 coordination symmetry. The transition $\Gamma_g \leftarrow \Sigma_g^+$ arises from the $\sigma_u^+ \phi_u$ configuration

[101a]. In D_{3d} (D_3) symmetry, the doubly degenerate Φ_g electronic state is split into the non-degenerate A_{1g} (A_1) and A_{2g} (A_2) states. The transition to the latter is electronically allowed in D_3 in z-polarization. Molecules are randomly oriented in solution. So, theoretically one third of the molecules in solution are directed with their trigonal axis along the x-axis, one third along the y-axis and one third along the z-axis, allowing this transition. The corresponding MCD signals for this transition are positive B-terms [101a]. An identification of the electronic transitions of $[UO_2(18\text{-crown-6})]^{2+}$ in $D_{\infty h}$, D_{3d}, D_3 symmetry is given in Table 5.14.

Table 5.14. Observed electronic transitions of $[UO_2(18\text{-crown-6})]^{2+}$ in acetonitrile at room temperature, assigned in $D_{\infty h}$, D_{3d} and D_3 coordination symmetry [101a]. Energies are given in wavenumber units (cm^{-1}).

Symmetry			ν / cm^{-1}
$D_{\infty h}$	D_{3d}	D_3	
$\Pi_g \leftarrow \Sigma_g^+$	$E_g \leftarrow A_{1g}$	$E\ (x,y) \leftarrow A_1$	20109
$\Phi_g \leftarrow \Sigma_g^+$	$A_{1g} \leftarrow A_{1g}$	$A_1 \leftarrow A_1$	--
	$A_{2g} \leftarrow A_{1g}$	$A_2\ (z) \leftarrow A_1$	21101
$\Delta_g \leftarrow \Sigma_g^+$	$E_g \leftarrow A_{1g}$	$E\ (x,y) \leftarrow A_1$	22578
$\Phi_g \leftarrow \Sigma_g^+$	$A_{1g} \leftarrow A_{1g}$	$A_1 \leftarrow A_1$	--
	$A_{2g} \leftarrow A_{1g}$	$A_2\ (z) \leftarrow A_1$	23299
$\Gamma_g \leftarrow \Sigma_g^+$	$E_g \leftarrow A_{1g}$	$E\ (x,y) \leftarrow A_1$	25432
$\Phi_g \leftarrow \Sigma_g^+$	$A_{1g} \leftarrow A_{1g}$	$A_1 \leftarrow A_1$	--
	$A_{2g} \leftarrow A_{1g}$	$A_2\ (z) \leftarrow A_1$	25981

It is obvious that the ϕ_u orbital has a strong effect on the spectra of uranyl crown ether complexes. The spectra clearly exhibit different phenomenological features with respect to those of the uranyl ion itself and the more equatorial planar $CsUO_2(NO_3)_3$ (D_{3h} symmetry) [101a].

EXAFS measurements have been carried out to confirm the inclusion of the uranyl ion in the crown ether cavity, as stated by UV-Vis absorption spectroscopy. The raw k^3-weighted uranium L_{III}-edge EXAFS data and the corresponding Fourier transform are shown in Figure 5.30.

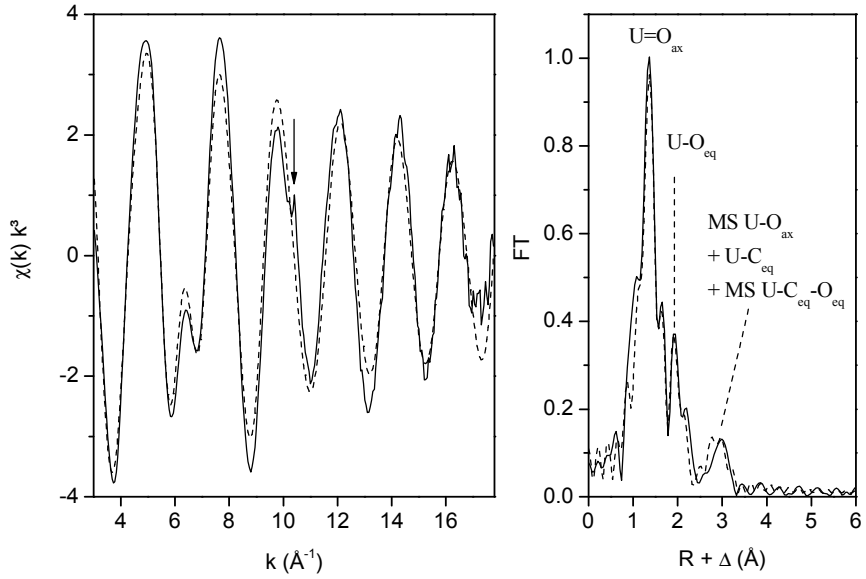

Figure 5.30. Uranium L_{III}-edge k^3-weighted EXAFS spectrum (left) and corresponding Fourier transform (right), taken over k = 3 - 17.8 $Å^{-1}$, of $[UO_2(18\text{-crown-}6)]^{2+}$ in acetonitrile. Experimental data are presented as a continuous line with the theoretical curve presented as a dashed line. The arrow indicates the [2p4f] double electron excitation [77].

As discussed for the previous EXAFS spectra, the largest peak in the Fourier transform represents the scattering contribution of the two axial oxygen atoms O_{ax}. This peak is embedded in artificial peaks (side lobes) as a result of the limited k-range. The peak at R + Δ = 1.9 Å originates from the equatorial oxygen shell. The peak at R + Δ = 3 Å comprises the four-legged multiple scattering path of the axial oxygen atoms and the scattering contribution of the equatorial carbon shell. This peak can only

be completely fitted by including the three-legged multiple scattering path U-C_{eq}-O_{eq}. The structural parameters of the EXAFS shell fit procedure including phase correction are summarized in Table 5.15. The coordination numbers of the equatorial oxygen and carbon atoms, O_{eq} and C_{eq}, are determined in an iterative manner, by a free fit.

Table 5.15. EXAFS structural parameters of $[UO_2(18\text{-crown-6})]^{2+}$ in acetonitrile.

	R (Å)	N	σ^2 (Å²)
U-O_{ax}	1.76	2*	0.0013
MS U-O_{ax}	3.52	2*	0.0026
U-O_{eq}	2.46	6.3	0.0121
U-C_{eq}	3.51	12.6	0.0134
MS U-C_{eq}-O_{eq}	3.72	23.1	0.0171

* value fixed during the shell fit procedure, error in distances R is ± 0.01 Å, error in coordination numbers N is ± 10%, ΔE = 3.7 eV.

The fit results indicate that the uranyl ion perfectly fits in the cavity of the crown ether, because it is surrounded by six oxygen atoms in the equatorial plane. In addition, the U-O_{eq} distance of 2.46 Å confirms the sixfold coordination. For a sixfold coordination of the uranyl ion, the U-O_{eq} distance ranges from 2.44 Å to 2.54 Å [46]. EXAFS spectroscopy reveals that the inclusion complex $[UO_2(18\text{-crown-6})]^{2+}$ is formed in acetonitrile. Furthermore, the EXAFS spectrum shows equatorial carbon atoms at 3.51 Å. Usually, carbon atoms at this distance are not detectable, but they are visible in this spectrum due to their high coordination number of twelve. If the uranyl ion was not introduced in the crown ether ring, we would not be able to identify this U-C_{eq} distance.

We remark that the Debye-Waller factors σ^2 of the O_{eq} and C_{eq} shells are quite high, compared to the Debye-Waller factor σ^2 of the equatorial shell in complexes with a similar high symmetry, e.g. $[UO_2(NO_3)_3]^-$ (σ^2 = 0.0069 Å²) and $[UO_2(CH_3COO)_3]^-$ (σ^2 = 0.0072 Å²) in acetonitrile. These

high values result from the variety of the U-O_{eq} and U-C_{eq} bond distances in the structure of $[UO_2(18\text{-crown-6})]^{2+}$. As expected from the Debye-Waller factors in acetonitrile solution, the crystal structure of $[UO_2(18\text{-crown-6})]^{2+}$ shows structural distortions, where the U-O_{eq} bond length varies between 2.44 Å and 2.55 Å, while the U-C_{eq} bond distance ranges from 3.34 Å to 3.61 Å [28]. However, the average value of the U-O_{eq} and U-C_{eq} bond distances corresponds well within the error limits to the bond lengths obtained by EXAFS spectroscopy in acetonitrile: 2.49 Å versus 2.46 Å for the U-O_{eq} distance and 3.48 Å versus 3.51 Å for the U-C_{eq} bond length. The high Debye-Waller factor of the multiple scattering path U-C_{eq}-O_{eq} can also be attributed to the variety of bond distances in the crystal structure.

It is interesting to note that the U-O_{ax} bond distance in acetonitrile solution (1.76 Å) is much longer compared with the value in the crystal structure of $[UO_2(18\text{-crown-6})]^{2+}$ (1.64 Å) [28]. This phenomenon can be explained by the possible interaction between the axial oxygen atoms and acetonitrile solvent molecules, resulting in a weakening of the U-O_{ax} bond and consequently, a longer bond distance in solution [102].

5 Conclusions

From this chapter, it is obvious that the combination UV-Vis absorption spectroscopy, luminescence spectroscopy and uranium L_{III}-edge EXAFS spectroscopy is an excellent tool for studying uranyl coordination complexes in solution. These techniques unambiguously point to the existence of a $[UO_2(H_2O)_5]^{2+}$ species in aqueous solution and the formation of a $[UO_2Cl_4]^{2-}$, $[UO_2(NO_3)_3]^-$, $[UO_2(CH_3COO)_3]^-$ and $[UO_2(18\text{-crown-6})]^{2+}$ limiting species in non-aqueous solvents.

- ✓ Weak complex formation of the uranyl ion with chloride and nitrate ions is observed in aqueous solution, as confirmed by the absence of spectral changes in the UV-Vis absorption spectra with respect to the

spectrum of the "free" uranyl ion, species distribution calculations and EXAFS spectroscopy. In contrast, the uranyl ion forms more easily complexes with acetate and carbonate ions in aqueous solution, as demonstrated by UV-Vis absorption spectroscopy.

- ✓ The maximum coordination of the uranyl ion with chloride ions in non-aqueous solution is four. The UV-Vis absorption spectrum of $[UO_2Cl_4]^{2-}$ is purely vibronic in nature due to the centrosymmetric D_{4h} coordination symmetry. Intensity is induced by coupling of ungerade vibrations: the asymmetric stretching ν_a (a_{2u}) and bending ν_b (e_u) vibrations of the uranyl ion itself and especially the U-Cl out-of-plane bending ν_{10} (b_{1u}). The latter is coupled to the first electronic transition $\Pi_g \leftarrow \Sigma_g^+$ ($E_g \leftarrow A_{1g}$) and to one component of the transition $\Delta_g \leftarrow \Sigma_g^+$ ($B_{2g} \leftarrow A_{1g}$). The spectrum is dominated by transitions arising from the $\sigma_u^+\delta_u$ configuration. Furthermore, there is a good agreement between the excitation energies obtained by spectroscopic measurements on $Cs_2UO_2Cl_4$ single crystals [44b] and $[UO_2Cl_4]^{2-}$ in solution and by theoretical calculations [58]. The $[UO_2Cl_4]^{2-}$ polyhedron consists of two axial oxygen atoms at 1.77 Å and four chloride ligands at 2.68 Å.
- ✓ In D_{3h} coordination symmetry, intensity is induced by the static ligand field. The very sharp, intense peaks at the low energy side (21000 cm^{-1} - 24000 cm^{-1}) of the UV-Vis absorption spectrum of $[UO_2(NO_3)_3]^-$ are characteristic for a trigonal symmetry (D_{3h}). The corresponding signals in MCD are intense negative A-terms. These intense peaks originate from the electronic transition $\Delta_g \leftarrow \Sigma_g^+$ ($E' \leftarrow A'_1$). In contrast, the first electronic transition $\Pi_g \leftarrow \Sigma_g^+$ ($E'' \leftarrow A'_1$) has low intensity. Besides the symmetric stretching vibration ν_s, the bending vibration is also superimposed on the electronic transitions. The trigonal symmetry of $[UO_2(NO_3)_3]^-$ is confirmed by uranium L_{III}-edge EXAFS spectroscopy. Three bidentate nitrate groups are coordinated to the uranyl ion with a U-O_{eq} distance of 2.48 Å. The

linear arrangement of the nitrate groups offers the possibility of the identification of the distal oxygen atoms at a large distance of 4.16 Å.

- ✓ $[UO_2(CH_3COO)_3]^-$ and $[UO_2(CO_3)_3]^{4-}$ also exhibit a trigonal D_{3h} coordination symmetry, as is obvious from UV-Vis absorption spectroscopy and EXAFS measurements. The UV-Vis absorption spectra are characterized by very sharp, intense peaks. The EXAFS spectrum of $[UO_2(CH_3COO)_3]^-$ shows the same structural features as that of $[UO_2(NO_3)_3]^-$. Therefore, the EXAFS data can be explained in a similar way, with a carbon and a distal carbon atom instead of a nitrogen and distal oxygen atom. The focusing effect is also observed in the acetate group.
- ✓ The differences in the U-O_{ax} bond length between $[UO_2(NO_3)_3]^-$, $[UO_2(CH_3COO)_3]^-$ and $[UO_2(CO_3)_3]^{4-}$ can be explained in terms of the effective ligand charge on the uranium atom. A correlation is found between the U-O_{ax} bond distance and the frequency of the symmetrical stretching vibration ν_s for the different complexes as well.
- ✓ UV-Vis absorption (luminescence) spectroscopy and uranium L_{III}-edge EXAFS spectroscopy have given evidence for the inclusion of the uranyl ion in the cavity of the crown ether 18-crown-6 in acetonitrile solution. The specific conformation of the crown ether implies a reduction of the symmetry from D_{6h} to D_{3d} (D_3). The absorption spectrum shows phenomenological features that differ from the spectrum of the "free" uranyl ion and more equatorial planar complexes like $[UO_2(NO_3)_3]^-$. While the spectra of $[UO_2Cl_4]^{2-}$ and $[UO_2(NO_3)_3]^-$ are dominated by transitions arising from the $\sigma_u^+\delta_u$ configuration, the ϕ_u orbital has a great influence on the spectrum of the inclusion complex $[UO_2(18\text{-crown-6})]^{2+}$. At higher energies (~ 25430 cm^{-1}), the $\Gamma_g \leftarrow \Sigma_g^+$ transition ($\sigma_u^+\phi_u$ configuration) appears, which is typical for a D_3 coordination symmetry. The high coordination number makes the equatorial carbon atoms at a distance of 3.51 Å visible. The variation of the U-O_{eq} and U-C_{eq} bond

distances in the crystal structure of $[UO_2(18\text{-crown-6})](CF_3SO_3)_2$ [28] is reflected by the high Debye-Waller factors σ^2 of the O_{eq} and C_{eq} shells in the curve fit.

References

[1] Görller-Walrand, C.; De Jaegere, S. *Spectrochim. Acta* **1972**, *28A*, 257-268.

[2] (a) Görller-Walrand, C.; De Jaegere, S. *J. Chim. Phys.* **1972,** *4*, 726-736. (b) Görller-Walrand, C.; De Jaegere, S. *J. Chim. Phys.* **1973**, *2*, 360-366. In this work, the authors mention a $[UO_2Cl_3]^-$ complex in acetone with a D_{3h} symmetry in Figure 2.5. (3a) and Figure 6b. This conclusion has been revised in ref. 57.

[3] Katz, J.J.; Seaborg, G.T.; Morss, L.R. *The Chemistry of the Actinide Elements*, **1986**, Chapman and Hall, New York.

[4] Allen, P.G.; Bucher, J.J.; Clark, D.L.; Edelstein, N.M.; Ekberg, S.A.; Gohdes, J.W.; Hudson, E.A.; Kaltsoyannis, N.; Lukens, W.W.; Palmer, P.D.; Reich, T.; Shuh, D.K.; Tait, C.D.; Zwick, B.D. *Inorg. Chem.* **1995**, *34*, 4797-4807.

[5] Crawford, M.J.; Mayer, P.; Noth, H.; Suter, M. *Inorg. Chem.* **2004**, *43*, 6860-6862.

[6] Jiang, J.; Renshaw, J.C.; Sarsfield, M.J.; Livens, F.R.; Collison, D.; Charnock, J.M.; Eccles, H. *Inorg. Chem.* **2003**, *42*, 1233-1240.

[7] Vallet, V.; Szabó, Z.; Grenthe, I. *Dalton Trans.* **2004**, 3799-3807.

[8] Curini, R.; Tentolini, U.; Materazzi, S.; Vasca, E.; Caruso, T.; Fontanella, C.; Palladino, G. *Thermochim. Acta* **2002**, *387*, 17-21.

[9] Sopo, H.; Väisänen, A.; Sillanpää, R. *Polyhedron* **2007**, *26*, 184-196.

[10] (a) Szabó, Z.; Glaser, J.; Grenthe, I. *Inorg. Chem.* **1996**, *35*, 2036-2044. (b) Szabó, Z.; Aas, W.; Grenthe, I. *Inorg. Chem.* **1997**, *36*, 5369-5375. (c) Szabó, Z.; Grenthe, I. *Inorg. Chem.* **1998**, *37*, 6214-6221. (d) Aas, W.; Szabó, Z.; Grenthe, I. *J. Chem. Soc., Dalton Trans.* **1999**, 1311-1317. (e) Szabó, Z.; Moll, H.; Grenthe, I. *J. Chem. Soc., Dalton Trans.* **2000**, 3158-3161.

[11] Szabó, Z.; Toaishi, T.; Vallet, V.; Grenthe, I. *Coord. Chem. Rev.* **2006**, *250*, 784-815.

[12] Farkas, I.; Banyai, I.; Szabó, Z.; Wahlgren, U.; Grenthe, I. *Inorg. Chem.* **2000**, *39*, 799-805.

[13] Vallet, V.; Wahlgren, U.; Szabó, Z.; Grenthe, I. *Inorg. Chem.* **2002**, *41*, 5626-5633.

[14] (a) Quilès, F.; Burneau, A. *Vibrational Spectroscopy* **1998**, *18*, 61-75. (b) Quilès, F.; Burneau, A. *Vibrational Spectroscopy* **2000**, *23*, 231-241.

[15] Nguyen-Trung, C.; Begun, G.M.; Palmer, D.A. *Inorg. Chem.* **1992**, *31*, 5280-5287.

[16] Toth, L.M.; Begun, G.M. *J. Phys. Chem.* **1981**, *85*, 547-549.

[17] Clark, D.L.; Conradson, S.D.; Donohoe, R.J.; Keogh, D.W.; Morris, D.E.; Palmer, P.D.; Rogers, R.D.; Tait, C.D. *Inorg. Chem.* **1999**, *38*, 1456-1466.

[18] Maya, L.; Begun, M. *J. Inorg. Nucl. Chem.* **1981**, *43*, 2827-2832.

[19] Danis, J.A.; Lin, M.R.; Scott, B.L.; Eichhorn, B.W.; Runde, W.H. *Inorg. Chem.* **2001**, *40*, 3389-3394.

[20] Ohwada, K.; Fujisawa, G. *Spectrochim. Acta* **1995**, *51A*, 309-318.

[21] Servaes, K.; De Houwer, S.; Görller-Walrand, C.; Binnemans, K. *Phys. Chem. Chem. Phys.* **2004**, *6*, 2946-2950.

[22] Dejean, A.; Charpin, P.; Folcher, G.; Rigny, P.; Navaza, A.; Tsoucaris, G. *Polyhedron* **1987**, *6*, 189-195.

[23] Fischer, A. *Z. Anorg. Allg. Chem.* **2003**, *629*, 1012-1016.

[24] Watkin, D.J.; Denning, R.G.; Prout, K. *Acta Cryst.* **1991**, *C47*, 2517-2519.

[25] Shuvalov, R.R.; Burns, P.C. *Acta Cryst.* **2003**, *C59*, i71-i73.

[26] Zalkin, A.; Templeton, L.K.; Templeton, D.H. *Acta Cryst.* **1989**, *C45*, 810-811.

[27] Templeton, D.H.; Zalkin, A.; Ruben, H.; Templeton, L.K. *Acta Cryst.* **1985**, *C41*, 1439-1441.

[28] Deshayes, L.; Keller, N.; Lance, M.; Navaza, A.; Nierlich, M.; Vigner, J. *Polyhedron* **1994**, *13*, 1725-1733.

[29] (a) Meinrath, G.; Lis, S.; Stryla, Z.; Noubactep, C. *J. Alloys Compd.* **2000**, *300-301*, 107-112. (b) Meinrath, G.; Volke, P.; Helling, C.; Dudel, E.G.; Merkel, B.J. *Fresen. J. Anal. Chem.* **1999**, *364*, 191-202. (c) Meinrath, G. *J. Alloys Compd.* **1998**, *275-277*, 777-781. (d) Meinrath, G.; Kato, Y.; Kimura, T.; Yoshida, Z. *Radiochim. Acta* **1998**, *82*, 115-120. (e) Meinrath, G. *J. Radioanal. Nucl. Chem.* **1997**, *224*, 119-126. (f) Meinrath, G.; Schweinberger, M. *Radiochim. Acta* **1996**, *75*, 205-210. (g) Meinrath, G.; Klenze, R.; Kim, J.I. *Radiochim. Acta* **1996**, *74*, 81-86. (h) Meinrath, G. *J. Radioanal. Nucl. Chem.* **1996**, *211*, 349-362. (i) Kato, Y.; Meinrath, G.; Kimura, T.; Yoshida, Z. *Radiochim. Acta* **1994**, *64*, 107-111. (j) Meinrath, G.; Kimura, T. *J. Alloys Compd.* **1993**, *202*, 89-93.

[30] Azenha, M.E.D.G.; Burrows, H.D.; Formosinho, S.J.; Miguel, M.G.M.; Daramanyan, A.P.; Khudyakov, I.V. *J. Lumin.* **1991**, *48-49*, 522-526.

[31] Rabinowitch, E.; Belford, R.L. *Spectroscopy and Photochemistry of Uranyl Compounds*, **1964**, Pergamon, Oxford.

[32] Bünzli, J.-C. G. *J. Alloys Compd.* **1993**, *192*, 266-270.

[33] Spencer, S.; Gagliardi, L.; Handy, H.C.; Ioannou, A.G.; Skylaris, C.-K.; Willets, A.; Simper, A.M. *J. Phys. Chem. A* **1999**, *103*, 1831-1837.

[34] Vallet, V.; Wahlgren, U.; Schimmelpfennig, B.; Moll, H.; Szabó, Z.; Grenthe, I. *Inorg. Chem.* **2001**, *40*, 3516-3525.

[35] Hennig, C.; Tutschku, J.; Rossberg, A.; Bernhard, G.; Scheinost, A.C. *Inorg. Chem.* **2005**, *44*, 6655-6661.

[36] Bühl, M.; Diss, R.; Wipff, G. *J. Am. Chem. Soc.* **2005**, *127*, 13506-13507.

[37] Neuefeind, J.; Soderholm, L.; Skanthakumar, S. *J. Phys. Chem. A* **2004**, *108*, 2733-2739.

[38] Hagberg, D.; Karlström, G.; Roos, B.O.; Gagliardi, L. *J. Am. Chem. Soc.* **2005**, *127*, 14250-14256.

[39] Sémon, L.; Boehme, C.; Billard, I.; Hennig, C.; Lützenkirchen, K.; Reich, T.; Rossberg, A.; Rossini, I.; Wipff, G. *Chem. Phys. Chem.* **2001**, *2*, 591-598.

[40] (a) Görller-Walrand, C.; Colen, W. *Chem. Phys. Lett.* **1982**, *93*, 82-85. (b) De Jaegere, S.; Görller-Walrand, C. *Spectrochim. Acta* **1969**, *25A*, 559-568.

[41] van Besien, E. *De invloed van complexvorming op het elektronische spectrum van uranyl: een computationele studie*, **2006**, PhD thesis, Katholieke Universiteit Leuven and references therein.

[42] Denning, R.G. *J. Phys. Chem. A* (Feature Article) **2007**, *111*, 4125-4143.

[43] Denning, R.G. *Struct. Bond.* **1992**, *79*, 215-276.

[44] (a) Denning, R.G.; Snellgrove, T.R.; Woodwark, D.R. *Mol. Phys.* **1979**, *37*, 1109-1143. (b) Denning, R.G.; Snellgrove, T.R.; Woodwark, D.R. *Mol. Phys.* **1976**, *32*, 419-442.

[45] Görller-Walrand, C.; Colen, W.; Dao, N.Q. *J. Chem. Phys.* **1982**, *76*, 13-19.

[46] Antonio, M.R.; Soderholm, L. "X-ray Absorption Spectroscopy of the Actinides" in *The Chemistry of the Actinide and Transactinide Elements* (3rd edition); Eds. Morss, L.R.; Edelstein, N.M.; Fuger, J., **2006**, Springer, Dordrecht, The Netherlands, p. 3086-3189.

[47] (a) Barker, T.J.; Denning, R.G.; Thorne, J.R.G. *Inorg. Chem.* **1987**, *26*, 1721-1732. (b) Barker, T.J.; Denning, R.G.; Thorne, J.R.G. *J. Lumin.* **1987**, *38*, 144-146. (c) Thorne, J.R.G.; Denning, R.G.; Barker, T.J.; Grimley, D.I. *J. Lumin.* **1985**, *34*, 147-165. (d) Denning, R.G.; Ironside, C.N.; Thorne, J.R.G.; Woodwark, D.R. *Mol. Phys.* **1981**, *44*, 209-224. (e) Denning, R.G.;

Snellgrove, T.R.; Woodwark, D.R. *Mol. Phys.* **1975**, *30*, 1819-1828.

[48] (a) Tanner, P.A. *J. Chem. Soc., Faraday Trans. 2* **1984**, *80*, 365-373. (b) Flint, C.D.; Tanner, P.A. *Mol. Phys.* **1981**, *44*, 411-425. (c) Flint, C.D.; Tanner, P.A. *J. Chem. Soc., Faraday Trans. 2* **1981**, *77*, 1865-1878. (d) Flint, C.D.; Tanner, P.A. *J. Chem. Soc., Faraday Trans. 2* **1979**, *75*, 1168-1178.

[49] Görller-Walrand, C.; Vanquickenborne, L.G. *J. Chem. Phys.* **1972**, *57*, 1436-1440.

[50] (a) Grenthe, I.; Fuger, J.; Konings, R.J.M.; Lemire, R.J.; Muller, A.B.; Nguyen-Trung, C.; Wanner, H. *Chemical Thermodynamics of Uranium*; Eds. Wanner, H.; Forest, I., **1992**, Elsevier Science Publishers, Amsterdam. (b) Guillaumont, R.; Fanghänel, T.; Fuger, J.; Grenthe, I.; Neck, V.; Palmer, D.A.; Rand, M.H. *Update on the chemical thermodynamics of uranium, neptunium, plutonium, americium and technetium*; Eds. Mompean, F.J.; Illemassene, M.; Domenech-Orti, C.; Ben Said, K., **2003**, Elsevier Science Publishers, Amsterdam.

[51] Allen, P.G.; Bucher, J.J.; Shuh, D.K.; Edelstein, N.M.; Reich, T. *Inorg. Chem.* **1997**, *36*, 4676-4683.

[52] Görller-Walrand, C.; De Houwer, S.; Fluyt, L.; Binnemans, K. *Phys. Chem. Chem. Phys.* **2004**, *6*, 3292-3298.

[53] Billard, I.; Rustenholtz, A.; Sémon, L.; Lützenkirchen, K. *Chem. Phys.* **2001**, *270*, 345-354.

[54] Gmelin Handbook, U, Uranium Suppl. Vol. D1, *Properties of uranium ions in solutions and melts*, System number 55, **1984**, Springer, Berlin.

[55] (a) Paviet-Hartmann, P.; Lin, M.R.; Runde, W. *Mat. Res. Soc. Symp. Proc.* **1999**, *556*, 977-984. (b) Paviet-Hartmann, P.; Lin, M.R. *Mat. Res. Soc. Symp. Proc.* **1999**, *556*, 977-984.

[56] Brittain, H.G.; Perry, D.L.; Tsao, L. *Spectrochim. Acta* **1984**, *40A*, 651-655.

[57] Morita, M.; Shoki, T. *J. Lumin.* **1988**, *40-41*, 678-679.

[58] (a) Pierloot, K. *Mol. Phys.* **2003**, *101*, 2083-2094. (b) Pierloot, K.; van Besien, E. *J. Chem. Phys.* **2005**, *123*, 204309. (c) van Besien, E.; Pierloot, K.; Görller-Walrand, C. *Phys. Chem. Chem. Phys.* **2006**, *8*, 4311-4319. (d) Pierloot, K.; van Besien, E.; van Lenthe, E.; Baerends, E.J. *J. Chem. Phys.* **2007**, *126*, 194311.

[59] Matsika, S.; Pitzer, R.M. *J. Phys. Chem. A* **2001**, *105*, 637-645.

[60] De Houwer, S. *Intensities of vibronic transitions in uranyl spectra: application to uranyl complexes in non-aqueous solvents*, **2003**, PhD thesis, Katholieke Universiteit Leuven.

[61] Hennig, C.; Reck, G.; Reich, T.; Rossberg, A.; Kraus, W.; Sieler, J. *Z. Kristallogr.* **2003**, *218*, 37-45.

[62] Malcic, S.S.; Manojlovic, L.M. *Bulletin of the Institute of Nuclear Science 'Boris Kidrich'* **1961**, *11*, 135-139.

[63] Barclay, G.A.; Sabine, T.M.; Taylor, J.C. *Acta Cryst.* **1965**, *19*, 205-209.

[64] Dieke, G.H.; Duncan, A.B.F. *Spectroscopic Properties of Uranium Compounds*, **1965**, McGraw Hill, New York.

[65] Brint, P.; McCaffery, A.J. *Mol. Phys.* **1973**, *25*, 311-322.

[66] Görller-Walrand, C.; Colen, W. *Inorg. Chim. Acta* **1984**, *84*, 183-188.

[67] (a) Denning, R.G.; Foster, D.N.P.; Snellgrove, T.R.; Woodwark, D.R. *Mol. Phys*. **1979**, *37*, 1089-1107. (b) Denning, R.G.; Short, L.G.; Woodwark, D.R. *Mol. Phys.* **1980**, *39*, 1281-1285. (c) Thorne, J.R.G.; Denning, R.G. *Mol. Phys.* **1985**, *54*, 701-711. (d) Denning, R.G.; Norris, J.O.W.; Brown, D. *Mol. Phys.* **1982**, *46*, 325-364. (e) Denning, R.G.; Norris, J.O.W.; Brown, D. *Mol. Phys.* **1982**, *46*, 287-323. (f) Barker, T.J.; Denning, R.G.; Thorne, J.R.G. *Inorg. Chem.* **1992**, *31*, 1344-1353.

[68] Thompson, H.A.; Brown Jr., G.E.; Parks, G.A. *Am. Min.* **1997**, *82*, 483-496.

[69] Barnes, C.E.; Shin, Y.; Saengkerdsub, S.; Dai, S. *Inorg. Chem.* **2000**, *39*, 862-864.

[70] Zolotov, Yu.A. *Macrocyclic Compounds in Analytical Chemistry*, **1997**, John Wiley & Sons, New York.

[71] (a) Fedorov, Yu. S.; Zilberman, B.Ya. *Radiochem.* **2000**, *42*, 242-246. (b) Fedorov, Yu.S.; Zilberman, B.Ya. *Radiochem.* **1999**, *41*, 545-550. (c) Fedorov, Yu.S.; Blazheva, I.V.; Zilberman, B.Ya. *Radiochem.* **2000**, *42*, 74-78. (d) Fedorov, Yu.S.; Zilberman, B.Ya.; Kulikov, S.M.; Blazheva, I.V.; Mishin, E.N. *Solvent Extr. Ion Exc.* **1999**, *17*, 243-257.

[72] Cŏmor, J.J.; Kopečni, M.M.; Petković, D.M. *Solvent Extr. Ion Exc.* **1997**, *15*, 991-1006.

[73] Oda, Y.; Funasaka, H.; Nakamura, Y.; Adachi, H. *J. Alloys Compd.* **1997**, *225*, 24-30.

[74] Mohammed, A.K.; Sullivan, J.C.; Nash, K.L. *Solvent Extr. Ion Exc.* **2000**, *18*, 809-820.

[75] (a) Den Auwer, C.; Lecouteux, C.; Charbonnel, M.C.; Madic, C.; Guillaumont, R. *Polyhedron* **1997**, *16*, 2233-2238. (b) Den Auwer, C.; Charbonnel, M.C.; Presson, M.T.; Madic, C.; Guillaumont, R. *Polyhedron* **1998**, *17*, 4507-4517. (c) Den Auwer, C.; Revel, R.; Charbonnel, M.C.; Presson, M.T.; Conradson, S.D.; Simoni, E.; Le Du, J.F.; Madic, C. *J. Synchrotron Rad.* **1999**, *6*, 101-104.

[76] Ruas, A.; Bernhard, O.; Caniffi, B.; Simonin, J.-P.; Turq, P.; Blum, L.; Moisy, P. *J. Phys. Chem. B* **2006**, *110*, 3435-3443.

[77] Hennig, C. *Phys. Rev. B.* **2007**, *75*, 035120.

[78] Teo, B.K. *EXAFS: Basic Principles and Data Analysis*, **1986**, Springer, Berlin, Heidelberg, New York, p. 183.

[79] Bernhard, G.; Geipel, G.; Reich, T.; Brendler, V.; Amayri, S.; Nitsche, H. *Radiochim. Acta* **2001**, *89*, 511-518.

[80] Leciejewicz, J.; Alcock, N.W.; Kemp, T.J. *Struct. Bond.* **1995**, *82*, 43-84.

[81] Denecke, M.A.; Reich, T.; Bubner, M.; Pompe, S.; Heise, K.H.; Nitsche, H.; Allen, P.G.; Bucher, J.J.; Edelstein, N.M.; Shuh, D.K. *J. Alloys Compd.* **1998**, *271-273*, 123-127.

[82] Bailey, E.H.; Mosselmans, J.F.W.; Schofield, P.F. *Geochim. Cosmochim. Acta* **2004**, *68*, 1711-1722.

[83] Ingram, K.I.M.; Häller, L.J.L.; Kaltsoyannis, N. *Dalton Trans.* **2006**, 2403-2414.

[84] McGlynn, S.P.; Smith, J.K.; Neely, W.C. *J. Chem. Phys.* **1961**, *35*, 105-116.

[85] Bartlett, J.R.; Cooney, R.P. *J. Mol. Struct.* **1989**, *193*, 295-300.

[86] de Jong, W.A.; Aprà, E.; Windus, T.L.; Nichols, J.A.; Harrison, R.J.; Gutowski, K.E.; Dixon, D.A. *J. Phys. Chem. A* **2005**, *109*, 11568-11577.

[87] Pederson, C.J. *J. Am. Chem. Soc.* **1967**, *89*, 7017-7036.

[88] Dai, S.; Ju, Y.H.; Barnes, C.E. *J. Chem. Soc., Dalton Trans.* **1999**, 1201-1202.

[89] (a) Dietz, M.L. *Sep. Sci. Technol.* **2006**, *41*, 2047-2063. (b) Dietz, M.L.; Dzielawa, J.A. *Chem. Commun.* **2001**, 2124-2125.

[90] Jensen, M.P.; Dzielawa, J.A.; Rickert, P.; Dietz, M.L. *J. Am. Chem. Soc.* **2002**, *124*, 10664-10665.

[91] (a) Bombieri, G.; De Paoli, G. *J. Inorg. Nucl. Chem.* **1978**, *40*, 799-802. (b) Bombieri, G.; De Paoli, G. *Inorg. Chim. Acta* **1976**, *18*, L23-L24.

[92] Eller, P.G.; Penneman, R.A. *Inorg. Chem.* **1976**, *15*, 2439-2442.

[93] (a) Rogers, R.D.; Kurihara, L.K.; Benning, M.M. *J. Incl. Phenom.* **1987**, *5*, 645-658. (b) Rogers, R.D.; Bond, A.H.; Hipple, W.G.; Rollins, A.N.; Henry, R.F. *Inorg. Chem.* **1991**, *30*, 2671-2679. (c) Rogers, R.D. *Acta Cryst.* **1988**, *C44*, 638-641. (d) Rogers, R.D.; Zhang, J.; Campbell, D.T. *J. Alloys Compd.* **1998**, *271-273*, 133-138. (e) Rogers, R.D.; Benning, M.W.; Etzenhouser, R.D.; Rollins, A.N. *J. Coord. Chem.* **1992**, *26*, 299-311.

[94] Mikhailov, Yu.N.; Kanishcheva, A.S.; Gorbunova, Yu.E.; Belomestnykh, V.I.; Sveshnikova, L.B. *Russ. J. Inorg. Chem.* **1997**, *42*, 1817-1823.

[95] (a) Deshayes, L.; Keller, N.; Lance, M.; Navaza, A.; Nierlich, M.; Vigner, J. *Polyhedron* **1994**, *13*, 1725-1733. (b) Nierlich, M.; Sabattie, J.-M.; Keller, N.; Lance, M.; Vigner, J.-D. *Acta Cryst.* **1994**, *C50*, 52-54.

[96] Navaza, A.; Villain, F.; Charpin, P. *Polyhedron* **1984**, *3*, 143-149.

[97] Folcher, G.; Charpin, P.; Coster, R.-M.; Keller, N.; de Villardi, G.-C. *Inorg. Chim. Acta* **1979**, *34*, 87-90.

[98] (a) Mohapatra, P.K.; Manchanda, V.K. *J. Radioanal. Nucl. Chem.* **1999**, *241*, 101-105. (b) Mohapatra, P.K.; Manchanda, V.K. *Talanta* **1998**, *47*, 1271-1278.

[99] (a) Shukla, J.P.; Kumar, A.; Singh, R.K. *Talanta* **1993**, *40*, 1261-1266. (b) Shukla, J.P.; Singh, R.K.; Kumar, A. *Radiochim. Acta* **1991**, *54*, 73-77.

[100] (a) Lagrange, J.; Metabanzoulou, J.P.; Fux, P.; Lagrange, P. *Polyhedron* **1989**, *8*, 2251-2254. (b) Brighli, M.; Fux, P.; Lagrange, J.; Lagrange, P. *Inorg. Chem.* **1985**, *24*, 80-84. (c) Fux, P.; Lagrange, J.; Lagrange, P. *J. Am. Chem. Soc.* **1985**, *107*, 5927-5931.

[101] (a) De Houwer, S.; Servaes, K.; Görller-Walrand, C. *Phys. Chem. Chem. Phys.* **2003**, *5*, 1164-1168. (b) Servaes, K.; De Houwer, S.; Görller-Walrand, C.; Binnemans, K. *Phys. Chem. Chem. Phys.* **2004**, *6*, 2946-2950.

[102] Burns, P. *Can. Miner.* **2005**, *43*, 1839-1894.

6 SPECIATION OF URANYL COMPLEXES IN IONIC LIQUIDS

1 Introduction

Ionic liquids are salts with a melting point below 100 °C [1-4]. Several types of these ionic liquids are even liquid at room temperature (room temperature ionic liquids or RTILs). Ionic liquids are composed of a (large) organic cation and an organic/inorganic anion. The most encountered cations in ionic liquids are imidazolium, pyridinium, pyrrolidinium, quaternary ammonium and phosphonium ions (Figure 6.1) [5]. A wide variety of anions is used like Cl^-, Br^-, NO_3^-, PF_6^- and BF_4^-. Recently, the bis(trifluoromethylsulfonyl)imide anion $[(CF_3SO_2)_2N]^-$ (abbreviated as Tf_2N^-) is a commonly used anion due to its remarkable properties. Ionic liquids based on the Tf_2N^- anion are chemically and

thermally more robust than ionic liquids with BF_4^- or PF_6^- anions. They exhibit also low viscosities and high electrical conductivities [5].

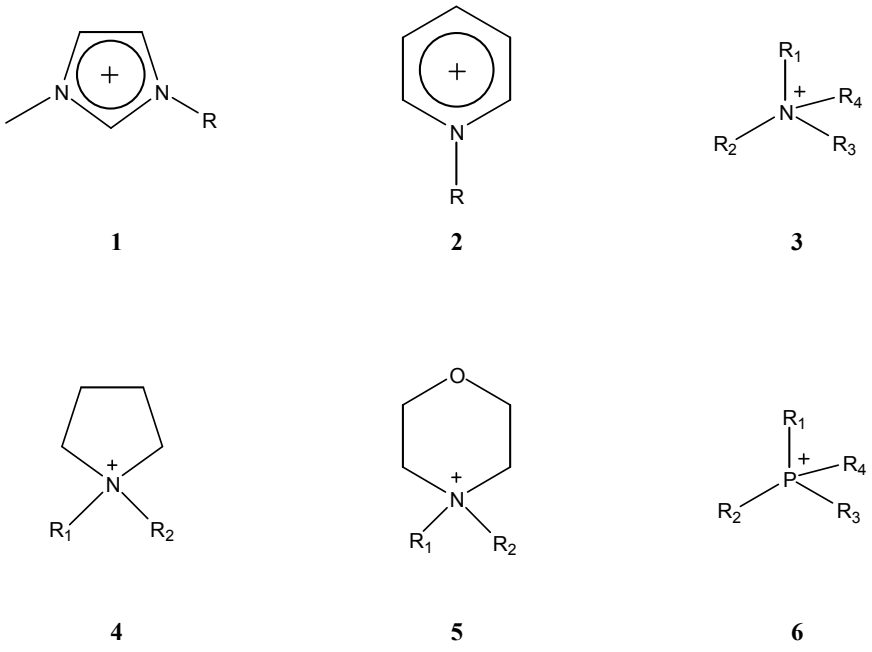

Figure 6.1. Examples of cations commonly used in ionic liquids: (**1**) 1-alkyl-3-methylimidazolium; (**2**) 1-alkylpyridinium; (**3**) quaternary ammonium; (**4**) 1,1'-dialkylpyrrolidinium; (**5**) 1,1'-dialkylmorpholinium; (**6**) phosphonium.

Ionic liquids possess a unique combination of properties: negligible vapour pressure due to the strong Coulombic forces within the liquid, high thermal stability, high electrical conductivity, wide temperature range of liquid state, non-flammable and non-explosive. Ionic liquids exhibit a large electrochemical window, so that they are very resistant against oxidation and reduction. Ionic liquids are polar solvents, with a polarity similar to that of the lower alcohols (*n*-propanol, *n*-butanol, *n*-pentanol) [5]. Furthermore, they are able to dissolve both ionic and non-ionic species. In addition, their physicochemical properties like miscibility with water, can be tuned by a suitable choice of anion/cation

combinations. Using Br^- and Cl^- anions yields hydrophilic ionic liquids (miscible with water), while PF_6^- and Tf_2N^- anions allow the preparation of hydrophobic ionic liquids (immiscible with water) [5]. The length of the alkyl chains of the cation affects the physical properties of the ionic liquid as well. The hydrophobicity of ionic liquids containing the BF_4^- anion depends on the length of the alkyl chain of the cation [5]. It has been shown that extending the alkyl chain increases the hydrophobicity of a series of $[C_nmim][PF_6]$ ionic liquids (C_nmim = 1-alkyl-3-methylimidazolium) [6]. Finally, their Lewis acid/base character can be influenced by changing the ratio of the different components of the ionic liquid. The Lewis acid/base properties of ionic liquids containing aluminium chloride ($AlCl_3$) can be adjusted by varying the composition of the mixture. Mixtures with > 50 mol % of $AlCl_3$ are Lewis acidic, while mixtures with < 50 mol % of $AlCl_3$ are Lewis basic. The composition with $AlCl_3$ equal to 50 mol % is called neutral [5,7-9].

Ionic liquids as "green solvents" are currently investigated as potential alternatives to conventional solvents, especially volatile organic compounds (VOCs), in different fields of chemistry. Numerous studies on their applicability in separation processes (liquid-liquid extraction), catalysis, organic synthesis, electrochemistry and biochemistry have been reported in the literature [4,5,8,9,10-19]. These investigations have demonstrated that the mechanisms of several synthetic reactions are the same in molecular solvents and RTILs, but this is not universally true [11]. In liquid-liquid partitioning, the differences between the chemical equilibria in RTILs and classical organic solvents can be very large. It has also been shown that the structure and the stoichiometry of europium(III) complexes with the ligand 2-thenoyltrifluoroacetone (Htta) in the ionic liquid $[C_4mim][Tf_2N]$ differ from the complexes observed in organic solvents at high [Htta] concentrations. The anionic species $[Eu(tta)_4]^-$ is formed in $[C_4mim][Tf_2N]$, whereas the neutral complex $[Eu(tta)_3(H_2O)_n]$ (n = 2 or 3) is more commonly observed in organic solvents [11].

Ionic liquids have started to gain interest in actinide chemistry and nuclear industry due to their potential applicability as solvents for actinide ion separations from spent nuclear fuel and radioactive waste as well as for electrochemical separation of actinides. The study of the behaviour of uranium in ionic liquids started almost two decades ago. In 1982, Dewaele et al. demonstrated that uranium(IV) chloride was soluble in acidic *N*-butylpyridinium chloroaluminate ionic liquids and could be electrochemically reduced to uranium(III) or oxidized to uranium(V), which could in turn be further oxidized to uranium(VI) [10]. These chloroaluminate ionic liquids, which are extremely air- and water-sensitive, have been extensively used to investigate the electrochemical behaviour and the spectroscopic properties of actinides in ionic liquids [7,9,10]. Nowadays, the research on uranium and other actinides in non-chloroaluminate ionic liquids is still ongoing, paying a lot of attention to the microscopic structure of the ionic liquid, the solvation of the uranyl ion and its complexes and the separation processes of actinides [5,8,20-25]. The results of the liquid-liquid extraction procedures carried out with ionic liquids and octyl(phenyl)-*N,N*-diisobutyl-carbamoylmethylphospine oxide (CMPO) and tri-*n*-butylphosphate (TBP) as extracting agents, are very promising. Therefore, the development of task-specific ionic liquids (TSILs), with a phosphonamide functional group in the pendant arm of the cation, has been extended to actinide chemistry. Such TSILs could help to reduce or even to eliminate the extractant loss into the aqueous phase [25].

Spectroscopic studies of the uranyl ion in ionic liquids are of practical interest as characterization tools for the coordination environment. In this chapter, our contribution to elucidate the coordination behaviour of the uranyl ion in ionic liquids will be discussed, thereby using several types of ionic liquids. For this purpose, UV-Vis absorption spectroscopy, luminescence spectroscopy and where possible MCD spectroscopy were applied. The existence of a $[UO_2(NO_3)_3]^-$ species in the ionic liquid $[C_4mim][Tf_2N]$ is confirmed by uranium L_{III}-edge EXAFS spectroscopy.

Although ionic liquids are classified as “green solvents”, it should be noted that all of the toxicological and safety aspects of these new solvents are not known yet [26,27]. We also have to remark that ionic liquids with fluorinated anions, and especially those containing the PF_6^- anion, are prone to hydrolysis [28]. This can lead to the formation of toxic and corrosive products like hydrogen fluoride. Concerning the stability of ionic liquids towards radioactive radiation (α-, β- and γ-radiation), preliminary investigations show that the radiochemical stability of 1,3-dialkylimidazolium ionic liquids with chloride and nitrate anions is comparable to benzene and is significantly higher than mixtures of tri-*n*-butylphosphate (TBP) and kerosene under similar degrees of irradiation. The imidazolium cation appears to be relatively radiation resistant due to the aromatic imidazolium ring. The aromatic ring can absorb radiation energy and can relax non-dissociatively [5,8,29].

2 Experimental details

Synthesis of ionic liquids

To investigate the speciation of the uranyl ion in ionic liquids, we used several types of room temperature ionic liquids, thereby varying either the cationic or the anionic component, i.e. 1-hexyl-3-methylimidazolium bis(trifluoromethylsulfonyl)imide ([C_6mim][Tf_2N]), 1-butyl-3-methylimidazolium bis(trifluoromethylsulfonyl)imide ([C_4mim] [Tf_2N]), 1-butyl-1-methylpyrrolidinium bis(trifluoromethyl-sulfonyl)imide ([bmpyr][Tf_2N]), 1-hexyl-3-methylimidazolium bromide ([C_6mim] [Br]) and 1-hexyl-3-methylimidazolium chloride ([C_6mim] [Cl]). Their structures are displayed in Figure 6.2.

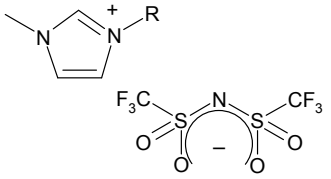

$[C_nmim][Tf_2N]$

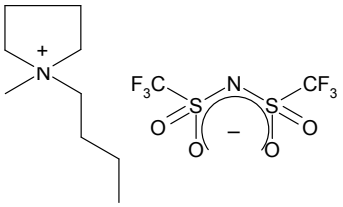

$[bmpyr][Tf_2N]$

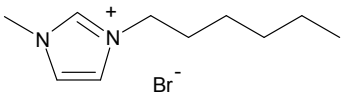

$[C_6mim][Br]$

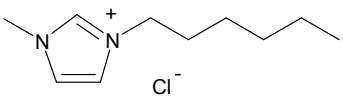

$[C_6mim][Cl]$

Figure 6.2. Structure of the ionic liquids $[C_nmim][Tf_2N]$, where n designates the number of carbons in the alkyl chain (n = 4 or 6), $[bmpyr][Tf_2N]$, $[C_6mim][Br]$ and $[C_6mim][Cl]$.

The ionic liquid $[bmpyr][Tf_2N]$ was kindly provided by Merck. The ionic liquids of spectroscopic quality $[C_4mim][Tf_2N]$, $[C_6mim][Tf_2N]$, $[C_6mim][Br]$ and $[C_6mim][Cl]$ were synthesized according to the procedures described in reference [30]. $[C_6mim][Br]$ and $[C_6mim][Cl]$ are an oil at room temperature. The ionic liquids with Tf_2N^- as anion are rather viscous at room temperature. To reduce the water content, the ionic liquids $[C_nmim][Tf_2N]$ were dried in vacuo at 70 °C before preparing the solutions for spectroscopic measurements. The ionic liquids $[C_nmim][Tf_2N]$ (n = 4 or 6), $[C_6mim][Br]$, $[C_6mim][Cl]$ and $[bmpyr][Tf_2N]$ do not interfere with the absorption of the uranyl ion, because they do not show any absorption in the wavelength region 600 nm - 300 nm [30].

Sample preparation

"Free" uranyl ion: $UO_2(Tf_2N)_2$ and $UO_2(ClO_4)_2{\cdot}xH_2O$ were dissolved in $[C_n mim][Tf_2N]$ and [bmpyr][Tf_2N]. The uranyl concentration was approximately 10^{-2} mol L^{-1} for $UO_2(Tf_2N)_2$ and 5×10^{-2} mol L^{-1} for $UO_2(ClO_4)_2{\cdot}xH_2O$.

Coordination with chloride: $UO_2(ClO_4)_2{\cdot}xH_2O$ was mixed with tetrabutylammonium chloride in $[C_4mim][Tf_2N]$ and [bmpyr][Tf_2N] in a metal-to-ligand ratio of 1:5. The uranyl concentration was approximately 5×10^{-2} mol L^{-1}.

Coordination with nitrate: Tetrabutylammonium nitrate was added to $UO_2(NO_3)_2{\cdot}6H_2O$ in $[C_4mim][Tf_2N]$ and [bmpyr][Tf_2N] in a total metal-to-ligand ratio of 1:4. An additional sample was prepared by the reaction of UO_3 with concentrated nitric acid in $[C_4mim][Tf_2N]$.

Coordination with acetate: $UO_2(CH_3COO)_2{\cdot}2H_2O$ was mixed with tetrabutylammonium acetate in $[C_4mim][Tf_2N]$ in a total metal-to-ligand ratio of 1:4. The uranyl concentration was approximately 5×10^{-2} mol L^{-1}.

Coordination with 18-crown-6: $UO_2(ClO_4)_2{\cdot}xH_2O$ was mixed with 18-crown-6 in $[C_4mim][Tf_2N]$ and [bmpyr][Tf_2N] in a uranyl-to-ligand ratio of 1:2. The uranyl concentration was approximately 5×10^{-2} mol L^{-1}. To study the influence of small inorganic ligands on the uranyl crown complex in ionic liquids, UO_2Br_2 and UO_2Cl_2 were dissolved in $[C_6mim][Br]$ and $[C_6mim][Cl]$, respectively, in the presence of the crown ether 18-crown-6. The uranyl concentration was approximately 2×10^{-2} mol L^{-1}.

NOTE: The total dissolution of the uranyl salt and the ligand in the ionic liquid was only observed after three days, yielding a transparent, yellow-coloured solution. Initial spectroscopic measurements on mixtures of the uranyl salt and the ligand in the ionic liquid did not allow observing the characteristic UV-Vis absorption spectrum of the corresponding uranyl complex. However, when these mixtures were measured again after several days, the typical absorption bands were clearly visible. This

indicates that the kinetics for the formation of uranyl complexes in ionic liquids is slow. Gaillard et al. have found a correlation between this kinetic effect and the viscosity of ionic liquids [13]. Different stoichiometries have been observed for europium(III) chloro complexes in a series of 1-butyl-3-methylimidazolium based ionic liquids with BF_4^-, PF_6^-, OTf^- and Tf_2N^- as their anionic counterparts. The hexachloro complex $[EuCl_6]^{3-}$ is formed in $[C_4mim][Tf_2N]$, whereas europium(III) is coordinated with approximately three chloride ions in $[C_4mim][BF_4]$. No chloride coordination is observed in $[C_4mim][PF_6]$. Complex formation of Eu^{3+} with chloride ligands can be observed in $[C_4mim][OTf]$, but it was not possible to determine the exact stoichiometry. The complex formation rate of europium(III) is affected by the viscosity of the ionic liquids. The viscosity at room temperature of the ionic liquids used by Gaillard et al., increases in the order $[C_4mim][Tf_2N]$ (35-70 mPa) < $[C_4mim][OTf]$ (≈ 90 mPa) < $[C_4mim][BF_4]$ (150-220 mPa) < $[C_4mim][PF_6]$ (240-450 mPa). Moreover, the addition of halide ions (Cl^-, F^-) enhances the viscosity [13]. Thus, we can assume that the absence of a typical vibrational fine structure in the initial spectra of uranyl complexes in ionic liquids is due to the slow kinetics of anion exchange, which is related to the viscosity of the ionic liquid.

Uranium L_{III}-edge EXAFS spectroscopy

So far, we were only able to perform EXAFS measurements on the uranyl ion coordinated with nitrate ions in ionic liquids due to the limited beamtime. The data analysis as well as the curve fit procedure of these EXAFS data and the corresponding Fourier transforms were carried out in the same way as discussed in Chapter 5 for the $[UO_2(NO_3)_3]^-$ complex in acetonitrile. In addition, the same theoretical phase and amplitude functions were used, derived from the crystal structure of $RbUO_2(NO_3)_3$ (see Chapter 5).

Uranium L_{III}-edge EXAFS spectra of the other uranyl complexes in ionic liquids, described in this chapter, will be recorded in future.

3 Results and discussion

3.1 "Free" uranyl ion (hydrated uranyl ion)

The bis(trifluoromethylsulfonyl)imide anion, Tf_2N^-, is often used in ionic liquid synthesis. To reduce the influence of anions other than the ionic liquid constituents, a $UO_2(Tf_2N)_2$ complex has been synthesized. The Tf_2N^- ligand is known for its weak-coordinating properties [5,13,31,32]. The low tendency for coordination of the Tf_2N^- ion is due to the delocalization of the negative charge over an extended area of functional groups [32]. The weak-coordinating properties of the Tf_2N^- anion have been confirmed by spectroscopic techniques (EXAFS spectroscopy, time-resolved emission spectroscopy) and theoretical calculations [31]. Coordination of the uranyl ion with the bis(trifluoromethylsulfonyl)imide anion is not observed, not even at high anion concentrations. Therefore, HTf_2N/$NaTf_2N$ would be a safer alternative for $HClO_4$/$NaClO_4$, of which the oxidizing and the explosive properties form a hazard.

Dissolution of $UO_2(Tf_2N)_2$ in $[C_6mim][Tf_2N]$ yields a bright yellow solution. The UV-Vis absorption spectrum of $UO_2(Tf_2N)_2$ in $[C_6mim][Tf_2N]$ is shown in Figure 6.3. Since $UO_2(ClO_4)_2{\cdot}xH_2O$ is a source of the "free" uranyl ion in aqueous solution as well, the UV-Vis absorption spectra of this uranyl salt, dissolved in both $[C_4mim][Tf_2N]$ and $[bmpyr][Tf_2N]$, were recorded (Figure 6.3).

Comparison of the UV-Vis absorption spectra in Figure 6.3 reveals the same spectral features, regardless which uranyl salt has been dissolved or which type of ionic liquid has been used. Moreover, the three absorption spectra exhibit the same characteristic vibrational fine

structure as the spectrum of the "free" uranyl ion in aqueous solution (see Chapter 5, Figure 5.5). The absorption maxima are observed at 24085 cm^{-1}, 23946 cm^{-1} and 23929 cm^{-1} for $UO_2(Tf_2N)_2$ in $[C_6mim][Tf_2N]$, $UO_2(ClO_4)_2{\cdot}xH_2O$ in $[C_4mim][Tf_2N]$ and $UO_2(ClO_4)_2{\cdot}xH_2O$ in $[bmpyr][Tf_2N]$, respectively. These values resemble the absorption maxima of $UO_2(ClO_4)_2{\cdot}xH_2O$ in aqueous solution (24140 cm^{-1}) and in acetonitrile (24079 cm^{-1}).

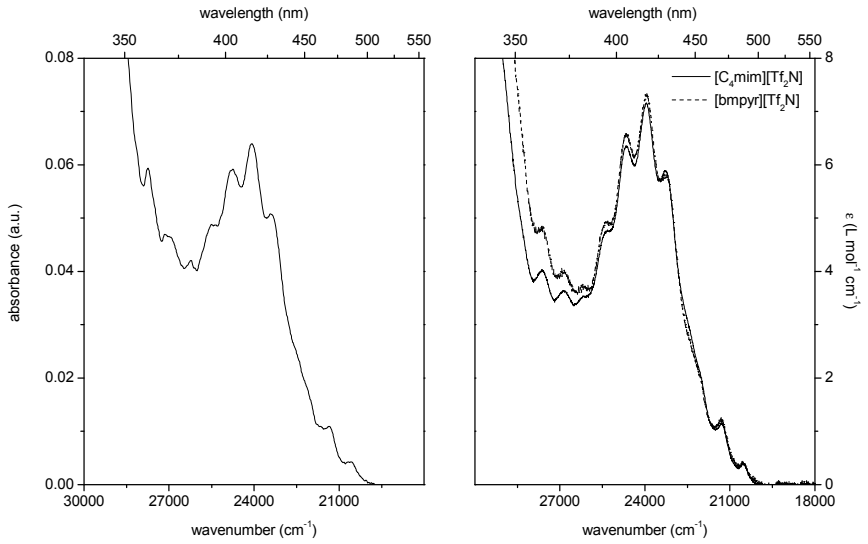

Figure 6.3. UV-Vis absorption spectra of $UO_2(Tf_2N)_2$ in $[C_6mim][Tf_2N]$ (left) and $UO_2(ClO_4)_2{\cdot}xH_2O$ in $[C_4mim][Tf_2N]$ and $[bmpyr][Tf_2N]$ (right) at room temperature. The uranyl concentration is 5×10^{-2} mol L^{-1} ($UO_2(ClO_4)_2{\cdot}xH_2O$).

The ionic liquids $[C_4mim][Tf_2N]$ and $[C_6mim][Tf_2N]$ exhibit a strong fluorescence between 14000 cm^{-1} and 20000 cm^{-1}, which is the same spectral region as the green luminescence of the uranyl ion [5,24,33]. The emission intensity of the uranyl ion in $[bmpyr][Tf_2N]$ is also not strong enough to overcome the background fluorescence of the ionic liquid. Therefore, the emission spectrum of the "free" uranyl ion could not be measured in the ionic liquids used for this study.

Whereas the "free" uranyl ion is surrounded by five water molecules in aqueous solution, the coordination environment of the uranyl ion dissolved in ionic liquids, is rather difficult to determine. Chaumont and Wipff have studied the solvation of trivalent lanthanide ions (Eu^{3+}, La^{3+}, Yb^{3+}) and uranyl in room-temperature ionic liquids by means of theoretical calculations and molecular dynamics simulations [22]. The calculations predicted that the "free" uranyl ion in $[C_4mim][PF_6]$ is surrounded by approximately six PF_6^- anions in the first shell, which shield the uranyl ion from approximately five $[C_4mim]^+$ cations (Figure 6.4) [22b]. So, one can imagine that the uranyl ion in $[C_nmim][Tf_2N]$ is surrounded by Tf_2N^- anions, which in turn are enclosed by a shell of $[C_nmim]^+$ cations in a way similar to $[C_4mim][PF_6]$.

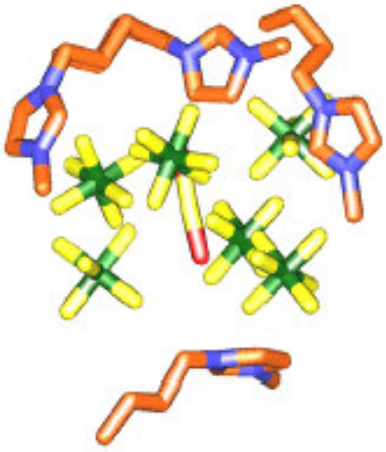

Figure 6.4. Snapshot of the first solvation shell of the uranyl ion in the ionic liquid $[C_4mim][PF_6]$, obtained by means of molecular dynamics calculations [22b]. The uranyl ion is represented by the red-yellow bar.

However, a difference in the coordination environment was observed between dry and wet ionic liquids. Whereas the "free" uranyl ion is surrounded by PF_6^- anions in dry $[C_4mim][PF_6]$, the hydrated uranyl ion

$[UO_2(H_2O)_5]^{2+}$ is immediately formed in wet $[C_4mim][PF_6]$, according to molecular dynamics calculations [22c]. As already mentioned, the bis(trifluoromethylsulfonyl)imide anion is weakly coordinating. No complex formation of the uranyl ion with Tf_2N^- was observed in acidic aqueous solution, not even at high Tf_2N^- concentrations [31]. Therefore, we can conclude that the Tf_2N^- anion does not coordinate to the uranyl ion in wet $[C_nmim][Tf_2N]$. Instead, the uranyl ion is coordinated by five water molecules. On the contrary, in dry ionic liquids or ionic liquids with low water content, the Tf_2N^- ion can no longer be considered as a non-coordinating anion [5]. A few crystal structures of lanthanide(III) bis(trifluoromethylsulfonyl)imide complexes have been reported in the literature [5]. For example, $[La(Tf_2N)_3(H_2O)_3]$ crystallizes in the cubic space group $P2_13$. The Tf_2N^- anion acts as a bidentate ligand and coordination occurs through an oxygen atom of each sulfonyl group [34].

Since the UV-Vis absorption spectra of both $UO_2(Tf_2N)_2$ and $UO_2(ClO_4)_2{\cdot}xH_2O$ in $[C_nmim][Tf_2N]$ (n = 4, 6) and $[bmpyr][Tf_2N]$ exhibit the typical vibrational fine structure of the hydrated "free" uranyl ion ($[UO_2(H_2O)_5]^{2+}$), there is probably still an amount of water present in the ionic liquids, which is coordinated to the uranyl ion in the equatorial plane.

3.2 $[UO_2Cl_4]^{2-*}$

The UV-Vis absorption spectra of the uranyl ion in the presence of chloride ions in the ionic liquids $[C_4mim][Tf_2N]$ and $[bmpyr][Tf_2N]$ are depicted in Figure 6.5. A metal-to-ligand ratio of 1:5 was used, because an earlier study in acetone and acetonitrile indicated that no further spectral changes appear in the spectrum upon addition of chloride ions

* Supporting material (see Appendix 3): absorption and luminescence spectra as well as numerical data on $[UO_2Cl_4]^{2-}$ in $[C_4mim][Tf_2N]$ and $[bmpyr][Tf_2N]$.

beyond this ratio [35,36]. Both UV-Vis absorption spectra exhibit the same remarkable vibrational fine structure, which is typical for the $[UO_2Cl_4]^{2-}$ species with D_{4h} coordination symmetry (see Chapter 5, Figure 5.12) [35-38]. Thus, a uranyl tetrachloro complex is formed in the ionic liquids $[C_4mim][Tf_2N]$ and $[bmpyr][Tf_2N]$ by dissolving $UO_2(ClO_4)_2{\cdot}xH_2O$ and tetrabutylammonium chloride. The maximum number of chloro ligands coordinating to the uranyl ion in ionic liquids is four, just like in acetone and acetonitrile.

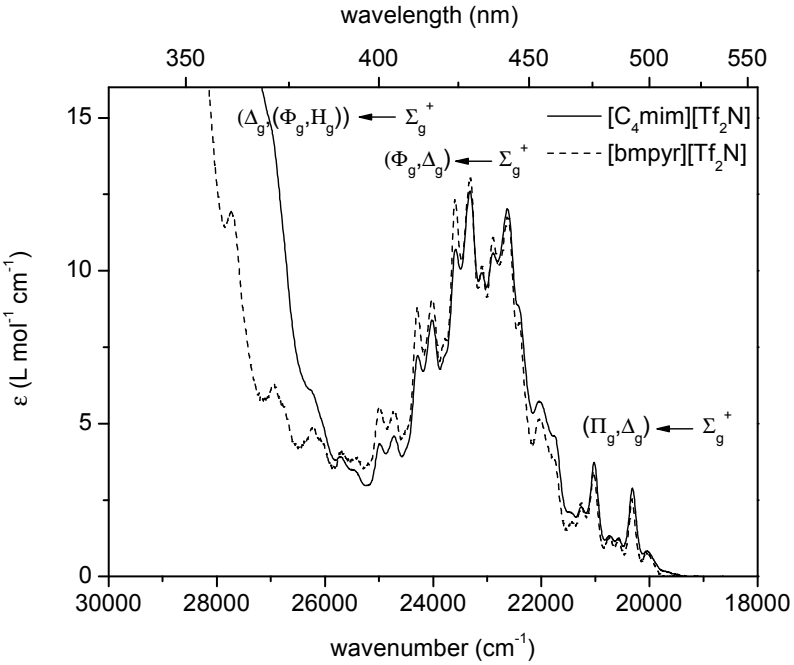

Figure 6.5. UV-Vis absorption spectra of $[UO_2Cl_4]^{2-}$ in $[C_4mim][Tf_2N]$ and $[bmpyr][Tf_2N]$ at room temperature, where $[UO_2^{2+}]/[Cl^-] = 1:5$. The uranyl concentrations are 5×10^{-2} mol L^{-1} in $[C_4mim][Tf_2N]$ and 10^{-2} mol L^{-1} in $[bmpyr][Tf_2N]$.

The ionic liquid, and in particular the cationic part of the ionic liquid, has no significant influence on the peak positions in the UV-Vis

absorption spectrum of $[UO_2Cl_4]^{2-}$. There is a good agreement between the absorption maxima in $[C_4mim][Tf_2N]$ and $[bmpyr][Tf_2N]$, which in turn correspond well to the absorption peaks in acetonitrile (see Chapter 5). On the other hand, the cation of the ionic liquid can have an influence on the intensity of certain peaks in the UV-Vis absorption spectrum of $[UO_2Cl_4]^{2-}$, as reported in the literature. Sornein et al. have noticed that the absorbance is a little higher in $[MeBu_3N][Tf_2N]$ than in $[C_4mim][Tf_2N]$, except for the peaks at 21008 cm^{-1} and 20325 cm^{-1} in the spectrum of $[UO_2Cl_4]^{2-}$ [24]. Ryan has demonstrated that the intensity of these two peaks at the low energy end of the spectrum of $[UO_2Cl_4]^{2-}$ increases if the uranyl tetrachloro complex is hydrogen bonded [39]. Therefore, Sornein et al. has assigned the intensity enhancement at 21008 cm^{-1} and 20325 cm^{-1} from $[MeBu_3N][Tf_2N]$ to $[C_4mim][Tf_2N]$ to the ability of the imidazolium cations to form C-H···Cl hydrogen bonds [24,40]. The outcome of this investigation should mean that the peaks at 20312 cm^{-1} and 21021 cm^{-1} in $[C_4mim][Tf_2N]$ on one hand and at 20321 cm^{-1} and 21039 cm^{-1} in $[bmpyr][Tf_2N]$ on the other hand experience an increase in intensity due to hydrogen bonding with the imidazolium and the pyrrolidinium cations of the ionic liquids.

The emission spectrum of $[UO_2Cl_4]^{2-}$ in $[bmpyr][Tf_2N]$ shows the typical splitting of the peaks, as also observed for $[UO_2Cl_4]^{2-}$ in acetonitrile and acetone (Figure 6.6) [35]. Furthermore, the emission maxima in $[bmpyr][Tf_2N]$ correspond well to the peaks in the spectrum of $[UO_2Cl_4]^{2-}$ in non-aqueous solution (see Chapter 5). The ground state frequency of the symmetric stretching vibration ν_s is approximately 825 cm^{-1}. This value is in good agreement with the frequency of ν_s, i.e. 832 cm^{-1}, obtained from the FT Raman spectrum of $[UO_2Cl_4]^{2-}$ in the 40:60 $AlCl_3$-$[C_2mim][Cl]$ ionic liquid [7].

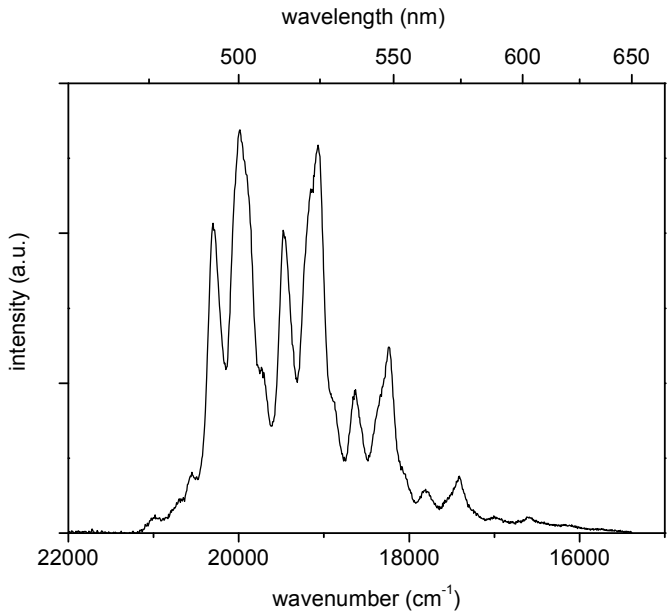

Figure 6.6. Emission spectrum of $[UO_2Cl_4]^{2-}$ in [bmpyr][Tf_2N] at room temperature. The uranyl concentration is 10^{-2} mol L^{-1}. The excitation wavelength is 418.5 nm (23895 cm^{-1}).

The transitions in the spectrum of $[UO_2Cl_4]^{2-}$ are dominated by the electronic configuration $(\sigma_u^+)^2 \rightarrow \sigma_u^+\delta_u$. Yet, in a D_{4h} coordination symmetry, all electronic transitions are parity forbidden by the Laporte selection rule. Therefore, the spectrum of $[UO_2Cl_4]^{2-}$ is purely vibronic in nature, where intensity is induced by coupling of vibrations of ungerade parity [35-37]. One of these ungerade vibrations, i.e. the U-Cl out-of-plane bending ν_{10} (b_{1u}), is coupled to the first electronic transition $\Pi_g \leftarrow \Sigma_g^+$ ($E_g \leftarrow A_{1g}$ in D_{4h}) and to one component of the transition $\Delta_g \leftarrow \Sigma_g^+$ ($B_{2g} \leftarrow A_{1g}$). For more detailed information on the electronic transitions and the coupling of vibrations in the spectrum of $[UO_2Cl_4]^{2-}$, we refer to Chapter 5. The positions of the electronic transitions in the spectrum of $[UO_2Cl_4]^{2-}$ in the ionic liquids [C_4mim][Tf_2N] and [bmpyr][Tf_2N] agree well with those of $[UO_2Cl_4]^{2-}$ in acetonitrile (Table 6.1) [36]. For

comparison, the energy values of $Cs_2UO_2Cl_4$ single crystals [37] and $[UO_2Cl_4]^{2-}$ in 40:60 $AlCl_3$-[C_2mim][Cl] [7] are also included.

Chaumont and Wipff have carried out molecular dynamics calculations to get insight into the surrounding of the $[UO_2Cl_4]^{2-}$ species in dry and wet [C_4mim][PF_6] [22b,c]. In dry [C_4mim][PF_6], the imidazolium cations efficiently solvate the $[UO_2Cl_4]^{2-}$ complexes: each $[UO_2Cl_4]^{2-}$ ion is surrounded by six imidazolium cations. In the wet ionic liquid, however, the direct environment of the $[UO_2Cl_4]^{2-}$ species consists of a shell of water molecules, followed by a shell of eight imidazolium cations. Probably, the microscopic structure around $[UO_2Cl_4]^{2-}$ in [C_4mim][Tf_2N] and [bmpyr][Tf_2N] is built up in a similar way, where Tf_2N^- anions replace the PF_6^- anions. Up to now, no molecular dynamics simulations of the solvation of the uranyl ion or its complexes in [$C_n$mim][Tf_2N] ionic liquids have been published.

3.3 $[UO_2(NO_3)_3]^-$ and $[UO_2(CH_3COO_3)]^-$*

As discussed in Chapter 5, the UV-Vis absorption spectra of complexes exhibiting a trigonal D_{3h} coordination symmetry like $[UO_2(NO_3)_3]^-$, are characterized by a series of very intense, sharp peaks at the low energy side of the spectrum, called the *"magnetic series"* [41-44]. We have investigated if this type of complexes is also formed in the ionic liquids [C_4mim][Tf_2N] and [bmpyr][Tf_2N].

We have applied two experimental approaches to obtain the $[UO_2(NO_3)_3]^-$ complex in ionic liquids. The UV-Vis absorption spectrum of $UO_2(NO_3)_2{\cdot}6H_2O$ with tetrabutylammonium nitrate in a total metal-to-ligand ratio of 1:4 in [C_4mim][Tf_2N] and [bmpyr][Tf_2N] is depicted in Figure 6.7.

* Supporting material (see Appendix 3): absorption and MCD spectra as well as numerical data on $[UO_2(NO_3)_3]^-$ in [C_4mim][Tf_2N] and [bmpyr][Tf_2N].

Table 6.1. Observed electronic transitions of $[UO_2Cl_4]^{2-}$ in $[C_4mim][Tf_2N]$ and [bmpyr][Tf_2N] at room temperature, assigned in $D_{\infty h}$ and D_{4h} symmetry. For an assignment of each peak in the spectrum, we refer to previous work [35-38] and Appendix 3. Energies are given in wavenumber units (cm^{-1}). The frequency in the ground state of the U-Cl out-of-plane bending ν_{10} is approximately 100 cm^{-1}.

Symmetry		$[C_4mim][Tf_2N]$ Origin + ν_{10}	[bmpyr][Tf_2N] Origin + ν_{10}	acetonitrile [36] Origin + ν_{10}	$Cs_2UO_2Cl_4$ [37] Origin + ν_{10}	$AlCl_3$-[C_2mim][Cl][7] Band origin
$D_{\infty h}$	D_{4h}					
$\Pi_g \leftarrow \Sigma_g^+$	$E_g \leftarrow A_{1g}$	20144	20132	20208	20200	19992
$\Delta_g \leftarrow \Sigma_g^+$	$B_{2g} \leftarrow A_{1g}$	20563	20568	20635	20512	20323
$\Phi_g \leftarrow \Sigma_g^+$	$E_g \leftarrow A_{1g}$	--	--	--	22135	--
$\Delta_g \leftarrow \Sigma_g^+$	$B_{2g} \leftarrow A_{1g}$	22894	22894	22935	(22850)	22722
$(\Phi_g, H_g) \leftarrow \Sigma_g^+$	$E_g \leftarrow A_{1g}$	26400	26347	26388	26365	26202

The more pronounced increase of the baseline in the spectrum of [bmpyr][Tf_2N] is possibly caused by the presence of a suspension in the solution, not visible with the naked eye.

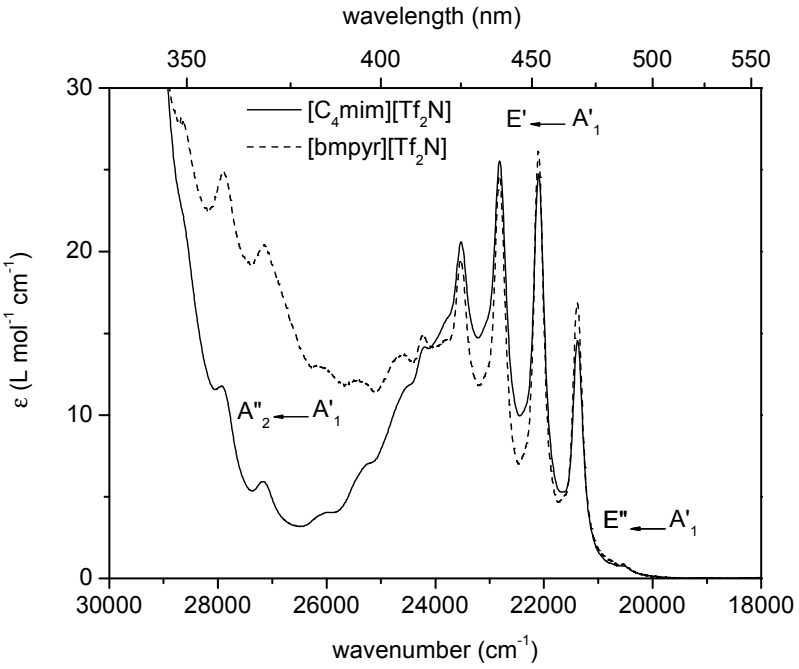

Figure 6.7. UV-Vis absorption spectra of $[UO_2(NO_3)_3]^-$ in [C_4mim][Tf_2N] and [bmpyr][Tf_2N] at room temperature, where $[UO_2^{2+}]/[NO_3^-]_{tot}$ = 1:4. The uranyl concentrations are 5×10^{-2} mol L^{-1} in [C_4mim][Tf_2N] and 10^{-2} mol L^{-1} in [bmpyr][Tf_2N].

A second method consists of dissolving uranium(VI) oxide (UO_3) with concentrated nitric acid in the ionic liquid [C_4mim][Tf_2N]. A similar sample preparation was found in the literature for the oxidative dissolution of uranium(IV) oxide [21]. Concentrated nitric acid contains a certain amount of water. Yet, the ionic liquid [C_4mim][Tf_2N] is immiscible with water, resulting in a phase separation. The UV-Vis

absorption spectrum was taken from the ionic liquid phase, separated from the aqueous phase with a separatory funnel (Figure 6.8). The y-axis is expressed in arbitrary units, because we do not know the exact uranyl concentration in the ionic liquid after the equilibrium has been established.

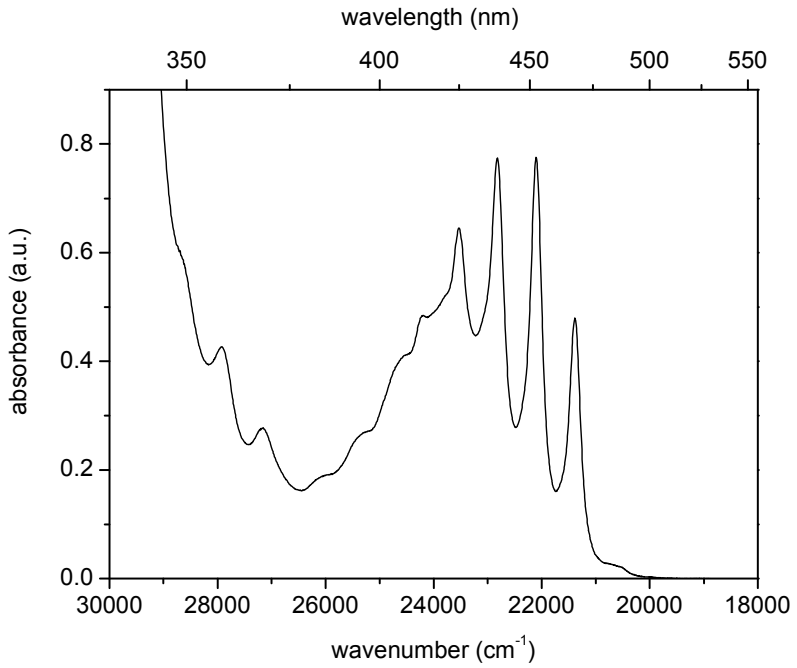

Figure 6.8. UV-Vis absorption spectrum of $[UO_2(NO_3)_3]^-$ in $[C_4mim][Tf_2N]$ at room temperature, by dissolving UO_3 in $HNO_3/[C_4mim][Tf_2N]$. The initial uranyl concentration is 5×10^{-2} mol L^{-1}.

In the ionic liquids, the absorption coefficient of the uranyl ion in the presence of nitrate ions is of the same order of magnitude as in acetonitrile. The UV-Vis absorption spectra of $UO_2(NO_3)_2 \cdot 6H_2O$ with nitrate ions added in $[C_4mim][Tf_2N]$ and $[bmpyr][Tf_2N]$ as well as the spectrum of UO_3 in $HNO_3/[C_4mim][Tf_2N]$ display very intense, sharp

peaks between 21000 cm^{-1} and 24000 cm^{-1}. This observation is a first indication of the formation of $[UO_2(NO_3)_3]^-$ in the ionic liquids. Additional evidence originates from the corresponding MCD spectra. Indeed, very intense negative A-terms catch the eye in the MCD spectrum of $[UO_2(NO_3)_3]^-$, as described in Chapter 5 [45,46]. Recording the MCD spectra of both $UO_2(NO_3)_2 \cdot 6H_2O$ with nitrate ions in $[C_4mim][Tf_2N]$ and UO_3 in $HNO_3/[C_4mim][Tf_2N]$ yields very intense negative A-terms, as clearly observed in Figure 6.9. Thus, the features in the long-wavelength part of the UV-Vis absorption spectra and the MCD spectra as well as a comparison with the well-known spectrum of the $[UO_2(NO_3)_3]^-$ complex in non-aqueous solvents unambiguously point to the formation of a $[UO_2(NO_3)_3]^-$ species with D_{3h} coordination symmetry in the ionic liquids $[C_4mim][Tf_2N]$ and [bmpyr][Tf_2N], regardless of the sample preparation used.

The emission spectrum of $[UO_2(NO_3)_3]^-$ in [bmpyr][Tf_2N] shows the typical vibrational fine structure of the uranyl trinitrato complex (Figure 6.10) (see Chapter 5, Figure 5.21). Three sharp and intense peaks are observed between 19000 cm^{-1} and 22000 cm^{-1}. The ground state value of ν_s is approximately 867 cm^{-1}, which resembles the value in acetonitrile (872 cm^{-1}).

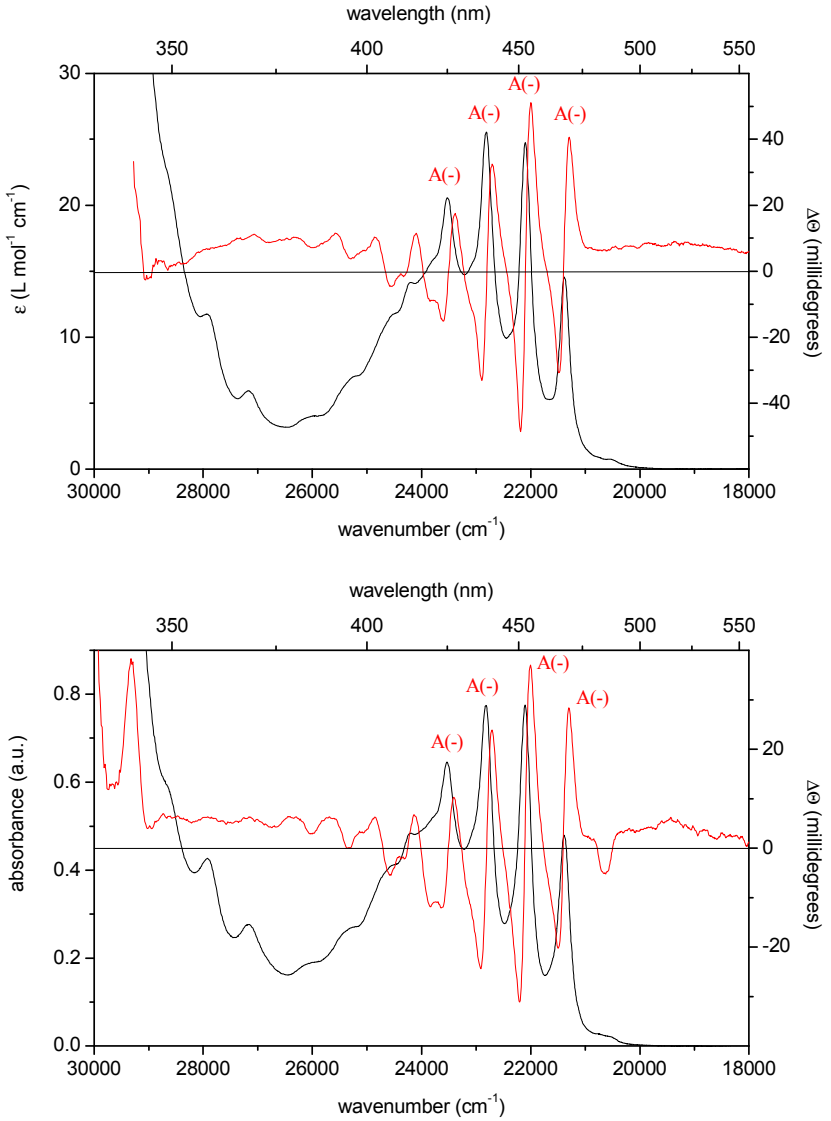

Figure 6.9. UV-Vis absorption (black line) and MCD (red line) spectra of $[UO_2(NO_3)_3]^-$ in $[C_4mim][Tf_2N]$ (upper graph) and UO_3 in $HNO_3/[C_4mim][Tf_2N]$ (lower graph) at room temperature. The uranyl concentration is 5×10^{-2} mol L^{-1}.

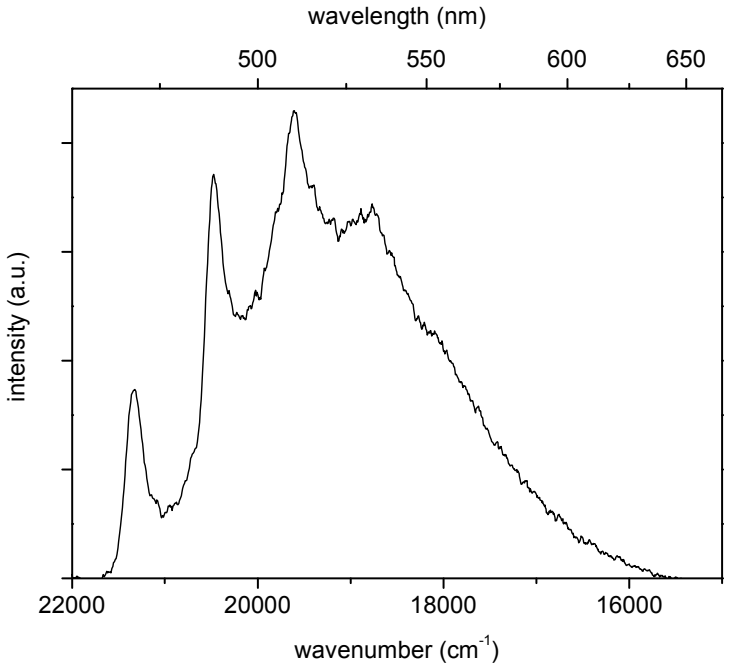

Figure 6.10. Emission spectrum of $[UO_2(NO_3)_3]^-$ in [bmpyr][Tf_2N] at room temperature. The concentrations are $[UO_2^{2+}] = 10^{-2}$ mol L^{-1} ($UO_2(NO_3)_2 \cdot 6H_2O$) and $[NO_3^-] = 2 \times 10^{-2}$ mol L^{-1} (total metal-to-ligand ratio = 1:4). The excitation wavelength is 438.2 nm (23105 cm^{-1}).

The UV-Vis absorption spectra of $[UO_2(NO_3)_3]^-$ in the ionic liquids [C_4mim][Tf_2N] and [bmpyr][Tf_2N] can be interpreted in a similar way as that of $[UO_2(NO_3)_3]^-$ in acetonitrile. In D_{3h} coordination symmetry, the intensity is induced by the static ligand field. The series of very intense, sharp peaks at the low energy side of the UV-Vis absorption spectrum and the corresponding intense negative A-terms in the MCD spectrum, which are typical for a D_{3h} symmetry, originate from the electronic transition $\Delta_g \leftarrow \Sigma_g^+$ (E' $\leftarrow$ A'$_1$ in D_{3h}) [41,43,45,46]. In contrast, the first electronic transition $\Pi_g \leftarrow \Sigma_g^+$ (E" $\leftarrow$ A'$_1$), situated at approximately 20563 cm^{-1}, has low intensity and gives no distinct MCD signal. For a

more detailed interpretation of the electronic transitions in the spectrum of $[UO_2(NO_3)_3]^-$ (D_{3h}), we refer to Chapter 5 and Appendix 3. Table 6.2 lists the transitions we assign for $[UO_2(NO_3)_3]^-$ in $[C_4mim][Tf_2N]$ and [bmpyr][Tf_2N]. For comparison, the energy values of $CsUO_2(NO_3)_3$ single crystals [43] and $[UO_2(NO_3)_3]^-$ in acetonitrile are included.

Uranium L_{III}-edge EXAFS measurements have been carried out to obtain additional evidence for the formation of a $[UO_2(NO_3)_3]^-$ species in the ionic liquid $[C_4mim][Tf_2N]$ by dissolving either $UO_2(NO_3)_2 \cdot 6H_2O$ and tetrabutylammonium nitrate in $[C_4mim][Tf_2N]$ or UO_3 in $HNO_3/[C_4mim][Tf_2N]$. The raw k^3-weighted EXAFS data and the corresponding Fourier transforms are displayed in Figure 6.11. Both EXAFS spectra and corresponding Fourier transforms exhibit similar features as the EXAFS spectrum and the corresponding Fourier transform of $[UO_2(NO_3)_3]^-$ in acetonitrile (Figure 5.23). Besides the scattering contributions of the axial ($R + \Delta = 1.4$ Å) and the equatorial oxygen atoms ($R + \Delta = 2$ Å), the peaks at $R + \Delta = 2.5$ Å and $R + \Delta = 3.7$ Å in the Fourier transforms represent the nitrogen atoms and the distal oxygen atoms of the coordinated nitrate groups, respectively.

Structural parameters of the curve fit procedure including phase correction, are summarized in Table 6.3. The coordination numbers of the equatorial oxygen atoms (O_{eq}) and the nitrogen atoms were determined in an iterative manner, by a free fit. Subsequently, these coordination numbers were fixed during the shell fit procedure in order to avoid correlation problems between N and σ^2. The coordination number of the distal oxygen atoms (O_{dist}) was set equal to the coordination number of the nitrogen atoms.

Table 6.2. Observed electronic transitions of $[UO_2(NO_3)_3]^-$ in $[C_4mim][[Tf_2N]$ and $[bmpyr][Tf_2N]$ at room temperature, assigned in $D_{\infty h}$ and D_{3h} symmetry. Energy values are compared with those of $CsUO_2(NO_3)_3$ single crystals [43] and $[UO_2(NO_3)_3]^-$ in acetonitrile. Energies are given in wavenumber units (cm^{-1}).

Symmetry		$[C_4mim][Tf_2N]$	$[bmpyr][Tf_2N]$	UO_3 in HNO_3/ $[C_4mim][Tf_2N]$	$CsUO_2(NO_3)_3$ [43]	CH_3CN
$D_{\infty h}$	D_{3h}					
$\Pi_g \leftarrow \Sigma_g^+$	$E'' \leftarrow A'_1$	20563	20551	20597	21090	20585
$\Delta_g \leftarrow \Sigma_g^+$	$E' (x,y) \leftarrow A'_1$	21381	21359	21386	21694	21432
$\Phi_g \leftarrow \Sigma_g^+$	$A''_1 \leftarrow A'_1$	--	--	--	22300	--
$(\Delta_g, \Gamma_g) \leftarrow \Sigma_g^+$	$E' (x,y) \leftarrow A'_1$	--	--	--	23475	--
$\Phi_g \leftarrow \Sigma_g^+$	$A''_1 \leftarrow A'_1$	--	--	--	26640	--
$\Phi_g \leftarrow \Sigma_g^+$	$A''_2 \leftarrow A'_1$	27166	27166	27159	27480	27218

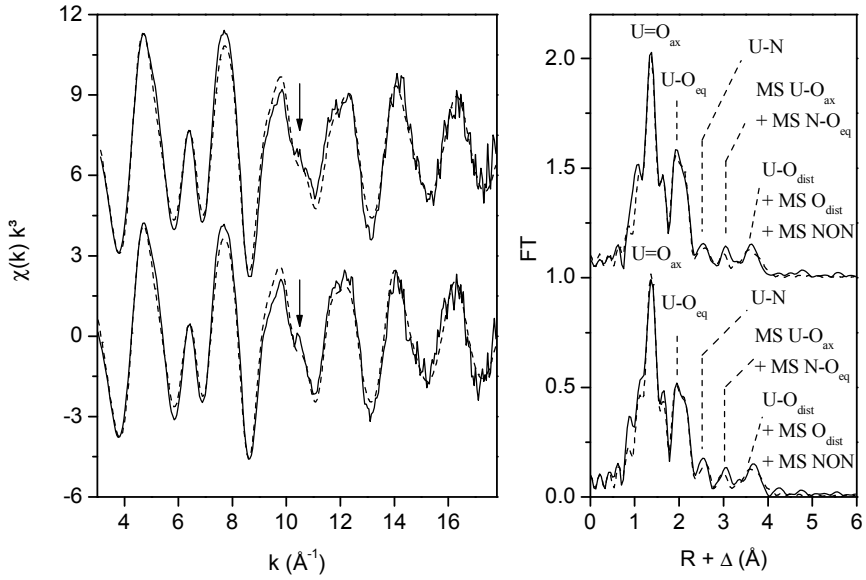

Figure 6.11. Uranium L_{III}-edge k^3-weighted EXAFS data (left) and corresponding Fourier transforms (right), taken over k = 3 - 17.8 Å^{-1}, of $UO_2(NO_3)_2 \cdot 6H_2O$ and tetrabutylammonium nitrate in $[C_4mim][Tf_2N]$ (lower graph) and UO_3 in $HNO_3/[C_4mim][Tf_2N]$ (upper graph). Experimental data are presented as a continuous line with the theoretical curve presented as a dashed line. The multiple scattering path $N\text{-}O_{dist}\text{-}N$ is abbreviated as MS NON. The arrow indicates the [2p4f] double electron excitation [47].

For both experimental approaches, the fit results validate the formation of a $[UO_2(NO_3)_3]^-$ species in the ionic liquid $[C_4mim][Tf_2N]$. The uranyl ion is surrounded by three bidentate nitrate groups in the equatorial plane. In addition, the $U\text{-}O_{eq}$ distance of 2.48-2.49 Å is characteristic for a sixfold coordination of the uranyl ion [48]. Furthermore, the U-N distance of 2.92-2.93 Å indicates a bidentate coordination of the nitrate group. The determination of the $U\text{-}O_{dist}$ distance of approximately 4.17 Å is possible due to the linear arrangement of the nitrogen and the distal oxygen atoms (focusing effect). All structural parameters, obtained by EXAFS spectroscopy, are

consistent with the parameters of $[UO_2(NO_3)_3]^-$ in acetonitrile (Table 5.13) and the crystal structure data of solid $RbUO_2(NO_3)_3$ [49].

Table 6.3. EXAFS structural parameters of $[UO_2(NO_3)_3]^-$ in $[C_4mim][Tf_2N]$.

$UO_2(NO_3)_2 \cdot 6H_2O$ and tetrabutylammonium nitrate in $[C_4mim][Tf_2N]$			
	R (Å)	N	σ^2 (Å²)
U-O_{ax}	1.77	2*	0.0012
MS U-O_{ax}	3.54	2*	0.0024
U-O_{eq}	2.49	6.1	0.0076
U-N	2.92	2.8	0.0036
MS N-O_{eq}	3.28	12.2	0.0054
U-O_{dist}	4.18	2.8	0.0062
MS O_{dist}	4.18	5.6	0.0062
MS N-O_{dist}-N	4.18	2.8	0.0062
UO_3 in HNO_3/$[C_4mim][Tf_2N]$			
	R (Å)	N	σ^2 (Å²)
U-O_{ax}	1.76	2*	0.0012
MS U-O_{ax}	3.53	2*	0.0025
U-O_{eq}	2.48	6.5	0.0072
U-N	2.93	3.1	0.0042
MS N-O_{eq}	3.28	13	0.0069
U-O_{dist}	4.17	3.1	0.0069
MS O_{dist}	4.17	6.2	00069
MS N-O_{dist}-N	4.17	3.1	0.0069

* value fixed during the shell fit procedure, error in distances R is ± 0.01 Å, error in coordination numbers N is ± 10%, ΔE = 3.99 eV and 2.97 eV, respectively.

Concerning the arrangement of the cations and the anions of the ionic liquids $[C_4mim][Tf_2N]$ and $[bmpyr][Tf_2N]$ around the $[UO_2(NO_3)_3]^-$ complex, similar conclusions can be drawn as for the $[UO_2Cl_4]^{2-}$ species [22b,c]. Up to now, no molecular dynamics calculations of the uranyl trinitrato complex in ionic liquids have been reported in the literature.

However, we can assume that a $[UO_2(NO_3)_3]^-$ species is most likely surrounded by the cationic parts of the ionic liquid in absence of water, whereas $[UO_2(NO_3)_3]^-$ is shielded from the cations by a shell of water molecules in wet ionic liquids. The presence of cations and anions of the ionic liquid around the $[UO_2(NO_3)_3]^-$ species is not observed in the uranium L_{III}-edge EXAFS data because of the large distances. Molecular dynamics simulations calculated that imidazolium cations are found within 7.8 Å and 8.9 Å around the $[UO_2Cl_4]^{2-}$ complex in a dry and wet ionic liquid, respectively [22b,c]. Depending on the system studied, EXAFS spectroscopy can merely determine bond distances up to 6 Å.

Besides $[UO_2(NO_3)_3]^-$, the uranyl triacetato complex $[UO_2(CH_3COO)_3]^-$ is a well-known example of species with a D_{3h} trigonal symmetry as well, as stated in Chapter 5 [43,44]. The very intense, sharp absorption maxima, characteristic for a D_{3h} coordination symmetry, are also observed at the low energy end of the UV-Vis absorption spectrum of a solution in $[C_4mim][Tf_2N]$ containing $UO_2(CH_3COO)_2{\cdot}2H_2O$ and tetrabutylammonium acetate in a total metal-to-ligand ratio of 1:4 (Figure 6.12). These spectral features point to the formation of a $[UO_2(CH_3COO)_3]^-$ complex in the ionic liquid $[C_4mim][Tf_2N]$. The UV-Vis absorption spectrum is expressed in arbitrary units, because there was a yellow turbidity present in the solution, lowering the effective uranyl concentration in solution.

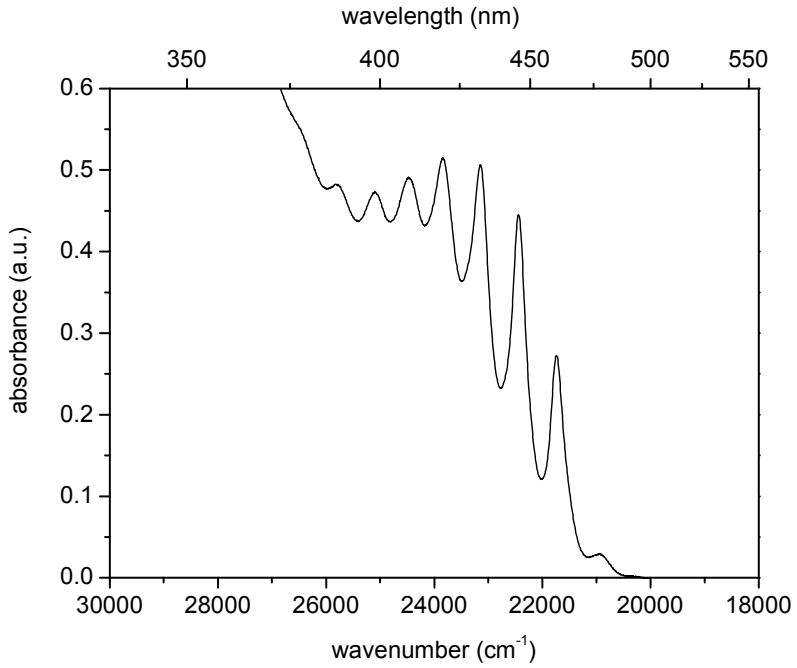

Figure 6.12. UV-Vis absorption spectrum of $[UO_2(CH_3COO)_3]^-$ in $[C_4mim][Tf_2N]$ at room temperature. The concentrations are $[UO_2^{2+}] = 5 \times 10^{-2}$ mol L^{-1} ($UO_2(CH_3COO)_2 \cdot 2H_2O$) and $[CH_3COO^-] = 10^{-2}$ mol L^{-1} (total metal-to-ligand ratio = 1:4).

*3.4 $[UO_2(18\text{-crown-6})]^{2+}$**

Crown ethers are commonly used as neutral extracting agents in separation processes of actinides and rare earths [50]. Nowadays, the application of room temperature ionic liquids in these solvent extraction procedures using crown ethers and other neutral extractants, is under

* Supporting material (see Appendix 3): absorption spectra and numerical data on $[UO_2(18\text{-crown-6})]^{2+}$ in $[C_4mim][Tf_2N]$ and $[bmpyr][Tf_2N]$.

investigation [12,14-16,19]. Good results are obtained for the extraction of Sr^{2+} from aqueous nitric acid media into a series of 1-alkyl-3-methylimidazolium-based room temperature ionic liquids containing dicyclohexano-18-crown-6 [14,16]. However, the extraction process seems to differ from that observed in conventional organic solvents [5,14,16].

The coordination of the uranyl ion with crown ethers has been investigated in acetonitrile and propylene carbonate [51,52]. The inclusion of the uranyl ion in the cavity of a crown ether of appropriate size is stated by means of the remarkable vibrational fine structure in the UV-Vis absorption spectrum [52]. Here, we are interested in the coordination behaviour of the uranyl ion with crown ethers in ionic liquids. The UV-Vis absorption spectrum of the uranyl ion in the presence of the crown ether 18-crown-6 in $[C_4mim][Tf_2N]$ and $[bmpyr][Tf_2N]$ is depicted in Figure 6.13.

From comparison with the UV-Vis absorption spectrum in acetonitrile, it is obvious that the spectra in the ionic liquids $[C_4mim][Tf_2N]$ and $[bmpyr][Tf_2N]$ exhibit spectral features which are characteristic for the inclusion of the uranyl ion in the crown ether ring (see Chapter 5, Figure 5.27) [52]. Thus, the uranyl ion is extracted from an aqueous phase into the ionic liquid as the inclusion complex $[UO_2(18\text{-crown-6})]^{2+}$. As already mentioned in Chapter 5, the cavity of 18-crown-6 (2.6 - 3.2 Å) matches perfectly with the ion diameter of the uranyl ion, 2.8 Å [51a]. The cationic and the anionic parts of the ionic liquid seem to have no influence on the positions of the absorption maxima of $[UO_2(18\text{-crown-6})]^{2+}$. Indeed, there is a good agreement with the UV-Vis data of $[UO_2(18\text{-crown-6})]^{2+}$ in acetonitrile and propylene carbonate [52a].

The luminescence of the $[UO_2(18\text{-crown-6})]^{2+}$ complex could not be detected in $[bmpyr][Tf_2N]$ due to the background fluorescence of the ionic liquid, which was too intense to exceed for $[UO_2(18\text{-crown-6})]^{2+}$.

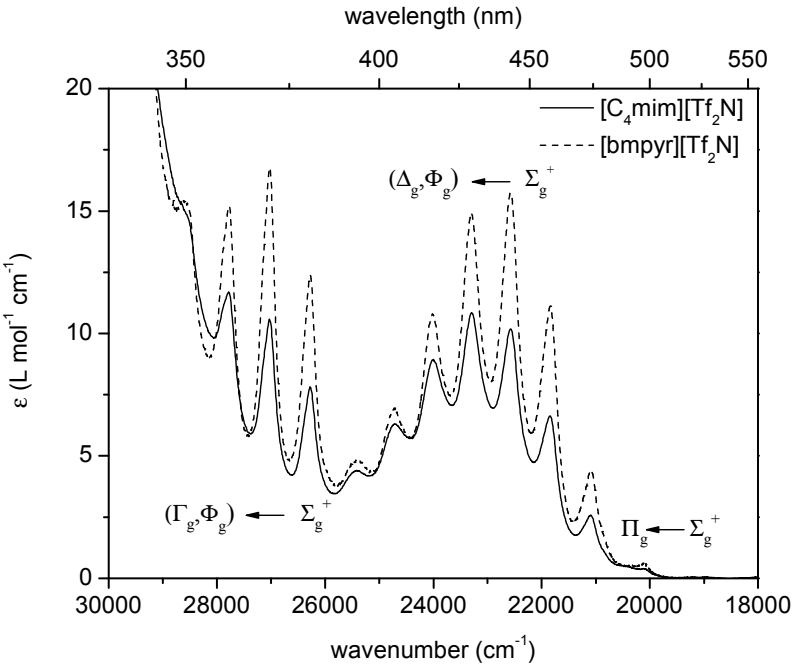

Figure 6.13. UV-Vis absorption spectra of $[UO_2(18\text{-crown-6})]^{2+}$ in $[C_4mim][Tf_2N]$ and $[bmpyr][Tf_2N]$ at room temperature. The uranyl concentrations are 5×10^{-2} mol L^{-1} and 10^{-2} mol L^{-1} in $[C_4mim][Tf_2N]$ and $[bmpyr][Tf_2N]$, respectively. The metal-to-ligand ratio is 1:2.

The vibrational fine structure in the spectrum of $[UO_2(18\text{-crown-6})]^{2+}$ can be explained in terms of a D_{3d} (D_3) coordination symmetry. The special features between 26000 cm^{-1} and 29000 cm^{-1} can only be attributed to the transition $\Gamma_g \leftarrow \Sigma_g^+$. This transition, arising from the $\sigma_u^+ \phi_u$ configuration, is typical for a D_3 coordination symmetry. The derivation of the coordination symmetry and the electronic transitions in the spectrum of $[UO_2(18\text{-crown-6})]^{2+}$ is described in more detail in Chapter 5. An overview of the energies of the different electronic transitions of $[UO_2(18\text{-crown-6})]^{2+}$ in $[C_4mim][Tf_2N]$ and $[bmpyr][Tf_2N]$ is listed in Table 6.4. For comparison, the assignment of the electronic

transitions in the spectrum of the inclusion complex in acetonitrile is included as well [52a].

Based on the molecular dynamics calculations of the solvation of the uranyl ion and $[UO_2Cl_4]^{2-}$ in dry and wet $[C_4mim][PF_6]$, it is reasonable to assume that the inclusion complex $[UO_2(18\text{-crown-6})]^{2+}$ is surrounded by Tf_2N^- anions in the absence of water molecules [22b,c]. But, in a wet ionic liquid the direct environment of $[UO_2(18\text{-crown-6})]^{2+}$ consists of a shell of water molecules, thereby keeping the anions of the ionic liquid at a larger distance.

Influence of ligand competition

Extraction processes of uranyl often occur in acidic media, for example with HNO_3 or HCl. De Houwer et al. have noticed that crown ethers are displaced from the first coordination sphere of the uranyl ion upon addition of small inorganic ligands like NO_3^- and Cl^-. Instead of the vibrational fine structure of the $[UO_2(18\text{-crown-6})]^{2+}$ inclusion complex, the characteristic features of $[UO_2(NO_3)_3]^-$ and $[UO_2Cl_4]^{2-}$ are observed [52b]. Since these ions affect the structure of the extracted complex and the extraction constant, it is important to know their influence on the uranyl crown complexes in ionic liquids, if one wants to use ionic liquids as potential alternatives to the classical organic solvents.

In case of UO_2Cl_2 dissolved in $[C_6mim][Cl]$ in the presence of the crown ether 18-crown-6, the same effect is detected as in acetonitrile and propylene carbonate: the UV-Vis absorption spectrum is highly vibronic in nature, characteristic for the $[UO_2Cl_4]^{2-}$ species (Figure 6.14).

Table 6.4. Observed electronic transitions of $[UO_2(18\text{-crown-}6)]^{2+}$ in $[C_4mim][Tf_2N]$ and $[bmpyr][Tf_2N]$ at room temperature, assigned in $D_{\infty h}$, D_{3d} and D_3 symmetry. For comparison, the energy values of $[UO_2(18\text{-crown-}6)]^{2+}$ in acetonitrile are included [52a]. Energies are given in wavenumber units (cm^{-1}).

Symmetry			$[UO_2(18C6)]^{2+}$	$[UO_2(18C6)]^{2+}$	$[UO_2(18C6)]^{2+}$
$D_{\infty h}$	D_{3d}	D_3	$[C_4mim][Tf_2N]$	$[bmpyr][Tf_2N]$	acetonitrile [52a]
$\Pi_g \leftarrow \Sigma_g^+$	$E_g \leftarrow A_{1g}$	$E\ (x,y) \leftarrow A_1$	20092	20125	20109
$\Phi_g \leftarrow \Sigma_g^+$	$A_{1g} \leftarrow A_{1g}$	$A_1 \leftarrow A_1$	--	--	--
	$A_{2g} \leftarrow A_{1g}$	$A_2\ (z) \leftarrow A_1$	21093	21088	21101
$\Delta_g \leftarrow \Sigma_g^+$	$E_g \leftarrow A_{1g}$	$E\ (x,y) \leftarrow A_1$	22578	22594	22578
$\Phi_g \leftarrow \Sigma_g^+$	$A_{1g} \leftarrow A_{1g}$	$A_1 \leftarrow A_1$	--	--	--
	$A_{2g} \leftarrow A_{1g}$	$A_2\ (z) \leftarrow A_1$	23299	23288	23299
$\Gamma_g \leftarrow \Sigma_g^+$	$E_g \leftarrow A_{1g}$	$E\ (x,y) \leftarrow A_1$	25419	25387	25432
$\Phi_g \leftarrow \Sigma_g^+$	$A_{1g} \leftarrow A_{1g}$	$A_1 \leftarrow A_1$	--	--	--
	$A_{2g} \leftarrow A_{1g}$	$A_2\ (z) \leftarrow A_1$	25947	25947	25981

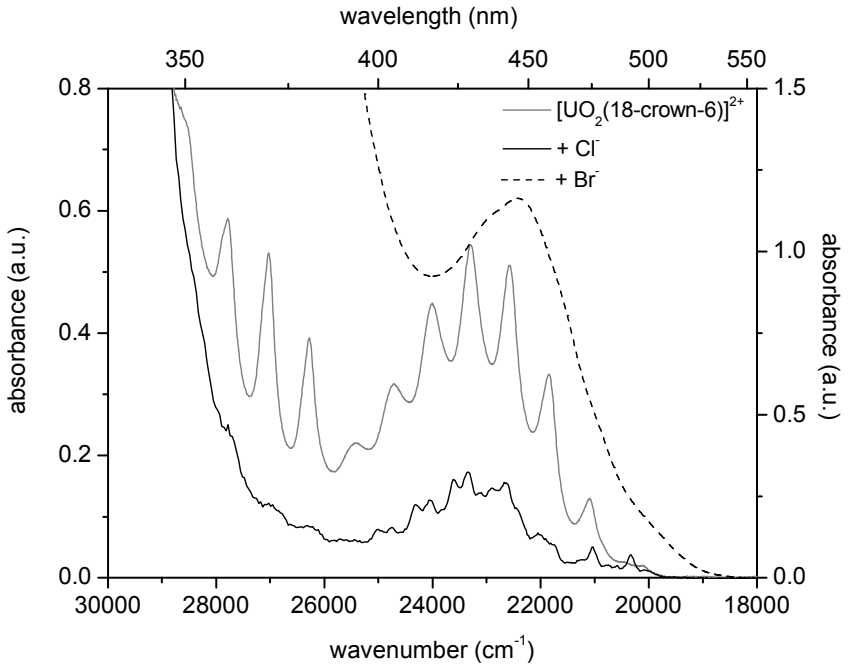

Figure 6.14. UV-Vis absorption spectrum of $[UO_2(18\text{-crown-6})]^{2+}$ with an excess of chloride and bromide ions at room temperature. The ionic liquids used are $[C_6mim][Cl]$, $[C_6mim][Br]$ and $[C_4mim][Tf_2N]$.

The effect of bromide ions on the formation of $[UO_2(18\text{-crown-6})]^{2+}$ in ionic liquids has been investigated as well. Therefore, UO_2Br_2 was dissolved in $[C_6mim][Br]$ together with the crown ether 18-crown-6. The corresponding UV-Vis absorption spectrum, displayed in Figure 6.14, coincides with neither the spectrum of $[UO_2(18\text{-crown-6})]^{2+}$ nor the spectrum of $[UO_2Br_4]^{2-}$ [38]. Instead, a broad, intense band without any fine structure is observed. In addition, the charge transfer band is shifted towards lower energies. However, literature data reveal that such a broad structureless band can be attributed to the hydrolysis products of the uranyl ion [53].

The uranyl ion is prone to hydrolysis in solutions with a pH value ≥ 2.5. With increasing pH, uranyl hydrolysis results in polynuclear species with the general formula $[(UO_2)_m(OH)_n]^{2m-n}$ [53,54]. Two of the most predominant complexes are the dimer $[(UO_2)_2(OH)_2]^{2+}$ and the trimer $[(UO_2)_3(OH)_5]^{+}$ [53]. When a certain amount of water is present in the ionic liquid, these water molecules can coordinate to the uranyl ion. This coordination to the uranyl ion results in a higher acidity of the protons of water. If in addition a base like non-reacted 1-methylimidazole, is present in the ionic liquid, these coordinated water molecules can be deprotonated, leading to the formation of hydrolysis products and the corresponding structureless band in the UV-Vis absorption spectrum.

Our presumption of the formation of hydrolysis products, caused by the presence of non-reacted 1-methylimidazole, was confirmed by a crystal structure determination. An aqueous solution of $[C_6mim][Br]$, UO_2Br_2 and 18-crown-6 was evaporated in air at room temperature, giving a suitable crystal for a X-ray crystal structure determination. The structure of the asymmetrical unit of $[(UO_2)_2(\mu_2\text{-}OH)_2(H_2O)_6][UO_2Br_4](18\text{-crown-}6)_4$ is shown in Figure 6.15. For the packing of the molecules in the unit cell and a table of the crystallographic data, we refer to Appendix 4. The hydrolysis product consists of two uranyl units, bridged by two hydroxide groups. The uranyl ions have completed their unsaturated coordination shell with water molecules, thereby achieving an equatorial coordination number of five. Strong hydrogen bonding is found for all coordinated water molecules and hydroxide groups. Besides the hydrolysis product of the uranyl ion, $[UO_2Br_4]^{2-}$ species are formed as well. But, their presence is not detected by UV-Vis absorption spectroscopy due to the high molar absorptivity of the hydrolysis product $[(UO_2)_2(\mu_2\text{-}OH)_2(H_2O)_6]^{2+}$ [53].

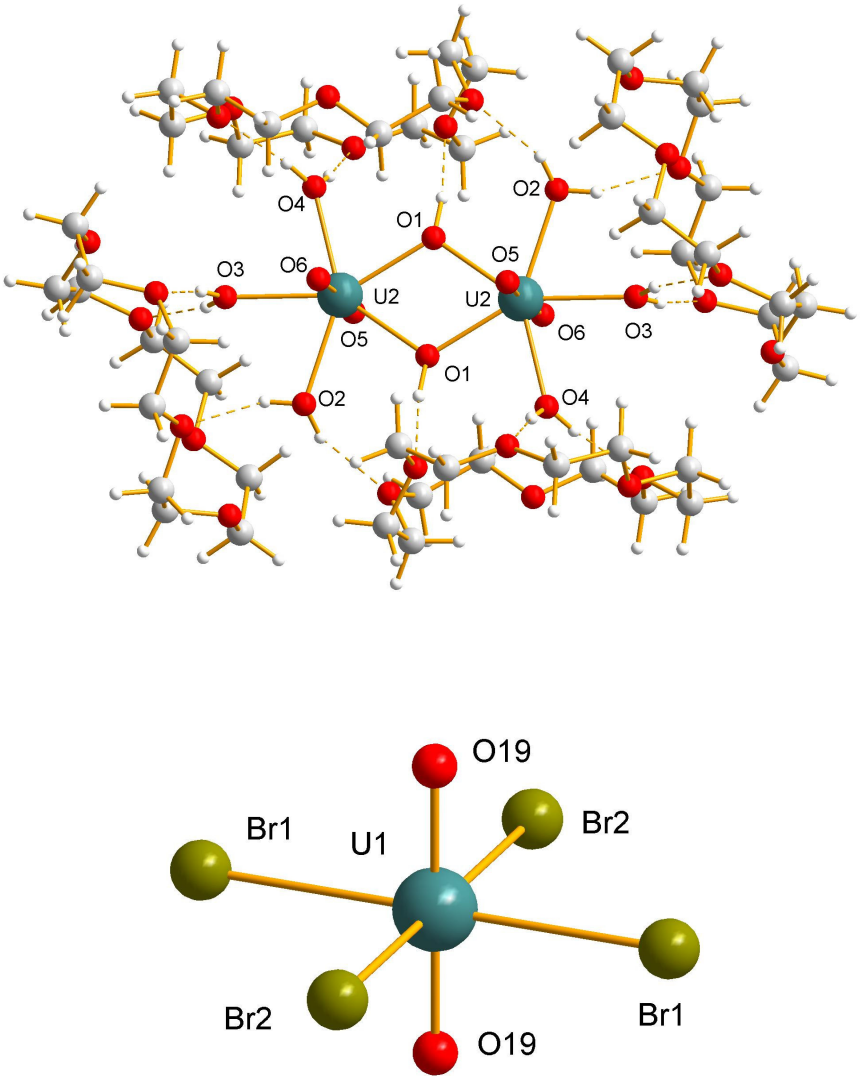

Figure 6.15. Cut-out from the crystal structure of $[(UO_2)_2(\mu_2\text{-}OH)_2(H_2O)_6][UO_2Br_4](18\text{-crown-}6)_4$, showing the $[(UO_2)_2(\mu_2\text{-}OH)_2(H_2O)_6]^{2+}$ cation surrounded by four 18-crown-6 moieties, attached by strong hydrogen bonding (upper part) and the $[UO_2Br_4]^{2-}$ anion of the structure $[(UO_2)_2(\mu_2\text{-}OH)_2(H_2O)_6][UO_2Br_4](18\text{-crown-}6)_4$ (lower part).

From this crystal structure determination, it is obvious that the uranyl ion prefers coordination to bromide ions rather than to the crown ether 18-crown-6. The $[(UO_2)_2(\mu_2\text{-}OH)_2(H_2O)_6]^{2+}$ cations are surrounded by four 18-crown-6 molecules.

Upon addition of hydrogen bromide, the hydrolysis of the uranyl ion is repelled. Only the $[UO_2Br_4]^{2-}$ complex is formed, which is clear from Figure 6.16. These crystals were grown from an aqueous solution of $[C_6mim][Br]$, UO_2Br_2 and 18-crown-6 with a pH value < 2.5. The packing of the molecules in the unit cell is shown in Appendix 4, together with the table of crystallographic data.

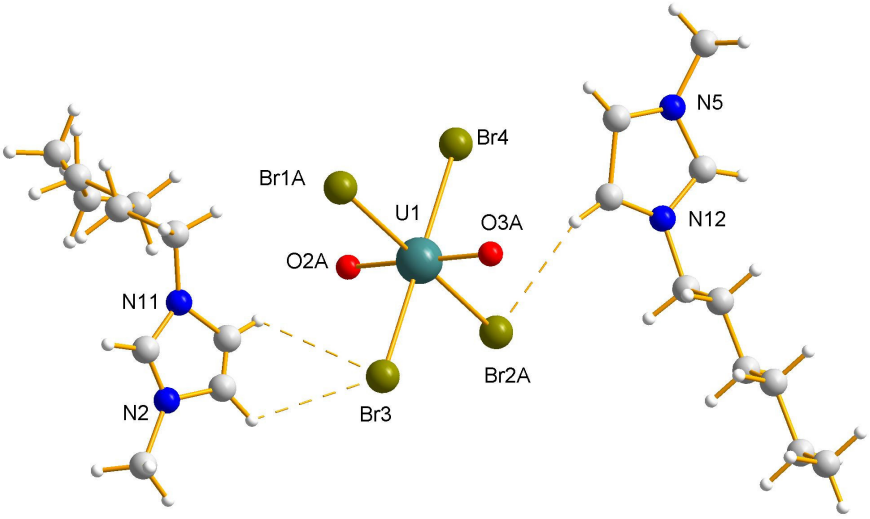

Figure 6.16. Cut-out from the crystal structure of $[C_6mim]_2[UO_2Br_4]$ showing the $[UO_2Br_4]^{2-}$ anion with weak hydrogen bonding to two surrounding $[C_6mim]^+$ cations.

The first coordination sphere of the uranyl ion consists of four bromide ions, which confirms again the preference of the uranyl ion to coordinate to small inorganic ligands (NO_3^-, Cl^-, Br^-) rather than to oxacrown ethers [52b]. Each $[UO_2Br_4]^{2-}$ unit is surrounded by two imidazolium cations of the ionic liquid, which is consistent with the

results of molecular dynamics simulations of the coordination environment of $[UO_2Cl_4]^{2-}$ in ionic liquids [22a]. Weak hydrogen bonding interactions are found between the bromide ions and the acidic hydrogen atoms of the imidazolium cations.

4 Conclusions and outlook

The speciation of uranyl complexes has been investigated in several imidazolium-based and pyrrolidinium-based room temperature ionic liquids by means of UV-Vis absorption spectroscopy, luminescence spectroscopy and uranium L_{III}-edge EXAFS spectroscopy. Thereby, the anionic components of the ionic liquids were varied.

By dissolving either $UO_2(Tf_2N)_2$ or $UO_2(ClO_4)_2{\cdot}xH_2O$ in ionic liquids of the type [A][Tf_2N] ([A] = [C_6mim], [C_4mim] or [bmpyr]), the spectrum of the hydrated "free" uranyl ion $[UO_2(H_2O)_5]^{2+}$ is obtained. Indeed, the anions Tf_2N^- and ClO_4^- are known to be weakly coordinating in aqueous solution. Probably, there was still some small amount of water present in the ionic liquids, which tends to coordinate to the uranyl ion. However, the coordination of Tf_2N^- anions can not be ruled out in dry ionic liquids. Up to now, we were not able to find indications for coordination of bis(trifluoromethylsulfonyl)imide anions to UO_2^{2+} in very dry ionic liquids.

The appearance of their own characteristic vibrational fine structure in the UV-Vis absorption spectrum gives evidence for the formation of the uranyl complexes $[UO_2Cl_4]^{2-}$, $[UO_2(NO_3)_3]^-$, $[UO_2(CH_3COO)_3]^-$ and $[UO_2(18\text{-crown-}6)]^{2+}$ in [C_4mim][Tf_2N] and [bmpyr][Tf_2N]. The cations and the anions of the ionic liquids seem to have no influence on the positions of the absorption maxima. There is a good agreement with the corresponding UV-Vis data in non-aqueous solvents. Only the luminescence of the uranyl tetrachloro complex and the uranyl trinitrato

species is intense enough to exceed the background fluorescence of the ionic liquid [bmpyr][Tf_2N].

Uranium L_{III}-edge EXAFS measurements confirm the formation of a $[UO_2(NO_3)_3]^-$ species in [C_4mim][Tf_2N], thereby using two different experimental approaches. Both mixing $UO_2(NO_3)_2 \cdot 6H_2O$ with tetrabutylammonium nitrate in [C_4mim][Tf_2N] and dissolving UO_3 with concentrated nitric acid in [C_4mim][Tf_2N] yield the uranyl trinitrato complex. The structural parameters of $[UO_2(NO_3)_3]^-$ in the ionic liquid correspond well to those obtained in acetonitrile (see Chapter 5) and to the crystal structure data of solid $RbUO_2(NO_3)_3$. The cations of the ionic liquid were not detected in the EXAFS spectrum due to the large distance.

Since small inorganic ligands (Cl^-, NO_3^-, Br^-) affect the extraction process of UO_2^{2+} with crown ethers, their influence on the formation of the inclusion complex $[UO_2(18\text{-crown-6})]^{2+}$ in ionic liquids was also investigated. A similar effect is encountered as in acetonitrile and propylene carbonate. Once chloride ions are present in solution, the crown ether is removed from the first coordination sphere. The characteristic vibrational fine structure of $[UO_2Cl_4]^{2-}$ appears in the UV-Vis absorption spectrum. The replacement of 18-crown-6 by bromide ions is stated by crystal structure determinations.

One has to make sure that all 1-methylimidazole has reacted during the synthesis of imidazolium-based ionic liquids. Otherwise, uranyl hydrolysis products will be formed, thereby altering the UV-Vis absorption spectrum into a broad and structureless band. The presence of non-reacted 1-methylimidazole can be probed with copper(II) chloride. This method is based on the complex formation of 1-methylimidazole with copper(II) chloride in ethanol, thereby forming the $[Cu(mim)_4]^{2+}$ ion, which has an intense blue colour [55].

Concerning the coordination environment of the uranyl complexes in ionic liquids, deductions can be made from the work of Chaumont and Wipff [22]. One can imagine that anionic complexes are surrounded by

the cationic components of the ionic liquids, while the ionic liquid anions shield the cationic complex $[UO_2(18\text{-crown-}6)]^{2+}$ from the imidazolium or pyrrolidinium cations in dry ionic liquids. But, in wet ionic liquids, all uranyl complexes are surrounded by a shell of water molecules.

In future, uranium L_{III}-edge EXAFS measurements will be performed on the other complexes obtained in ionic liquids, i.e. "free" uranyl ion, $[UO_2Cl_4]^{2-}$, $[UO_2(CH_3COO)_3]^-$ and $[UO_2(18\text{-crown-}6)]^{2+}$. In this way, the structural parameters in ionic liquids can be compared with those in acetonitrile. Furthermore, it is very interesting to study the kinetic effect, which is involved in the sample preparation, in more detail. A possible option for doing this is to monitor the UV-Vis absorption spectrum of a sample of a certain uranyl complex as a function of time to see when the typical vibrational fine structure is achieved.

References

[1] Welton, T. *Chem. Rev.* **1999**, *99*, 2071-2083.

[2] Earle, M.J.; Seddon, K.R. *Pure Appl. Chem.* **2000**, *72*, 1391-1398.

[3] Wasserscheid, P.; Keim, W. *Angew. Chem. Int. Ed.* **2000**, *39*, 3773-3789.

[4] Wasserscheid, P.; Welton, T. (Eds.) *Ionic Liquids in Synthesis*, **2002**, Wiley-VCH, Weinheim.

[5] Binnemans, K. *Chem. Rev*. **2007**, *107*, 2592-2614 and references therein.

[6] Visser, A.E.; Rogers, R.D. *J. Solid State Chem.* **2003**, *171*, 109-113.

[7] Hopkins, T.A.; Berg, J.M.; Costa, D.A.; Smith, W.H.; Dewey, H.J. *Inorg. Chem.* **2001**, *40*, 1820-1825.

[8] Cocalia, V.A.; Gutowski, K.E.; Rogers, R.D. *Coord. Chem. Rev.* **2006**, *250*, 755-764 and references therein.

[9] Anderson, C.J.; Deakin, M.R.; Choppin, G.R.; D'Olieslager, W.; Heerman, L.; Pruett, D.J. *Inorg. Chem.* **1991**, *30*, 4013-4016.

[10] Rogers, R.D.; Seddon, K.R.; Volkov, S. (Eds.) *Green Industrial Applications of Ionic Liquids*, **2003**, Kluwer Academic Publishers, Dordrecht-Boston-London, p. 209-226.

[11] Jensen, M.P.; Neuefeind, J.; Beitz, J.V.; Skanthakumar, S.; Soderholm, L. *J. Am. Chem. Soc.* **2003**, *125*, 15466-15473 and references therein.

[12] Dietz, M.L. *Sep. Sci. Technol.* **2006**, *41*, 2047-2063.

[13] Gaillard, C.; Billard, I.; Chaumont, A.; Mekki, S.; Ouadi, A.; Denecke, M.A.; Moutiers, G.; Wipff, G. *Inorg. Chem.* **2005**, *44*, 8355-8367.

[14] Dietz, M.L.; Dzielawa, J.A. *Chem. Commun.* **2001**, 2124-2125.

[15] Jensen, M.P.; Dzielawa, J.A.; Rickert, P.; Dietz, M.L. *J. Am. Chem. Soc.* **2002**, *124*, 10664-10665.

[16] Dai, S.; Ju, Y.H.; Barnes, C.E. *J. Chem. Soc., Dalton Trans.* **1999**, 1201-1202.

[17] Klingshirn, M.A.; Broker, G.A.; Holbrey, J.D.; Shaughnessy, K.H.; Rogers, R.D. *Chem. Commun.* **2002**, 1394-1395.

[18] Wasserscheid, P.; Gordon, C.M.; Hilgers, C.; Muldoon, M.J.; Dunkin, I.R. *Chem. Commun.* **2001**, 1186-1187.

[19] Giridhar, P.; Venkatesan, K.A.; Srinivasan, T.G.; Vasudeva Rao, P.R. *J. Radioanal. Nucl. Chem.* **2005**, *265*, 31-38.

[20] Visser, A.E.; Jensen, M.P.; Laszak, I.; Nash, K.L.; Choppin, G.R.; Rogers, R.D. *Inorg. Chem.* **2003**, *42*, 2197-2199.

[21] (a) Bradley, A.E.; Hardacre, C.; Nieuwenhuyzen, M.; Pitner, W.R.; Sanders, D.; Seddon, K.R.; Thied, R.C. *Inorg. Chem.* **2004**, *43*, 2503-2514. (b) Bradley, A.E.; Hatter, J.E.; Nieuwenhuyzen, M.; Pitner, W.R.; Seddon, K.R.; Thied, R.C. *Inorg. Chem.* **2002**, *41*, 1692-1694.

[22] (a) Chaumont, A.; Wipff, G. *Phys. Chem. Chem. Phys.* **2003**, *5*, 3481-3488. (b) Chaumont, A.; Engler, E.; Wipff, G. *Inorg. Chem.* **2003**, *42*, 5348-5356. (c) Chaumont, A.; Wipff, G. *Inorg. Chem.* **2004**, *43*, 5891-5901. (d) Chaumont, A.; Wipff, G. *Chem. Eur. J.* **2004**, *10*, 3919-3930. (e) Chaumont, A.; Wipff, G. *J. Phys. Chem. B* **2004**, *108*, 3311-3319. (f) Chaumont, A.; Wipff, G. *Phys. Chem. Chem. Phys.* **2005**, *7*, 1926-1932. (g) Chaumont, A.; Wipff, G. *Phys. Chem. Chem. Phys.* **2006**, *8*, 494-502.

[23] Bhatt, A.I.; du Fou de Kerdaniel, E.; Kinoshita, H.; Livens, F.R.; May, I.; Polovov, I.B.; Sharrad, C.A.; Volkovich, V.A.; Charnock, J.M.; Lewin, R.G. *Inorg. Chem.* **2005**, *44*, 2-4.

[24] Sornein, M.-O.; Cannes, C.; Le Naour, C.; Lagarde, G.; Simoni, E.; Berthet, J.-C. *Inorg. Chem.* **2006**, *45*, 10419-10421.

[25] Visser, A.E.; Rogers, R.D. *J. Solid State Chem.* **2003**, *171*, 109-113.

[26] Zhao, D.; Liao, Y.; Zhang, Z. *Clean* **2007**, *35*, 42-48.

[27] Nelson, W.M. *ACS Symp. Ser.* **2002**, *818*, 30-41.

[28] Swatloski, R.P.; Holbrey, J.D.; Rogers, R.D. *Green Chem.* **2003**, *5*, 361-363.

[29] Rogers, R.D.; Seddon, K.R. (Eds.) *Ionic liquids: Industrial Applications for Green Chemistry*; ACS Symposium Series 818, **2002**, American Chemical Society, Washington, DC.

[30] Nockemann, P.; Binnemans, K.; Driesen, K. *Chem. Phys. Lett.* **2005**, *415*, 131-136 and references therein.

[31] Gaillard, C.; El Azzi, A.; Billard, I.; Bolvin, H.; Hennig, C. *Inorg. Chem.* **2005**, *44*, 852-861.

[32] Mudring, A.-V.; Babai, A.; Arenz, A.; Giernoth, R. *Angew. Chem. Int. Ed.* **2005**, *44*, 5485-5488.

[33] Billard, I.; Moutiers, G.; Labet, A.; El Azzi, A.; Gaillard, C.; Mariet, C.; Lützenkirchen, K. *Inorg. Chem.* **2003**, *42*, 1726-1733.

[34] Bhatt, A.I.; May, I.; Volkovich, V.A.; Collison, D.; Helliwel, M.; Polovov, I.B.; Lewin, R.G. *Inorg. Chem.* **2005**, *44*, 4934-4940.

[35] Görller-Walrand, C.; De Houwer, S.; Fluyt, L.; Binnemans, K. *Phys. Chem. Chem. Phys.* **2004**, *6*, 3292-3298.

[36] Servaes, K.; Hennig, C.; Van Deun, R.; Görller-Walrand, C. *Inorg. Chem.* **2005**, *44*, 7705-7707.

[37] Denning, R.G.; Snellgrove, T.R.; Woodwark, D.R. *Mol. Phys.* **1976**, *32*, 419-442.

[38] Görller-Walrand, C.; De Jaegere, S. *J. Chim. Phys.* **1973**, *2*, 360-366.

[39] Ryan, J.L. *Inorg. Chem.* **1963**, *2*, 348-358.

[40] Deetlefs, M.; Hussey, C.L.; Mohammed, T.J.; Seddon, K.R.; van den Berg, J.-A.; Zora, J.A. *Dalton Trans.* **2006**, 2334-2341.

[41] Dieke, G.H.; Duncan, A.B.F. *Spectroscopic Properties of Uranium Compounds*, **1965**, McGraw Hill, New York.

[42] Rabinowitch, E.; Belford, R.L. *Spectroscopy and Photochemistry of Uranyl Compounds*, **1964**, Pergamon, Oxford.

[43] Denning, R.G.; Foster, D.N.P.; Snellgrove, T.R.; Woodwark, D.R. *Mol. Phys.* **1979**, *37*, 1089-1107.

[44] Görller-Walrand, C.; De Jaegere, S. *J. Chim. Phys.* **1972**, *4*, 726-736.

[45] Brint, P.; McCaffery, A.J. *Mol. Phys.* **1973**, *25*, 311-322.

[46] Görller-Walrand, C.; Colen, W. *Inorg. Chim. Acta* **1984**, *84*, 183-188.

[47] Hennig, C. *Phys. Rev. B.* **2007**, *75*, 035120.

[48] Antonio, M.R.; Soderholm, L. "X-ray Absorption Spectroscopy of the Actinides" in *The Chemistry of the Actinide and Transactinide Elements* (3rd edition); Eds. Morss, L.R.; Edelstein, N.M.; Fuger, J., **2006**, Springer, Dordrecht, The Netherlands, p. 3086-3189.

[49] Zalkin, A.; Templeton, L.K.; Templeton, D.H. *Acta Cryst.* **1989**, *C45*, 810-811.

[50] Zolotov, Yu. A. *Macrocyclic Compounds in Analytical Chemistry*, **1997**, John Wiley & Sons, New York.

[51] (a) Lagrange, J.; Metabanzoulou, J.P.; Fux, P.; Lagrange, P. *Polyhedron* **1989**, *8*, 2251-2254. (b) Brighli, M.; Fux, P.; Lagrange, J.; Lagrange, P. *Inorg. Chem.* **1985**, *24*, 80-84. (c) Fux, P.; Lagrange, J.; Lagrange, P. *J. Am. Chem. Soc.* **1985**, *107*, 5927-5931.

[52] (a) De Houwer, S.; Servaes, K; Görller-Walrand, C. *Phys. Chem. Chem. Phys.* **2003**, *5*, 1164-1168. (b) Servaes, K.; De Houwer, S.; Görller-Walrand, C.; Binnemans, K. *Phys. Chem. Chem. Phys.* **2004**, *6*, 2946-2950.

[53] Meinrath, G. *J. Radioanal. Nucl. Chem.* **1997**, *224*, 119-126.

[54] Katz, J.J.; Seaborg, G.T.; Morss, L.R. *The Chemistry of the Actinide Elements*, **1986**, Chapman and Hall, New York.

[55] Holbrey, J.D.; Seddon, K.R.; Wareing, R. *Green Chemistry* **2001**, *3*, 33-36.

7 SPECTROSCOPIC PROPERTIES OF $UO_2(NO_3)_2(TBP)_2$

1 Introduction

These days, the coordination behaviour of the uranyl ion is of growing interest due to the problem of nuclear waste treatment and environmental issues. Liquid-liquid extraction is a commonly used method in the treatment of nuclear waste. Indeed, at the end of the nuclear fuel cycle, reprocessing of the spent fuel mainly occurs by means of the liquid-liquid extraction procedure. The design of new, more selective extracting agents for the reprocessing of spent nuclear fuel demands an insight in the structure of the complexes formed during these extraction processes. Therefore, a lot of research is ongoing, not only to improve the liquid-liquid extraction processes of uranium and plutonium, but also to elucidate the structure of the extraction species formed [1-7]. Attempts are made to ameliorate the extraction procedures by using supercritical CO_2 or ionic liquids [8-10]. In most liquid-liquid extraction processes, organophosphate ($-OPO_3R_3$) ligands are used as neutral extracting agents. The influence of the steric effect of the alkyl groups in $[UO_2(NO_3)_2(OPO_3R_3)_2]$ (where R is an alkyl group) on the U-O bond

lengths has been studied by EXAFS spectroscopy. A full description of the geometry of the complexes can reveal a relation with the extracting power of the organophosphate compounds [1].

During the PUREX process (*Plutonium and Uranium Recovery by EXtraction*), the spent nuclear fuel is dissolved in a nitric acid solution. Plutonium and uranium are extracted from this aqueous nitric acid fuel solution with an organic phase (mostly kerosene) containing tri-*n*-butylphosphate (TBP) as extracting agent. The following reaction takes place [11]:

$$UO_2^{2+}{}_{(aq)} + 2NO_3^-{}_{(aq)} + 2TBP_{(org)} \rightleftharpoons UO_2(NO_3)_2(TBP)_{2(org)}$$

The structure of the extracted species $UO_2(NO_3)_2(TBP)_2$ has always fascinated many researchers [1,12]. A crystal structure of $UO_2(NO_3)_2(TBP)_2$ could not be determined, because the complex formed with the most frequently used neutral extractant is a liquid at room temperature. The crystal structures of analogous uranium(VI) organophosphate compounds, however, are already known for a long time [13-15]. For example, the analog with tri-*iso*-butylphosphate (TiBP) crystallizes readily [13]. Furthermore, Den Auwer and coworkers demonstrated that there is no structural difference between $UO_2(NO_3)_2(TiBP)_2$ in the solid state and liquid $UO_2(NO_3)_2(TBP)_2$ in tri-*n*-butylphosphate solution at 295 K by means of XAS spectroscopy and IR spectroscopy [1].

In this chapter, the extraction process of $UO_2(NO_3)_2{\cdot}6H_2O$ with tri-*n*-butylphosphate is studied by ^{31}P NMR spectroscopy, thereby determining the equilibrium constant and the thermodynamic parameters (ΔH, ΔS) of the complex formation of $UO_2(NO_3)_2{\cdot}6H_2O$ with TBP ligands in tri-*n*-butylphosphate solution. Furthermore, the coordination environment of the uranyl ion in $UO_2(NO_3)_2(TBP)_2$ is elucidated using the classical spectroscopic techniques (UV-Vis absorption, luminescence and MCD spectroscopy) as well as uranium L_{III}-edge EXAFS spectroscopy in order

to obtain extra structural information, e.g. bond distances, on the solution species.

2 Experimental details

Sample preparation

$UO_2(NO_3)_2(TBP)_2$: The solvate was prepared in an excess of TBP by dissolving $UO_2(NO_3)_2 \cdot 6H_2O$ in pure tri-*n*-butylphosphate [1,11].

For the ^{31}P NMR experiments in the temperature interval 295 K - 213 K, 125.5 mg of $UO_2(NO_3)_2 \cdot 6H_2O$ (5×10^{-2} mol L^{-1}) and tri-*n*-butylphosphate (2.5×10^{-1} mol L^{-1} in methyl-*iso*-butylketone) were dissolved in chloroform. For the determination of the equilibrium constant, the sample preparation was performed in the same way, but with a metal-to-ligand ratio of 1:2. 500 µL of the prepared solutions was transferred into a NMR tube to which 50 µL of $CDCl_3$ was added.

For the spectrophotometric measurements, the uranyl concentration was approximately 5×10^{-2} mol L^{-1}. For recording UV-Vis absorption spectra at low temperatures ranging from 273 K to 213 K, we prepared a solution in chloroform containing $UO_2(NO_3)_2 \cdot 6H_2O$ (5×10^{-2} mol L^{-1}) and tri-*n*-butylphosphate (2.5×10^{-1} mol L^{-1} in methyl-*iso*-butylketone). These experimental conditions are the same as used for the ^{31}P NMR experiments in order to compare the data of both techniques.

In the temperature interval 295 K - 213 K, no freezing of the sample solutions or formation of precipitates was observed. The freezing points of methyl-*iso*-butylketone, chloroform and tri-*n*-butylphosphate are 188 K, 209 K and 193 K, respectively.

Uranium L_{III}-edge EXAFS spectroscopy

For the uranium L_{III}-edge EXAFS measurements, the sample preparation, the experimental setup and the data analysis were performed as discussed in Chapter 3. Theoretical phase and amplitude functions were calculated using the crystal structure of $UO_2(NO_3)_2(TiBP)_2$ [13]. The (main) multiple scattering paths, with their relative importance, are defined according to the notation in Figure 7.1 and are listed in Table 7.1.

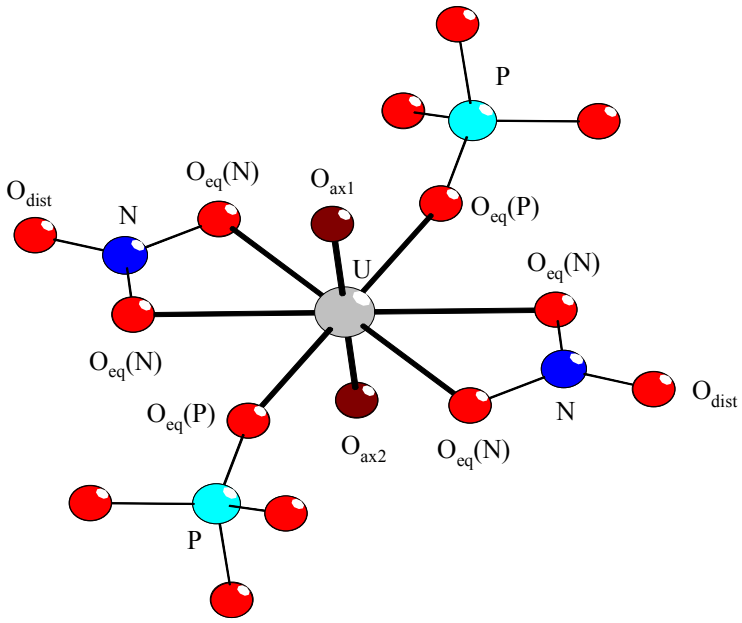

Figure 7.1. First coordination sphere of $UO_2(NO_3)_2(TiBP)_2$ [13]. The alkyl chains are left out for clarity.

In all fits, the coordination number of the uranyl oxygen atoms (O_{ax}) was held constant at two. The degeneracy of the multiple scattering paths was included in the coordination numbers N. So, the degeneracy of the dominating multiple scattering paths including the distal oxygen atoms (O_{dist}), i.e. U-N-O_{dist}-N (four-legged scattering path) and U-O_{dist}-N (three-legged scattering path, abbreviated as MS O_{dist}), was held constant at the

number of distal oxygen atoms present and to twice its value, respectively. Furthermore, the distances R of these multiple scattering paths were linked to the path length R of the single scattering path U-O_{dist}. The Debye-Waller factor σ^2 of the scattering path U-N-O_{dist}-N was linked to the corresponding parameter of the scattering path U-O_{dist}-N. The number of scattering paths of the three-legged multiple scattering path U-N-O_{eq}(N) was constrained to twice the coordination number of the equatorial oxygen atoms O_{eq}(N), whereas the Debye-Waller factor σ^2 was linked to the Debye-Waller factor of the single scattering path U-N.

Table 7.1. Principal scattering pathways[a], taken from $UO_2(NO_3)_2(TiBP)_2$ [13].

Pathway	Scattering length (Å)	Intensity (normalized)
U-O_{ax}	1.757	100
U-O_{ax1}-O_{ax2}	3.514	10.9
U-O_{ax1}-U-O_{ax2}	3.514	19
U-O_{ax1}-U-O_{ax1}	3.514	12.8
U-O_{eq}(P)	2.372	47.6
U-P	3.816	15.4
U-P-O_{eq}(P)	3.833	37.7
U-O_{eq}(P)-P-O_{eq}(P)	3.850	24
U-O_{eq}(N)	2.509	40.9
U-N	2.960	24.1
U-N-O_{eq}(N)	3.374	6.4
U-O_{dist}	4.167	8.8
U-O_{dist}-N	4.167	23
U-N-O_{dist}-N	4.168	14.8

[a] Scattering pathways only multiplied by a symmetry degeneration or with a scattering amplitude of less than 3% were not considered in the table.

For the multiple scattering paths involving TBP, we followed an analogous way of thinking. The degeneracy of the multiple scattering paths including phosphorus, i.e. the three-legged multiple scattering path

U-P-O_{eq}(P) (abbreviated as MS P) and the four-legged multiple scattering path U-O_{eq}(P)-P-O_{eq}(P), was held constant at the number of phosphorus atoms present and to twice its value, respectively. The distances R and the Debye-Waller factors σ^2 of these multiple scattering paths were linked to the corresponding parameters of the single scattering path U-P. Scattering contributions of less than 5% were not considered in the fit procedure.

3 Results and discussion

In the ^{31}P NMR spectrum, recorded at room temperature, of a chloroform solution containing $UO_2(NO_3)_2 \cdot 6H_2O$ and tri-*n*-butylphosphate, only one broad peak ($W_{1/2} \cong 45$ Hz) appears at -6.8 ppm. This observation of only one broad peak indicates a fast exchange between the coordinated and the free TBP ligands. Variable temperature NMR spectra were measured to investigate the dynamic process that leads to this broadening of the TBP resonances. Figure 7.2 shows the ^{31}P NMR spectra of $UO_2(NO_3)_2 \cdot 6H_2O$ with tri-*n*-butylphosphate in chloroform at four different temperatures.

By decreasing the temperature to 273 K, the single ^{31}P NMR resonance at room temperature resolves into a broad peak (-7 ppm) and a hump (-5.6 ppm). Upon further lowering of the temperature to 253 K, both ^{31}P NMR signals completely resolve into rather sharp peaks, detected at -5.3 ppm and -6.9 ppm. At 213 K, the ^{31}P resonances become very sharp, indicating that at this temperature the exchange between free and coordinated TBP ligands is slow on the NMR time scale.

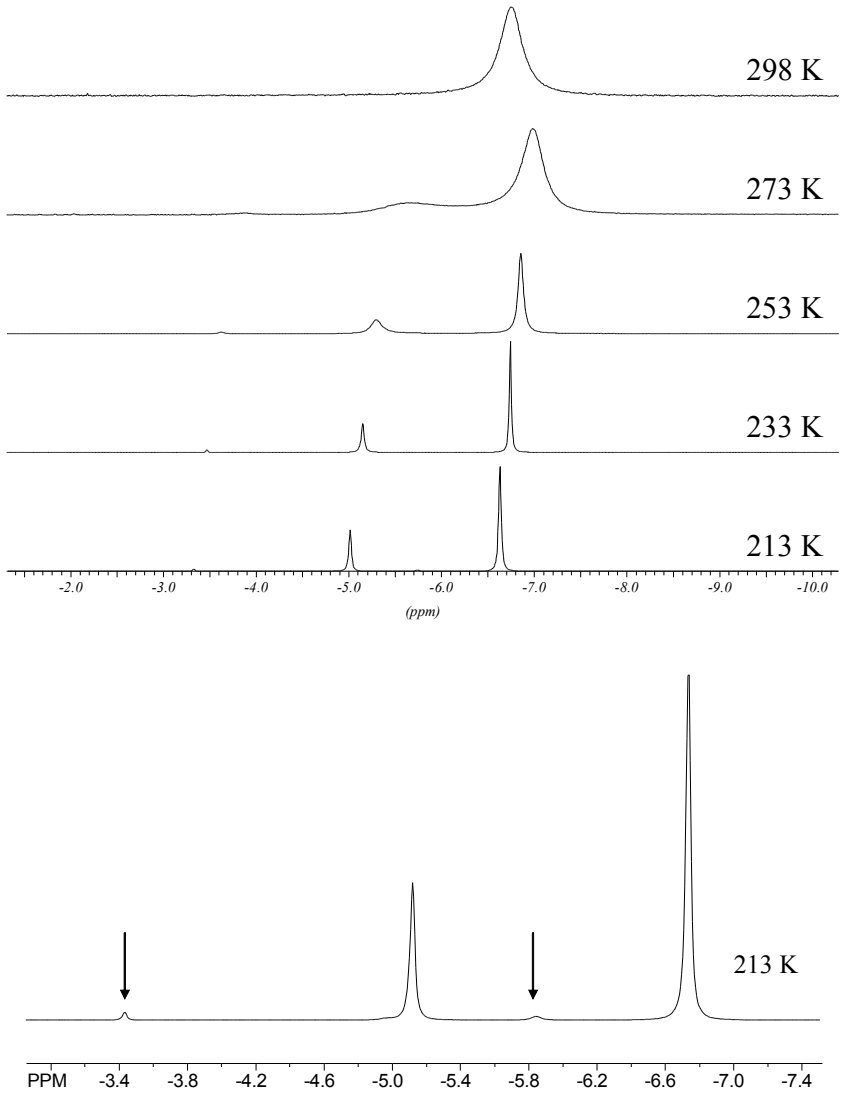

Figure 7.2. ^{31}P NMR spectra at variable temperatures (upper part) and detailed view of the ^{31}P NMR spectrum at 213 K, showing two minor peaks at -3.4 ppm and -5.8 ppm (indicated with an arrow) (lower part), of a solution in chloroform containing 5×10^{-2} mol L^{-1} $UO_2(NO_3)_2 \cdot 6H_2O$ and 2.5×10^{-1} mol L^{-1} tri-*n*-butylphosphate.

The number of coordinated TBP molecules was determined by integrating the area of the ^{31}P NMR signals of free (-6.6 ppm) and coordinated (-5.0 ppm) tri-*n*-butylphosphate at 213 K. The results reveal that there are two TBP ligands coordinated to the uranyl ion, together with two bidentate nitrate groups, in chloroform. This is analogous to previous studies performed in dichloromethane [16]. Furthermore, these results are consistent with the solid state structure of uranyl complexes with organophosphate ligands like tri-*iso*-butylphosphate (TiBP) and trimethylphosphate (TMP) [11,13-15,17]. ^{31}P NMR measurements of $UO_2(NO_3)_2 \cdot 6H_2O$ and tri-*n*-butylphosphate in acetone, however, indicated that only one TBP molecule is coordinated to the uranyl ion. This difference between the coordination number of TBP in acetone on one hand and that in dichloromethane and chloroform on the other hand can be explained in terms of the affinity of these solvents towards the uranyl ion. Acetone tends to compete with tri-*n*-butylphosphate for coordination with the uranyl ion [16]. Furthermore, the dielectric constant of chloroform ($\varepsilon_R = 5$) is low compared to those of acetone ($\varepsilon_R = 21$) and dichloromethane ($\varepsilon_R = 9$). Consequently, $UO_2(NO_3)_2(TBP)_2$ species are more easily formed in chloroform than in acetone and dichloromethane [16].

Interestingly, in addition to two main ^{31}P NMR resonances, corresponding to the free (-6.6 ppm) and the coordinated (-5.0 ppm) TBP ligands, two minor peaks at -3.4 ppm and -5.8 ppm are clearly visible in the NMR spectrum recorded at 213 K (Figure 7.2). The nature of these species is difficult to uncover. Since it has been commonly accepted that tri-*n*-butylphosphate coordinates to the uranyl ion in a monodentate mode through one oxygen atom, it is unlikely that different coordination modes of tri-*n*-butylphosphate would lead to the formation of new species. It is, however, plausible that the two minor species correspond to complexes in which one or two nitrate ligands are bound to the uranyl ion in a monodentate mode. Integration of the area under these two ^{31}P NMR peaks suggests that these two complexes are present in ca. 8% compared

with 91% of the major species, identified as the $UO_2(NO_3)_2(TBP)_2$ complex.

The equilibrium constant of the complex formation of $UO_2(NO_3)_2 \cdot 6H_2O$ with tri-*n*-butylphosphate was determined by measuring the area under the ^{31}P NMR resonances of a chloroform solution containing 5×10^{-2} mol L^{-1} $UO_2(NO_3)_2 \cdot 6H_2O$ and 10^{-1} mol L^{-1} tri-*n*-butylphosphate (metal-to-ligand ratio = 1:2). Due to the fast exchange between coordinated and free TBP, the accurate K_{eq} values can only be obtained at low temperatures. At 213 K, the value of K_{eq} is found to be 9.23×10^3 mol^{-2} L^2, while at 233 K the value of K_{eq} is 2.45×10^3 mol^{-2} L^2. The van 't Hoff plot affords calculation of the thermodynamic parameters of the complex formation reaction. The ΔH-value of -27.3 kJ mol^{-1} and the ΔS-value of -52.9 J K^{-1} mol^{-1} are consistent with an enthalpy driven process, in which the loss of entropy due to the complex formation of the uranyl ion with two TBP molecules is compensated by the favourable enthalpy contribution.

Due to the presence of only one major species in solution, as indicated by ^{31}P NMR spectroscopy, the remarkable vibrational fine structure in the UV-Vis absorption spectrum of $UO_2(NO_3)_2 \cdot 6H_2O$ in tri-*n*-butylphosphate solution can be completely attributed to the formation of the $UO_2(NO_3)_2(TBP)_2$ complex (Figure 7.3). The absorption bands of $UO_2(NO_3)_2(TBP)_2$ are slightly shifted to higher energies (~ 500 cm^{-1}), which is typical for coordination with nitrate ions [18]. The excited state value of the symmetrical stretching vibration (ν_s) of the uranyl ion is approximately 760 cm^{-1}, which is in accordance with literature data [18,19].

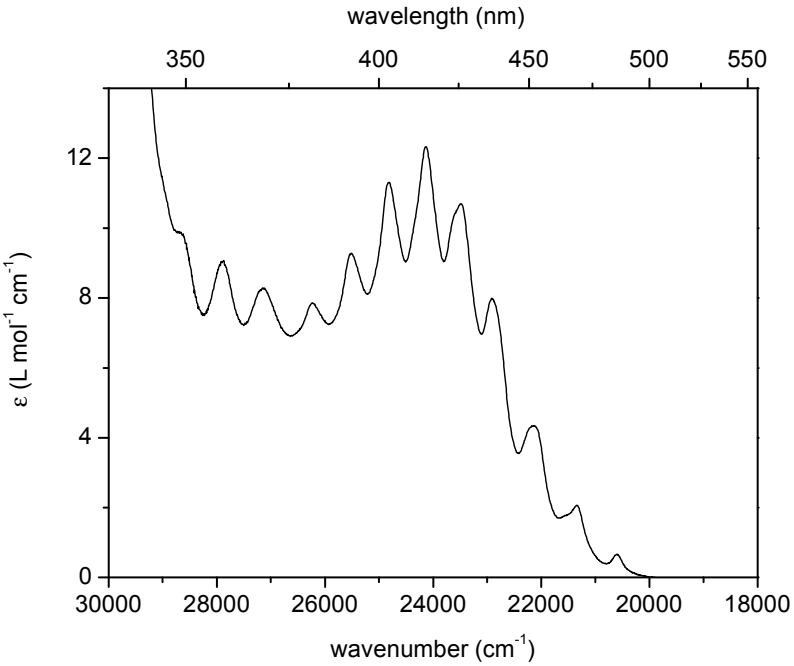

Figure 7.3. UV-Vis absorption spectrum of the $UO_2(NO_3)_2(TBP)_2$ complex in tri-*n*-butylphosphate at room temperature. The uranyl concentration is approximately 5×10^{-2} mol L^{-1}.

The UV-Vis absorption spectra of the $UO_2(NO_3)_2(TBP)_2$ complex in chloroform in the temperature interval 295 K - 213 K are depicted in Figure 7.4. The addition of chloroform has no influence on the spectroscopic properties of $UO_2(NO_3)_2(TBP)_2$, since no spectral changes are observed. By decreasing the temperature to 213 K, no shift of the absorption maxima is detected. Furthermore, the absorption peaks do not become sharper at low temperatures. We only notice a slight decline of the molar absorptivity by lowering the temperature to 233 K - 213 K.

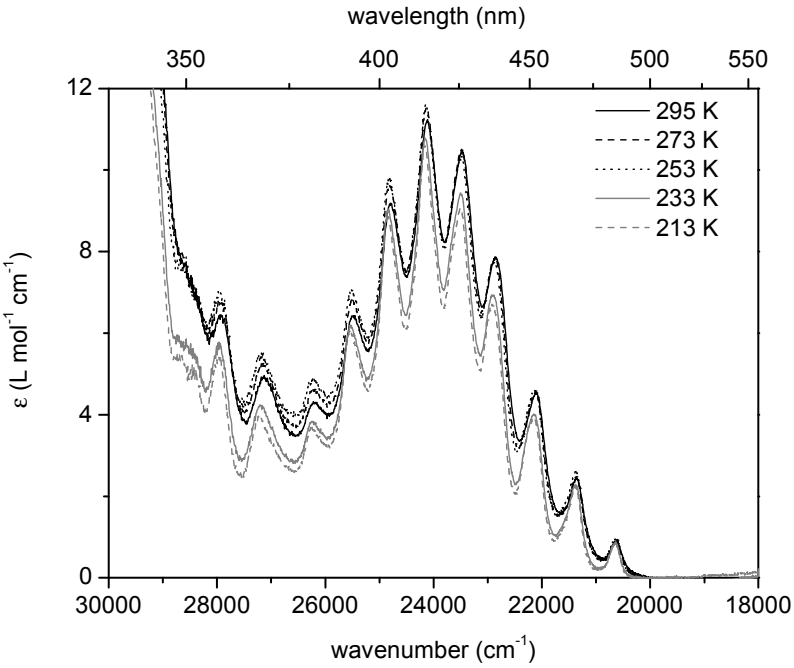

Figure 7.4. UV-Vis absorption spectra of the $UO_2(NO_3)_2(TBP)_2$ complex in chloroform at low temperatures (295 K - 213 K). The uranyl concentration is approximately 5×10^{-2} mol L^{-1}.

The vibrational fine structure in the emission spectrum of the $UO_2(NO_3)_2(TBP)_2$ complex in tri-*n*-butylphosphate is typical for spectra of uranyl complexes (Figure 7.5). The frequency of the symmetrical stretching vibration (ν_s) of the uranyl ion in the ground state is approximately 880 cm^{-1}.

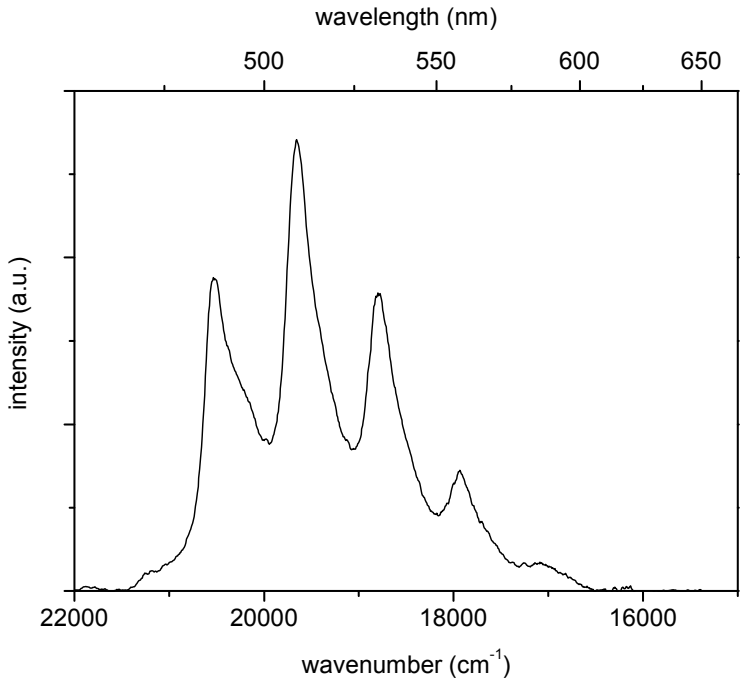

Figure 7.5. Emission spectrum of the $UO_2(NO_3)_2(TBP)_2$ complex in tri-*n*-butylphosphate at room temperature. The uranyl concentration is approximately 5×10^{-2} mol L^{-1}. The excitation wavelength is 425.6 nm (23496 cm^{-1}).

By means of the mirror-relationship between the emission spectrum and the first electronic transition in absorption (and excitation), the absorption peaks belonging to the first electronic transition in the spectrum of $UO_2(NO_3)_2(TBP)_2$ can be identified. This mirror-relationship, displayed in Figure 7.6, indicates that only the first peak at approximately 20610 cm^{-1} in absorption (excitation) originates from the first electronic transition $\Pi_g \leftarrow \Sigma_g^+$.

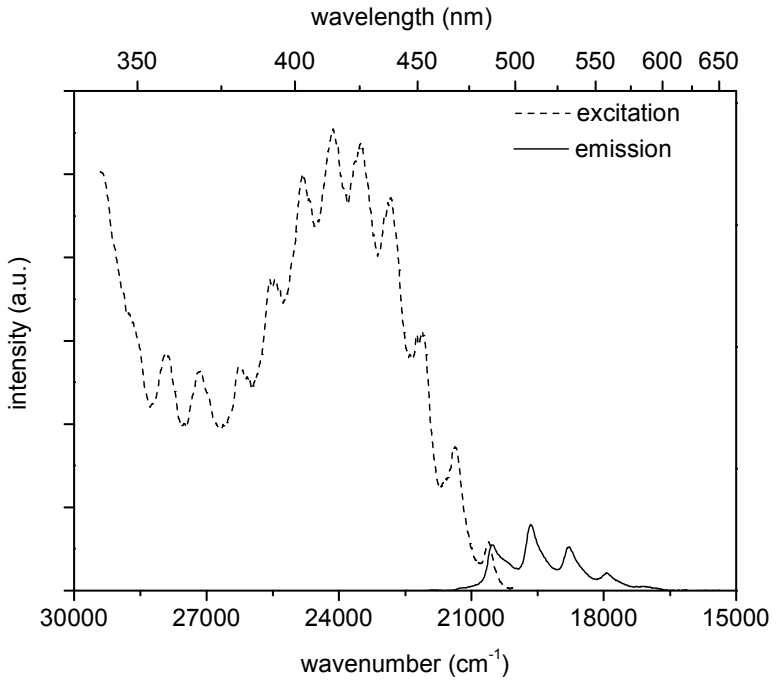

Figure 7.6. Excitation and emission spectra of the $UO_2(NO_3)_2(TBP)_2$ complex in tri-*n*-butylphosphate at room temperature. The uranyl concentration is 5×10^{-2} mol L^{-1}. The excitation and emission wavelengths are 425.6 nm (23496 cm^{-1}) and 509.0 nm (19646 cm^{-1}), respectively.

The MCD spectrum of $UO_2(NO_3)_2(TBP)_2$ in tri-*n*-butylphosphate is shown in Figure 7.7. The first peak in the absorption spectrum does not generate a distinct MCD signal. The MCD spectrum only consists of B-terms (positive or negative). Small shoulders are superimposed on the positive B-terms, which is clearly visible between 24000 cm^{-1} and 27000 cm^{-1}.

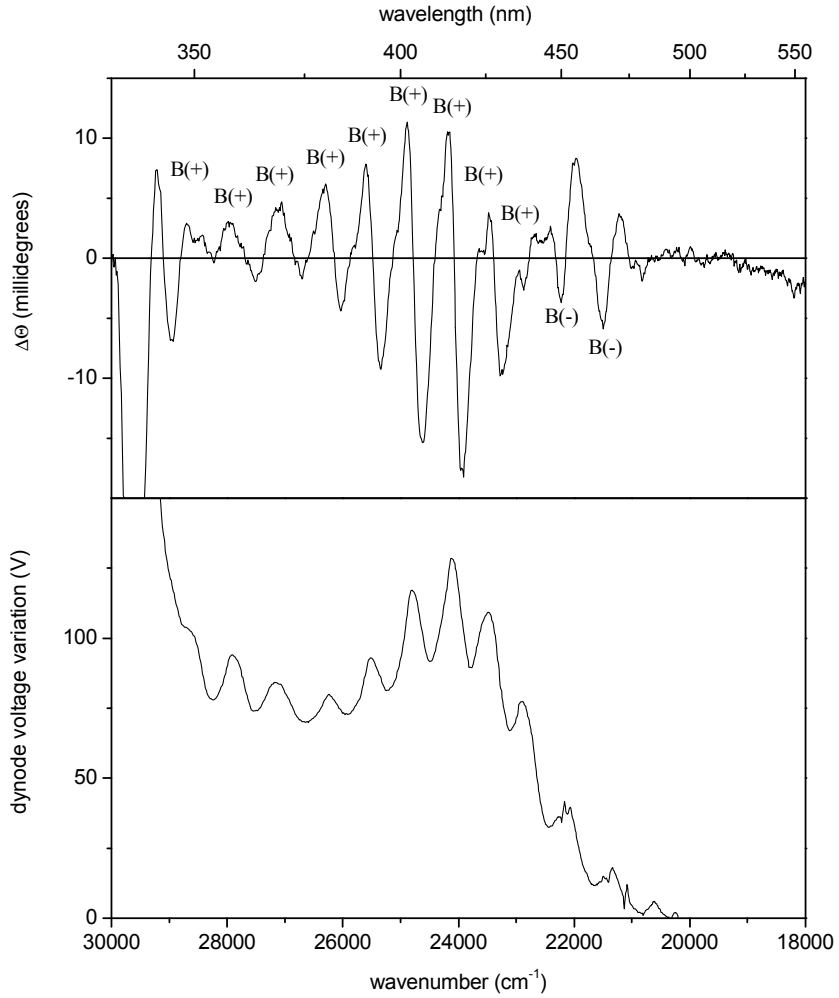

Figure 7.7. MCD (upper graph) and dynode voltage (lower graph) spectra of the $UO_2(NO_3)_2(TBP)_2$ complex in tri-*n*-butylphosphate at room temperature with $[UO_2^{2+}] = 5 \times 10^{-2}$ mol L^{-1}.

The symmetry of the first coordination sphere of the uranyl ion affects the vibrational fine structure in the absorption spectrum. Based on the typical vibrational fine structure in the UV-Vis absorption spectrum of the $UO_2(NO_3)_2(TBP)_2$ complex, we propose a D_{2h} coordination symmetry. Recently, Oda and coworkers assumed a C_{2v} coordination

symmetry for $UO_2(NO_3)_2(TBP)_2$ in their relativistic molecular orbital calculations [12]. They proposed a structure with the phosphorus atom as well as one of the three alkyl groups of the TBP ligands in the equatorial plane to avoid steric hindrance with the nitrate groups. The other alkyl groups are located out of the equatorial plane. In contrast, a D_{2h} coordination symmetry was proposed for $UO_2(NO_3)_2(H_2O)_2$ [12].

Nevertheless, comparison of the UV-Vis absorption spectrum of $UO_2(NO_3)_2(TBP)_2$ in tri-*n*-butylphosphate solution with the spectrum of solid $UO_2(NO_3)_2{\cdot}6H_2O$ reveals the same vibrational fine structure. The group of Görller-Walrand has studied the UV-Vis absorption spectrum of solid $UO_2(NO_3)_2{\cdot}6H_2O$ in detail and classified this compound into the group of complexes exhibiting a D_{2h} coordination symmetry with six atoms in the first coordination sphere of the uranyl ion [20]. Indeed, from crystal structure determinations it is known that solid $UO_2(NO_3)_2{\cdot}6H_2O$ is made up of the uranyl ion surrounded by two bidentate nitrate groups and two water molecules in the equatorial plane [21,22]. Moreover, the calculated single component spectrum of $UO_2(NO_3)_2$ in solution (D_{2h} symmetry) shows the same structural features as the spectra of solid $UO_2(NO_3)_2{\cdot}6H_2O$ and liquid $UO_2(NO_3)_2(TBP)_2$ [23]. Thus, the comparison with literature data confirms our statement that the $UO_2(NO_3)_2(TBP)_2$ species has a D_{2h} coordination symmetry with two bidentate nitrate groups and two TBP ligands in trans positions in the equatorial plane of the uranyl ion. The $UO_2(NO_3)_2(TBP)_2$ complex has the same structure as $UO_2(NO_3)_2(H_2O)_2$, where water molecules occupy the sites of the phosphate groups [13]. In addition, there is a good agreement between the UV-Vis data of $UO_2(NO_3)_2(TBP)_2$ and $UO_2(NO_3)_2{\cdot}6H_2O$ [20] and the calculated spectra of $UO_2(NO_3)_2$ [23] and $UO_2(NO_3)_2(H_2O)_2$ [24], i.e. all complexes with a D_{2h} coordination symmetry.

No degenerate states are encountered in a D_{2h} coordination symmetry. The degeneracy is lifted going from $D_{\infty h}$ (UO_2^{2+}) to D_{2h}. This is consistent with the observation of only B-terms in the MCD spectrum of

$UO_2(NO_3)_2(TBP)_2$. Indeed, B-terms correspond to the absence of degenerate states, before applying the magnetic field. Both Π_g and Φ_g states transform as B_{2g} and B_{3g} in D_{2h}. Therefore, they mix with one another under the influence of the equatorial ligand field. In the centrosymmetric point group D_{2h}, all transitions of the type $(\sigma_u^+)^2 \rightarrow \sigma_u^+\delta_u$, $\sigma_u^+\phi_u$ are according to the Laporte selection rule parity forbidden. Consequently, the oscillator strength, which is related to the intensity, of all electronic transitions is equal to zero in theoretical calculations [24]. The UV-Vis absorption spectrum of a uranyl complex with D_{2h} symmetry is purely vibronic in nature, as is the case for $[UO_2Cl_4]^{2-}$ (D_{4h}). Intensity can only be induced in the electronic transitions by coupling of vibrations of ungerade parity (ν_a, ν_b or ungerade equatorial vibrations). Furthermore, the vibronic nature of the UV-Vis absorption spectrum of the $UO_2(NO_3)_2(TBP)_2$ complex is confirmed by the UV-Vis measurements at low temperatures. At low temperature, the vibrations of the uranyl ion itself as well as the ligand vibrations are frozen, resulting in a lower molar absorptivity and an unaltered vibrational fine structure.

An assignment of each peak in the spectrum of the $UO_2(NO_3)_2(TBP)_2$ species (D_{2h}) is more complicated than in the vibronic spectrum of $[UO_2Cl_4]^{2-}$ (D_{4h}), because none of the states are degenerate, thereby only generating MCD signals of the B-type. Therefore, an identification of the electronic transitions is not unambiguous and will not be discussed here.

The coordination environment of the uranyl ion in the $UO_2(NO_3)_2(TBP)_2$ complex proposed by UV-Vis absorption spectroscopy, i.e. two bidentate coordinated nitrate groups and two monodentate coordinated TBP molecules, is confirmed by uranium L_{III}-edge EXAFS spectroscopy. In addition, since only one major species is present in solution, some structural information on the $UO_2(NO_3)_2(TBP)_2$ complex in tri-*n*-butylphosphate solution like the bond distances, can be obtained. The raw k^3-weighted EXAFS data and the corresponding Fourier transform of $UO_2(NO_3)_2(TBP)_2$ in tri-*n*-butylphosphate are depicted in Figure 7.8.

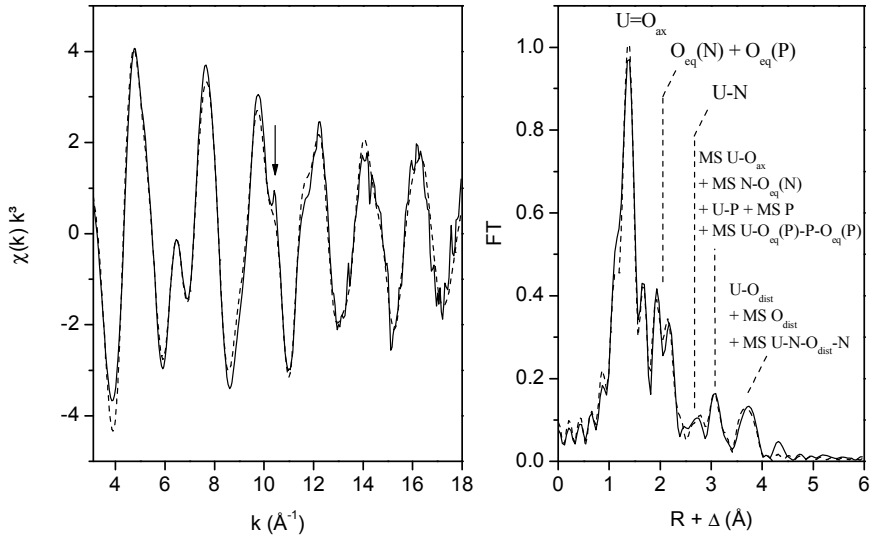

Figure 7.8. Uranium L_{III}-edge k^3-weighted EXAFS data (left) and corresponding Fourier transform (right), taken over k = 3.1 - 18 $Å^{-1}$, of the $UO_2(NO_3)_2(TBP)_2$ complex in tri-*n*-butylphosphate. Experimental data are presented as a continuous line with the theoretical curve presented as a dashed line.

The three-legged multiple scattering paths U-P-O_{eq}(P) and U-O_{dist}-N are abbreviated as MS P and MS O_{dist}, respectively, in Figure 7.8. In the EXAFS spectrum, a small, very sharp feature appears at k = 10.4 $Å^{-1}$ (indicated by an arrow), which can be attributed to the [2p4f] double electron excitation [25].

The largest peak in the Fourier transform at R + Δ ≅ 1.36 Å represents the scattering contribution of the two axial oxygen atoms (O_{ax}). The double peak at R + Δ ≅ 2 Å arises from two equatorial oxygen (O_{eq}) shells: a O_{eq}(N) shell from the nitrate ligands and a O_{eq}(P) shell from the phosphate groups. Indeed, the peak at R + Δ ≅ 2 Å can not be completely covered by including one single shell of equatorial oxygen atoms in the curve fit procedure. The structural parameters of the shell fit procedure including phase correction are summarized in Table 7.2. The coordination numbers of the equatorial oxygen atoms, O_{eq}(N) and O_{eq}(P),

as well as of the nitrogen atoms were determined in an iterative manner, by a free fit. Subsequently, these coordination numbers were fixed in the curve fit in order to avoid correlation problems between N and σ^2. The coordination numbers of the distal oxygen atoms (O_{dist}) and the phosphorus atoms were set equal to the coordination number of the nitrogen atoms and the equatorial oxygen atoms $O_{eq}(P)$, respectively.

Table 7.2. EXAFS structural parameters of $UO_2(NO_3)_2(TBP)_2$ in tri-*n*-butylphosphate.

	R (Å)	N	σ^2 (Å²)
U-O_{ax}	1.77	2*	0.0013
MS U-O_{ax}	3.54	2*	0.0027
U-O_{eq}(P)	2.37	2.6	0.0080
U-P	3.68	2.6	0.0050
MS U-P-O_{eq}(P)	3.79	5.2	0.0050
MS U-O_{eq}(P)-P-O_{eq}(P)	3.85	2.6	0.0050
U-O_{eq}(N)	2.52	4.8	0.0080
U-N	2.95	2.5	0.0056
MS U-N-O_{eq}(N)	3.31	9.6	0.0056
U-O_{dist}	4.22	2.5	0.0024
MS U-O_{dist}-N	4.22	5.1	0.0060
MS U-N-O_{dist}-N	4.22	2.5	0.0060

Error in distances R is ± 0.01 Å, error in coordination numbers N is ± 10%, * value fixed during the shell fit procedure, ΔE = 5.86 eV.

The fit results reveal that the uranyl ion is surrounded by two bidentate coordinated nitrate groups and two monodentate phosphate ligands in the equatorial plane. The uranium coordination polyhedron is composed of two axial oxygen atoms located at 1.77 ± 0.01 Å, four nitrate (bidentate) oxygen atoms at 2.52 ± 0.01 Å and two oxygen atoms from tri-*n*-butylphosphate at 2.37 ± 0.01 Å. These bond distances in the first coordination sphere of the uranyl ion correspond well to the

distances from crystal structure determinations of $UO_2(NO_3)_2(TiBP)_2$ and $UO_2(NO_3)_2(TMP)_2$ [13,14] as well as to the structural parameters obtained by Den Auwer and coworkers by means of EXAFS spectroscopy [1]. The possibility of a monodentate coordinated nitrate group has been rejected by Den Auwer et al. because of the presence of the two typical stretching frequencies of bidentate coordinated nitrate ligands in the IR spectrum of liquid $UO_2(NO_3)_2(TBP)_2$, which also appear in the IR spectrum of solid $UO_2(NO_3)_2(TiBP)_2$. These stretching frequencies of the bidentate nitrate ligands emerge at 1522 cm^{-1} and 1278 cm^{-1} for the liquid, compared with 1533 cm^{-1} and 1269 cm^{-1} for the solid [1,26]. There is a weak peak from nitrogen backscattering in the EXAFS spectrum indicating a U-N distance of 2.95 Å. Indeed, this U-N distance is characteristic for a bidentate coordination mode of the nitrate group and resembles the U-N distance in solid $UO_2(NO_3)_2(TiBP)_2$, $Him_2[\{UO_2(\mu\text{-}OH)(NO_3)_2\}_2]$, $UO_2(NO_3)_2 \cdot 6H_2O$ and in the $[UO_2(NO_3)_3]^-$ complex in acetonitrile solution [13,27,28].

Complex multiple scattering features are the result of the linear arrangement of the nitrogen and the distal oxygen (O_{dist}) atoms in the nitrate ligands and the equatorial oxygen ($O_{eq}(P)$) and the phosphorus atoms in tri-*n*-butylphosphate. Indeed, the bond angle U-N-O_{dist} in the crystal structure of $UO_2(NO_3)_2(TiBP)_2$ is 177°, whereas the bond angle U-O_{eq}(P)-P is 164° [13]. For both ligands, the bond angles are close to linear. In case of a linear arrangement, the focusing effect plays a dominant role, thereby identifying the distal oxygen atoms (O_{dist}) and the phosphorus atoms in a large distance of 4.22 Å and 3.68 Å, respectively (see Chapter 3) [29]. A similar effect is encountered in the uranium L_{III}-edge EXAFS spectra of uranyl carbonato complexes [28,30], uranyl nitrato complexes [27,28] and uranyl acetato complexes [28,31,32] (see Chapter 5). The amplitude of the multiple scattering paths U-O_{dist}-N (MS O_{dist}) and U-N-O_{dist}-N of the nitrate ligand as well as of the scattering paths U-P-O_{eq}(P) (MS P) and U-O_{eq}(P)-P-O_{eq}(P) of the phosphate group are much more pronounced than that of the single scattering paths U-O_{dist}

and U-P, respectively. The U-O_{dist} distance (4.22 Å) in liquid $UO_2(NO_3)_2(TBP)_2$ is in good agreement with the U-O_{dist} bond length in solid $UO_2(NO_3)_2(TiBP)_2$ (4.22 Å) [13]. Conversely, the U-P distance of 3.68 Å is shorter than the U-P bond length (3.81 Å) in $UO_2(NO_3)_2(TiBP)_2$ [13]. However, this distance in the $UO_2(NO_3)_2(TBP)_2$ complex agrees well with the U-P distance in some inorganic phosphates, like $Ca(UO_2)_2(PO_4)_2{\cdot}6H_2O$ (meta-autunite) and $K_2(UO_2)_2(PO_4)_2{\cdot}6H_2O$ [28]. In theory, the distances of the single and the multiple scattering paths of the P shell should be the same. The larger difference between the distance of the single scattering path U-P and those of the two multiple scattering paths can be related with the bond angle U-O_{eq}(P)-P. In the solid state, this bond angle is close to 180°. Using the U-O_{eq}(P) and U-P distances determined by EXAFS spectroscopy and the O_{eq}(P)-P bond length taken from the crystal structure of $UO_2(NO_3)_2(TiBP)_2$, the U-O_{eq}(P)-P bond angle can be theoretically calculated. In this way, a U-O_{eq}(P)-P bond angle of 145° is found for the solution species. Therefore, the direct distance U-P (hypotenuse) is shorter than the sum of the U-O_{eq}(P) and O_{eq}(P)-P bond lengths, explaining the longer distance of the multiple scattering paths for $UO_2(NO_3)_2(TBP)_2$ in tri-*n*-butylphosphate solution.

EXAFS studies on uranyl complexes with different organophosphate ligands have revealed that the U-P bond distance decreases in the order TBP > TMP ≈ TPhP (TPhP = triphenylphosphate) at room temperature [1,13]. The extracting ability of these compounds for $UO_2(NO_3)_2$ ranges in the order TBP > TMP >> TPhP. However, a correlation between the U-P bond distance and the extraction affinity was not established. Other factors like steric hindrance and lipophilicity of the organophosphates have to be taken into account to explain the extracting ability of these ligands [1].

4 Conclusions

All techniques applied, i.e. ^{31}P NMR spectroscopy, UV-Vis absorption spectroscopy, luminescence and excitation spectroscopy, magnetic circular dichroism and uranium L_{III}-edge EXAFS spectroscopy, unambiguously point to the existence of a $UO_2(NO_3)_2(TBP)_2$ species in solution, when $UO_2(NO_3)_2 \cdot 6H_2O$ is dissolved in tri-*n*-butylphosphate. ^{31}P NMR measurements at low temperatures indicate only one major species in solution (91%). Integrating the area of the NMR signals of free and coordinated TBP gives a coordination number of two for the tri-*n*-butylphosphate ligand. Furthermore, we were able to calculate the equilibrium constant K_{eq} as well as the thermodynamic parameters of the complex formation reaction, based on these ^{31}P NMR data. At 213 K and 233 K, the value of K_{eq} is found to be 9.23×10^3 mol^{-2} L^2 and 2.45×10^3 mol^{-2} L^2, respectively. The values of ΔH (-27.3 kJ mol^{-1}) and ΔS (-52.9 J K^{-1} mol^{-1}) are consistent with an enthalpy driven process.

The UV-Vis absorption spectrum of the $UO_2(NO_3)_2(TBP)_2$ complex in tri-*n*-butylphosphate exhibits the same spectroscopic features as the spectrum of solid $UO_2(NO_3)_2 \cdot 6H_2O$ [20] and the calculated spectrum of $UO_2(NO_3)_2$ [23]. Based on the remarkable vibrational fine structure, a D_{2h} coordination symmetry with two bidentate coordinated nitrate groups and two monodentate TBP ligands in the equatorial plane is proposed. In a D_{2h} symmetry, all electronic transitions are according to the Laporte selection rule parity forbidden. Therefore, the spectrum is purely vibronic in nature, where intensity is gained by vibronic coupling of ungerade vibrations (ν_a, ν_b or ungerade equatorial vibrations). In addition, all degeneracy is lifted in a D_{2h} coordination symmetry. This is consistent with the observation of only B-terms (positive or negative) in the MCD spectrum of the $UO_2(NO_3)_2(TBP)_2$ complex. The presence of non-degenerate states in D_{2h}, generating only MCD signals of the B-type, makes the assignment of each peak in the spectrum more complicated than in the vibronic spectrum of $[UO_2Cl_4]^{2-}$ (D_{4h}).

According to uranium L_{III}-edge EXAFS spectroscopy, the $UO_2(NO_3)_2(TBP)_2$ coordination polyhedron consists of two axial oxygen atoms at 1.77 ± 0.01 Å, four equatorial oxygen atoms of two bidentate nitrate groups at 2.52 ± 0.01 Å and two equatorial oxygen atoms of two phosphate groups at 2.38 ± 0.01 Å. Complex multiple scattering features have to be included in the curve fit procedure due to the linear arrangement within the nitrate groups (bond angle U-N-O_{dist} ≅ 177° in solid $UO_2(NO_3)_2(TiBP)_2$) and the tri-*n*-butylphosphate ligands (bond angle U-O_{eq}(P)-P ≅ 164° in solid $UO_2(NO_3)_2(TiBP)_2$) [13].

References

[1] (a) Den Auwer, C.; Lecouteux, C.; Charbonnel, M.C.; Madic, C.; Guillaumont, R. *Polyhedron* **1997**, *16*, 2233-2238 and references therein. (b) Den Auwer, C.; Charbonnel, M.C.; Presson, M.T.; Madic, C.; Guillaumont, R. *Polyhedron* **1998**, *17*, 4507-4517. (c) Den Auwer, C.; Revel, R.; Charbonnel, M.C.; Presson, M.T.; Conradson, S.D.; Simoni, E.; Le Du, J.F.; Madic, C. *J. Synchrotron Rad.* **1999**, *6*, 101-104.

[2] Baaden, M.; Schurhammer, R.; Wipff, G. *J. Phys. Chem. B* **2002**, *106*, 434-441.

[3] Schurhammer, R.; Wipff, G. *J. Phys. Chem. A* **2005**, *109*, 5208-5216.

[4] Hutschka, F.; Dedieu, A.; Troxler, L.; Wipff, G. *J. Phys. Chem. A* **1998**, *102*, 3773-3781.

[5] Zilberman, B.Ya.; Fedorov, Yu. S.; Kopyrin, A.A.; Arkhipov, S.A.; Blazheva, I.V.; Glekov, R.G. *Radiochem.* **2001**, *43*, 172-176.

[6] Pathak, P.N.; Prabhu, D.R.; Kanekar, A.S.; Manchanda, V.K. *Radiochim. Acta* **2006**, *94*, 193-198.

[7] Stas, J.; Dahdouh, A.; Shlewitt, H. *Periodica Polytechnica Ser. Chem. Eng.* **2005**, *49*, 3-18.

[8] Joung, S.N.; Yoon, S.J.; Kim, S.Y.; Yoo, K.-P. *J. Supercrit. Fluids* **2000**, *18*, 157-166.

[9] (a) Shimada, T.; Ogumo, S.; Sawada, K.; Enokida, Y.; Yamamoto, I. *Anal. Sci.* **2006**, *22*, 1387-1391. (b) Sawada, K.; Uruga, K.; Koyama, T.; Shimada, T.; Mori, Y.; Enokida, Y.; Yamamoto, I. *J. Nucl. Sci. Tech.* **2005**, *42*, 301-304.

[10] Giridhar, P.; Venkatesan, K.A.; Srinivasan, T.G.; Vasudeva Rao, P.R. *J. Radioanal. Nucl. Chem.* **2005**, *265*, 31-38.

[11] Katz, J.J.; Seaborg, G.T.; Morss, L.R. *The Chemistry of the Actinide Elements*, **1986**, Chapman and Hall, London.

[12] Oda, Y.; Funasaka, H.; Nakamura, Y.; Adachi, H. *J. Alloys Compd.* **1997**, *255*, 24-30.

[13] Burns, J.H.; Brown, G.M.; Ryan, R.R. *Acta Cryst*. **1985**, *C41*, 1446-1448 and references therein.

[14] Agostini, G.; Giacometti, G.; Clemente, D.A.; Vicentini, M. *Inorg. Chim. Acta* **1982**, *62*, 237-240.

[15] Fleming, J.E.; Lynton, H. *Chem. Ind.* **1959**, 1409.

[16] Hatakeyama, K.; Park, Y.; Tomiyasu, H. *J. Nucl. Sci. Technol*. **1997**, *34*, 298-303.

[17] Marcus, Y.; Kertes, A.S. *Ion Exchange and Solvent Extraction of Metal Complexes*, **1969**, Wiley, New York.

[18] Denning, R.G.; Foster, D.N.P.; Snellgrove, T.R.; Woodwark, D.R. *Mol. Phys.* **1979**, *37*,1089-1107.

[19] Denning, R.G.; Snellgrove, T.R.; Woodwark, D.R. *Mol. Phys.* **1976**, *32*, 419-442.

[20] Görller-Walrand, C.; De Jaegere, S. *J. Chim. Phys*. **1972**, *4*, 726-736.

[21] Taylor, J.C.; Mueller, H. *Acta Cryst.* **1965**, *19*, 536-543.

[22] Hall, D.; Rae, A.D.; Waters, T.N. *Acta Cryst*. **1965**, *19*, 389-395.

[23] De Houwer, S.; Görller-Walrand, C. *J. Alloys Compd.* **2001**, *323-324*, 683-687.

[24] van Besien, E. *De invloed van complexvorming op het elektronische spectrum van uranyl: een computationele studie*, **2006**, PhD thesis, Katholieke Universiteit Leuven.

[25] Hennig, C. *Phys. Rev. B* **2007**, *75*, 035120

[26] Nukada, K.; Naito, K.; Maeda, U. *Bull. Chem. Soc. Jpn.* **1960**, *33*, 894-898.

[27] Barnes, C.E.; Shin, Y.; Saengkerdsub, S.; Dai, S. *Inorg. Chem.* **2000**, *39*, 862-864.

[28] Thompson, H.A.; Brown Jr., G.E.; Parks, G.A. *Am. Min.* **1997**, *82*, 483-496.

[29] Teo, B.K. *EXAFS: Basic Principles and Data Analysis*, **1986**, Springer, Berlin, Heidelberg, New York, p. 183.

[30] Bernhard, G.; Geipel, G.; Reich, T.; Brendler, V.; Amayri, S.; Nitsche, H. *Radiochim. Acta* **2001**, *89*, 511-518.

[31] Denecke, M.A.; Reich, T.; Bubner, M.; Pompe, S.; Heise, K.H.; Nitsche, H.; Allen, P.G.; Bucher, J.J.; Edelstein, N.M.; Shuh, D. *J. Alloys Compd.* **1998**, *271-273*, 123-127.

[32] Bailey, E.H.; Mosselmans, J.F.W.; Schofield, P.F. *Geochim. Cosmochim. Acta* **2004**, *68*, 1711-1722.

8 THE PHOTOCHEMICAL BEHAVIOUR OF THE URANYL ION: A DIFFERENT PERSPECTIVE AND OUTLOOK

1 Photochemistry of the uranyl ion

The photochemistry of actinide compounds is almost exclusively dominated by reactions involving the uranyl ion. This photochemical behaviour of the uranyl ion is already known for two centuries. Consequently, uranyl has been extensively investigated in the 1970's and 1980's [1,2]. Many studies of the photo-oxidation of various substrates, particularly organic molecules (alcohols, oxalic and other carboxylic acids, aldehydes, etc.) have been summarized in books [3,4] and reviews [5-7]. Nevertheless, it is still one of the most confusing chapters of chemistry with many contradictions and unresolved problems. However, the study of the photochemistry of the uranyl ion has to be a challenge due to the presence of uranium(VI) as uranyl in our environment, like in various ores (autunite, carnotite and torbernite). Even seawater contains 3.3×10^{-3} mg uranium per litre.

For two centuries (1805), the photochemical behaviour of uranyl oxalate is known. It was noticed that CO and CO_2 gas bubbles evolve from an aqueous solution containing uranyl and oxalate ions ($C_2O_4^{2-}$), when exposed to visible light [3]. The yield of the decomposition of oxalic acid, induced by uranyl and UV-visible light, is well reproducible.

Therefore, this photochemical reaction was applied in chemical actinometry. In fact, uranyl oxalate was the first actinometer ever used. The produced CO concentration is related to the light intensity according to the reaction

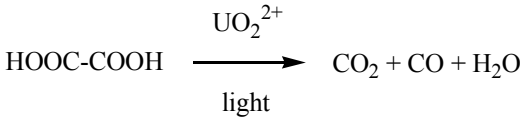

Similar photochemical reactions have been observed for formic acid, acetic acid and other monobasic and dibasic carboxylic acids (Scheme 8.1) [3]. In all these reactions, the uranyl ion serves, together with UV-visible light, as a catalyst to induce the decomposition of the carboxylic acid, thereby forming CO_2 gas bubbles.

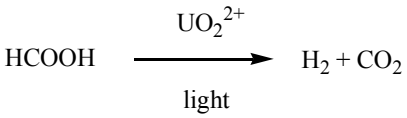

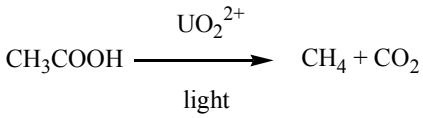

Scheme 8.1. Photochemical reactions of formic acid and acetic acid in the presence of UO_2^{2+} and light [3].

Although the phenomenon is well-known, the mechanism behind the photochemical reaction of oxalic acid has not yet been elucidated. Balzani et al. wrote in 1970: *"Spectrophotometric and potentiometric measurements show that various complex species (e.g. $UO_2(C_2O_4)$ and $[UO_2(C_2O_4)]^{2-}$) are present in aqueous solutions containing UO_2^{2+} and oxalic acid. However, the role played by these complexes in the photochemical behaviour has not yet been clarified"* [4].

Recently, research on the uranyl ion gained a growing interest from a theoretical point of view due to the increase of computer power and the possibility of taking relativistic effects into account. The uranyl tetrachloro complex $[UO_2Cl_4]^{2-}$ has been successfully investigated by means of multiconfigurational perturbation theory (CASSCF/CASPT2) by the group of Pierloot [8]. This theoretical study exactly reproduced the excitation energies and the frequencies of the symmetric stretching vibration ν_s determined in detail by Denning et al., by measuring polarized absorption spectra of $Cs_2UO_2Cl_4$ single crystals at 4.2 K [9].

Studies of the uranyl-oxalate system in solution have been carried out using UV-Vis absorption spectroscopy, uranium L_{III}-edge EXAFS spectroscopy and theoretical calculations [10-12]. When reproducing the solutions used by Vallet et al. for their EXAFS measurements, we noticed that the photocatalytic effect of the uranyl ion was completely overlooked [10]. Therefore, we do not agree with the speciation proposed for the different test solutions. They assume that an aqueous solution of 0.0122 mol L^{-1} sodium oxalate and 0.0601 mol L^{-1} uranyl nitrate contains more than 99% of $[UO_2(C_2O_4)_2(H_2O)]^{2-}$, whereas 95% of the $[UO_2(C_2O_4)_3]^{4-}$ complex is present in an aqueous solution containing 1.68 mol L^{-1} potassium oxalate and 0.0601 mol L^{-1} uranyl nitrate [10]. Moreover, the uranyl oxalato complexes are partly or even completely destroyed in these solutions by the photocatalytic effect. Consequently, uranyl oxalato complexes are no longer present in the solutions studied. In his paper on the determination of the stability constants of uranyl oxalato complexes, Havel points to the photochemical behaviour of the uranyl ion. Furthermore, he stated that the stability constant associated with the formation of a trioxalato complex, has to be considered with caution because of the possible competing formation of polynuclear 2:3 and 2:5 species [11].

As a guideline for the type of bonding formed between the uranyl unit and oxalate ions, the crystal structures of solid uranyl oxalato complexes are a useful starting point. Crystal structure determinations of uranyl

oxalato complexes reveal different modes of coordination of the oxalate group. The oxalate ligand is chelated through one oxygen atom from each carboxylate group, coordinated through two oxygen atoms of the same carboxylate group or bound to a single carboxylate oxygen atom. In most of these crystal structures, the oxalate ions are bridging different uranyl units [13-15]. These structures of solid state complexes, however, have to be considered with caution when applying them for the determination of the geometry of solution species.

In this chapter, we present our point of view on the complex formation of the uranyl ion with oxalate ions, mainly based on spectroscopic measurements, i.e. UV-Vis absorption spectroscopy, luminescence and excitation spectroscopy as well as magnetic circular dichroism. The experiments were performed in non-aqueous solution because of the higher stability of the complexes. This is analogous to the observation of $[UO_2Cl_4]^{2-}$ and $[UO_2(NO_3)_3]^-$ in acetonitrile, whereas no significant complex formation with chloride and nitrate ions occurs in aqueous solution. In addition, we believe that the photochemical reaction is slower in non-aqueous solvents. But, we have also studied the complex formation with oxalate ions in aqueous solution. We were only able to record UV-Vis absorption spectra, since the luminescence of the uranyl ion is completely quenched, possibly due to the photocatalytic effect, once a trace of oxalate ions is present. Indeed, CO_2 and CO gas bubbles evolved from these aqueous solutions. This complete quenching of the uranyl luminescence in the presence of oxalate ions in aqueous solution has already been reported in the literature [16].

2 Experimental details

***$UO_2Cl_x(TBP)_y$*:** UO_3 was dissolved in hydrochloric acid (2 mol L^{-1}) and extracted with TBP (30% in methyl-*iso*-butylketone). $CaCl_2$ was added to promote the extraction of the solvate $UO_2Cl_x(TBP)_y$ [17].

Subsequent coordination of uranyl with chloride: Tetrabutylammonium chloride was added to a solution of $UO_2(ClO_4)_2{\cdot}xH_2O$ in acetone in uranyl-to-chloride ratios of 1:0 to 1:5, with steps of 0.5. The uranyl concentration was approximately 5×10^{-3} mol L^{-1}. The tetrabutylammonium chloride concentration was varied from 5×10^{-3} mol L^{-1} to 2.5×10^{-2} mol L^{-1}.

Subsequent coordination of uranyl with oxalate $^{-}OOC\text{-}COO^{-}$: $UO_2(ClO_4)_2{\cdot}xH_2O$ was mixed with oxalic acid ($H_2C_2O_4$) in acetone in metal-to-ligand ratios of 1:0 to 1:6, with steps of 1. The uranyl concentration was approximately 5×10^{-3} mol L^{-1}.

3 Uranyl oxalato complexes in acetone

The UV-Vis absorption spectra of uranyl complexes with oxalate ions in acetone exhibit spectral features, which differ from the characteristic vibrational fine structure of the "free" (hydrated) uranyl ion (Figure 8.1). The uranyl-to-oxalate ratio was varied from 1:0 to 1:6. Upon addition of oxalate ions, an increase in intensity occurs in the first region of the spectrum (20500 cm^{-1} - 23000 cm^{-1}) with respect to the spectrum of the "free" uranyl ion. The energies of the involved peaks, indicated by an arrow in Figure 8.1, are 21195 cm^{-1}, 21920 cm^{-1} and 22675 cm^{-1}.

We have to remark that a decline of the intensity is observed, when a metal-to-ligand ratio of 1:3 is reached. At the moment, it is hard to distinguish whether or not it concerns a real effect. Indeed, a yellow precipitate is formed by increasing the oxalate concentration, thereby lowering the effective uranyl concentration in solution. However, the composition of the precipitate is not known yet.

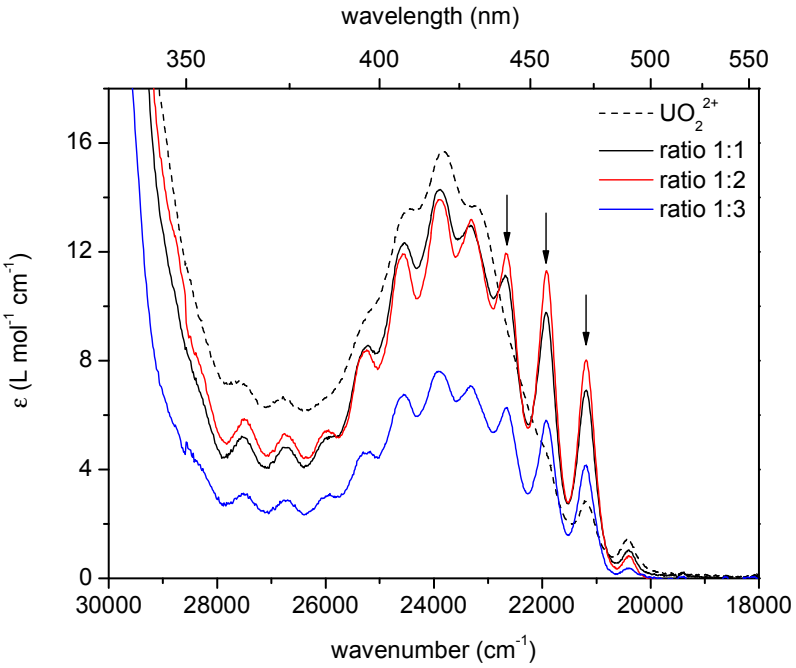

Figure 8.1. UV-Vis absorption spectra of uranyl complexes with oxalate ions in acetone at room temperature, where $[UO_2^{2+}]/[C_2O_4^{2-}]$ = 1:0 (UO_2^{2+}), 1:1, 1:2 and 1:3. The uranyl concentration is 5×10^{-3} mol L^{-1}. The arrows indicate the absorption peaks belonging to the same progression.

In analogy to the three high absorption bands in the UV-Vis absorption spectra, the same increase in intensity also appears in the excitation spectra (Figure 8.2).

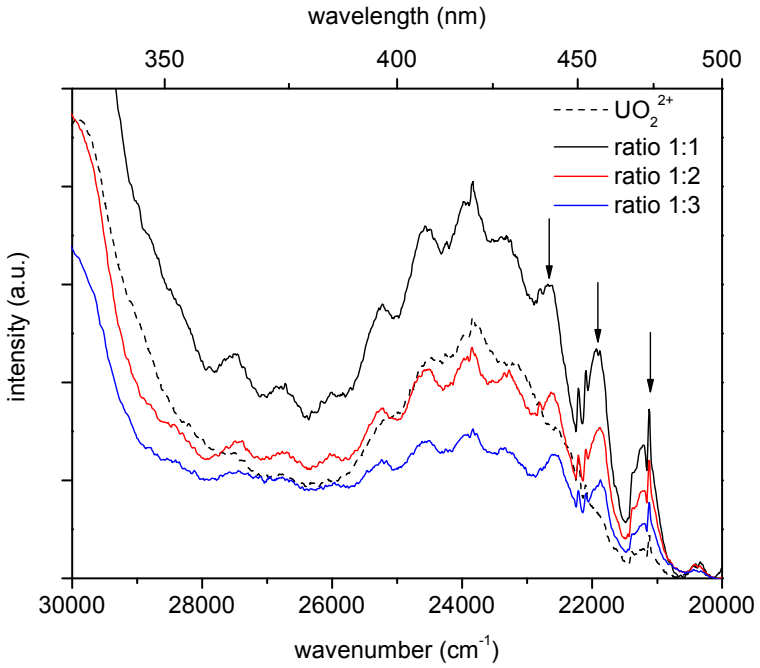

Figure 8.2. Excitation spectra of uranyl complexes with oxalate ions in acetone at room temperature, where $[UO_2^{2+}]/[C_2O_4^{2-}]$ = 1:0 (UO_2^{2+}), 1:1, 1:2 and 1:3. The uranyl concentration is 5×10^{-3} mol L^{-1}. The emission wavelength was set at 513.8 nm (19463 cm^{-1}). The arrows indicate the peaks belonging to the same progression.

In the emission spectra, we also observe remarkable changes in the intensity upon subsequent coordination of the uranyl ion with oxalate ions (Figure 8.3).

We re-emphasize that neither luminescence nor excitation spectra of uranyl oxalato complexes could be measured in aqueous solution due to a complete quenching. The remarkable absorption features, i.e. the enhancement in intensity at the low energy side of the UV-Vis absorption spectra, are also visible in the spectra recorded in aqueous solution. However, they are less pronounced than in acetone. No precipitation is observed in aqueous solution.

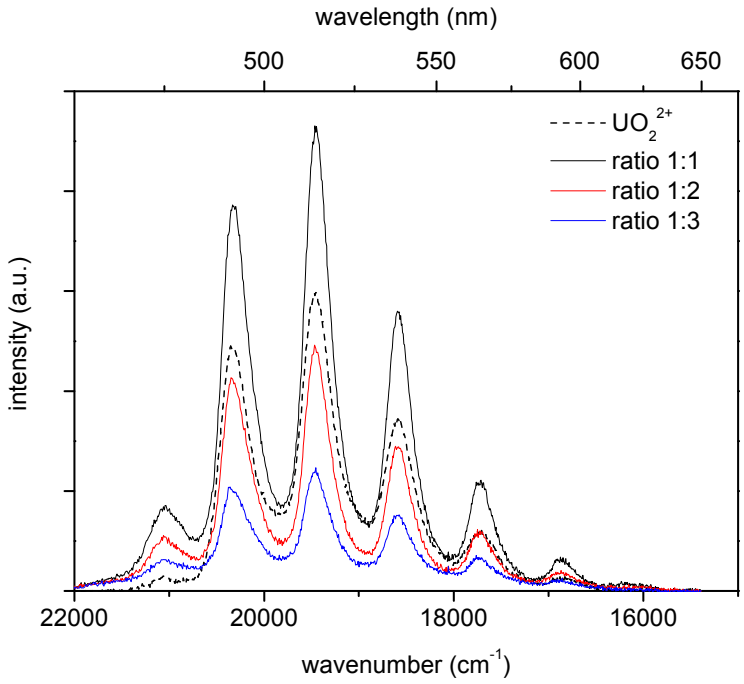

Figure 8.3. Emission spectra of uranyl complexes with oxalate ions in acetone at room temperature, where $[UO_2^{2+}]/[C_2O_4^{2-}]$ = 1:0 (UO_2^{2+}), 1:1, 1:2 and 1:3. The uranyl concentration is 5×10^{-3} mol L^{-1}. The excitation wavelength is 420.0 nm (23809 cm^{-1}).

The hypothesis, developed in the next section, is based on the assumption that the increase in intensity of the progression at the low energy side of the UV-Vis absorption spectra is responsible for the decomposition of the oxalate ions. At the moment, the most relevant question is to find the geometry of the species, which on one hand can explain the intensity enhancement in the transitions $\Pi_g \leftarrow \Sigma_g^+$ and $\Delta_g \leftarrow \Sigma_g^+$ and which on the other hand points to a mechanism behind the photochemical reaction of oxalate ions.

4 Discussion and outlook

The intensity enhancement in the long-wavelength part of the spectra of uranyl oxalato complexes in acetone reminds us of the remarkable vibrational fine structure in the UV-Vis absorption spectra of $UO_2Cl_x(TBP)_y$ and the intermediately formed uranyl chloro complexes – before $[UO_2Cl_4]^{2-}$ is formed (Figures 8.4 and 8.5)[18].

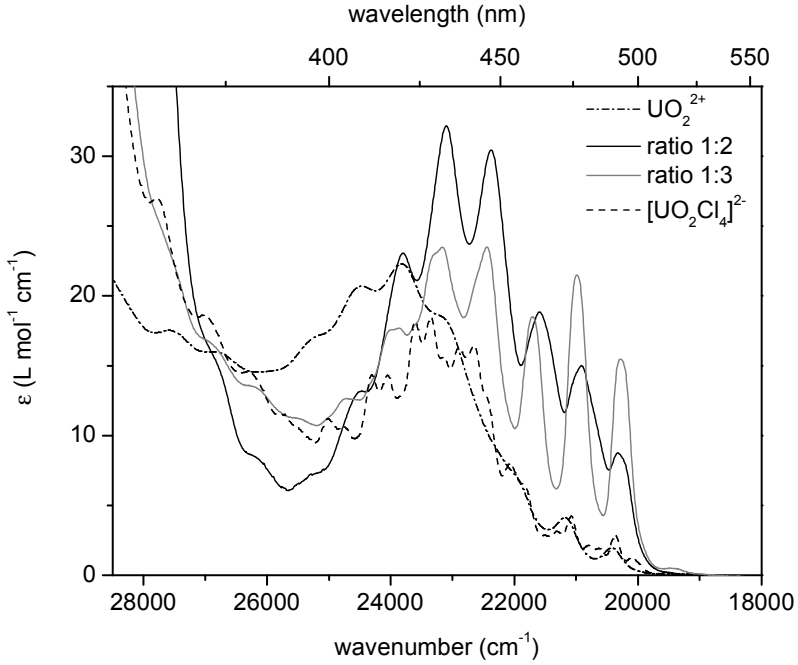

Figure 8.4. UV-Vis absorption spectra of uranyl complexes with chloride ions in acetone at room temperature, where $[UO_2^{2+}]/[Cl^-]$ = 1:0 (UO_2^{2+}), 1:2, 1:3 (intermediate chloro complexes) and 1:5 ($[UO_2Cl_4]^{2-}$).

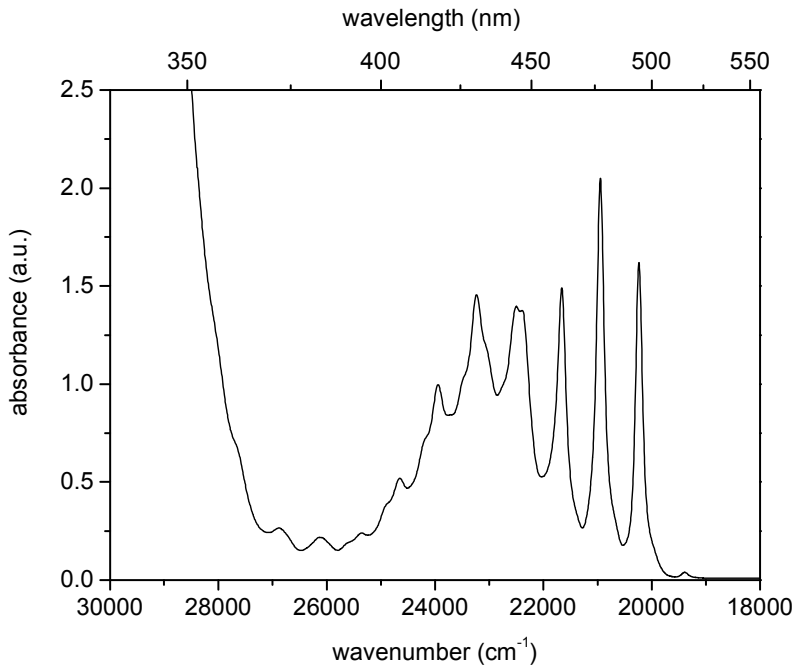

Figure 8.5. UV-Vis absorption spectrum of $UO_2Cl_x(TBP)_y$ in methyl-*iso*-butylketone at room temperature.

The very intense peaks in the low energy region of the absorption spectra of the intermediate chloro complexes have always been explained by the formation of monomeric species. For a long time, Görller-Walrand et al. assigned these spectral features to the presence of a $[UO_2Cl_3]^-$ complex with D_{3h} coordination symmetry in organic solvents [19]. Recently, however, this assignment has been countered by Görller-Walrand and coworkers. They suggested a dihedral symmetry for the intermediately formed chloro complexes, thereby describing the structure as $UO_2Cl_2(solv)_4$ [18].

A theoretical CASSCF/CASPT2 study on the electronic spectra of the intermediate chloro complexes has been performed by the group of Pierloot [20]. Four possible structures have been investigated: $UO_2Cl_2(ac)_4$ (D_2 symmetry), $UO_2Cl_2(ac)_3$, $[UO_2Cl_3(ac)_2]^-$ and

$[UO_2Cl_3(ac)]^-$, the latter three structures all exhibiting C_{2v} symmetry. The calculated excitation energies for the different complexes are similar and correspond well to the experimental values. Thus, all four complexes are a plausible intermediate chloro complex. Nevertheless, the most remarkable feature in the experimental spectra, i.e. the increase in intensity in the low energy part of the UV-Vis absorption spectrum, is not reproduced by the calculations. Indeed, the oscillator strengths are too low to point to a significant intensity enhancement, not even after the inclusion of the intensity inducing U-Cl out-of-plane bending vibration ν_{10} (b_{1u}). Possible explanations were given for this observation by the authors: either the calculations fail to reproduce the increase in intensity or another intermediate complex like a binuclear complex, plays an important role as well [20].

The optical properties of the uranyl oxalato complexes can not be attributed to a D_{3h} coordination symmetry, since no intense negative A-terms are observed in the MCD spectra. Furthermore, the UV-Vis absorption spectra do not coincide with the vibronic spectrum of the uranyl tetrachloro complex $[UO_2Cl_4]^{2-}$ either, thereby rejecting the possibility of monomeric oxalato complexes with D_{4h} symmetry. Vallet et al. proposed a fivefold coordination of the uranyl ion in oxalato complexes, where two oxalate groups are bidentate and one oxalate ligand is coordinated through one single carboxylate oxygen atom [10]. But, in case of a D_{5h} coordination symmetry, Γ_g states would be detected in the UV-Vis absorption spectra of uranyl oxalato complexes, as observed in the spectrum of $[UO_2F_5]^{3-}$ (D_{5h}) [21]. All the assignments mentioned above are only based on the formation of *monomeric species* [10,18-20].

At the moment, we tentatively propose a *dimeric structure* with D_{2h} coordination symmetry for the uranyl oxalato complexes formed in acetone. Each uranyl unit in this dimer is a pentagonal bipyramid (Figure 8.6). The structure, depicted in Figure 8.6, has been reported in the literature for solid uranyl oxalato complexes, where one oxalate group is

1,4-coordinated to two uranyl ions. The other oxalate ligand is bidentate to one uranyl ion and monodentate to another. In the solid state, infinite double chains $[C_2O_4(UO_2)C_2O_4(UO_2)C_2O_4]_n^{2n-}$ are produced in this way [15]. In solution, however, this chain is limited to a dimeric species with a bridging oxalate group. Coordinated water molecules instead of the monodentate carboxylate group have also been observed in crystal structures of oxalato complexes [15].

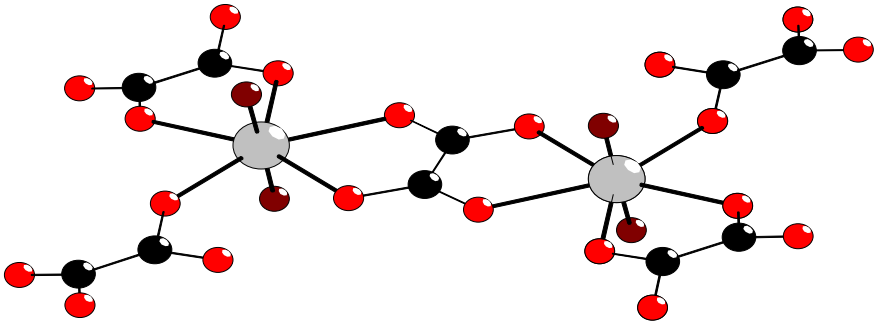

Figure 8.6. Proposed dimeric structure of uranyl oxalato complexes in solution [15].

Analogous dimeric structures have been published for solid uranyl sulphate compounds, which also exhibit sharp peaks in the low energy part of their UV-Vis absorption spectra at low temperatures [22-24]. Recently, a crystal structure determination revealed that the complex $[(UO_2)_2(Bet)_6(H_2O)_2](Tf_2N)_4$ (bet = betaine; $(CH_3)_3N^+CH_2COO^-$) is built up of two uranyl units bridged by two betaine ligands [25].

A slight distortion of the ideal D_{2h} symmetry results in a D_2 coordination symmetry. All the spectroscopic data of uranyl oxalato complexes are consistent with the formation of a dimeric species with D_2 coordination symmetry.

✓ The transitions between the totally symmetric ground state Σ_g^+ (A in D_2) and the B_3 and B_2 excited states, both arising from Π_g, are electric dipole allowed along the x- and y-axis, respectively. The transition to the B_1 component of the Δ_g state is electric dipole allowed along the z-axis.

These electric dipole transitions induce intensity between 20500 cm^{-1} and 23000 cm^{-1} in the UV-Vis absorption spectra of uranyl oxalato complexes.

✓ The origins of the transitions to the B_3, B_2 and B_1 excited states can not be distinguished. However, these transitions appear in the correct region, i.e. between 20500 cm^{-1} and 23000 cm^{-1}, when compared with the assignment of the electronic transitions in the spectra of $Cs_2UO_2Cl_4$ single crystals [9].

✓ In the MCD spectra of uranyl oxalato complexes in acetone, only B-terms are observed, which is consistent with the absence of degenerate states in a D_2 coordination symmetry. In addition, the MCD signals are very weak.

✓ The single equatorial vibration mentioned by Denning, is the out-of-plane bending ν_{10} (b_{1u} in D_{4h} and a_u in D_{2h}) [9,26]. Two ligands are vibrating upwards and two ligands downwards out of the equatorial plane, as displayed in Figure 8.7. This vibration becomes totally symmetric and transforms as *a* in D_2 coordination symmetry.

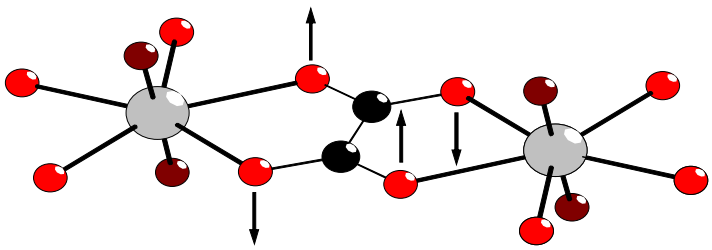

Figure 8.7. Out-of-plane bending ν_{10} (*a* in D_2) inducing an intramolecular twisting mechanism.

▪ From the photochemical point of view, the vibration ν_{10} induces an intramolecular twisting mechanism, thereby destroying the oxalate ions.

- From a spectroscopic viewpoint, this vibration correlates with the symmetric stretching vibration ν_s of the uranyl ion, both vibrations transforming as *a* in D_2 (Table 2.3). This out of-plane bending induces intensity in the low energy region of the UV-Vis absorption spectrum.
- From the theoretical point of view, this is the only equatorial vibration explicitly stated in reference [26], in which the complex intensity mechanisms are described. The vibration ν_{10} has the same symmetry as the LUMO, a fact which was probably overlooked (Figure 2.1). Consequently, the otherwise parity forbidden transition $\delta_u \leftarrow \sigma_u^+$ is allowed along the z-axis due to the simultaneous excitation of the b_{1u} vibration according to $B_{1u} \times B_{1u} \leftarrow A_{2u}$ in D_{4h}. This becomes $A_u \times A_u \leftarrow B_{1u}$ in D_{2h} and $A \times A \leftarrow B_1$ in D_2.

Based on spectroscopic measurements, we have tentatively proposed a structure of the uranyl oxalato complexes formed in acetone as well as a mechanism behind the photochemical reaction of oxalic acid. We believe that optical spectroscopic techniques have given us all possible information. In addition, the vibration ν_{10} is neither Raman nor IR active. Therefore, we hope that this hypothesis can be confirmed in future by the analyses of uranium L_{III}-edge EXAFS spectra of uranyl oxalato complexes in acetone and by theoretical calculations on dimeric species.

References

[1] Jørgensen, C.K.; Reisfeld, R. *J. Electrochem. Soc.* **1983**, *130*, 681-684.

[2] Jørgensen, C.K.; Reisfeld, R. *Struct. Bond.* **1982**, *50*, 121-171.

[3] Rabinowitch, E.; Belford, L.R. *Spectroscopy and Photochemistry of Uranyl Compounds*, **1964**, Pergamon, Oxford.

[4] Balzani, V.; Carassiti, V. *Photochemistry of Coordination Compounds*, **1970**, Academic Press Inc., London.

[5] Baird, C.P.; Kemp, T.J. *Prog. React. Kinet.* **1997**, *22*, 87-139 and references therein.

[6] Güsten, H. *Gmelin Handbook of Inorganic Chemistry, Uranium, Suppl. Vol. A6*, **1983**, Springer-Verlag, Berlin-Heidelberg.

[7] Yusov, A.B.; Shilov, V.P. *Russ. Chem. Bull., Int. Ed.* **2000**, *49*, 1925-1953.

[8] Pierloot, K.; van Besien, E. *J. Chem. Phys.* **2005**, *123*, 204309.

[9] Denning, R.G.; Snellgrove, T.R.; Woodwark, D.R. *Mol. Phys.* **1976**, *32*, 419-442.

[10] Vallet, V.; Moll, H.; Wahlgren, U.; Szabó, Z.; Grenthe, I. *Inorg. Chem.* **2003**, *42*, 1982-1993.

[11] (a) Havel, J. *Coll. Czech. Chem. Commun.* **1969**, *34*, 3248-3265. (b) Havel, J.; Soto-Guerrero, J.; Lubal, P. *Polyhedron* **2002**, *21*, 1411-1420.

[12] Ferri, D.; Iuliano, M.; Manfredi, C.; Vasca, E.; Caruso, T.; Clemente, M.; Fontanella, C. *J. Chem. Soc., Dalton Trans.* **2000**, 3460-3466.

[13] Szabó, Z.; Fischer, A. *Acta Cryst.* **2002**, *E58*, i56-i58.

[14] (a) Alcock, N.W. *J. Chem. Soc., Dalton Trans.* **1973**, 1610-1613. (b) Alcock, N.W. *J. Chem. Soc., Dalton Trans.* **1973**, 1614-1616. (c) Alcock, N.W. *J. Chem. Soc., Dalton Trans.* **1973**, 1616-1620.

[15] Leciejewicz, J.; Alcock, N.W.; Kemp, T.J. *Struct. Bond.* **1995**, *82*, 43-84.

[16] McCleskey, T.M.; Foreman, T.M.; Hallman, E.E.; Burns, C.J.; Sauer, N.N. *Environ. Sci. Technol.* **2001**, *35*, 547-551.

[17] De Houwer, S. *Intensities of vibronic transitions in uranyl spectra: application to uranyl complexes in non-aqueous solvents*, **2003**, PhD thesis, Katholieke Universiteit Leuven.

[18] Görller-Walrand, C.; De Houwer, S.; Fluyt, L.; Binnemans, K. *Phys. Chem. Chem. Phys.* **2004**, *6*, 3292-3298.

[19] Görller-Walrand, C.; De Jaegere, S. *J. Chim. Phys.* **1973**, *2*, 360-366.

[20] van Besien, E.; Pierloot, K.; Görller-Walrand, C. *Phys. Chem. Chem. Phys.* **2006**, *8*, 4311-4319.

[21] Görller-Walrand, C.; Colen, W.; Dao, N.Q. *J. Chem. Phys.* **1982**, *76*, 13-19.

[22] Gos, M.-P. *Spectrale studie van uranylsulfaten*, Master thesis, **1986**, Katholieke Universiteit Leuven.

[23] Niinistö, L.; Toivonen, J.; Valkonen, J. *Acta Chem. Scand.* **1979**, *A33*, 621-624.

[24] Zalkin, A.; Ruben, H.; Templeton, D.H. *Inorg. Chem.* **1978**, *17*, 3701-3702.

[25] Nockemann, P. personal communication.

[26] Denning, R.G.; Snellgrove, T.R.; Woodwark, D.R. *Mol. Phys.* **1979**, *37*, 1109-1143.

GENERAL CONCLUSIONS AND SUMMARY

The uranyl ion (UO_2^{2+}) has been extensively studied for decades and nowadays it is still a hot topic in a number of contemporary issues like nuclear waste treatment and the Balkan syndrome. Therefore, besides our fundamental interest in this complex system, the aim of this study was to provide a convenient and straightforward approach to identify the structure of various uranyl complexes formed in solution. To achieve this goal, spectroscopic techniques like UV-Vis absorption spectroscopy, luminescence and excitation spectroscopy as well as magnetic circular dichroism (MCD) were used, thereby focusing on typical eye-catching features like intense peaks and vibrational fine structure. This vibrational fine structure in the spectra of uranyl compounds is affected by the symmetry of the first coordination sphere of UO_2^{2+}. In this work, we obtained the optical spectra of a number of symmetry groups, i.e. D_{4h}, D_{3h}, D_{2h} and D_3 coordination symmetry, which can be used as fingerprints of a certain symmetry group.

These spectroscopic data were complemented with *Extended X-ray Absorption Fine Structure* (EXAFS) spectroscopy on the L_{III}-edge of uranium. This modern experimental technique enables us to obtain structural information like bond distances, on solution species. Moreover, the equatorial bond distances can be related with the coordination number of the uranyl ion. For example, a U-O_{eq} bond distance between 2.34 Å and 2.42 Å is characteristic for a fivefold coordination of the uranyl unit. We have chosen some well-known systems like $[UO_2(H_2O)_5]^{2+}$ and $[UO_2Cl_4]^{2-}$ to get familiar with the curve fitting procedure of EXAFS data. Afterwards we applied the knowledge we had obtained from these simple compounds to more complicated systems like $[UO_2(NO_3)_3]^-$ and $UO_2(NO_3)_2(TBP)_2$. These uranium L_{III}-edge EXAFS data have given additional evidence for the geometry of the complexes proposed by optical spectroscopic techniques. It is obvious

that the unique combination of optical spectroscopic techniques, available fingerprint spectra and uranium L_{III}-edge EXAFS spectroscopy provides us with a valuable tool for determining the first coordination sphere of unknown uranyl complexes in solution. The most important conclusions of this work are summarized in the following paragraphs.

✓ The optical spectra of the solution species have been compared with the spectra measured on single crystals. There is a good agreement between the energy values of the different electronic transitions of the single crystals and those of the same species in solution. We have to remark, however, that the spectroscopic properties of a uranyl complex in solution differ from those of the same compound in the solid state. First, in solution the absorption and luminescence bands are much broader. Consequently, overlap between the several electronic and vibronic transitions in the uranyl spectrum is inevitable. Furthermore, the molecules are randomly oriented in solution, so any polarization can be observed, making the spectrum in solution more complicated to analyse.

✓ All electronic transitions in the spectrum of the uranyl ion ($D_{\infty h}$) are parity forbidden by the Laporte selection rule. Two intensity mechanisms are currently invoked: either the static ligand field or the coupling of vibrations of ungerade parity (vibronic coupling).

✓ The maximum coordination of the uranyl ion with chloride ions in **non-aqueous solution** is four. The UV-Vis absorption spectrum can be explained in the centrosymmetric $\boldsymbol{D_{4h}}$ **coordination symmetry**. Thus, the spectrum is purely vibronic in nature. The UV-Vis absorption spectrum of the uranyl tetrachloro complex $[UO_2Cl_4]^{2-}$ is dominated by the vibronic coupling mechanism. Intensity is induced by coupling of the asymmetric stretching (ν_a, a_{2u}) and the bending (ν_b, e_u) vibrations of the uranyl ion itself and especially of one equatorial ligand vibration, i.e. ν_{10} (b_{1u}). This U-Cl out-of-plane bending, transforming as the f_{xyz} orbital, is coupled to the first electronic transition $\Pi_g \leftarrow \Sigma_g^+$ ($E_g \leftarrow A_{1g}$) and to one component of the transition $\Delta_g \leftarrow \Sigma_g^+$ ($B_{2g} \leftarrow A_{1g}$). The fourfold coordination of the uranyl ion with chloride ions is also demonstrated by uranium L_{III}-edge

EXAFS spectroscopy. The $[UO_2Cl_4]^{2-}$ polyhedron contains two axial oxygen atoms at 1.77 Å and four chloride ligands at 2.68 Å.

✓ The UV-Vis absorption spectra of complexes exhibiting a **trigonal D_{3h} coordination symmetry** like $[UO_2(NO_3)_3]^-$ and $[UO_2(CH_3COO)_3]^-$, both formed in **organic solvents**, are characterized by very sharp, intense peaks at the low energy side of the spectrum, i.e. between 21000 cm^{-1} and 24000 cm^{-1}. The corresponding MCD signals are intense negative A-terms. The spectra of $[UO_2(NO_3)_3]^-$ and $[UO_2(CH_3COO)_3]^-$ are affected by the static ligand field. In D_{3h} symmetry, the transition $\Delta_g \leftarrow \Sigma_g^+$ ($E' \leftarrow A'_1$) is electronically allowed along the x- and y-axis, thereby inducing intensity in the first region of the spectrum (21000 cm^{-1} - 24000 cm^{-1}), which results in the typical sharp and intense peaks. Uranium L_{III}-edge EXAFS data have given evidence for the trigonal symmetry of $[UO_2(NO_3)_3]^-$ and $[UO_2(CH_3COO)_3]^-$ species in non-aqueous solution. The uranyl ion is surrounded by three bidentate nitrate groups at 2.48 Å in the equatorial plane in the uranyl trinitrato complex. Special features at larger distances, indicating the presence of distal oxygen atoms at 4.16 Å, are observed in the Fourier transform due to the linear arrangement within the nitrate groups. The uranium L_{III}-edge EXAFS spectrum of $[UO_2(CH_3COO)_3]^-$ exhibits the same structural features as that of $[UO_2(NO_3)_3]^-$ and can be explained in a similar way. The first coordination sphere of the uranyl ion in $[UO_2(CH_3COO)_3]^-$ consists of three acetate ligands with the U-O_{eq} distance equal to 2.48 Å. The focusing effect is also important within the acetate groups, thereby identifying the distal carbon atoms at a distance of 4.37 Å.

✓ Whereas the UV-Vis absorption spectra of $[UO_2Cl_4]^{2-}$ and $[UO_2(NO_3)_3]^-$ are dominated by the $\sigma_u^+\delta_u$ configuration, the $\sigma_u^+\phi_u$ configuration plays a dominant role in the spectrum of the inclusion complex $[UO_2(18\text{-crown-}6)]^{2+}$. At higher energies the $\Gamma_g \leftarrow \Sigma_g^+$ transition ($\sigma_u^+\phi_u$) appears, which is typical for a **D_3 coordination symmetry**. The identification of six equatorial oxygen atoms at 2.46 Å and twelve equatorial carbon atoms at 3.51 Å in the EXAFS spectrum

and the corresponding Fourier transform indicates the inclusion of UO_2^{2+} in the crown ether cavity. The U-O_{eq} and U-C_{eq} bond distances cover a large range, which is reflected in the high Debye-Waller factors σ^2.

✓ The uranyl complexes mentioned above are obtained in non-aqueous solvents (acetonitrile, acetone). The stability constants of the different complexes in these solvents are not known, unlike those in **aqueous solution**. The ligand affinity towards the uranyl ion changes from non-aqueous solvents to aqueous solutions. Whereas $[UO_2Cl_4]^{2-}$ and $[UO_2(NO_3)_3]^-$ are formed in acetonitrile and acetone, no significant complex formation occurs between the uranyl ion and chloride or nitrate ions in aqueous solution. This weak complex formation is confirmed by the absence of spectral changes in the UV-Vis absorption spectra with respect to the spectrum of the "free" uranyl ion, the observation of the typical features of $[UO_2(H_2O)_5]^{2+}$ in the EXAFS spectra and the species distribution calculations using the known stability constants.

✓ **Ionic liquids** are salts, composed of an organic cation and an organic/inorganic anion, with a melting point below 100 °C. Currently, studies are performed to replace the classical organic solvents by these ionic liquids in numerous fields of chemistry like separation processes, catalysis and organic synthesis. Due to the growing interest in ionic liquids, we have investigated the speciation of uranyl complexes in imidazolium-based and pyrrolidinium-based ionic liquids by means of spectroscopic techniques (UV-Vis absorption spectroscopy, luminescence and excitation spectroscopy, magnetic circular dichroism, uranium L_{III}-edge EXAFS spectroscopy). Thereby, the anionic component of the ionic liquids was varied. The comparison of the spectroscopic properties in ionic liquids with the fingerprint spectra in non-aqueous solvents unambiguously points to the formation of $[UO_2Cl_4]^{2-}$, $[UO_2(NO_3)_3]^-$ and $[UO_2(CH_3COO)_3]^-$ species as well as to the presence of the inclusion complex $[UO_2(18\text{-crown-}6)]^{2+}$ in the ionic liquids $[C_4mim][Tf_2N]$ and $[bmpyr][Tf_2N]$. The cations and the anions of the ionic liquids seem to have no influence on the positions of the electronic transitions. Indeed,

there is a good agreement with the corresponding UV-Vis data in non-aqueous solution. The presence of a $[UO_2(NO_3)_3]^-$ species in $[C_4mim][Tf_2N]$ is demonstrated by uranium L_{III}-edge EXAFS spectroscopy. The structural parameters of the $[UO_2(NO_3)_3]^-$ coordination polyhedron in the ionic liquid are comparable with those in acetonitrile. Uranium L_{III}-edge EXAFS measurements on the other complexes studied in ionic liquids, will be performed in future.

✓ The presence of small inorganic ligands inhibits the formation of the inclusion complex $[UO_2(18\text{-crown-}6)]^{2+}$ in ionic liquids. This is consistent with the observations in acetonitrile and propylene carbonate. Once a trace of chloride or bromide ions is added to the ionic liquid, the crown ether is removed from the first coordination sphere, as established by UV-Vis absorption spectroscopy and crystal structure determinations.

✓ During the synthesis of imidazolium-based ionic liquids, one has to take care that all 1-methylimidazole has reacted. Otherwise, hydrolysis products of the uranyl ion are formed in the ionic liquids, giving a broad, structureless band in the UV-Vis absorption spectra. Furthermore, kinetic effects are involved in the sample preparation of uranyl-containing ionic liquids. It would be very interesting to study these kinetic effects in more detail in future, for example by means of UV-Vis absorption spectroscopy.

✓ **Tri-*n*-butylphosphate** (TBP) is a commonly used neutral extracting agent in liquid-liquid extraction processes for nuclear waste treatment. Knowledge of the geometry of the species involved in these extraction procedures can provide insight in the development of new, more selective extracting agents. Therefore, we have investigated the first coordination sphere of the uranyl ion in a tri-*n*-butylphosphate solution containing $UO_2(NO_3)_2{\cdot}6H_2O$. Both ^{31}P NMR spectroscopy and UV-Vis absorption spectroscopy indicate the formation of the **$UO_2(NO_3)_2(TBP)_2$** complex in solution. The vibrational fine structure in the spectrum can be attributed to a ***D_{2h}* coordination symmetry**. Hence, the spectrum is purely vibronic in nature. In the MCD spectrum, only B-terms are observed, which is

consistent with the removal of all degeneracy in D_{2h} symmetry. Furthermore, we were able to calculate the equilibrium constant K_{eq} and the thermodynamic parameters (ΔH, ΔS) of the complex formation reaction between $UO_2(NO_3)_2 \cdot 6H_2O$ and tri-n-butylphosphate, based on the ^{31}P NMR data. Uranium L_{III}-edge EXAFS spectroscopy also reveals the coordination of two bidentate coordinated nitrate groups ($U\text{-}O_{eq}$ = 2.52 Å) and two monodentate phosphate groups ($U\text{-}O_{eq}$ = 2.37 Å). Complex multiple scattering features have to be included in the analysis of the spectra due to the linear arrangement within the nitrate groups and the tri-*n*-butylphosphate ligands. Investigation of the structure of $UO_2(NO_3)_2(TBP)_2$ in ionic liquids might contribute to the studies of the potential replacement of organic solvents in liquid-liquid extraction processes.

✓ The **photochemistry** of the actinide compounds is almost exclusively dominated by the uranyl ion. However, the mechanisms of most of these photochemical reactions are not known yet. An interesting topic is the structure of **uranyl oxalato complexes** involved in these photochemical reactions. We have presented a different perspective on the complex formation of the uranyl ion with oxalate ions. Based on spectroscopic measurements in acetone solution, we have proposed a dimeric species with a bridging oxalate group, where each uranyl unit is a pentagonal bipyramid. In addition, the UV-Vis absorption spectra, which exhibit an increase in intensity in the low energy part, are consistent with a dimeric structure with D_2 coordination symmetry. Furthermore, we believe that the out-of-plane bending ν_{10} (*a* in D_2) can induce an intramolecular twisting mechanism, thereby destroying the oxalate ligands. Hopefully our hypothesis will be confirmed in future by uranium L_{III}-edge EXAFS spectroscopy and theoretical calculations on dimeric structures.

✓ It has been emphasized in our studies that for a metal-to-ligand ratio of 1:2 or 1:3 a di- or tricomplex is not necessarily formed, which is often overlooked in the literature. Many mistakes are also made by assuming that the dissolution of a solid uranyl compound will give the same

structure as the solid in solution. For example, the salt $UO_2(NO_3)_2 \cdot 6H_2O$ dissolved in aqueous solution is fully dissociated, thereby forming the hydrated "free" uranyl ion.

It is obvious that uranium L_{III}-edge EXAFS spectroscopy offers good prospects for future work concerning the coordination environment of the uranyl ion in solution as well as in ionic liquids. However, an important disadvantage is encountered using EXAFS spectroscopy. In case of a mixture of species, the EXAFS data will only give average coordination numbers and bond distances, which hampers the clarification of the structure of solution species. Therefore, we would suggest that the combination of UV-Vis absorption spectroscopy, luminescence spectroscopy, where possible magnetic circular dichroism, group theoretical analysis as well as uranium L_{III}-edge EXAFS spectroscopy, NMR spectroscopy, theoretical calculations and principal component analysis is an excellent tool for elucidating the geometry and the composition of the first coordination sphere of several unknown uranyl complexes. The determination of the structure of the intermediately formed chloro and nitrato complexes in non-aqueous solvents by a combination of the techniques mentioned above is a real challenge! But, at first, it would be very helpful to get insight in the structure of the solvated uranyl ion in anhydrous acetonitrile.

SAMENVATTING

Hoewel men reeds jaren uitgebreid onderzoek op het uranylion (UO_2^{2+}) heeft verricht, blijft het ook nu nog een belangrijk onderwerp in het licht van een aantal hedendaagse problemen zoals nucleaire afvalverwerking en het Balkansyndroom. Naast onze fundamentele interesse in dit complex systeem, werd de structuurbepaling van verschillende uranylcomplexen in oplossing tot doel gesteld. Om dit doel te bereiken, werden spectroscopische technieken zoals UV-zichtbaar absorptiespectroscopie, luminescentie- en excitatiespectroscopie en magnetisch circulair dichroïsme (MCD) gebruikt, waarbij we ons vooral toelegden op in het oog springende eigenschappen, zoals intense pieken of typische vibrationele fijnstructuur. Deze vibrationele fijnstructuur in de spectra van uranylverbindingen wordt beïnvloed door de symmetrie van de eerste coördinatiesfeer van het uranylion. In dit doctoraatsproefschrift werden de optische spectra van een aantal symmetriegroepen, namelijk D_{4h}, D_{3h}, D_{2h} en D_3, verzameld die als het ware fingerprints zijn voor een bepaalde coördinatiesymmetrie.

Deze spectroscopische gegevens werden aangevuld met data verkregen uit *Extended X-ray Absorption Fine Structure* (EXAFS) spectroscopie. Deze moderne experimentele techniek laat toe om structurele informatie zoals bindingsafstanden te achterhalen van deeltjes in oplossing. Deze bindingsafstanden kunnen bovendien in verband gebracht worden met het coördinatiegetal van het uranylion. Zo is een U-O_{eq} bindingafstand tussen 2.34 Å en 2.42 Å karakteristiek voor een vijfvoudige coördinatie van het uranylion. We hebben gekozen voor enkele beter gekende systemen zoals $[UO_2(H_2O)_5]^{2+}$ en $[UO_2Cl_4]^{2-}$ om vertrouwd te worden met de verwerking van de EXAFS-data. Vervolgens werd de verkregen kennis toegepast op ingewikkeldere systemen zoals $[UO_2(NO_3)_3]^-$ en $UO_2(NO_3)_2(TBP)_2$. Deze EXAFS-metingen leverden bijkomende aanwijzingen voor de geometrie van de

uranylcomplexen, die voorgesteld werd op basis van de optische spectroscopische technieken. Het is duidelijk dat de unieke combinatie van optische spectroscopische technieken, beschikbare fingerprint spectra en uraan L_{III}-edge EXAFS spectroscopie waardevolle informatie biedt over de eerste coördinatiesfeer van uranylcomplexen in oplossing. De volgende paragrafen geven een overzicht van de belangrijkste conclusies van het uitgevoerde onderzoek.

✓ Wanneer we de spectroscopische eigenschappen van een complex in oplossing vergelijken met deze van dezelfde verbinding in de vaste toestand, stellen we duidelijke verschillen in de spectra vast. In de eerste plaats zijn de absorptie- en luminescentiebanden in oplossing veel breder. Bijgevolg is overlapping tussen de verschillende elektronische en vibronische overgangen in het uranylspectrum onvermijdelijk. Ook zijn de moleculen in oplossing willekeurig georiënteerd, wat eveneens een effect op de spectra heeft. Dit alles samen maakt de analyse van een uranylspectrum in oplossing zeer moeilijk. Ondanks deze verschillen is er een goede overeenkomst tussen de elektronische overgangen van het complex in de vaste toestand en deze van dezelfde verbinding in oplossing.

✓ Alle elektronische overgangen in het spectrum van het uranylion ($D_{\infty h}$) zijn door de Laporte selectieregel pariteitverboden. Daarom wordt er beroep gedaan op twee intensiteitmechanismen: hetzij het statische ligandveld hetzij de koppeling van vibraties met ungerade pariteit (vibronische koppeling).

✓ De maximale coördinatie van het uranylion met chloride-ionen in **niet-waterige oplossing** is vier. Het UV-zichtbaar absorptiespectrum kan toegeschreven worden aan de centrosymmetrische $\boldsymbol{D_{4h}}$ **symmetrie** en is bijgevolg zuiver vibronisch. Het UV-zichtbaar absorptiespectrum van $[UO_2Cl_4]^{2-}$ is het resultaat van vibronische koppeling. Intensiteit wordt geïnduceerd door de koppeling van de asymmetrische rekvibratie (ν_a, a_{2u}) en de buigvibratie (ν_b, e_u) van het uranylion zelf en in het bijzonder door de koppeling van één equatoriale vibratie, namelijk de U-Cl buigvibratie

uit het vlak ν_{10} (b_{1u}). Deze laatste vibratie transformeert zoals het f_{xyz} orbitaal en is gekoppeld aan de eerste elektronische overgang $\Pi_g \leftarrow \Sigma_g^+$ ($E_g \leftarrow A_{1g}$) evenals aan één component van de overgang $\Delta_g \leftarrow \Sigma_g^+$ ($B_{2g} \leftarrow A_{1g}$). De viervoudige coördinatie van het uranylion met chloride-ionen wordt eveneens bevestigd door uraan L_{III}-edge EXAFS spectroscopie. De $[UO_2Cl_4]^{2-}$ polyeder bestaat uit twee axiale zuurstofatomen op 1.77 Å en vier chlorideliganden op 2.68 Å.

✓ De UV-zichtbaar absorptiespectra van complexen met een **trigonale D_{3h} symmetrie**, zoals $[UO_2(NO_3)_3]^-$ en $[UO_2(CH_3COO)_3]^-$ in **niet-waterige oplossingen**, worden gekenmerkt door zeer scherpe, intense pieken bij lage energie, d.i. tussen 21000 cm^{-1} en 24000 cm^{-1}. De overeenkomstige MCD-signalen zijn intense negatieve A-termen. De UV-zichtbaar absorptiespectra van $[UO_2(NO_3)_3]^-$ en $[UO_2(CH_3COO)_3]^-$ worden door het statische ligandveld beïnvloed. In D_{3h} symmetrie is de overgang $\Delta_g \leftarrow \Sigma_g^+$ ($E' \leftarrow A'_1$) elektrisch dipool toegelaten volgens de x- en y-as. Hierdoor wordt intensiteit geïnduceerd in de overgangen tussen 21000 cm^{-1} en 24000 cm^{-1}, hetgeen resulteert in de typisch scherpe, intense pieken. De trigonale symmetrie van $[UO_2(NO_3)_3]^-$ en $[UO_2(CH_3COO)_3]^-$ werd bovendien aangetoond met de overeenkomstige uraan L_{III}-edge EXAFS-spectra. Het uranylion in $[UO_2(NO_3)_3]^-$ wordt omringd door drie bidentaat gecoördineerde nitraatgroepen in het equatoriale vlak. Speciale structuren op grotere afstanden, die duiden op de aanwezigheid van zuurstofatomen op 4.16 Å, worden waargenomen in de Fourier getransformeerde. De bepaling van dergelijke grote afstanden wordt mogelijk gemaakt door de lineaire ordening in de nitraatgroepen. Het uraan L_{III}-edge EXAFS spectrum van $[UO_2(CH_3COO)_3]^-$ vertoont dezelfde eigenschappen en kan dus op een analoge manier geanalyseerd worden. De eerste coördinatiesfeer van het uranylion in $[UO_2(CH_3COO)_3]^-$ bestaat uit drie acetaatliganden, waarbij de $U\text{-}O_{eq}$ bindingsafstand gelijk is aan 2.48 Å. Het 'focusing effect' speelt ook een belangrijke rol in het spectrum van $[UO_2(CH_3COO)_3]^-$, waardoor de

identificatie van de koolstofatomen op een afstand van 4.37 Å mogelijk is.

✓ Daar waar de UV-zichtbaar absorptiespectra van $[UO_2Cl_4]^{2-}$ en $[UO_2(NO_3)_3]^-$ hoofdzakelijk het resultaat zijn van overgangen van de $\sigma_u^+\delta_u$ configuratie, wordt het spectrum van het insluitingcomplex $[UO_2(18\text{-kroon-}6)]^{2+}$ gedomineerd door de $\sigma_u^+\phi_u$ configuratie. Bij hogere energie verschijnt de transitie $\Gamma_g \leftarrow \Sigma_g^+$ ($\sigma_u^+\phi_u$), hetgeen karakteristiek is voor een ***D*$_3$ coördinatiesymmetrie**. De aanwezigheid van zes equatoriale zuurstofatomen op een afstand van 2.46 Å en twaalf equatoriale koolstofatomen op een afstand van 3.51 Å, zoals blijkt uit de fitprocedure van het EXAFS-spectrum en de Fourier getransformeerde, wijst op de insluiting van UO_2^{2+} in de holte van de kroonether. De grote variatie in de U-O_{eq} en U-C_{eq} bindingsafstanden wordt weerspiegeld in de hoge waarde van de overeenkomstige Debye-Waller factoren σ^2.

✓ De bovenvermelde complexen worden verkregen in organische solventen, zoals acetonitril en aceton. De stabiliteitsconstanten van de verschillende complexen in deze solventen zijn echter niet gekend, in tegenstelling tot deze in **waterige oplossing**. De sterkte waarmee liganden met het uranylion coördineren, hangt sterk af van het gebruikte solvent. Daar waar $[UO_2Cl_4]^{2-}$ en $[UO_2(NO_3)_3]^-$ gevormd worden in acetonitril en aceton, treedt er geen significante complexvorming van het uranylion met chloride- of nitraationen op in waterige oplossingen. Deze zwakke complexvorming wordt bevestigd door de afwezigheid van spectrale veranderingen in de UV-zichtbaar absorptiespectra ten opzichte van het spectrum van het "vrij" uranylion, door de typische structuur van $[UO_2(H_2O)_5]^{2+}$ in de EXAFS-spectra en door concentratieberekeningen van de gevormde complexen met behulp van de gekende stabiliteitsconstanten.

✓ **Ionische vloeistoffen** zijn zouten bestaande uit een organisch kation en een organisch/anorganisch anion met een smeltpunt beneden 100 °C. Momenteel wordt onderzoek verricht naar het gebruik van deze ionische vloeistoffen in verschillende takken van de chemie, zoals

scheidingsprocedures, katalyse en organische synthese, en dit ter vervanging van de klassieke organische solventen. Omwille van deze groeiende interesse in ionische vloeistoffen hebben we de coördinatie van het uranylion bestudeerd in ionische vloeistoffen met 1-alkyl-3-methylimidazolium en 1,1'-dialkylpyrrolidinium als kation met behulp van spectroscopische technieken (UV-zichtbaar absorptiespectroscopie, luminescentie- en excitatiespectroscopie, magnetisch circulair dichroïsme, uraan L_{III}-edge EXAFS spectroscopie). Hierbij werd de anionische component van de ionische vloeistoffen gevarieerd. De vergelijking van de spectroscopische eigenschappen in ionische vloeistoffen met de fingerprint spectra in niet-waterige oplossingen wijst éénduidig op de vorming van $[UO_2Cl_4]^{2-}$, $[UO_2(NO_3)_3]^-$ en $[UO_2(CH_3COO)_3]^-$ alsook op de aanwezigheid van het insluitingcomplex $[UO_2(18\text{-kroon-}6)]^{2+}$ in de ionische vloeistoffen $[C_4mim][Tf_2N]$ en $[bmpyr][Tf_2N]$. De kationen en de anionen van de ionische vloeistoffen lijken geen invloed te hebben op de posities van de elektronische overgangen, aangezien een goede overeenkomst wordt vastgesteld met de UV-zichtbaar spectra in niet-waterige solventen. De vorming van $[UO_2(NO_3)_3]^-$ in de ionische vloeistof $[C_4mim][Tf_2N]$ werd bovendien aangetoond met uraan L_{III}-edge EXAFS spectroscopie. De structurele parameters van de $[UO_2(NO_3)_3]^-$ coördinatiepolyeder in de ionische vloeistof zijn analoog aan deze in acetonitril. In de toekomst zullen EXAFS-metingen uitgevoerd worden op de andere complexen die bestudeerd werden in ionische vloeistoffen.

✓ De toevoeging van kleine anorganische liganden verhindert de insluiting van het uranylion in de kroonetherring in de ionische vloeistoffen. Een gelijkaardig effect werd in acetonitril en propyleencarbonaat waargenomen. Zodra een spoortje chloride- of bromide-ionen aanwezig is, wordt de kroonether uit de eerste coördinatiesfeer verdreven, zoals bevestigd door UV-zichtbaar absorptiespectroscopie en kristalstructuurbepalingen.

✓ Tijdens de synthese van imidazolium ionische vloeistoffen moet erover gewaakt worden dat het startproduct, d.i. 1-methylimidazool, volledig weggereageerd is. Anders worden hydrolyseproducten van het uranylion in de ionische vloeistoffen gevormd, hetgeen aanleiding geeft tot een brede, structuurloze band in de UV-zichtbaar absorptiespectra. Verder spelen kinetische effecten een rol bij het oplossen van uranylzouten in ionische vloeistoffen. Het is zeer interessant om deze kinetische effecten door middel van bijvoorbeeld UV-zichtbaar absorptiespectroscopie meer in detail te bestuderen.

✓ **Tri-*n*-butylfosfaat** (TBP) is een veelgebruikt neutraal extractiemiddel in vloeistof-vloeistof extractiemethoden voor de verwerking van kernafval. Inzicht in de geometrie van de deeltjes die betrokken zijn in deze processen, kan bijdragen tot de ontwikkeling van nieuwe, selectievere extractiemiddelen. Daarom werd de eerste coördinatiesfeer van het uranylion onderzocht in een tri-*n*-butylfosfaatoplossing van $UO_2(NO_3)_2 \cdot 6H_2O$. Zowel ^{31}P NMR spectroscopie als UV-zichtbaar absorptiespectroscopie bevestigt de vorming van het $\mathbf{UO_2(NO_3)_2(TBP)_2}$ complex in oplossing. De vibrationele fijnstructuur kan toegekend worden aan een $\boldsymbol{D_{2h}}$ **symmetrie** en is bijgevolg zuiver vibronisch van aard. In het MCD-spectrum worden enkel B-termen waargenomen, hetgeen te verklaren is door de opheffing van alle ontaarding in een D_{2h} symmetrie. Op basis van de ^{31}P NMR-data werd de evenwichtsconstante K_{eq} en de thermodynamische parameters (ΔH, ΔS) van de complexvormingsreactie van $UO_2(NO_3)_2 \cdot 6H_2O$ met tri-*n*-butylphosphate bepaald. De uraan L_{III}-edge EXAFS-gegevens wijzen eveneens op de omringing van het uranylion door twee bidentaat gecoördineerde nitraatgroepen ($U\text{-}O_{eq}$ = 2.52 Å) en twee monodentaat fosfaatliganden ($U\text{-}O_{eq}$ = 2.37 Å). Ingewikkelde meervoudige verstrooiingspaden moeten opgenomen worden in de analyse van de spectra, wat te wijten is aan de lineaire ordening in de nitraatgroepen en tri-*n*-butylfosfaat.

✓ De **fotochemie** van actinidenverbindingen wordt door het uranylion gedomineerd. Nochtans zijn de mechanismen van de meeste fotochemische reacties nog niet gekend. Een interessante onderzoeksvraag is onder andere welke structuur de **oxalato-uranylcomplexen**, betrokken in dergelijke fotochemische reacties, hebben. We hebben een andere kijk op de complexvorming van het uranylion met oxalaationen voorgesteld op basis van spectroscopische metingen in aceton. De voorgestelde structuur voor de oxalato-uranylcomplexen is een dimeer met een brugvormende oxalaatgroep (***D_2* symmetrie**). Daarbij vormt elke uranyleenheid een pentagonale bipyramide. De UV-zichtbaar absorptiespectra, die een sterke intensiteitstijging vertonen bij lage energie, zijn bovendien te verklaren in een D_2 symmetrie. Verder geloven we dat de buigvibratie uit het vlak ν_{10} (*a* in D_2) een intramoleculair twistingmechanisme kan induceren, waardoor de oxalaationen ontbonden worden. Wij zouden deze hypothese in de toekomst graag bevestigd zien door uraan L_{III}-edge EXAFS spectroscopie en theoretische berekeningen op dimeren.

✓ Wij willen benadrukken dat een metaal-ligand verhouding van 1:2 of 1:3 niet noodzakelijk inhoudt dat een di- of tricomplex gevormd wordt. Dit wordt in de literatuur echter dikwijls over het hoofd gezien. Verder worden dikwijls fouten gemaakt tegen het feit dat het oplossen van een vaste uranylverbinding niet dezelfde structuur geeft als in de vaste toestand. Bijvoorbeeld is het uranylzout $UO_2(NO_3)_2{\cdot}6H_2O$ in waterige oplossing volledig gedissocieerd, waarbij het gehydrateerd uranylion gevormd wordt.

Het is duidelijk dat uraan L_{III}-edge EXAFS spectroscopie goede vooruitzichten biedt voor toekomstig werk betreffende de coördinatieomgeving van het uranylion in oplossingen en in ionische vloeistoffen. Toch worden we geconfronteerd met een belangrijk nadeel van EXAFS spectroscopie. Wanneer we te maken hebben met een mengsel van deeltjes in oplossing, geeft EXAFS spectroscopie enkel

gemiddelde coördinatiegetallen en bindingsafstanden. Dit bemoeilijkt uiteraard de structuurbepaling van deeltjes in oplossing. Daarom stellen we voor dat de combinatie van UV-zichtbaar absorptiespectroscopie, luminescentiespectroscopie, indien mogelijk magnetisch circulair dichroïsme, groepentheoretische analyses evenals uraan L_{III}-edge EXAFS spectroscopie, NMR spectroscopie, theoretische berekeningen en principal component analysis een uitstekend uitgangspunt is voor de bepaling van de geometrie en de samenstelling van de eerste coördinatiesfeer van allerhande nieuwe uranylcomplexen. Het vinden van de structuur van de intermediair gevormde chloro- en nitrato-uranylcomplexen in niet-waterige oplossing met behulp van de bovenstaande technieken vormt een echte uitdaging voor de toekomst! Maar allereerst is het nuttig inzicht te krijgen in de omringing van het gesolvateerde uranylion in 100% watervrije acetonitril.

PUBLICATIONS AND ATTENDED CONFERENCES

Publications

1 "*The inclusion of the uranyl ion UO_2^{2+} in the cavity of the crown ether 18-crown-6 in acetonitrile: a UV-Vis and EXAFS study*".
Servaes, K.; Hennig, C.; Görller-Walrand, C. in preparation.

2 "*Speciation of uranyl nitrato complexes in acetonitrile and in the ionic liquid 1-butyl-3-methylimidazolium bis(trifluoromethyl-sulfonyl)imide*".
Servaes, K.; Hennig, C.; Billard, I.; Gaillard, C.; Binnemans, K.; Van Deun, R.; Görller-Walrand, C. *Eur. J. Inorg. Chem.*, accepted.

3 "*EXAFS and UV-Vis investigation of the first coordination sphere of the uranyl ion in $UO_2(NO_3)_2(TBP)_2$*".
Servaes, K.; Hennig, C.; Görller-Walrand, C. Proceedings to the 4th Workshop on Speciation, Techniques and Facilities for Radioactive Materials at Synchrotron Light Sources, Karlsruhe, Germany, September 18th - 20th, 2006 (in print).

4 "*Structure of $[UO_2Cl_4]^{2-}$ in Acetonitrile*".
Servaes, K.; Hennig, C.; Van Deun, R.; Görller-Walrand, C. *Inorg. Chem.* **2005**, *44*, 7705-7707.

5 "*Spectroscopic properties of uranyl crown ether complexes in non-aqueous solvents*".
Servaes, K.; De Houwer, S.; Görller-Walrand, C.; Binnemans, K. *Phys. Chem. Chem. Phys.* **2004**, *6*, 2946-2950.

6 "*On the site symmetry of uranyl crown compounds in solution*".
De Houwer, S.; Servaes, K.; Görller-Walrand, C. *Phys. Chem. Chem. Phys.* **2003**, *5*, 1164-1168.

Conferences

1 4th Workshop on Speciation, Techniques and Facilities for Radioactive Materials at Synchrotron Light Sources (Actinide XAS Workshop), Karlsruhe, Germany, September 18th-20th, 2006.
Poster: "*EXAFS and UV-Vis investigation of the first coordination sphere of the uranyl ion in solution*".

2 23rd European Crystallographic Meeting, Leuven, Belgium, August 6th-11th, 2006.
Poster: "*A comparative UV-Vis and EXAFS investigation of the uranyl coordination in solution*".

3 8th Junior Conference of Chemistry in Flanders (VJC8), Leuven, Belgium, April 7th, 2006.
Poster: "*Onderzoek van de uranylcoördinatie met UV-Vis en EXAFS*".

4 7th Junior Conference of Chemistry in Flanders (VJC7), Gent, Belgium, April 16th, 2004.
Lecture: "*Een nieuwe kijk op de complexvorming van uranyl UO_2^{2+} met oxalaat $^-OOC\text{-}COO^-$: fotochemie van uranyloxalaat*".

5 33èmes Journées des Actinides, Prague, Czech Republic, April 27th-29th, 2003.
Poster: "*Spectroscopic study of sol-gel glasses doped with uranyl and uranyl complexes*".

A1 SAFETY ISSUES ON HANDLING URANYL SAMPLES

The uranyl salts used in this work like $UO_2(ClO_4)_2 \cdot xH_2O$, $UO_2(CH_3COO)_2 \cdot 2H_2O$ and $UO_2(NO_3)_2 \cdot 6H_2O$, contain a considerable amount of uranium. But, one has to warn against jumping to conclusions about the risks of doing research on these compounds.

Handling of uranyl samples

- The spectroscopic measurements described in this work were carried out with very small amounts of uranyl salts. The uranyl salts were weighed wearing gloves and a dust mask. Afterwards, the products were dissolved and handled in volumetric flasks. Any α-radiation is well confined within these flasks or within the uranyl salt containers.
- After use, the solutions are kept in separate waste containers.
- The solutions prepared in volumetric flasks, were transferred into a polyethylene pipette for the EXAFS measurements. After filling, the pipette is hot-sealed with a soldering iron. Finally, the pipette is encapsulated in a polyethylene bag, the second confinement. These samples were transported to the European Synchrotron Radiation Facility (ESRF) in Grenoble by a firm specialized in the transport of radioisotopes.
- Experiments on samples containing thorium, natural or depleted uranium can often be performed without special authorization. They do not present any particular radiation safety hazard, on condition that the samples are contained in such a way to ensure their integrity during the

experiment. Nevertheless, their presence has to be reported to the safety group of the synchrotron radiation facility.

- Before the start and at the end of each experiment, a gamma-measurement of the samples was carried out by the ESRF safety group to ensure that nobody was exposed to a high level of radiation.

A2 MOLECULAR ORBITALS

1 Altmann-Herzig definition and relationship to Y_q^k

We give a short definition of the Altmann-Herzig symbolics and the conventions used throughout Chapter 2. For more information on the Altmann-Herzig notation, we refer to Altmann et al.*

$|jm\rangle$ represents normalized spherical harmonics in the Condon-Shortley convention. In case of an orbital, j and m equal l (orbital angular momentum) and m_l (orbital magnetic momentum), respectively, whereas for tensors they stand for k (rang) and q (component).

$$|jm\rangle_+ \equiv \frac{1}{\sqrt{2}}\left(|jm\rangle + |j\overline{m}\rangle\right) \qquad \text{(A2.1)}$$

* Altmann, S.P.; Herzig, P. *Point-Group Theory Tables*, **1994**, Clarendon Press, Oxford.

$$\begin{aligned} \left|jm\right\rangle_{-} &\equiv \frac{1}{\sqrt{2}}\left(\left|jm\right\rangle - \left|j\overline{m}\right\rangle\right) \\ &= -\frac{1}{\sqrt{2}}\left(\left|j\overline{m}\right\rangle - \left|jm\right\rangle\right) \end{aligned} \qquad \text{(A2.2)}$$

$\left|jm\right\rangle_{+}$ and $\left|jm\right\rangle_{-}$ correspond to the real *s*, *p*, *d* and *f* orbitals (Table A2.1). In the general notation p_x and p_y can be written as:

p_x $\quad \frac{\sqrt{3}}{\sqrt{4\pi}}\left(Y_{-1}^{1} - Y_{+1}^{1}\right)$

p_y $\quad \frac{\sqrt{3}}{\sqrt{4\pi}}\left(Y_{-1}^{1} + Y_{+1}^{1}\right)$

Table A2.1. Altmann-Herzig notation for *s*, *p*, *d* and *f* orbitals.

p_z	$\left\|10\right\rangle_{+}$	f_{z^3}	$\left\|30\right\rangle_{+}$
p_x	$\left\|11\right\rangle_{-}$	f_{xz^2}	$\left\|31\right\rangle_{-}$
p_y	$\left\|11\right\rangle_{+}$	f_{yz^2}	$\left\|31\right\rangle_{+}$
d_{z^2}	$\left\|20\right\rangle_{+}$	$f_{z(x^2-y^2)}$	$\left\|32\right\rangle_{+}$
d_{xz}	$\left\|21\right\rangle_{-}$	f_{xyz}	$\left\|32\right\rangle_{-}$
d_{yz}	$\left\|21\right\rangle_{+}$	$f_{x(x^2-3y^2)}$	$\left\|33\right\rangle_{-}$
$d_{x^2-y^2}$	$\left\|22\right\rangle_{+}$	$f_{y(3x^2-y^2)}$	$\left\|33\right\rangle_{+}$
d_{xy}	$\left\|22\right\rangle_{-}$		

For orbitals the general description of $Y_{m_l}^{l}$ is given by:

$$Y_{m_l}^{l}(\theta,\varphi) = (-1)^{(m_l+|m_l|)/2} \cdot \sqrt{\frac{(2l+1)(l-|m_l|)!}{2(l+|m_l|)!}} \cdot \frac{1}{\sqrt{2\pi}} \cdot P_l^{|m_l|}(\cos\theta) \cdot e^{im\varphi} \qquad \text{(A2.3)}$$

where $P_l^{|m_l|}$ is a Legendre function and $e^{im\varphi} = \cos m\varphi + i \sin m\varphi$.

Therefore, Y_{-1}^1 and Y_{+1}^1 of p_x and p_y correspond to:

$$Y_{\pm 1}^1 = \mp \frac{\sqrt{3}}{\sqrt{2}\sqrt{4\pi}} sin\theta \cdot e^{\pm i\varphi} \qquad \text{(A2.4)}$$

2 Group orbitals of the two oxygen atoms of UO_2^{2+}

The oxygen group orbitals are formed by simple addition and substraction of the atomic orbitals, followed by multiplication with a normalization factor. The oxygen group orbitals are generated from the 2*p* AO, i.e. p_x, p_y and p_z. McGlynn et al. described the formation of the oxygen group orbitals by means of the p_x, p_y and p_σ atomic orbitals, where p_σ may be considered as *sp* hybrids directed towards the central metal atom.*

$\frac{1}{\sqrt{2}}(p_{z1} + p_{z2})$ σ_g^+

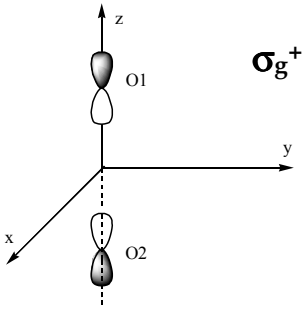

$\frac{1}{\sqrt{2}}(p_{z1} - p_{z2})$ σ_u^+

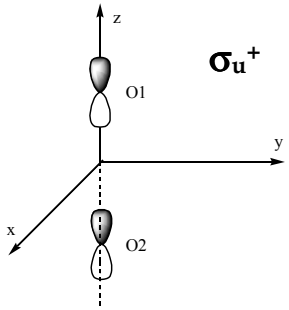

* McGlynn, S.P.; Smith, J.K. *J. Mol. Spectrosc.* **1961**, *6*, 164-187.

$\frac{1}{\sqrt{2}}(p_{x1} + p_{x2})$ and $\frac{1}{\sqrt{2}}(p_{y1} + p_{y2})$

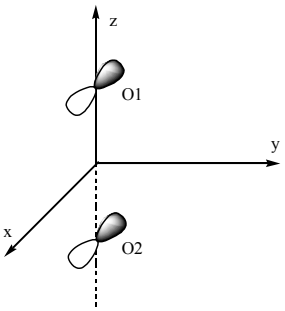

π_u

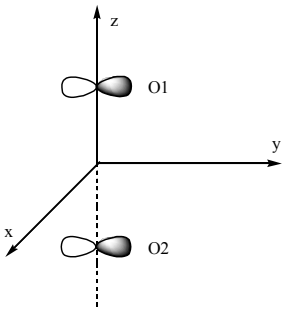

$\frac{1}{\sqrt{2}}(p_{x1} - p_{x2})$ and $\frac{1}{\sqrt{2}}(p_{y1} - p_{y2})$

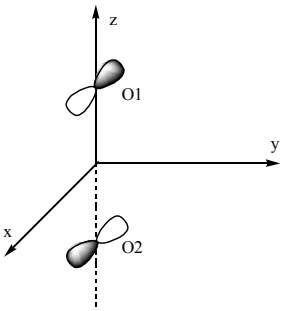

π_g

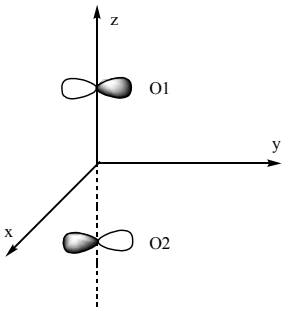

3 Molecular orbitals of the uranyl ion

3.1 Bonding molecular orbitals

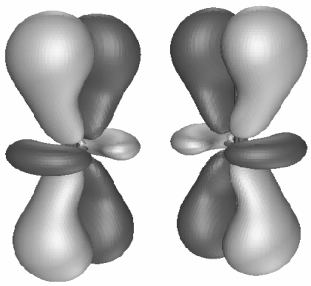

π_u

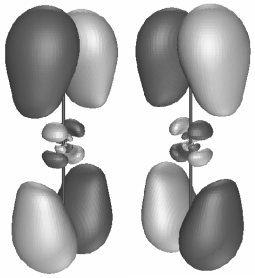

π_g

σ_g^+

σ_u^+

3.2 Non-bonding molecular orbitals

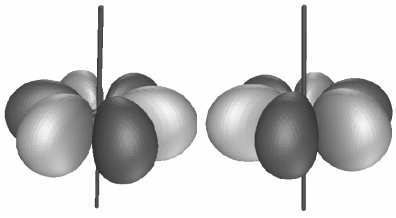

ϕ_u

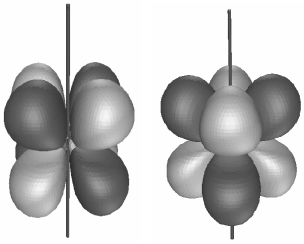

δ_u

3.3 Anti-bonding molecular orbitals

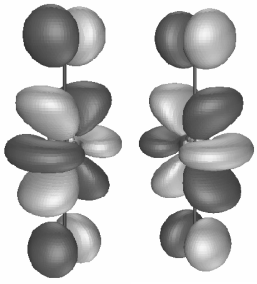

π_u

σ_u^+

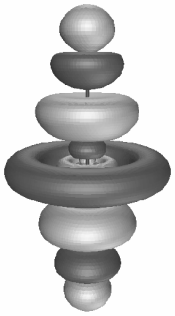

σ_g^+

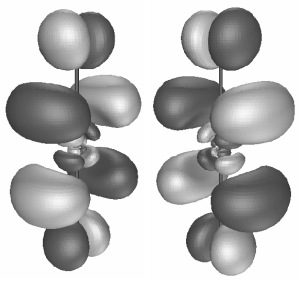

π_g

A3 SUPPORTING MATERIAL: SPECTRA AND NUMERICAL DATA

In this appendix, supporting material on some important compounds discussed in this work is given. UV-Vis, luminescence and MCD spectra in both organic solvents and ionic liquids are shown. The peak positions, the energy interval ($\Delta\nu$) between the vibrations, relative peak intensities, sign and type of the MCD term as well as the assignments of the electronic states in different symmetries are tabulated. The peaks are labelled with Roman numbers, the same number corresponding to one electronic transition. The subnumbering indicates a progression in ν_s, whilst an apostrophe suggests that another vibration is coupled to the same electronic transition.

Vibration assignments *(irreducible representations in a D_{4h} symmetry)*: (ν_s,a_{1g}) O-U-O sym. str.; (ν_a, a_{2u}) O-U-O asym. str.; (ν_b, e_u) O-U-O bend.; (ν_{10}, b_{1u}) U-Cl out-of plane bend.; (ν_{11}, e_g) O-U-O rock.

1 $[UO_2Cl_4]^{2-}$

1.1 Acetonitrile

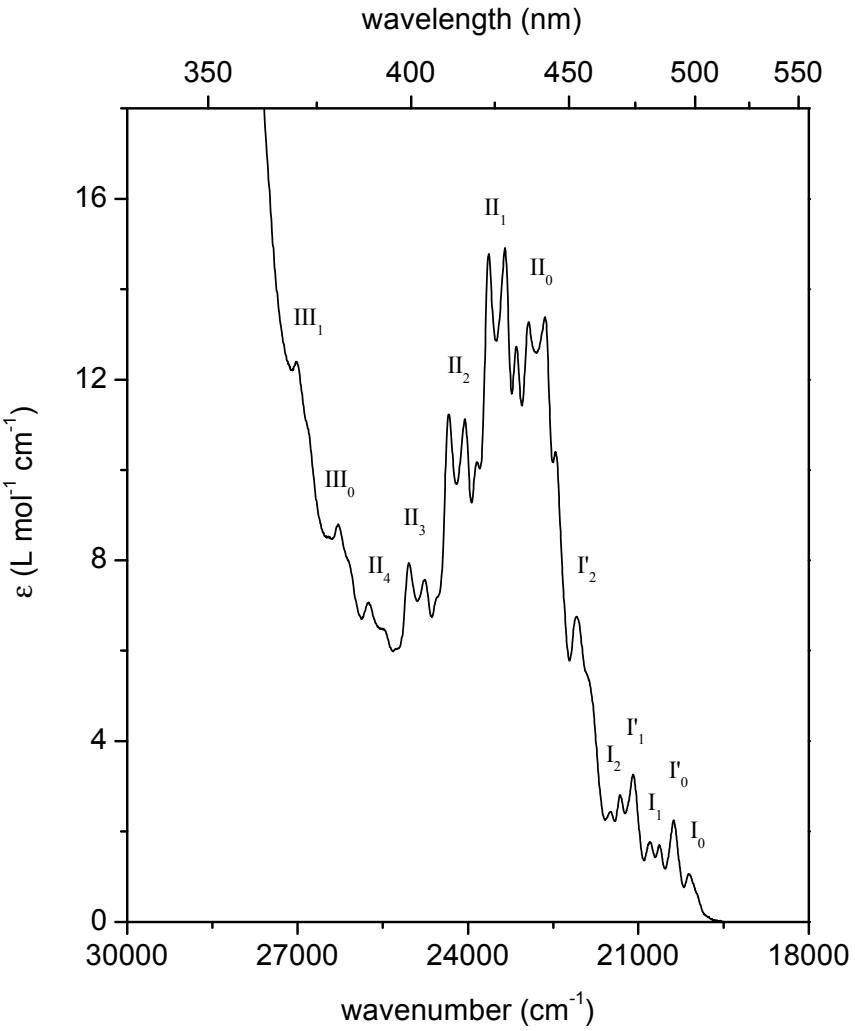

Figure A3.1. UV-Vis absorption spectrum of $[UO_2Cl_4]^{2-}$ in acetonitrile at room temperature. Metal-to-ligand ratio is 1:5. Concentrations are $[UO_2^{2+}] = 5 \times 10^{-2}$ mol L^{-1} and $[Cl^-] = 2.5 \times 10^{-1}$ mol L^{-1}.

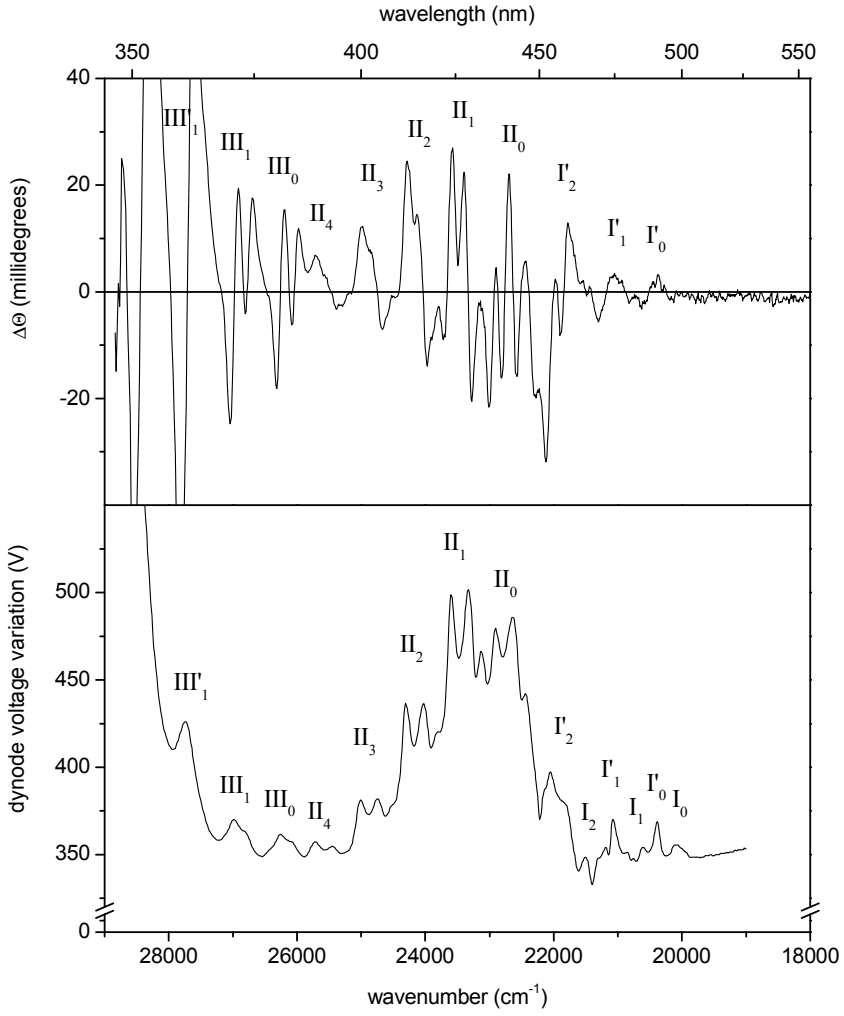

Figure A3.2. MCD (upper graph) and dynode voltage (lower graph) spectra of $[UO_2Cl_4]^{2-}$ in acetone at room temperature. Metal-to-ligand ratio is 1:5. Concentrations are $[UO_2^{2+}] = 4.5 \times 10^{-2}$ mol L^{-1} and $[Cl^-] = 2.25 \times 10^{-1}$ mol L^{-1}. *

* Görller-Walrand, C.; De Houwer, S.; Fluyt, L.; Binnemans, K. *Phys. Chem. Chem. Phys.* **2004**, *6*, 3292-3298.
De Houwer, S. *Intensities of vibronic transitions in uranyl spectra: application to uranyl complexes in non-aqueous solvents*, **2003**, PhD thesis, Katholieke Universiteit Leuven.

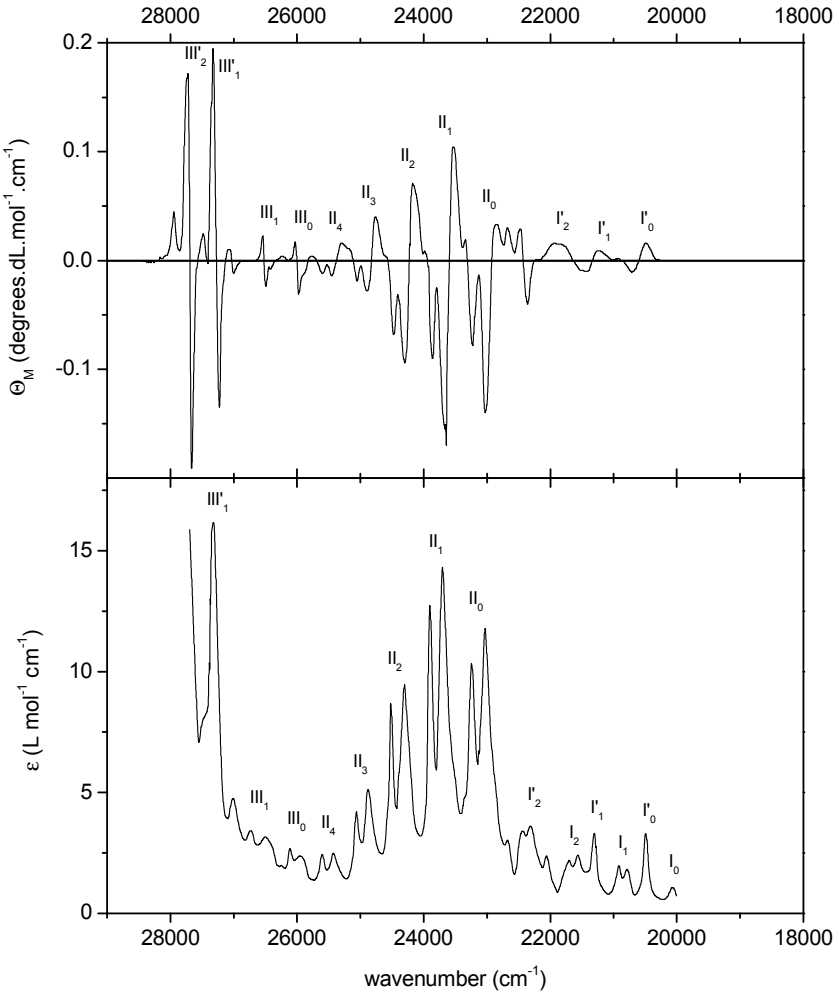

Figure A3.3. MCD (upper graph) and absorbance (lower graph) spectra of $(NBu_4)_2UO_2Cl_4$ in a PMMA matrix at 4K.*

* Colen, W., *Bijdrage tot de kennis van de electronenstructuur van uranylkompleksen*, **1980**, PhD thesis, Katholieke Universiteit Leuven.
De Houwer, S. *Intensities of vibronic transitions in uranyl spectra: application to uranyl complexes in non-aqueous solvents*, **2003**, PhD thesis, Katholieke Universiteit Leuven.

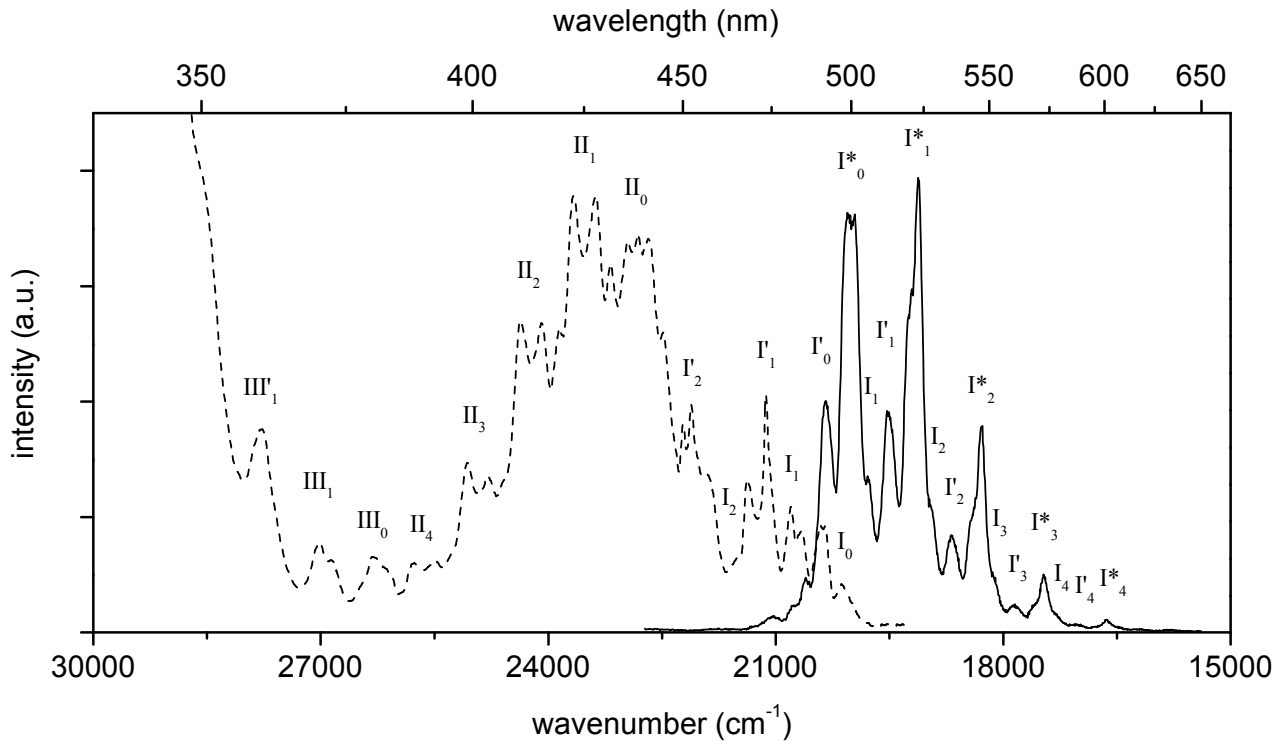

Figure A3.4. Emission (——) and excitation (-----) spectra of $[UO_2Cl_4]^{2-}$ in acetonitrile at room temperature. Metal-to-ligand ratio is 1:5. Concentrations are $[UO_2^{2+}] = 5 \times 10^{-3}$ mol L^{-1} and $[Cl^-] = 2.5 \times 10^{-2}$ mol L^{-1}.

Table A3.1. UV-Vis data of $[UO_2Cl_4]^{2-}$ in acetonitrile at room temperature. Peak positions in the excitation spectrum correspond to those in the absorption spectrum. The column MCD gives the type and sign of the MCD term. MCD data are taken from Görller-Walrand et al., *Phys. Chem. Chem. Phys.* **2004**, *6*, 3292-3298.

Band	ν /cm^{-1}	$\Delta\nu$ / cm^{-1}	λ / nm	ε / L mol^{-1} cm^{-1}	MCD	Identification	
						$D_{\infty h}$	D_{4h}
I_0	20109	--	497	1.4	--	Π_g	E_g
I'_0	20362	253	491	2.5	+B	$\Pi_g + \nu_b$	$E_g + \nu_b$
	20636	274	485	2.0	–B	$\Delta_g + \nu_{10}$; $\Delta_g + \nu_b$	$B_{2g} + \nu_{10}$; $B_{2g} + \nu_b$
I_1	20799	163	481	2.1	–B	$\Pi_g + \nu_s$	$E_g + \nu_s$
I'_1	21093	294	474	3.6	+B	$\Pi_g + \nu_b + \nu_s$	$E_g + \nu_b + \nu_s$
	21322	229	469	3.1	–B	$\Delta_g + \nu_{10} + \nu_s$; $\Delta_g + \nu_b + \nu_s$	$B_{2g} + \nu_{10} + \nu_s$; $B_{2g} + \nu_b + \nu_s$
I_2	21491	169	465	2.7	--	$\Pi_g + 2\nu_s$	$E_g + 2\nu_s$
I'_2	21877	386	457	5.7	–A	$\Pi_g + \nu_b + 2\nu_s$	$E_g + \nu_b + 2\nu_s$
	22085	208	453	7.1	–A	$\Delta_g + \nu_{10} + 2\nu_s$; $\Delta_g + \nu_b + 2\nu_s$	$B_{2g} + \nu_{10} + 2\nu_s$; $B_{2g} + \nu_b + 2\nu_s$
II_0	22457	372	445	10.7			
	22640	183	442	13.7	+A	$\Phi_g + \nu_b + \nu_{11}$	$E_g + \nu_b + \nu_{11}$
	22936	296	436	13.6	+B	$\Delta_g + \nu_{10}$	$B_{2g} + \nu_{10}$
II_1	23143	207	432	13.0			
	23348	205	428	15.2	+A	$\Phi_g + \nu_b + \nu_{11} + \nu_s$	$E_g + \nu_b + \nu_{11} + \nu_s$
	23635	287	423	15.1	+B	$\Delta_g + \nu_{10} + \nu_s$	$B_{2g} + \nu_{10} + \nu_s$

(Table A3.1 continued)

	23844	209	419	10.5			
II_2	24056	212	416	11.4	+A	$\Phi_g + \nu_b + \nu_{11} + 2\nu_s$	$E_g + \nu_b + \nu_{11} + 2\nu_s$
	24337	281	411	11.5	+B	$\Delta_g + \nu_{10} + 2\nu_s$	$B_{2g} + \nu_{10} + 2\nu_s$
	24534	197	408	7.5			
II_3	24759	225	404	7.9	+A	$\Phi_g + \nu_b + \nu_{11} + 3\nu_s$	$E_g + \nu_b + \nu_{11} + 3\nu_s$
	25044	285	399	8.2	+B	$\Delta_g + \nu_{10} + 3\nu_s$	$B_{2g} + \nu_{10} + 3\nu_s$
	25265	221	396	6.3			
II_4	25517	252	392	6.8	+A	$\Phi_g + \nu_b + \nu_{11} + 4\nu_s$	$E_g + \nu_b + \nu_{11} + 4\nu_s$
	25747	230	388	7.4	+B	$\Delta_g + \nu_{10} + 4\nu_s$	$B_{2g} + \nu_{10} + 4\nu_s$
III_0	26110	363	383	8.3	–B	Δ_g	B_{2g}
	26288	178	380	9.1	–A	(Φ_g, H_g)	E_g
III_1	26860	572	372	11.4	–B	$\Delta_g + \nu_s$	$B_{2g} + \nu_s$
	27027	167	370	12.7	–A	$(\Phi_g, H_g) + \nu_s$	$E_g + \nu_s$
III'_1	27809	782	360	21.7	–A	$(\Phi_g, H_g) + \nu_a + \nu_s$	$E_g + \nu_a + \nu_s$

Table A3.2. Emission data of $[UO_2Cl_4]^{2-}$ in acetonitrile at room temperature.

Band	ν / cm^{-1}	$\Delta\nu$ / cm^{-1}	λ / nm	I / a.u.	Identification	
					$D_{\infty h}$	D_{4h}
I'_0	20342	--	492	6.2	$\Pi_g - \nu_b$	$E_g - \nu_b$
I^*_0	20056	286	499	11.3	$\Pi_g - \nu_{10} - \nu_{11}$; $\Pi_g - \nu_b - \nu_{11}$	$E_g - \nu_{10} - \nu_{11}$; $E_g - \nu_b - \nu_{11}$
	19960	96	501	11.3		
I_1	19786	174	505	4.2	$\Pi_g - \nu_s$	$E_g - \nu_s$
I'_1	19531	255	512	6.0	$\Pi_g - \nu_b - \nu_s$	$E_g - \nu_b - \nu_s$
I^*_1	19238	293	520	9.2	$\Pi_g - \nu_{10} - \nu_{11} - \nu_s$; $\Pi_g - \nu_b - \nu_{11} - \nu_s$	$E_g - \nu_{10} - \nu_{11} - \nu_s$; $E_g - \nu_b - \nu_{11} - \nu_s$
	19120	118	523	12.3		
I_2	18961	159	527	3.4	$\Pi_g - 2\nu_s$	$E_g - 2\nu_s$
I'_2	18685	276	535	2.6	$\Pi_g - \nu_b - 2\nu_s$	$E_g - \nu_b - 2\nu_s$
I^*_2	18389	296	544	3.4	$\Pi_g - \nu_{10} - \nu_{11} - 2\nu_s$; $\Pi_g - \nu_b - \nu_{11} - 2\nu_s$	$E_g - \nu_{10} - \nu_{11} - 2\nu_s$; $E_g - \nu_b - \nu_{11} - 2\nu_s$
	18275	114	547	5.6		
I_3	18129	146	552	1.5	$\Pi_g - 3\nu_s$	$E_g - 3\nu_s$
I'_3	17844	285	560	0.7	$\Pi_g - \nu_b - 3\nu_s$	$E_g - \nu_b - 3\nu_s$
I^*_3	17581	263	569	0.8	$\Pi_g - \nu_{10} - \nu_{11} - 3\nu_s$; $\Pi_g - \nu_b - \nu_{11} - 3\nu_s$	$E_g - \nu_{10} - \nu_{11} - 3\nu_s$; $E_g - \nu_b - \nu_{11} - 3\nu_s$
	17470	111	572	1.6		
I_4	17295	175	578	0.5	$\Pi_g - 4\nu_s$	$E_g - 4\nu_s$
I'_4	16995	300	588	0.2	$\Pi_g - \nu_b - 4\nu_s$	$E_g - \nu_b - 4\nu_s$
I^*_4	16756	239	597	0.2	$\Pi_g - \nu_{10} - \nu_{11} - 4\nu_s$; $\Pi_g - \nu_b - \nu_{11} - 4\nu_s$	$E_g - \nu_{10} - \nu_{11} - 4\nu_s$; $E_g - \nu_b - \nu_{11} - 4\nu_s$
	16628	128	601	0.3		

1.2 Ionic liquids [C₄mim][Tf₂N] and [bmpyr][Tf₂N]

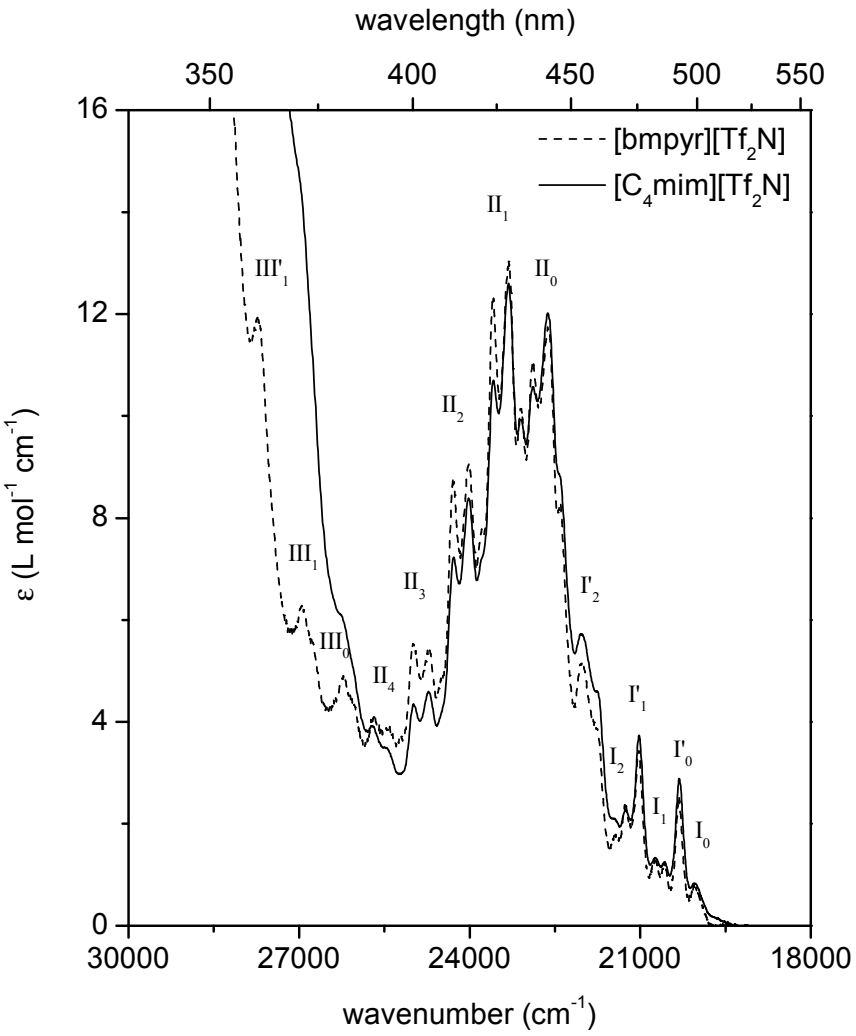

Figure A3.5. UV-Vis absorption spectra of $[UO_2Cl_4]^{2-}$ in $[C_4mim][Tf_2N]$ and $[bmpyr][Tf_2N]$ at room temperature. Metal-to-ligand ratio is 1:5. Concentrations are $[UO_2^{2+}] = 5 \times 10^{-2}$ mol L^{-1} and $[Cl^-] = 2.5 \times 10^{-1}$ mol L^{-1} in $[C_4mim][Tf_2N]$ and $[UO_2^{2+}] = 10^{-2}$ mol L^{-1} and $[Cl^-] = 5 \times 10^{-2}$ mol L^{-1} in $[bmpyr][Tf_2N]$.

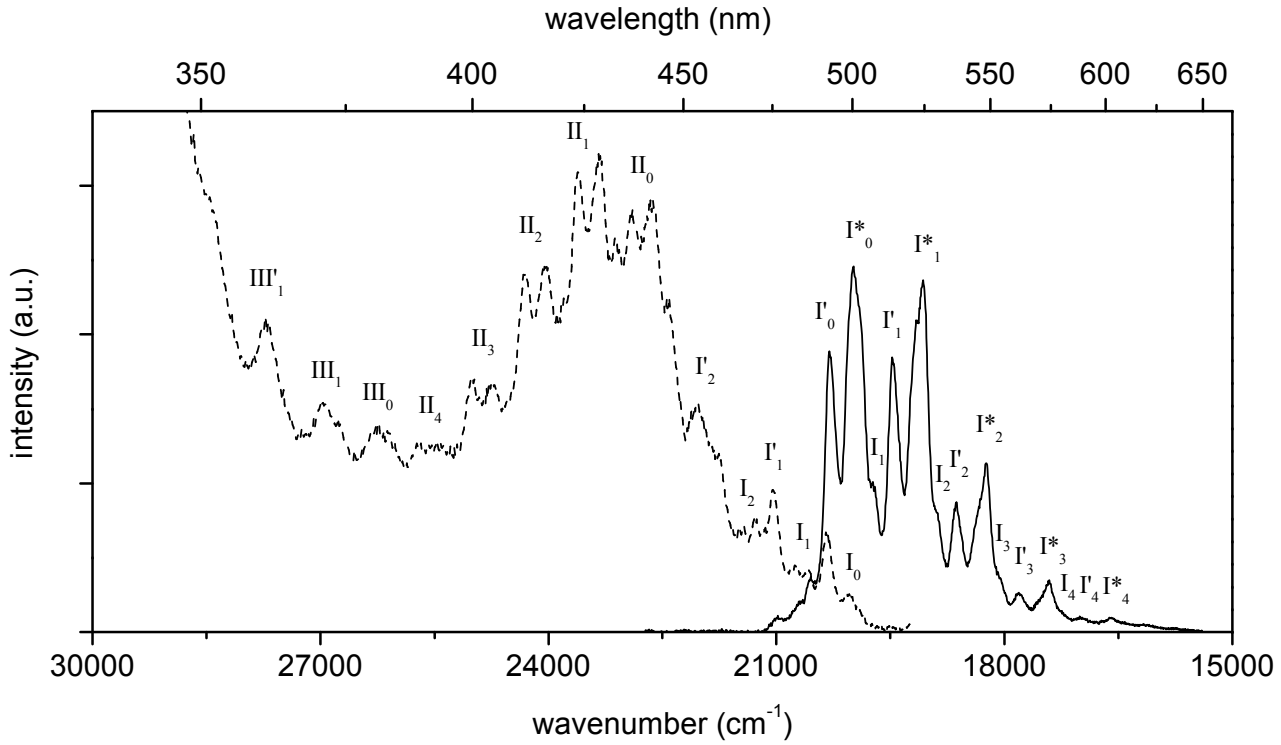

Figure A3.6. Emission (——) and excitation (-----) spectra of $[UO_2Cl_4]^{2-}$ in [bmpyr][Tf_2N] at room temperature. Metal-to-ligand ratio is 1:5. Concentrations are $[UO_2^{2+}] = 10^{-2}$ mol L^{-1} and $[Cl^-] = 5 \times 10^{-2}$ mol L^{-1}.

Table A3.3. UV-Vis data of $[UO_2Cl_4]^{2-}$ in $[C_4mim][Tf_2N]$ and [bmpyr][Tf_2N] at room temperature. Peak positions in the excitation spectrum in [bmpyr][Tf_2N] correspond to those in the absorption spectrum.

	$[UO_2Cl_4]^{2-}$ in $[C_4mim][Tf_2N]$			$[UO_2Cl_4]^{2-}$ in [bmpyr][Tf_2N]			Identification	
Band	ν / cm^{-1}	$\Delta\nu$ / cm^{-1}	ε / L mol^{-1} cm^{-1}	ν / cm^{-1}	$\Delta\nu$ / cm^{-1}	ε / L mol^{-1} cm^{-1}	$D_{\infty h}$	D_{4h}
I_0	20044	--	0.8	20032	--	0.7	Π_g	E_g
I'_0	20313	269	2.9	20321	289	2.5	$\Pi_g + \nu_b$	$E_g + \nu_b$
	20563	250	1.2	20568	247	1.2	$\Delta_g + \nu_{10}$; $\Delta_g + \nu_b$	$B_{2g} + \nu_{10}$; $B_{2g} + \nu_b$
I_1	20738	175	1.3	20734	166	1.3	$\Pi_g + \nu_s$	$E_g + \nu_s$
	21022	284	3.7	21039	305	3.4	$\Pi_g + \nu_b + \nu_s$	$E_g + \nu_b + \nu_s$
I'_1	21254	232	2.3	21258	219	2.4	$\Delta_g + \nu_{10} + \nu_s$; $\Delta_g + \nu_b + \nu_s$	$B_{2g} + \nu_{10} + \nu_s$; $B_{2g} + \nu_b + \nu_s$
I_2	21468	214	2.1	21468	210	1.8	$\Pi_g + 2\nu_s$	$E_g + 2\nu_s$
	21763	295	4.6	21815	347	4.0	$\Pi_g + \nu_b + 2\nu_s$	$E_g + \nu_b + 2\nu_s$
I'_2	22046	283	5.7	22046	231	5.1	$\Delta_g + \nu_{10} + 2\nu_s$; $\Delta_g + \nu_b + 2\nu_s$	$B_{2g} + \nu_{10} + 2\nu_s$; $B_{2g} + \nu_b + 2\nu_s$
	22432	386	8.9	22416	370	8.3		
II_0	22629	197	12.0	22630	214	11.7	$\Phi_g + \nu_b + \nu_{11}$	$E_g + \nu_b + \nu_{11}$
	22894	265	10.6	22894	264	11.1	$\Delta_g + \nu_{10}$	$B_{2g} + \nu_{10}$
	23100	206	9.9	23111	217	10.1		
II_1	23315	215	12.6	23315	204	13.0	$\Phi_g + \nu_b + \nu_{11} + \nu_s$	$E_g + \nu_b + \nu_{11} + \nu_s$
	23579	264	10.7	23596	281	12.3	$\Delta_g + \nu_{10} + \nu_s$	$B_{2g} + \nu_{10} + \nu_s$

(Table A3.3 continued)

	23759	180	7.3	23787	191	7.8		
II_2	24021	262	8.4	24015	228	9.1	$\Phi_g + \nu_b + \nu_{11} + 2\nu_s$	$E_g + \nu_b + \nu_{11} + 2\nu_s$
	24278	257	7.2	24295	280	8.8	$\Delta_g + \nu_{10} + 2\nu_s$	$B_{2g} + \nu_{10} + 2\nu_s$
	24498	220	4.2	24504	209	4.8		
II_3	24722	224	4.6	24710	206	5.4	$\Phi_g + \nu_b + \nu_{11} + 3\nu_s$	$E_g + \nu_b + \nu_{11} + 3\nu_s$
	24987	265	4.3	25006	296	5.5	$\Delta_g + \nu_{10} + 3\nu_s$	$B_{2g} + \nu_{10} + 3\nu_s$
	25221	234	3.0	25202	196	3.7		
II_4	25458	237	3.5	25504	302	3.8	$\Phi_g + \nu_b + \nu_{11} + 4\nu_s$	$E_g + \nu_b + \nu_{11} + 4\nu_s$
	25700	242	3.9	25720	216	4.1	$\Delta_g + \nu_{10} + 4\nu_s$	$B_{2g} + \nu_{10} + 4\nu_s$
III_0	--	--	--	26082	362	4.5	Δ_g	B_{2g}
	26302	602	6.1	26247	165	4.8	(Φ_g, H_g)	E_g
III_1	--	--	--	26831	584	5.8	$\Delta_g + \nu_s$	$B_{2g} + \nu_s$
	--	--	--	26961	130	6.3	$(\Phi_g, H_g) + \nu_s$	$E_g + \nu_s$
III'_1	--	--	--	27731	770	11.9	$(\Phi_g, H_g) + \nu_a + \nu_s$	$E_g + \nu_a + \nu_s$

Table A3.4. Emission data of $[UO_2Cl_4]^{2-}$ in [bmpyr][Tf_2N] at room temperature.

Band	ν / cm^{-1}	$\Delta\nu$ / cm^{-1}	λ / nm	I / a.u.	Identification	
					$D_{\infty h}$	D_{4h}
I'_0	20300	--	493	12.4	Π_g - ν_b	E_g - ν_b
I^*_0	19984	316	500	16.1	Π_g - ν_{10} - ν_{11}; Π_g - ν_b - ν_{11}	E_g - ν_{10} - ν_{11}; E_g - ν_b - ν_{11}
I_1	19732	252	507	6.6	Π_g - ν_s	E_g - ν_s
I'_1	19475	257	513	12.1	Π_g - ν_b - ν_s	E_g - ν_b - ν_s
I^*_1	19157 19069	318 88	522 524	13.8 15.5	Π_g - ν_{10} - ν_{11} - ν_s; Π_g - ν_b - ν_{11} - ν_s	E_g - ν_{10} - ν_{11} - ν_s; E_g - ν_b - ν_{11} - ν_s
I_2	18911	158	529	5.4	Π_g - $2\nu_s$	E_g - $2\nu_s$
I'_2	18629	282	537	5.7	Π_g - ν_b - $2\nu_s$	E_g - ν_b - $2\nu_s$
I^*_2	18335 18235	294 100	545 548	5.5 7.4	Π_g - ν_{10} - ν_{11} - $2\nu_s$; Π_g - ν_b - ν_{11} - $2\nu_s$	E_g - ν_{10} - ν_{11} - $2\nu_s$; E_g - ν_b - ν_{11} - $2\nu_s$
I_3	18090	145	553	2.6	Π_g - $3\nu_s$	E_g - $3\nu_s$
I'_3	17806	284	562	1.7	Π_g - ν_b - $3\nu_s$	E_g - ν_b - $3\nu_s$
I^*_3	17513 17409	293 104	571 574	1.5 2.3	Π_g - ν_{10} - ν_{11} - $3\nu_s$; Π_g - ν_b - ν_{11} - $3\nu_s$	E_g - ν_{10} - ν_{11} - $3\nu_s$; E_g - ν_b - ν_{11} - $3\nu_s$
I_4	17235	174	580	0.9	Π_g - $4\nu_s$	E_g - $4\nu_s$
I'_4	17007	228	588	0.7	Π_g - ν_b - $4\nu_s$	E_g - ν_b - $4\nu_s$
I^*_4	16711 16622	296 89	598 602	0.5 0.6	Π_g - ν_{10} - ν_{11} - $4\nu_s$; Π_g - ν_b - ν_{11} - $4\nu_s$	E_g - ν_{10} - ν_{11} - $4\nu_s$; E_g - ν_b - ν_{11} - $4\nu_s$

2 $[UO_2(NO_3)_3]^-$

2.1 Acetonitrile

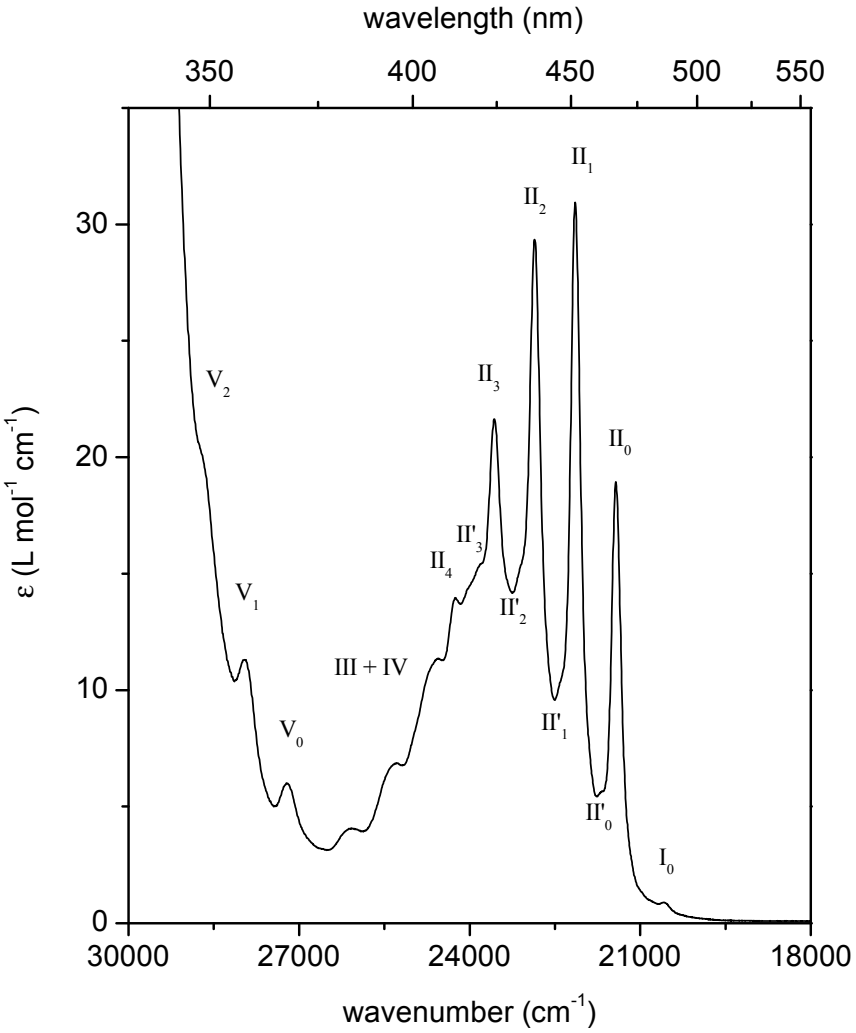

Figure A3.7. UV-Vis absorption spectrum of $[UO_2(NO_3)_3]^-$ in acetonitrile at room temperature. Metal-to-ligand ratio is 1:4. Concentrations are $[UO_2^{2+}] = 5 \times 10^{-2}$ mol L^{-1} and $[NO_3^-] = 2 \times 10^{-1}$ mol L^{-1}.

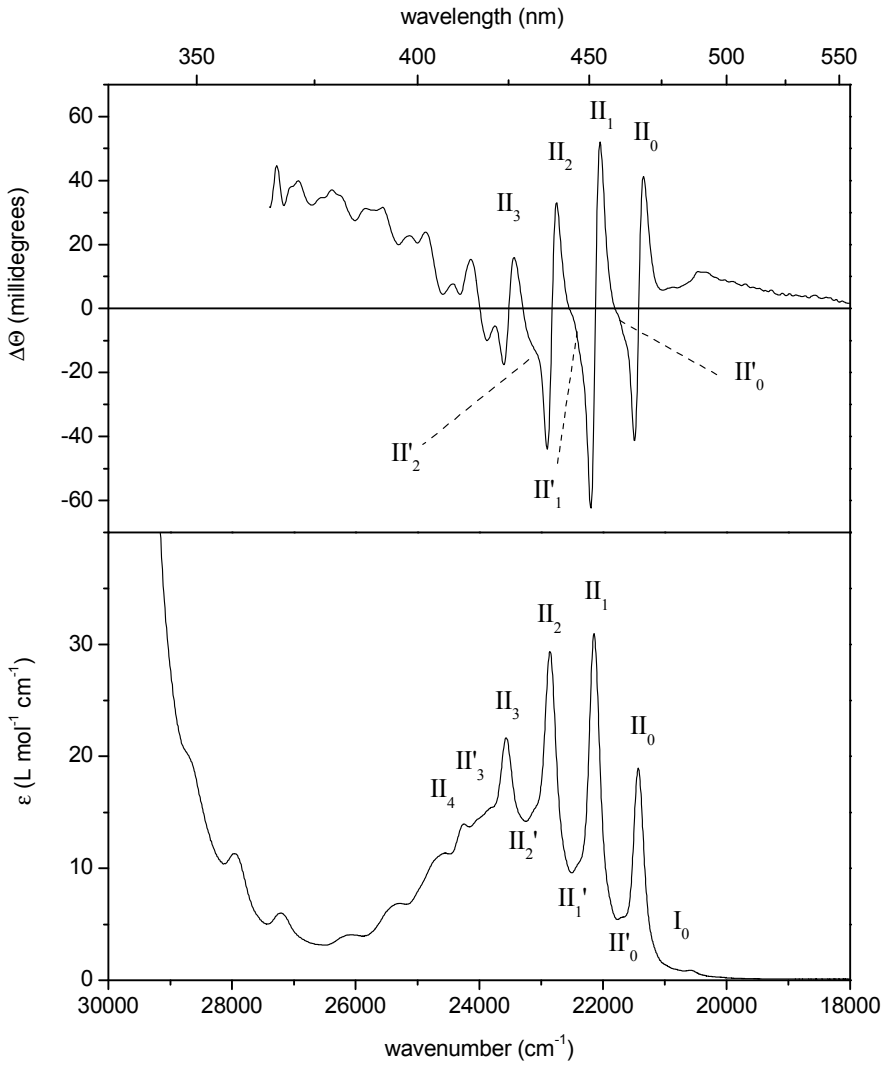

Figure A3.8. MCD (upper graph) and UV-Vis absorption (lower graph) spectra of $[UO_2(NO_3)_3]^-$ in acetonitrile at room temperature. Metal-to-ligand ratio is 1:4. Concentrations are $[UO_2^{2+}] = 5 \times 10^{-2}$ mol L^{-1} and $[NO_3^-] = 2 \times 10^{-1}$ mol L^{-1}.

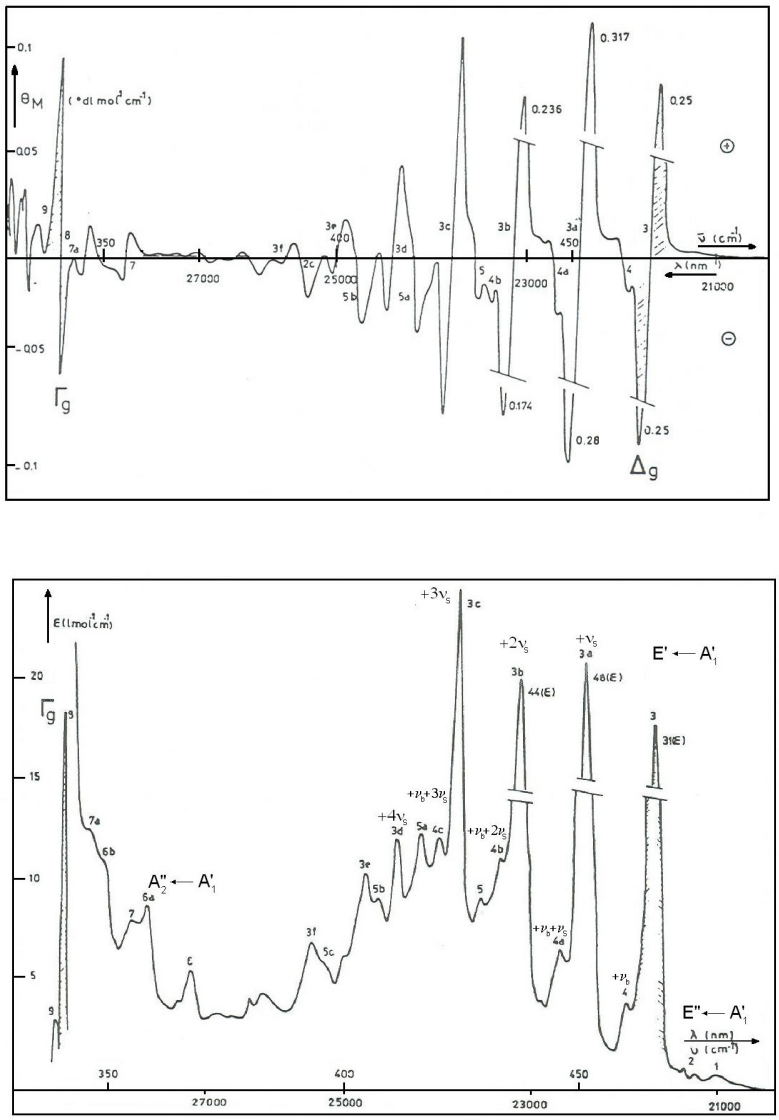

Figure A3.9. MCD spectrum (upper graph) and UV-Vis absorption spectrum (lower graph) of $NBu_4UO_2(NO_3)_3$ in a PMMA matrix at 4 K.*

* Görller-Walrand, C.; Colen, W. *Inorg. Chim. Acta* **1984**, *84*, 183-188.

Table A3.5. UV-Vis and MCD data of $[UO_2(NO_3)_3]^-$ in acetonitrile at room temperature. The MCD column gives the type and sign of the MCD term.

Band	ν / cm^{-1}	$\Delta\nu$ / cm^{-1}	λ / nm	ε / L mol^{-1} cm^{-1}	MCD	Identification	
						$D_{\infty h}$	D_{3h}
I_0	20585	--	486	0.9	--	Π_g	E”
II_0	21432	847	467	18.9	–A	Δ_g	E’
II'_0	21668	236	461	5.7	+A	$\Delta_g + \nu_b$	E’ + ν_b
II_1	22143	475	452	30.9	–A	$\Delta_g + \nu_s$	E’ + ν_s
II'_1	22386	243	447	10.5	+A	$\Delta_g + \nu_b + \nu_s$	E’ + ν_b + ν_s
II_2	22857	471	437	29.3	–A	$\Delta_g + 2\nu_s$	E’ + $2\nu_s$
II'_2	23111	254	433	15.3	+A	$\Delta_g + \nu_b + 2\nu_s$	E’ + ν_b + $2\nu_s$
II_3	23563	452	424	21.6	–A	$\Delta_g + 3\nu_s$	E’ + $3\nu_s$
II'_3	23866	303	419	15.2	+A	$\Delta_g + \nu_b + 3\nu_s$	E’ + ν_b + $3\nu_s$
II_4	24015	149	416	14.4		(Δ_g, Γ_g) + ν_s; $\Delta_g + 4\nu_s$	E’ + ν_s; E’ + $4\nu_s$
	24254	239	412	14.0			
III + IV	24564	310	407	11.3	--	This part of the spectrum contains the progressions in the symmetric stretching vibration ν_s of the electronic transitions $\Delta_g \leftarrow \Sigma_g^+$ and (Δ_g, Γ_g) $\leftarrow \Sigma_g^+$ (both E’ $\leftarrow$ A’$_1$ in D_{3h}).	
	25284	720	395	6.9	--		
	26082	798	383	4.1	--		
V_0	27218	1136	367	6.0	--	Φ_g	A”$_2$
V_1	27964	746	358	11.3	--	$\Phi_g + \nu_s$	A”$_2$ + ν_s
V_2	28744	780	348	20.4	--	$\Phi_g + 2\nu_s$	A”$_2$ + $2\nu_s$

2.2 Ionic liquids [C₄mim][Tf₂N] and [bmpyr][Tf₂N]

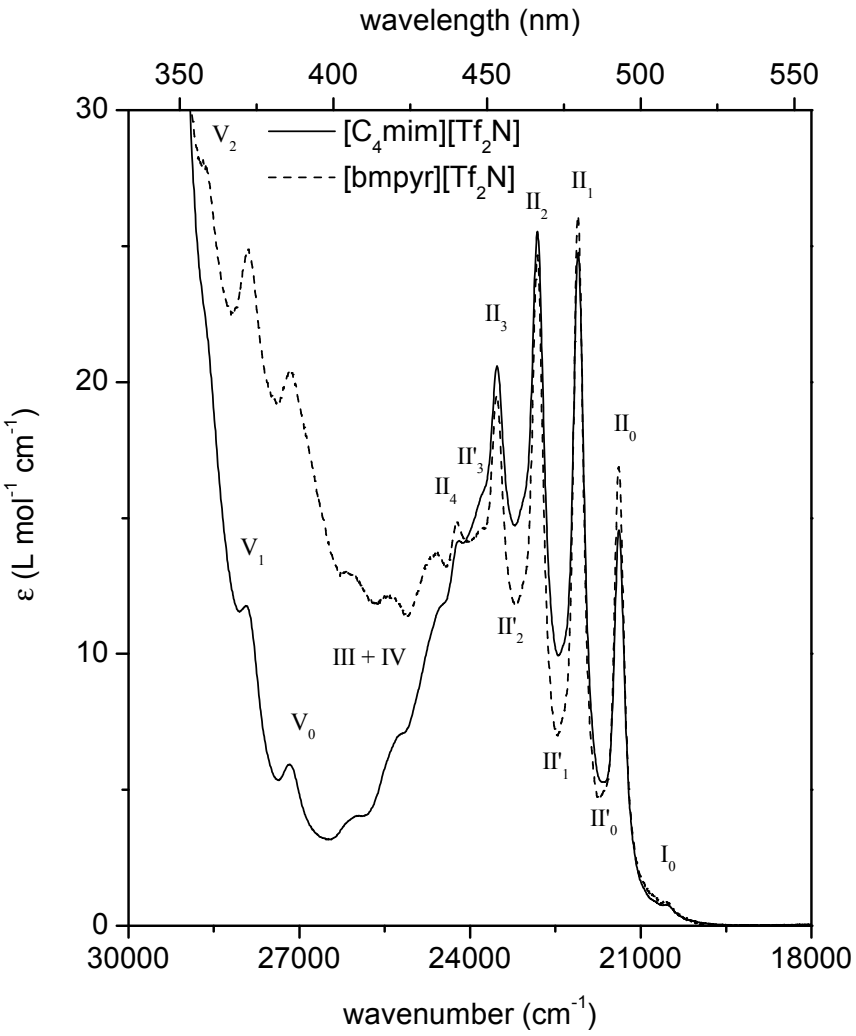

Figure A3.10. UV-Vis absorption spectra of $[UO_2(NO_3)_3]^-$ in $[C_4mim][Tf_2N]$ and $[bmpyr][Tf_2N]$ at room temperature. Metal-to-ligand ratio is 1:4. The uranyl concentrations are 5×10^{-2} mol L^{-1} in $[C_4mim][Tf_2N]$ and 10^{-2} mol L^{-1} in $[bmpyr][Tf_2N]$.

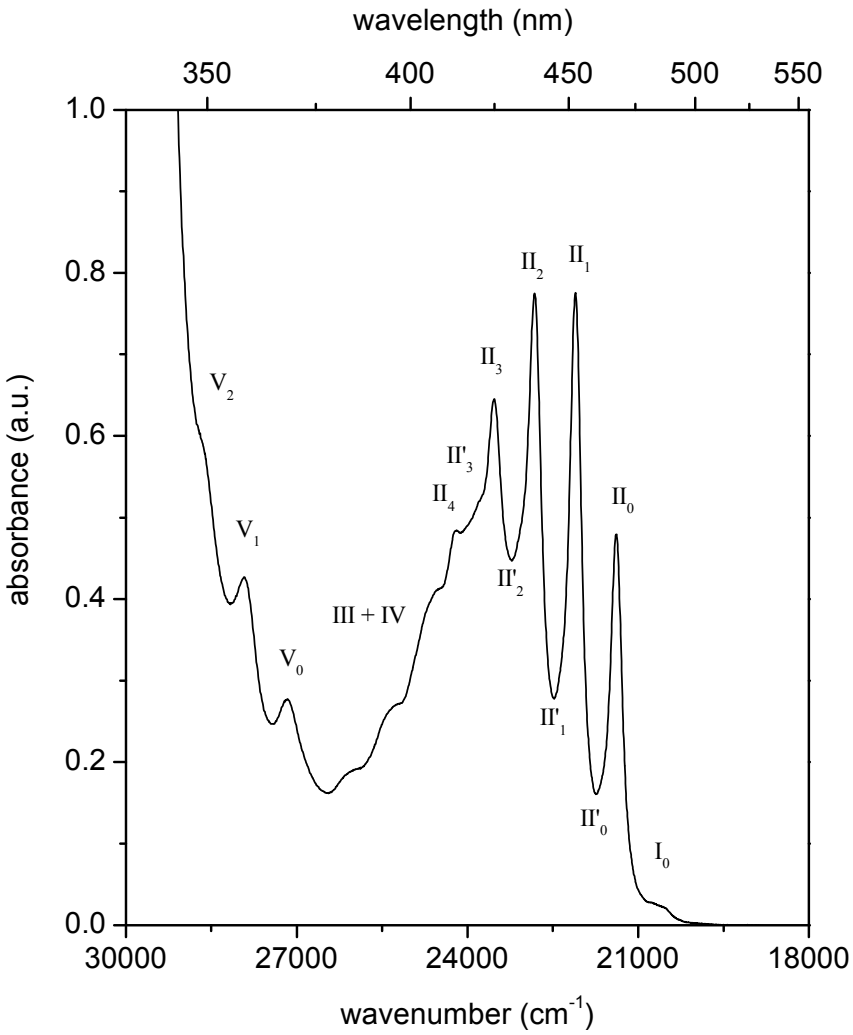

Figure A3.11. UV-Vis absorption spectrum of UO_3 in HNO_3/[C_4mim][Tf_2N] at room temperature. The uranyl concentration is 5×10^{-2} mol L^{-1}.

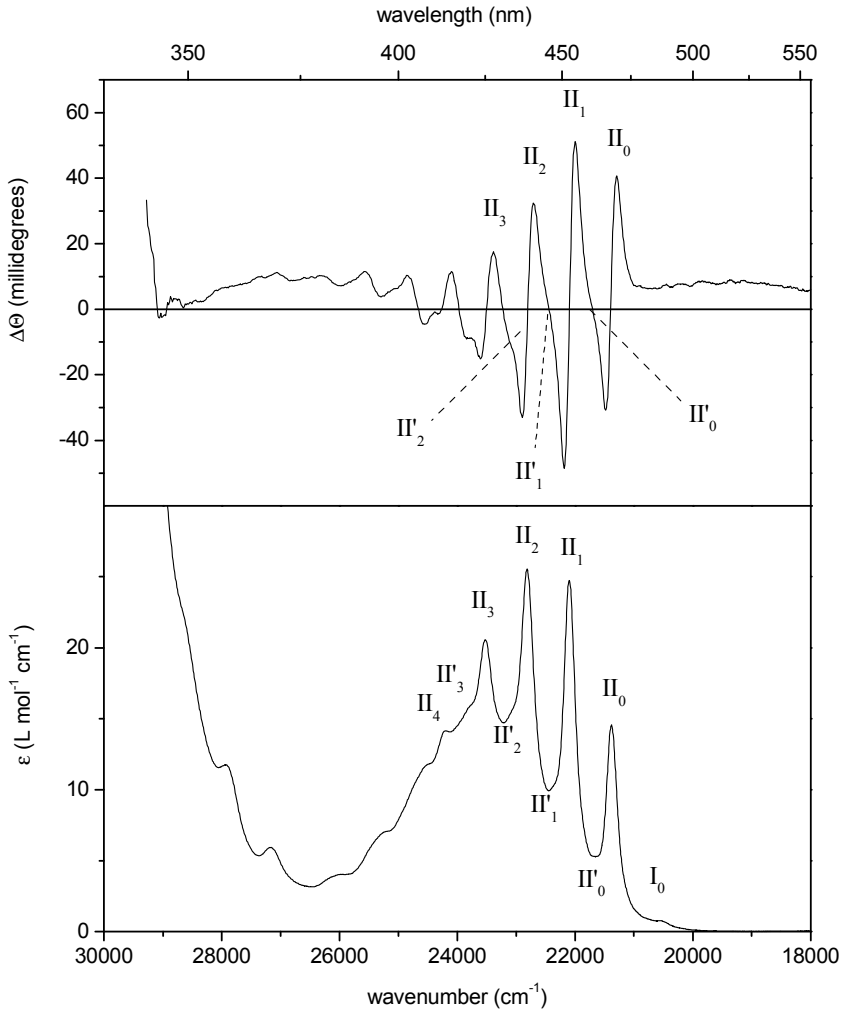

Figure A3.12. MCD (upper graph) and UV-Vis absorption (lower graph) spectra of $[UO_2(NO_3)_3]^-$ in $[C_4mim][Tf_2N]$ at room temperature. Metal-to-ligand ratio is 1:4. Concentrations are $[UO_2^{2+}] = 5 \times 10^{-2}$ mol L^{-1} and $[NO_3^-] = 2 \times 10^{-1}$ mol L^{-1}.

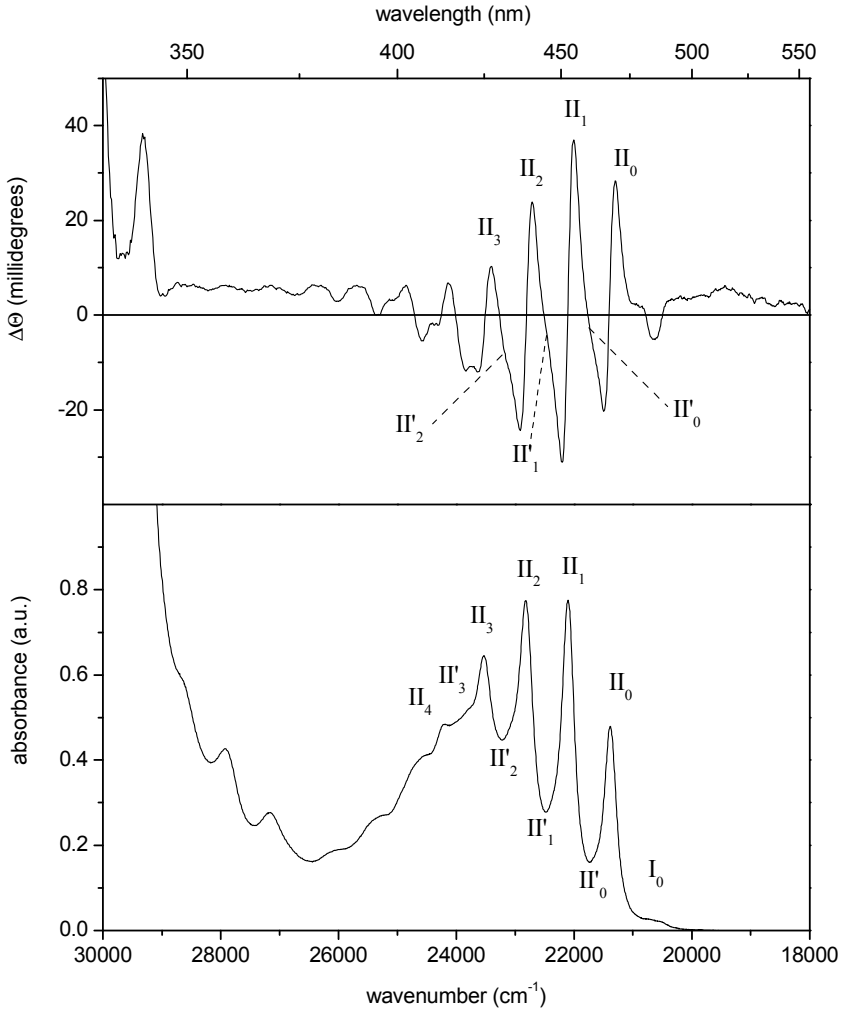

Figure A3.13. MCD (upper graph) and UV-Vis absorption (lower graph) spectra of UO_3 in HNO_3/[C_4mim][Tf_2N] at room temperature. The uranyl concentration is 5×10^{-2} mol L^{-1}.

Table A3.6. UV-Vis and MCD data of $[UO_2(NO_3)_3]^-$ in $[C_4mim][Tf_2N]$ and $[bmpyr][Tf_2N]$ at room temperature. The numbers in parentheses represent the data of UO_3 in $HNO_3/[C_4mim][Tf_2N]$, expressed in absorbance (arbitrary units). The MCD column gives the type and sign of the MCD term.

	$[C_4mim][Tf_2N]$					$[bmpyr][Tf_2N]$				Identification	
Band	ν / cm^{-1}		Δν / cm^{-1}	ε / L mol^{-1} cm^{-1}		ν / cm^{-1}	Δν / cm^{-1}	ε / L mol^{-1} cm^{-1}	MCD	$D_{\infty h}$	D_{3h}
I_0	20563	(20610)	--	0.8	(0.2)	20551	--	0.9	--	Π_g	E"
II_0	21381	(21386)	818	14.6	(0.50)	21359	808	16.9	–A	Δ_g	E'
II'_0	21566	(21650)	185	5.6	(0.18)	21650	291	5.0	+A	$\Delta_g + \nu_b$	$E' + \nu_b$
II_1	22099	(22104)	533	24.8	(0.77)	22099	449	26.1	–A	$\Delta_g + \nu_s$	$E' + \nu_s$
II'_1	22356	(22391)	257	10.3	(0.30)	22371	272	7.7	+A	$\Delta_g + \nu_b + \nu_s$	$E' + \nu_b + \nu_s$
II_2	22815	(22821)	459	25.5	(0.77)	22815	444	24.7	–A	$\Delta_g + 2\nu_s$	$E' + 2\nu_s$
II'_2	23084	(23127)	269	15.5	(0.46)	23089	274	12.4	+A	$\Delta_g + \nu_b + 2\nu_s$	$E' + \nu_b + 2\nu_s$
II_3	23529	(23529)	445	20.6	(0.64)	23535	446	19.5	–A	$\Delta_g + 3\nu_s$	$E' + 3\nu_s$
II'_3	23747	(23759)	218	16.0	(0.52)	23826	291	14.6	+A	$\Delta_g + \nu_b + 3\nu_s$	$E' + \nu_b + 3\nu_s$
II_4	24004	(24010)	257	14.5	(0.49)	24102	276	14.2		$(\Delta_g, \Gamma_g) + \nu_s$; $\Delta_g + 4\nu_s$	$E' + \nu_s$; $E' + 4\nu_s$
	24201	(24190)	197	14.2	(0.48)	24225	123	14.9			
III + IV	24510	(24498)	309	11.8	(0.41)	24612	387	13.7	--	The progressions in the symmetric stretching vibration ν_s of the electronic transitions $\Delta_g \leftarrow \Sigma_g^+$ and $(\Delta_g, \Gamma_g) \leftarrow \Sigma_g^+$ (both $E' \leftarrow A'_1$ in D_{3h}).	
	25259	(25291)	749	7.0	(0.27)	25419	807	12.1	--		
	26021	(25947)	762	4.0	(0.19)	26076	657	12.9	--		
V_0	27166	(27159)	1145	5.9	(0.28)	27166	1090	20.4	--	Φ_g	$A"_2$
V_1	27941	(27925)	775	11.8	(0.43)	27910	744	24.9	--	$\Phi_g + \nu_s$	$A"_2 + \nu_s$
V_2	28694	(28694)	753	23.0	(0.60)	28736	826	28.1	--	$\Phi_g + 2\nu_s$	$A"_2 + 2\nu_s$

3 $[UO_2(18\text{-crown-6})]^{2+}$

3.1 Acetonitrile

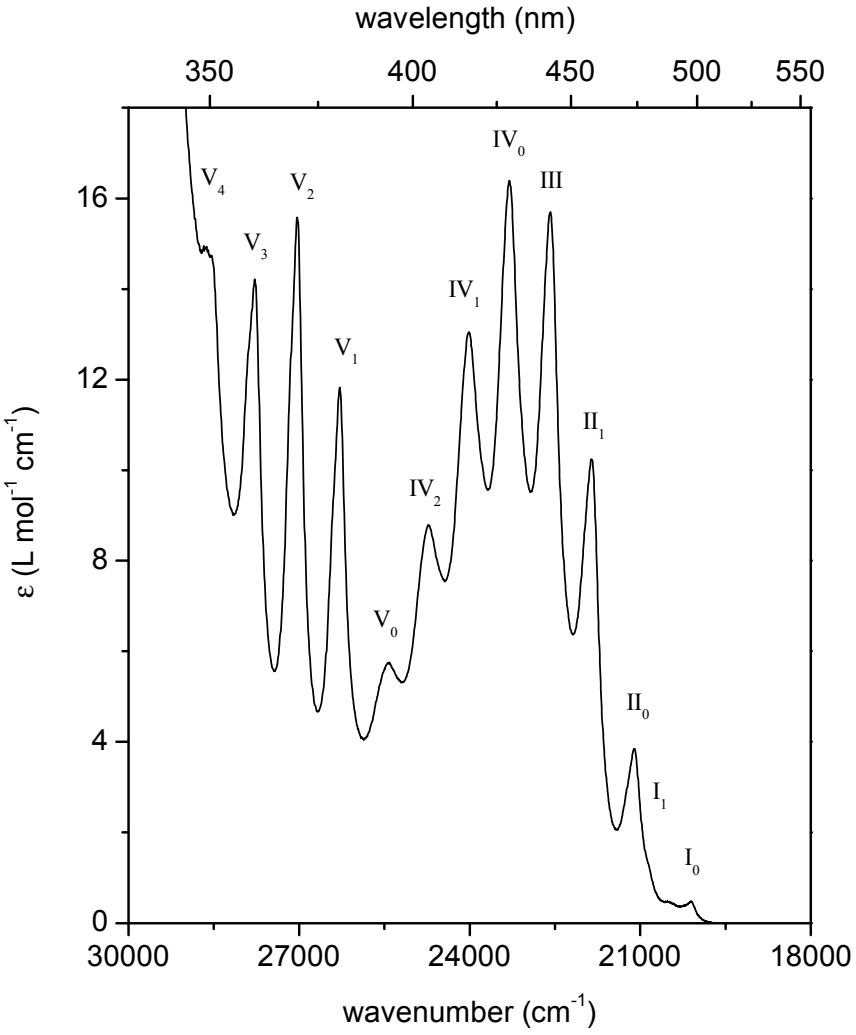

Figure A3.14. UV-Vis absorption spectrum of $[UO_2(18\text{-crown-6})]^{2+}$ in acetonitrile at room temperature. Metal-to-ligand ratio is 1:2. Concentrations are $[UO_2^{2+}] = 5 \times 10^{-2}$ mol L^{-1} and [18-crown-6] = 10^{-1} mol L^{-1}.

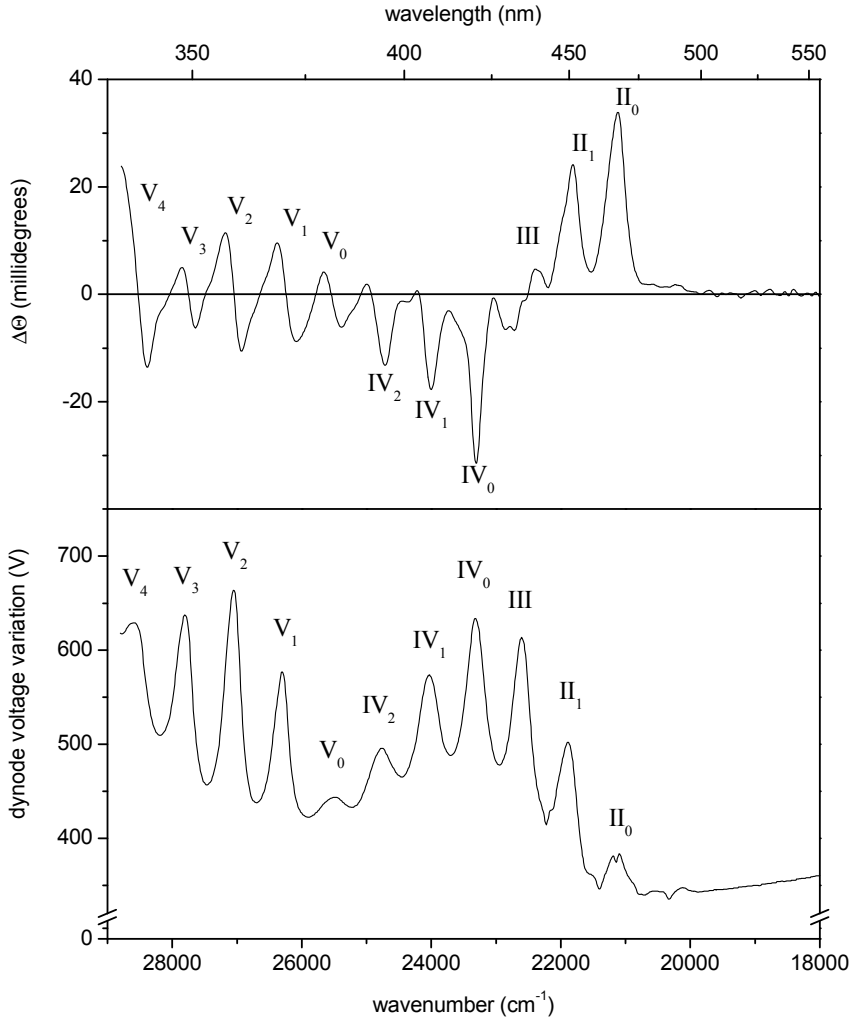

Figure A3.15. MCD (upper graph) and dynode voltage (lower graph) spectra of $[UO_2(18\text{-crown-6})]^{2+}$ in acetonitrile at room temperature. The uranyl concentration is approximately 10^{-1} mol L^{-1}.*

* De Houwer, S.; Servaes, K.; Görller-Walrand, C. *Phys. Chem. Chem. Phys.* **2003**, *5*, 1164-1168.

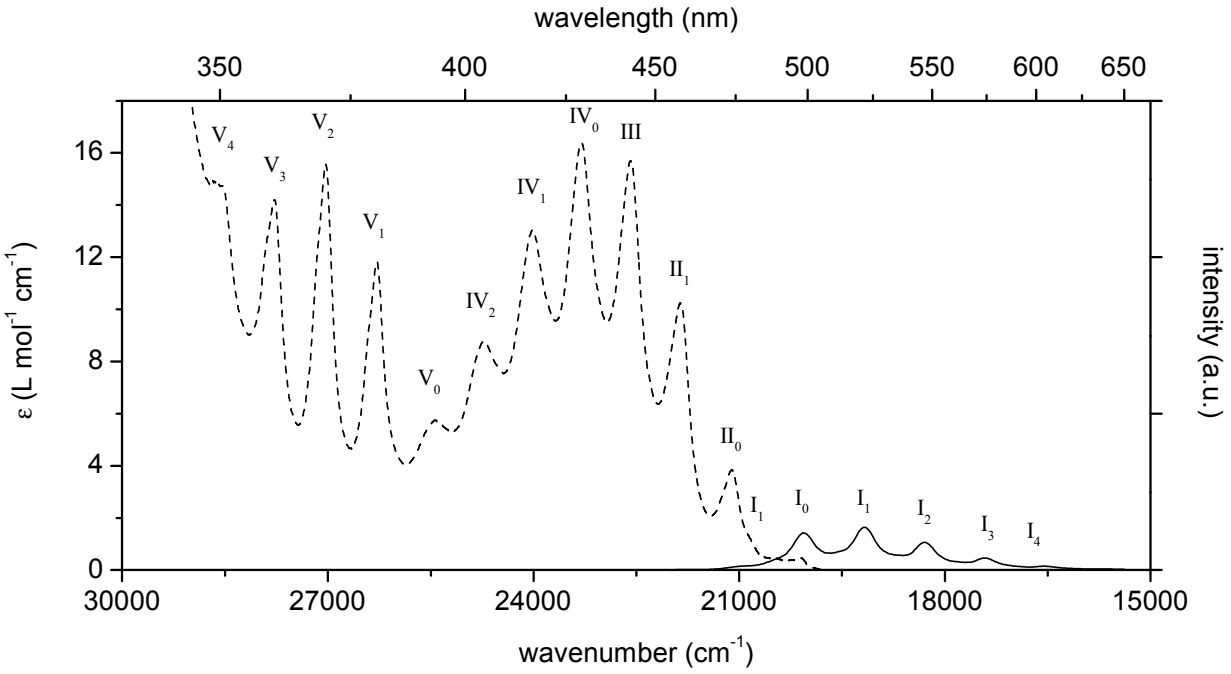

Figure A3.16. Emission (——) and absorption (-----) spectra of $[UO_2(18\text{-crown-6})]^{2+}$ in acetonitrile at room temperature. Metal-to-ligand ratio is 1:2. Concentrations are $[UO_2^{2+}] = 5 \times 10^{-2}$ mol L^{-1} for absorption and $[UO_2^{2+}] = 4 \times 10^{-3}$ mol L^{-1} for emission.

Table A3.7. UV-Vis and MCD data of $[UO_2(18\text{-crown-6})]^{2+}$ in acetonitrile at room temperature. The column MCD gives the type and sign of the MCD term. MCD data are taken from De Houwer et al., *Phys. Chem. Chem. Phys.* **2003**, *5*, 1164-1168.

Band	ν / cm^{-1}	$\Delta\nu$ / cm^{-1}	λ / nm	ε / L mol^{-1} cm^{-1}	MCD	Identification		
						$D_{\infty h}$	D_{3d}	D_3
I_0	20109	--	497	0.5	--	Π_g	E_{1g}	E
I_1	20859	750	479	1.4	--	$\Pi_g + \nu_s$	$E_{1g} + \nu_s$	$E + \nu_s$
II_0	21101	242	474	3.9	+B	Φ_g	A_{2g}	A_2
II_1	21858	757	457	10.3	+B	$\Phi_g + \nu_s$	$A_{2g} + \nu_s$	$A_2 + \nu_s$
III	22578	720	443	15.8	–A	Δ_g	E_g	E
IV_0	23299	721	429	16.5	–B	Φ_g	A_{2g}	A_2
IV_1	24015	716	416	13.1	–B	$\Phi_g + \nu_s$	$A_{2g} + \nu_s$	$A_2 + \nu_s$
IV_2	24734	719	404	8.8	–B	$\Phi_g + 2\nu_s$	$A_{2g} + 2\nu_s$	$A_2 + 2\nu_s$
V_0	25432	698	393	5.8	+A	Γ_g	E_g	E
V_1	26281	849	380	11.9	+A	$\Gamma_g + \nu_s$	$E_g + \nu_s$	$E + \nu_s$
V_2	27034	753	370	15.6	+A	$\Gamma_g + 2\nu_s$	$E_g + 2\nu_s$	$E + 2\nu_s$
V_3	27778	744	360	14.3	+A	$\Gamma_g + 3\nu_s$	$E_g + 3\nu_s$	$E + 3\nu_s$
V_4	28629	851	349	15.0	+A	$\Gamma_g + 4\nu_s$	$E_g + 4\nu_s$	$E + 4\nu_s$

Table A3.8. Emission data of $[UO_2(18\text{-crown-6})]^{2+}$ in acetonitrile at room temperature.

Band	ν / cm^{-1}	$\Delta\nu$ / cm^{-1}	λ / nm	I / a.u.	Identification		
					$D_{\infty h}$	D_{3d}	D_3
I_0	20071	--	498	11.8	Π_g	E_{1g}	E
I_1	19182	889	521	13.6	$\Pi_g - \nu_s$	$E_{1g} - \nu_s$	$E - \nu_s$
I_2	18297	885	546	8.9	$\Pi_g - 2\nu_s$	$E_{1g} - 2\nu_s$	$E - 2\nu_s$
I_3	17443	854	573	3.9	$\Pi_g - 3\nu_s$	$E_{1g} - 3\nu_s$	$E - 3\nu_s$
I_4	16563	880	604	1.2	$\Pi_g - 4\nu_s$	$E_{1g} - 4\nu_s$	$E - 4\nu_s$

3.2 Ionic liquids [C₄mim][Tf₂N] and [bmpyr][Tf₂N]

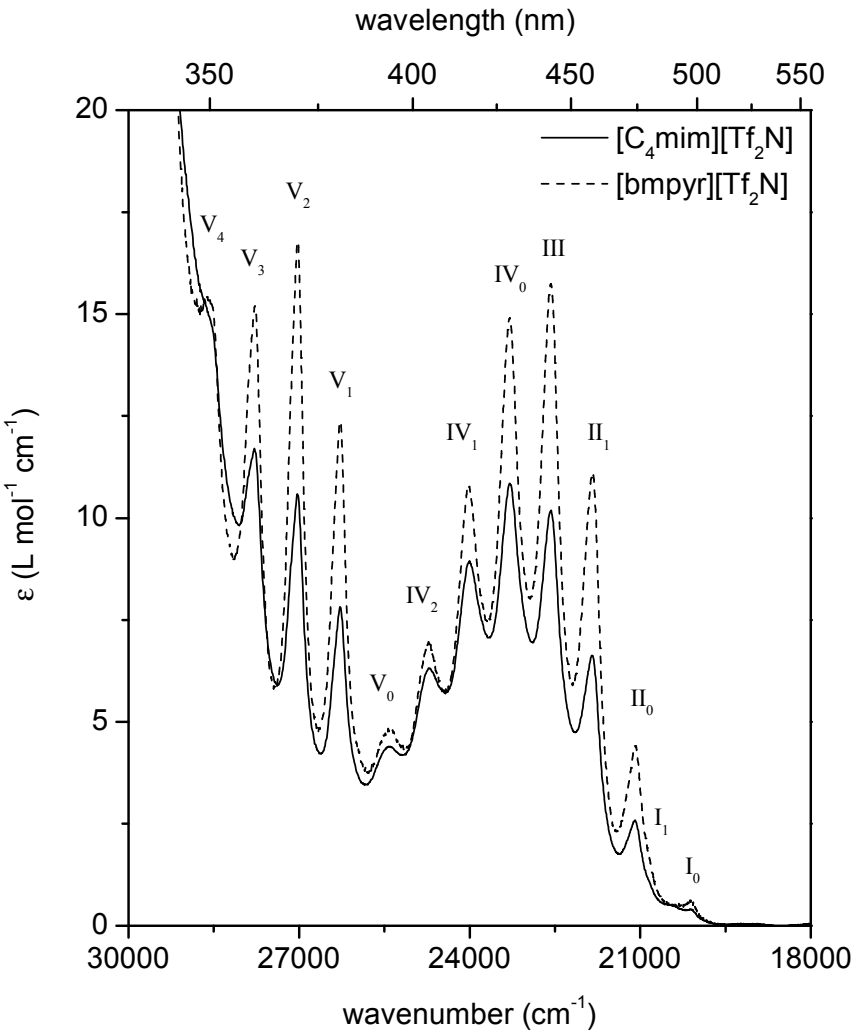

Figure A3.17. UV-Vis absorption spectra of $[UO_2(18\text{-crown-6})]^{2+}$ in $[C_4mim][Tf_2N]$ and $[bmpyr][Tf_2N]$ at room temperature. Metal-to-ligand ratio is 1:2. The uranyl concentrations are 5×10^{-2} mol L^{-1} in $[C_4mim][Tf_2N]$ and 10^{-2} mol L^{-1} in $[bmpyr][Tf_2N]$.

Table A3.9. UV-Vis data of $[UO_2(18\text{-crown-6})]^{2+}$ in $[C_4mim][Tf_2N]$ and $[bmpyr][Tf_2N]$ at room temperature.

$[C_4mim][Tf_2N]$				$[bmpyr][Tf_2N]$			Identification		
Band	ν / cm^{-1}	$\Delta\nu$ / cm^{-1}	ε / L mol^{-1} cm^{-1}	ν / cm^{-1}	$\Delta\nu$ / cm^{-1}	ε / L mol^{-1} cm^{-1}	$D_{\infty h}$	D_{3d}	D_3
I_0	20092	--	0.4	20125	--	0.6	Π_g	E_{1g}	E
I_1	20851	759	1.1	20890	765	2.0	$\Pi_g + \nu_s$	$E_{1g} + \nu_s$	$E + \nu_s$
II_0	21093	242	2.6	21088	198	4.4	Φ_g	A_{2g}	A_2
II_1	21844	751	6.6	21839	751	11.1	$\Phi_g + \nu_s$	$A_{2g} + \nu_s$	$A_2 + \nu_s$
III	22578	734	10.2	22594	755	15.6	Δ_g	E_g	E
IV_0	23299	721	10.8	23288	694	14.9	Φ_g	A_{2g}	A_2
IV_1	24004	705	8.9	24021	733	10.8	$\Phi_g + \nu_s$	$A_{2g} + \nu_s$	$A_2 + \nu_s$
IV_2	24722	718	6.3	24722	701	7.0	$\Phi_g + 2\nu_s$	$A_{2g} + 2\nu_s$	$A_2 + 2\nu_s$
V_0	25419	697	4.4	25387	665	4.8	Γ_g	E_g	E
V_1	26274	855	7.8	26274	887	12.4	$\Gamma_g + \nu_s$	$E_g + \nu_s$	$E + \nu_s$
V_2	27027	753	10.6	27027	753	16.8	$\Gamma_g + 2\nu_s$	$E_g + 2\nu_s$	$E + 2\nu_s$
V_3	27785	758	11.7	27778	751	15.2	$\Gamma_g + 3\nu_s$	$E_g + 3\nu_s$	$E + 3\nu_s$
V_4	28653	868	15.3	28629	851	15.5	$\Gamma_g + 4\nu_s$	$E_g + 4\nu_s$	$E + 4\nu_s$

A4 CRYSTALLOGRAPHIC DATA

1 Crystal structure of $[(UO_2)_2(\mu_2\text{-}OH)_2(H_2O)_6][UO_2Br_4]$ (18-crown-6)$_4$

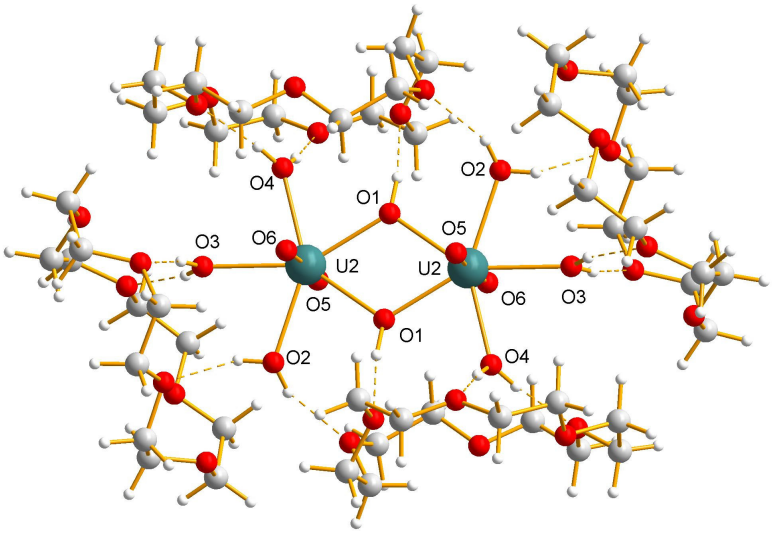

Figure A4.1. Cut-out from the crystal structure of $[(UO_2)_2(\mu_2\text{-}OH)_2(H_2O)_6][UO_2Br_4]$ (18-crown-6)$_4$, showing the $[(UO_2)_2(\mu_2\text{-}OH)_2(H_2O)_6]^{2+}$ cation surrounded by four 18-crown-6 moieties, attached by strong hydrogen bonding.

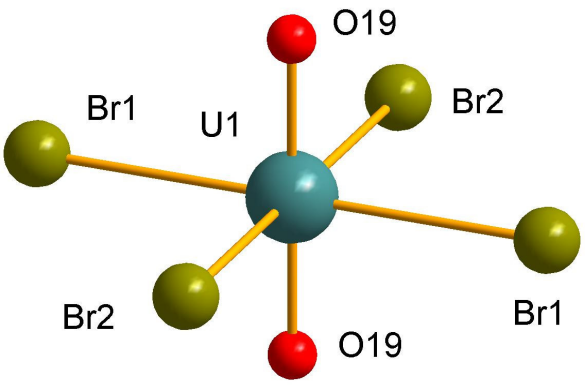

Figure A4.2. $[UO_2Br_4]^{2-}$ anion of the structure $[(UO_2)_2(\mu_2\text{-}OH)_2(H_2O)_6][UO_2Br_4](18\text{-crown-}6)_4$.

The crystal structure of $[(UO_2)_2(\mu_2\text{-}OH)_2(H_2O)_6][UO_2Br_4](18\text{-crown-}6)_4$ consists of $[(UO_2)_2(\mu_2\text{-}OH)_2(H_2O)_6]^{2+}$ cations, $[UO_2Br_4]^{2-}$ anions and 18-crown-6 moieties, attached by hydrogen bonding. The $[(UO_2)_2(\mu_2\text{-}OH)_2(H_2O)_6]^{2+}$ cations consist of UO_2^{2+}-dimers bridged by two hydroxides (distances: U1-O1 = 2.3022(29) Å and U1-O1' = 2.3022(27) Å). Additionally, three water molecules are coordinated to each uranyl unit (distances: U1-O2 = 2.4088(25) Å, U1-O3 = 2.4332(25) Å and U1-O4 = 2.4228(24) Å). An inversion centre is located in the centre of this moiety. All hydrogen atoms of the coordinating water molecules and the hydroxide groups could be localized in the difference Fourier map. The $[(UO_2)_2(\mu_2\text{-}OH)_2(H_2O)_6]^{2+}$ cations are surrounded by four 18-crown-6 molecules. Strong hydrogen bonding is found for all coordinated water molecules and hydroxide groups and ranges from 2.710 Å to 2.828 Å.

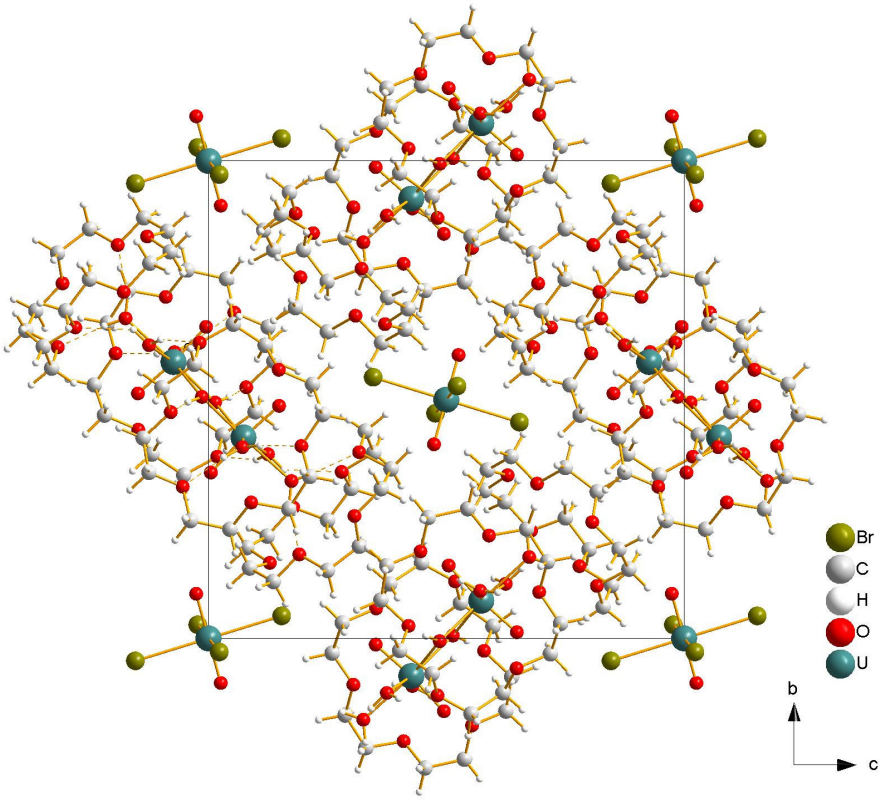

Figure A4.3. Packing of the crystal structure of $[(UO_2)_2(\mu_2\text{-}OH)_2(H_2O)_6][UO_2Br_4](18\text{-crown-}6)_4$, viewed along the a-axis.

Table A4.1. Crystallographic data of $[(UO_2)_2(\mu_2\text{-}OH)_2(H_2O)_6][UO_2Br_4](18\text{-crown-}6)_4$.

$[(UO_2)_2(\mu_2\text{-}OH)_2(H_2O)_6][UO_2Br_4](18\text{-crown-}6)_4$	
Empirical formula	$4(C_{12}H_{24}O_6)\cdot H_2O_{12}U_2\cdot Br_4O_2U$
Formula mass	2316.95 g mol^{-1}
Lattice constants	a = 12.1149(9) Å b = 17.6649(11) Å c = 17.7492(10) Å β = 99.113(4)°
Cell volume	3750.5(4) Å³
Z	2
Crystal system	monoclinic
Space group	$P2_1/c$ (no. 14)
Density / g cm^{-3}	2.052
F(000)	2212
Absorption correction	multi-scan Bruker SADABS
μ	21.28 mm^{-1}
Reflections measured	37605
Symm. independent	7179
R_{int}	0.118
Parameters	461
R_1 ($F_0 > 2s(F_0)$)	0.051
wR_2 (all data)	0.117
Goodness of fit	1.00
Crystal size	0.25 × 0.14 × 0.1 mm
Crystal shape	block, yellow

2 Crystal structure of $[C_6mim]_2[UO_2Br_4]$

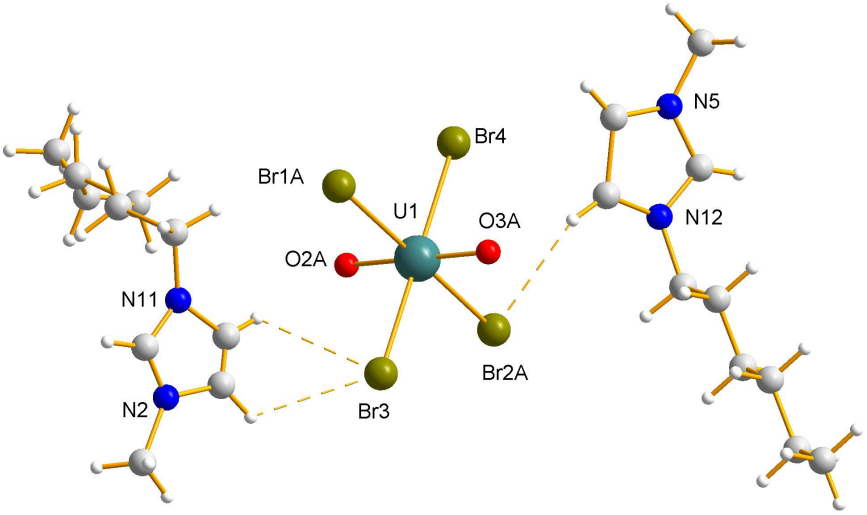

Figure A4.4. Cut-out from the crystal structure of $[C_6mim]_2[UO_2Br_4]$, showing the $[UO_2Br_4]^{2-}$ anion with weak hydrogen bonding to two surrounding $[C_6mim]^+$ cations.

The crystal structure of $[C_6mim]_2[UO_2Br_4]$ consists of $[C_6mim]^+$ cations (C_6mim = 1-hexyl-3-methylimidazolium) and $[UO_2Br_4]^{2-}$ anions. Weak hydrogen bonding interactions can be found between the bromides and the acidic hydrogen atoms of the imidazolium cations and range from 2.871 Å to 3.143 Å. Each two bromide atoms and the two axial oxygen atoms of each of the three crystallographic independent $[UO_2Br_4]^{2-}$ anions in the unit cell are disordered.

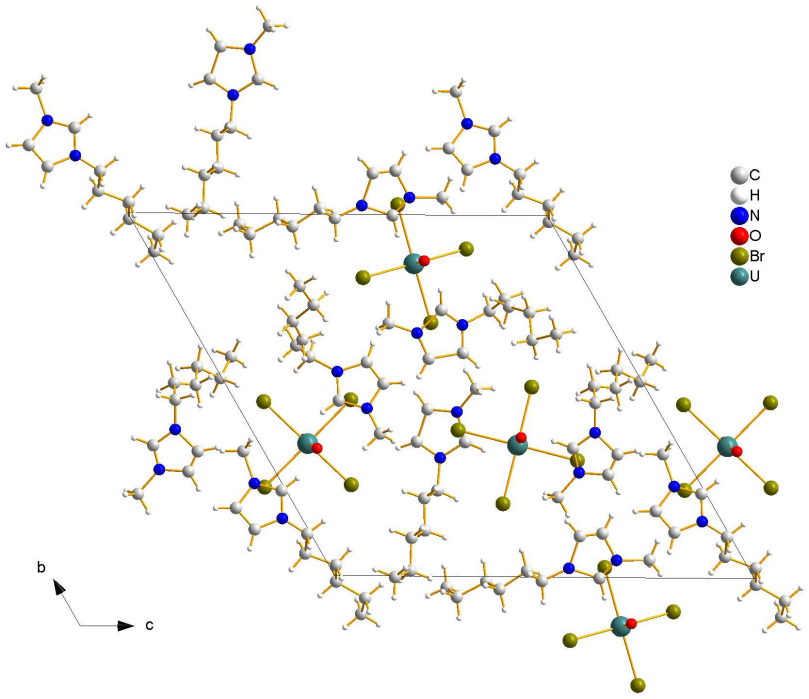

Figure A4.5. Packing of the crystal structure of $[C_6mim]_2[UO_2Br_4]$, viewed along the a-axis.

Table A4.2. Crystallographic data of $[C_6mim]_2[UO_2Br_4]$.

$[C_6mim]_2[UO_2Br_4]$	
Empirical formula	$C_{80}H_{100}Br_{16}N_8O_{32}U_4$
Formula mass	3916.36 g mol^{-1}
Lattice constants	a = 7.167 Å b = 19.372 Å c = 19.373 Å α = 118.51° β = 97.03° γ = 97.11°
Cell volume	3916.36
Z	1
Crystal system	triclinic
Space group	*P*1 (no. 1)
Density / g cm^{-3}	2.835
F(000)	2832
Absorption correction	multi-scan Bruker SADABS
μ	28.56 mm^{-1}
Reflections measured	8420
Symm. independent	8420
R_{int}	0.1347
Parameters	151
R_1 ($F_0 > 2s(F_0)$)	0.047
wR_2 (all data)	0.121
Goodness of fit	1.02
Crystal size	0.3 × 0.2 × 0.2 mm
Crystal shape	block, yellow

3 Experimental details

X-ray intensity data were collected on a SMART 6000 diffractometer, equipped with a CCD detector, using Cu-Kα radiation (λ = 1.54178 Å). The images were interpreted and integrated with the program SAINT from Bruker[1]. All four structures were solved by direct methods and refined by full-matrix least-squares on F2 using the SHELXTL program package[2]. Non-hydrogen atoms were anisotropically refined and the hydrogen atoms in the riding mode with isotropic temperature factors were fixed at 1.2 times U(eq) of the parent atoms (1.5 times for methyl groups).

[1] SAINT, Bruker Analytical X-ray Systems Inc., Madison, WI, Manual Version 5/6.0, **1997**.
[2] SHELXTL-PC, Bruker Analytical X-ray Systems Inc., Madison, WI, Manual Version 5.1, **1997**.